Carbon dioxide in binary geothermal systems

Origin, handling and utilisation possibilities

Zur Erlangung des akademischen Grades einer

DOKTORIN DER NATURWISSENSCHAFTEN

(Dr. rer. nat.)

von der KIT-Fakultät für
Bauingenieur-, Geo- und Umweltwissenschaften
des Karlsruher Instituts für Technologie (KIT)

genehmigte

DISSERTATION

von

M.Sc. Dorothee Fechner
(geb. Siefert)
aus Ettenheim

Tag der mündlichen Prüfung:
30. Juni 2023

Referent: Prof. Dr. Jochen Kolb
Korreferentin: apl. Prof. Dr. Kirsten Drüppel

Karlsruhe (2023)

Danke.

Als ich mich nach meinem Masterstudium entschied den Weg einer Promotion zu gehen, hatte ich schon von meiner Kollegin Hanna teilweise mitbekommen, was das bedeutet. Und dann, als ich im Büro Sören gegenübersaß, habe ich auch schnell bemerkt, wie viel Durchhaltevermögen und Fleiß, aber auch vor allem Motivation für das Thema notwendig ist.

Jedoch, auch wenn das Thema bei der Anmeldung grob umrissen wurde, mit was beginnt man eigentlich? Und dann folgen Jahre, in denen sich öfter mal was ändert, das Thema fast gesamt umgeworfen wird, auch manche Tränen fließen, und am Ende ist man verwundert, was genau nun daraus geworden ist. Man stellt recht schnell fest, dass man nicht alle Antworten auf die sich zuvor gestellten Fragen hat. Man weiß aber, dass man ein Teil des Ganzen sein kann, und einen kleinen Schritt nach vorne geht, um ein wichtiges Zukunftsthema weiterzubringen.

Und man stellt auch bald fest, dass man das nicht allein schafft. Mit der Familie und Freunden habe ich einen Prozess durchgemacht, bei dem ich bald gemerkt habe, dass ich die Arbeit für andere nicht greifbar machen kann. Dann aber, auch als das Thema selbst in mir reifte, konnte ich immer besser umreißen, worum es geht, und es kommen dann auch plötzlich präzisere Fragen. Allerdings ist es nicht das, was wichtig ist. Es ist die Unterstützung, die man erfährt.

Hier möchte ich mich zutiefst bei meinen engsten Freunden und meiner Familie bedanken. Für die Zeit, die ich teilweise wenig bei Ihnen sein konnte, eher unaufmerksam war, weil andere Themen in meinem Kopf schwirrten, sie mich aber nie aufgegeben haben und mir gut zugeredet haben. Und dennoch: die Zeit mit euch war für mich so wertvoll. Vor allem, wenn ich mit meinen Nichten, meiner Schwester und Schwager Zeit verbringen konnte oder im Garten mit meinen Eltern abschalten konnte. Danke Mama und Papa für all die Jahre der Unterstützung. Das war sehr wichtig für mich. Danke an meine Schwiegereltern, die auch ihren Teil beigetragen haben, dass ich nach Karlsruhe gegangen bin. Theresa, Marie und David, die meine für sie sicherlich nicht so interessanten Texte durchgesehen haben. Piet, der auch wunderbar mein Englisch überprüft und dort viel Zeit investiert hat. Danke Lena, dass du immer ein offenes Ohr für mich hast.

Louise, die mich immer unterstützt hat und eigentlich immer zuversichtlicher war als ich selbst, dass ich das dann doch packe. Ich bin dir sehr dankbar für das gute Zureden, immer wieder. Vielen Dank für die vielen Postkarten und Päckchen, die mich immer aufgebaut haben.

Theresa, danke für die vielen Anregungen und lieben, sehr unterstützenden Worte. Du schaust einfach auf viele Themen viel genauer und hast mich dadurch manchmal weiter gebracht, in dem ich in einem anderen Blickwinkel auf die Themen schaute.

Carmen, danke für die Zeit in der WG, in der du mich beim Abendessen doch so oft aufgebaut hast. Ich werde diese Zeit nie vergessen. Danke an Sina, die immer meine Fragen beantwortet hat. Und ein Dank an Niko, der auch immer unterstützt hat, wo er konnte.

Danke an Nico, Vroni und Jonas, die mir in der Corona-Zeit die Mittagspausen zu einer noch wertvolleren Zeit gemacht haben - und da passt auch ein Dankeschön an die Offenburger Mädels-WG für die kulinarischen Mittagspausen.

Ein wichtiger Teil stellen natürlich auch meine Kolleg*Innen dar. Danke an die gesamten T-F Kolleg*Innen, Kolleg*Innen des Instituts. An Hanna, die anfangs immer zur Seite stand. Sören, mein Büropartner, der sich sehr viel Zeit nahm und immer ein offenes Ohr hat. An Eva, mit der ich viele tolle Lauf- und Kaffeedates hatte.

Ein Riesen-Dankeschön geht auch an die vielen lieben Menschen auf der Halilbeyli-Site in der Türkei, die mich mit vielen technischen, aber auch wunderbaren persönlichen Gesprächen weitergebracht haben: Danke unter anderem an Mehmet, Burçin, Tom, Dimi, Julia, Jörg, Ingmar, Stefan, Jens, Christian und, und, und... Es war eine tolle Zeit!

Ein riesiger Dank gilt Thomas (und seiner wunderbaren Familie), der immer mit neuen Ideen und sonst auch allem, unterstützt, wo er kann. Danke für diese Möglichkeit der Weiterentwicklung, danke für die Zeit in der Türkei und die immer tollen Abende bei euch.

Und natürlich: Danke, Elif (und auch an Søren und deine Familie), mit der jede Diskussion auf der Terrasse oder im Büro zwischen Tür und Angel wunderbar hilfreich war. Die mich aufgenommen hat, als wäre es selbstverständlich, beherbergt und vor allem bekocht hat. Ich liebe türkisches Essen, danke für diese wunderbare Erfahrung und Horizonterweiterung. Das ist so wertvoll für mich. Danke auch an Laura und Milena, die wunderbare Wegbegleiterinnen und Unterstützerinnen waren. Ich werde den „blue butterfly“-Abend nie vergessen. Danke an Guillaume, Carole und Albert (und das ganze Team von ÉSG), die mir einige Kongresse versüßt haben.

So - das Beste kommt zum Schluss: Danke an dich, Felix. Du hast alles abbekommen, hast mit mir gezweifelt, geweint, gelacht, mich unterstützt, hast zurückgesteckt, bist mit mir durch dick und dünn gegangen. Ich weiß, dass es nicht einfach war für dich. Ich kann nicht genug danken, danke für die Wegbegleitung. Das hat mich weiter gebracht, die Urlaube und Zeit mit dir abgelenkt. Danke für dein enormes Durchhaltevermögen, dein unendliches Verständnis, das Halt und Kraft geben. Wir sind dadurch noch mehr zusammengewachsen.

“Perfer et obdura, dolor hic tibi proderit olim.

Be patient and tough - someday this struggle will be useful to you.”

Ovid[1]

[1] Amores 3,11,7

Abstract

This study investigates the origin, handling and utilisation of Carbon dioxide (CO_2) in binary geothermal systems in three publications. Geothermal energy is an attractive option for decarbonising power and heat production, but non-condensable gases naturally present in the majority of geothermal reservoirs, especially CO_2, pose a challenge in terms of corrosion, precipitation, and environmental impact.

The importance of a multi-proxy approach is highlighted to obtain reliable stratigraphic correlations in geothermal exploration. Carbonate reservoir fluids are most likely saturated with CO_2 due to thermal decomposition of the rocks. Petrographical and geochemical data were used to correlate two different marble horizons from a geothermal exploration well in western Turkey with surface analogues. This correlation is essential for a better understanding of the reservoir geometry and supports the conceptual geological model prior to further geothermal drilling.

Furthermore, three different technical options are being explored, including pressure maintenance, a gas bypass system and a secondary gas turbine, to overcome the challenge of CO_2 handling during plant operation. The geothermal plant in Bruchsal, Germany, serves as a case study for process simulation and further analysis. The study concludes that a gas bypass that excludes CO_2 from the heat exchanger system is the best option to avoid CO_2 emissions and achieve the highest possible power output for Bruchsal plant conditions. At moderate to high gas content (5–20 g/L; 0.5–2 wt-%), a secondary gas turbine may be a suitable option for generating power in addition to usual plant layout. At lower brine CO_2 content (0–5 g/L or 0–0.5 wt-%; low salinity between 0–100 g/L), conventional pressure maintenance at a suitable pressure level is sufficient to handle the CO_2.

In addition to mitigating CO_2 emissions, this study also investigates the utilisation of CO_2 in precipitating lithium carbonate. The experiments reveal that CO_2 from a geothermal power plant, as well as potentially any other industrial CO_2, can be used to precipitate lithium carbonate. The recovery rate for lithium is comparable between the laboratory heterogeneous (up to 31.8 %) and homogeneous precipitation (up to 53.4 %) processes, with comparable purity achieved. The purity of the precipitates from the on-site experiments (Bruchsal geothermal power plant, Germany) with 84.4 and 93.3 % at 5 g/L and 10 g/L initial Li concentration, respectively, are only slightly lower than the results obtained with the laboratory set-up (88.3 and 94.8 %). The observations during the precipitation experiments reveal that the heterogeneous precipitation at 50 °C and higher initial Li concentration have a better performance in

terms of reaction time compared with the experiments at 25 °C and confirm supersaturation and precipitation kinetics being enhanced at higher reaction temperatures.

The utilisation of CO_2 in this way is sustainable since CO_2 is captured. One advantage would be the reduction of the CO_2 footprint and the positive environmental impact for both the product and the industrial process as the source of the CO_2 used. Further optimisation of the precipitation process could increase recovery rates. Recycling of the residual LiCl solution may also represent a viable option for increasing recovery.

Overall, this work presents a comprehensive study to the origin, handling, and utilisation of CO_2 in binary geothermal systems. The results offer profound insights into the challenges and potential opportunities for decarbonising power and heat production using deep geothermal energy. Utilising CO_2 in the production of lithium carbonate offers a promising avenue to reduce carbon emissions and increase resource recovery.

Zusammenfassung

Diese Studie untersucht in drei Veröffentlichungen die Herkunft, Handhabung und Nutzung von Kohlenstoffdioxid (CO_2) in binären geothermischen Systemen. Die geothermische Energiegewinnung ist eine attraktive Option für die Dekarbonisierung der Strom- und Wärmeerzeugung. Nicht kondensierbare Gase, die in den meisten geothermischen Reservoiren natürlicherweise vorhanden sind, insbesondere CO_2, stellen eine Herausforderung in Bezug auf Korrosion, Ausfällung und Umweltauswirkungen dar.

Die Bedeutung eines Multi-Proxy-Ansatzes wird aufgezeigt bei der Charakterisierung von Karbonat-Reservoiren, um eine zuverlässige stratigraphische Korrelation bei der geothermischen Exploration zu erhalten. Die karbonatischen Reservoirfluide sind aufgrund der thermischen Zersetzung der Gesteine sehr wahrscheinlich mit CO_2 gesättigt. Petrographische und geochemische Daten wurden verwendet, um zwei verschiedene Marmorhorizonte aus einer geothermischen Explorationsbohrung in der Westtürkei mit Oberflächenanaloga zu korrelieren. Diese Korrelation ist für ein besseres Verständnis der Reservoirgeometrie von wesentlicher Bedeutung und unterstützt das konzeptionelle geologische Modell vor weiteren geothermischen Bohrungen.

Darüber hinaus werden drei verschiedene technische Optionen untersucht: darunter Druckhaltung, ein Gas-Bypass-System und eine sekundäre Gasturbine, um die Herausforderung der CO_2-Handhabung während des Anlagenbetriebs zu meistern. Die geothermische Anlage in Bruchsal, Deutschland, dient als Fallbeispiel für die Prozesssimulation und weitere Analysen. Die Studie kommt zu dem Schluss, dass ein Gasbypass, der CO_2 aus dem Wärmetauschersystem ausschließt, die beste Option ist, um CO_2-Emissionen zu vermeiden und die höchstmögliche Leistung für die Bruchsaler Anlagenbedingungen zu erreichen. Bei einem mittleren bis höheren Gasgehalt (5–20 g/L; 0,5–2 wt-%) kann eine sekundäre Gasturbine eine geeignete Option zur Stromerzeugung zusätzlich zur üblichen Anlagenauslegung darstellen. Bei geringerem CO_2-Gehalt (0–5 g/L oder 0–0,5 wt-%; geringe Salinität zwischen 0–100 g/L) der Sole ist eine konventionelle Druckhaltung auf einem geeigneten Druckniveau ausreichend, um das CO_2 optimal handzuhaben.

Neben der Minderung der CO_2-Emissionen wird in dieser Studie auch die Nutzung von CO_2 bei der Ausfällung von Lithiumcarbonat untersucht. Die Experimente zeigen, dass CO_2 aus einer geothermischen Anlage, sowie potenziell jedes andere industrielle CO_2, für die Ausfällung von Lithiumcarbonat verwendet werden kann.

Die Rückgewinnungsrate für Lithium ist zwischen dem heterogenen (bis zu 31,8 %) und dem homogenen Fällungsprozess (bis zu 53,4 %) im Labor vergleichbar, wobei auch eine vergleichbare Reinheit erreicht wird. Die Reinheit der Ausfällungen aus den Experimenten an der Geothermieanlage (Bruchsal, Deutschland) mit einer initialen Li-Konzentration von 5 g/L und 10 g/L beträgt 84,4 % bzw. 93,3 %, was nur geringfügig niedriger ist als die Ergebnisse des Laboraufbaus (88,3 % bzw. 94,8 %). Die Beobachtungen während der Ausfällungsversuche zeigen, dass die heterogene Ausfällung bei 50 °C und höheren initialen Li-Konzentrationen im Vergleich zu den Experimenten bei 25 °C eine bessere Performance in Bezug auf die Reaktionszeit aufweist und bestätigen, dass die Übersättigung und die Fällungskinetik bei höheren Reaktionstemperaturen verbessert werden.

Die Verwendung von CO_2 auf diese Weise ist nachhaltig, da das CO_2 aufgefangen und wiederverwendet wird. Eine weitere Optimierung des Fällungsprozesses könnte die Rückgewinnungsraten erhöhen. Die Weiterverwendung der restlichen LiCl-Lösung könnte ebenfalls eine praktikable Option zur Steigerung der Rückgewinnung darstellen.

Insgesamt präsentiert diese Arbeit eine umfassende Betrachtung zur Herkunft, Handhabung und Nutzung von CO_2 in binären geothermischen Systemen. Die Ergebnisse zeigen detaillierte Ansätze für die Herausforderungen und potenziellen Möglichkeiten der Dekarbonisierung der Strom- und Wärmeerzeugung mit Hilfe der Tiefengeothermie. Die Nutzung von CO_2 bei der Herstellung von Lithiumcarbonat bietet einen vielversprechenden Weg zur Verringerung der Kohlenstoffemissionen und zur Steigerung der Ressourcengewinnung.

Acknowledgements

First of all, I would like to express my deep thanks to EnBW AG for the great support of my research and work. Without Thomas by my side, supporting me in all decisions, inspiring me with new thoughts and motivating me in all situations, this work would not have been possible. Thank you.

A big thank you goes to the Energy Joint Venture Borusan EnBW for the permission to work on the cutting samples of GP1 well in Western Turkey.

Furthermore, I want to thank the teams from laboratories at Karlsruhe Institute of Technology (Laboratory of Environmental and Raw Materials Analysis), CAU Kiel, University of Greifswald for the help with analysis and data interpretation. I am grateful for the support by C. Kotschenreuther, C. Mößner (both KIT), J. Herwig (GFZ) and C. Buse (GTN). I am thankful for the support and assistance by K. Slunitschek, R. Reich, M. Denker and J. Wagner (all KIT).

I want to thank the Geothermie-Gesellschaft Bruchsal GmbH and for the possibility to access the Bruchsal power plant. Thank you, Robin, for the assistance with the data management and the possibility to access the gas bypass and the support with gas measurements. Furthermore, I want to thank Thomas Kruse (KIT) for the great help with the software application.

A big thank you goes to all my co-authors, without whose support the work would not have been possible. Many thanks to J. Kolb, T. Kölbel, E. Eiche, M. Wolfgramm, J. Glodny, M. Kondek, E. Kaymakci, L. Herrmann, M. Graczyk-Zajac and T. Kluge. Thank you very much, Jochen, for your valuable support and your appreciative and detailed revisions throughout all these years.

Contents

List of Figures xv

List of Tables xvii

List of Abbreviations xix

List of Symbols xxiii

I. Fundamentals, motivation and objectives of the thesis 1

1. Introduction and fundamentals 3
1.1. Motivation . . . 4
1.2. Research Questions . . . 7
1.3. Scientific approach . . . 8
1.4. Thesis structure . . . 10
1.5. Fundamentals . . . 12
1.5.1. State of the art concepts of geothermal energy . . . 12
1.5.2. Deep geothermal energy in Turkey and Germany . . . 14
1.5.3. Non-condensable gases in geothermal energy - focus on carbon dioxide . . . 19
1.5.4. Gas breakout tests in Bruchsal (Germany) . . . 25

II. Geothermal reservoir rock characterisation and origin of Carbon dioxide 29

2. Geothermal reservoir rocks of the Büyük Menderes Graben 33
2.1. Introduction and basics . . . 34
2.2. Regional geology . . . 38
2.3. Study area . . . 40
2.4. Methods . . . 42
2.4.1. General procedure and petrography . . . 42
2.4.2. ICP-MS and ICP-OES analysis . . . 46

2.4.3. Stable carbon and oxygen isotopes . . . 47
2.4.4. Rb-Sr geochronology . . . 47
2.5. Results . . . 48
2.5.1. Petrography . . . 48
2.5.2. Geochemistry . . . 56
2.6. Discussion . . . 68
2.6.1. Comparison and stratigraphic correlation of cuttings with Paleozoic and Cretaceous marble from outcrops . . . 68
2.7. Conclusion of part II . . . 78

III. CO_2 handling in binary geothermal systems 79

3. CO_2 handling in binary geothermal systems 83
3.1. Introduction and basics . . . 84
3.2. Bruchsal geothermal power plant . . . 88
3.3. Methodological approach . . . 89
3.3.1. ASPEN Plus . . . 89
3.3.2. Model setup . . . 91
3.3.3. Thermal water composition . . . 92
3.3.4. Solubility calculation . . . 93
3.3.5. Technical solutions for CO_2 handling (options 1, 2 and 3) . . . 94
3.4. CO_2 solubility models . . . 96
3.5. Simulation results of three different CO_2 handling technical solutions . 97
3.6. Interpretation of simulation results . . . 102
3.7. Investigation of influencing parameters . . . 104
3.8. Conclusion of part III . . . 110

IV. Utilisation of geothermal brine related carbon dioxide 113

4. Utilisation of geothermal brine related carbon dioxide 117
4.1. Introduction . . . 118
4.2. Materials and methods . . . 120
4.2.1. Materials . . . 120
4.2.2. Precipitation method . . . 121
4.2.3. Mineralogical and geochemical characterisation . . . 123
4.2.4. Theoretical considerations . . . 124
4.3. Results . . . 126
4.3.1. Heterogeneous precipitation experiments in the laboratory and on-site . . . 126

4.3.2. Homogeneous precipitation experiments in the laboratory . . 127
4.3.3. Composition, purity and recovery of the precipitates 128
4.3.4. Mineralogy of the precipitate 131
4.4. Discussion 133
4.4.1. Precipitation performance: comparison of homogeneous and heterogeneous precipitation 133
4.4.2. Assessment of the utilisation of geothermal CO_2 for the precipitation of lithium carbonate 137
4.5. Conclusion of part IV 139

V. Implications and perspectives **141**

5. Major outcomes, conclusion and perspectives **143**
5.1. Major outcome for research 143
5.2. Major outcome for industrial exploitation 145
5.3. Conclusion and perspectives 147

Appendices **151**

Bibliography **171**

List of Figures

1.1. Geothermal potential of Turkey according to General Directorate of Mineral Research and Exploration (MTA) (2015). . . . 15
1.2. Three major geothermal provinces of Germany and the projects of the Upper Rhine Graben. . . . 18
1.3. Phase diagram of CO_2. . . . 22
1.4. Schematic illustration of the gas breakout (GBO) measurement device at the Bruchsal power plant. . . . 25

2.1. Simplified geological map of the Menderes Massif. . . . 34
2.2. Geological map of the study area with borehole GP-1 and outcrop locations. . . . 36
2.3. Methodological diagram to differentiate various marble types. . . . 43
2.4. Paleozoic marble: marble quarry SE of Koçarli village, southern escarpment of the BMG (Location T13). . . . 49
2.5. SEM-EDX of sample T13-2. . . . 50
2.6. Marble of three different outcrops at the northern escarpment of the BMG. . . . 51
2.7. Representative photomicrographs of Cretaceous marble (T1, T3 and T5). . . . 53
2.8. Marble-bearing sections of the geothermal exploration well GP-1. . . . 54
2.9. Representative photomicrographs of cutting samples of the GP-1 well. 55
2.10. Comparison of maximum grain size of various marbles. . . . 56
2.11. Major oxide geochemistry in wt-%. a) surface samples (Paleozoic, Cretaceous); b) cutting samples (well^S; well^D). . . . 58
2.12. PAAS-normalised Y and REE patterns for cutting and surface samples. 60
2.13. Boxplot showing the PAAS-normalised values and quartiles of Gd_{PAAS} /Lu_{PAAS} ratios. . . . 61
2.14. Cross plot of $\delta^{18}O$ and $\delta^{13}C$ isotopic signatures. . . . 63
2.15. a) $\delta^{18}O_{VSMOW}$ isotopic values and b) $\delta^{13}C_{VPDB}$ in ‰ from the samples in this study in comparison with common ranges of different rocks and waters . . . 64
2.16. Rb-Sr isochrons. . . . 67
2.17. Ce/Ce* vs. Pr/Pr* with Ce anomalies. . . . 73

2.18. Simplified cross-section of the BMG as half-graben structure with allocated nappes and the exploration well GP-1. 75

3.1. Gas bypass installed in Bruchsal to handle the CO_2 not dissolved in the brine at operational conditions. 90
3.2. Schematic process schemes of options 1-3. 95
3.3. CO_2 solubility in the H_2O - NaCl - CO_2 system 98
3.4. Theoretically minimum required pressures for single-phase conditions at different salinity and various CO_2 contents. 100
3.5. Simulation results of options 1, 2 and 3. 101
3.6. Simulation results of (a) option 1, (b) option 2 and (c) option 3 in terms of the power output according to various CO_2 contents and salinity. . 102
3.7. Results of sensitivity analysis. 106

4.1. a) On-site experimental set-up at the Bruchsal geothermal power plant with implemented Li-extraction; b) set-up for heterogeneous precipitation with CO_2. 123
4.2. Fraction of carbonic acid (H_2CO_3), hydrogen carbonate (HCO_3^-) and of carbonate (CO_3^{2-}) in water as a function of the pH. Modified after Wisotzky (2011). 125
4.3. a) Diagram (at 8 g/L Li concentration and 25 °C) showing the duration of heterogeneous precipitation with CO_2 until pH of 8 was reached. At the start of the CO_2 supply, the temperature rises to 35 °C; b) Li_2CO_3 purity of heterogeneous and homogeneous precipitation (laboratory and on-site); c) Li_2CO_3 recovery of heterogeneous and homogeneous precipitation (laboratory and on-site). Legend is given in b); d) Composition of precipitate of on-site experiments. 128
4.4. Evaluation of homogeneous and heterogeneous precipitates with and without washing step regarding recovery and purity. 130
4.5. XRD patterns and SEM images of precipitates. 133

B.1. Depiction of the simulation results for the specific heat capacity and thermal power of options 1, 2 and 3. 163
B.2. Depiction of the simulation results for the specific heat capacity and thermal power of options 1, 2 and 3 at different salinity and gas content. 164
B.3. Comparison of electrical gross efficiency of (a) option 1, (b) option 2 and (c) option 3. 165
C.1. Supplementary XRD patterns of samples precipitated with CO_2. 168
C.2. Supplementary SEM images of samples precipitated with CO_2. 169

List of Tables

1.1. Radioactive elements in common rocks in the Earth's crust based on DiPippo, 2012. . . . 12
1.2. List of down hole and surface gas measurement at Bruchsal production well. . . . 26

2.1. Comparison of the metamorphic rocks and the related nomenclature of the Menderes Massif. . . . 41
2.2. List of methods applied to the different samples. . . . 44
2.3. Calcite content as a result of point counting of the sampled cuttings. mTVD: meters in total vertical depth. . . . 52
2.4. Summary of petrographical observations. c: Cretaceous, p: Paleozoic. 57
2.5. Results of the $\delta^{13}C_{VPDB}$ and $\delta^{18}O_{VSMOW}$ stable isotope measurements. 62
2.6. Rb-Sr data. n.d.: not determined. . . . 65
2.7. Characterisation of samples by petrographical properties. . . . 69
2.8. Characterisation of samples by geochemical properties. c: Cretaceous, p: Paleozoic. . . . 70
2.9. Information gained by applying REY and C and O isotopic signatures regarding formation environment. . . . 74

3.1. List of unit operations. . . . 93
3.2. List of different simulated technical solutions. . . . 99
3.3. The standard composition of input parameters for the simulation (Bruchsal power plant conditions). . . . 100
3.4. Recommendation of different simulated options 1, 2 and 3 depending on different simulated ranges. . . . 107

4.1. Composition of geothermal gas sampled from gas bypass at Bruchsal geothermal power plant. . . . 121
4.2. Results of ICP-OES analysis of all experiments V-1 to V-15 including standard deviation. . . . 129
4.3. Results of ICP-OES analysis with purity and recovery of on-site experiments. . . . 131

A.1. Results of major, trace and REE elements (ICP-MS/OES). c: Cretaceous; p: Paleozoic. . . . 154

B.1. Polynomial coefficients of equations B.1 and B.2 for the solubility calculation. . . . 156
B.2. Measured values for the thermal water in Bruchsal. . . . 157
B.3. The different calculated mass compositions in wt-% as simulation input for different simulation runs are listed. . . . 158
B.4. Listing the specific heat capacity, thermal output and power output as results of the simulations of options 1-3. . . . 159
B.5. Listing the specific heat capacity as a result of the simulations of options 1-3. . . . 160
B.6. Listing the thermal output as a result of the simulations of options 1-3. 161
B.7. Listing the power output as a result of the simulations of options 1-3. . 162

List of Abbreviations

AM	System points of secondary cycle
bg	Blueish light grey
BMG	Büyük Menderes Graben
C, c	Cretaceous
cc	Calcitic
CHP	Combined heat and power
CMM	Central Menderes Massif
CW	System points of cooling water cycle
DLE	Direct lithium extraction
dol	Dolomitic
E	East
ELECNRTL	Electrolyte non-random two-liquid
EOS	Equation of state
GBO	Gas breakout
GP-1	Geothermal exploration well
HREE	Heavy rare earth elements
i	Impure
ICP-MS	Inductively coupled plasma mass spectrometry
ICP-OES	Inductively coupled plasma optical emission spectroscopy
LLE	Liquid-liquid extraction
M	Molar
MA	Million years
MAE	Mean absolute error
MGS	Maximum grain size
N	North
NCG	Non-condensable gases
NMM	Northern Menderes Massif
ORC	Organic Rankine Cycle
P, p	Paleozoic
PAAS	Post Archean Australian Shale standard
ppl	Plane polarised light
REY	Rare earth elements and yttrium
S	South
SEM	Scanning electron microscopy
SEM-EDX	Coupled SEM and energy dispersive X-ray fluorescence analysis
SET Plan	Strategic Energy Technology Plan of the European Commission
SMM	Southern Menderes Massif
TDS	Total dissolved solids
T_H	Temperature at heat source
T_L	Temperature at heat sink
TVD	Total vertical depth
TW	System points of thermal water cycle

VPDB	Vienna Pee Dee Belemnite standard
VSMOW	Vienna standard mean ocean water
W	West
w	White
well^D	Investigated samples from deep section of GP-1 well (part II)
well^S	Investigated samples from shallow section of GP-1 well (part II)
XRD	X-ray diffraction

Elements and chemical compounds

Al	Aluminium
As	Arsenic
B	Boron
Ba	Barium
Ca	Calcium
C	Carbon
$CaCO_3$	Calcium carbonate, Calcite
Cd	Cadmium
Ce	Cerium
CH_4	Methane
Cl	Chloride
CO_3^-	Carbonate
CO_2	Carbon dioxide
Co	Cobalt
Cr	Cromium
Cs	Caesium
Cu	Copper
Dy	Dysprosium
Er	Erbium
Eu	Europium
Fe	Iron
Gd	Gadolinium
H	Hydrogen
HCl	Hydrochloric acid
H_2CO_3	Carbonic acid
H_2O	Water
H_3O^+	Oxonium ion
H_2S	Hydrogen sulfide
HCO_3^-	Hydrogen carbonate
HF	Hydrofluoric acid
HNO_3	Nitric acid
Ho	Holmium
K	Potassium
La	Lanthanum
Li	Lithium
Li_2CO_3	Lithium carbonate
LiCl	Lithium chloride

LiOH	Lithium hydroxide
Lu	Lutetium
Mg	Magnesium
Mn	Manganese
MnO_x	Manganese compound with X oxygen atoms
N_2	Nitrogen
Na	Sodium
NaCl	Sodium chloride
$NaCl_{eq}$	Sodium chloride equivalent
Na_2CO_3	Sodium carbonate, Soda ash, Soda
NaOH	Sodium hydroxide
Nd	Neodymium
Ni	Nickel
O	Oxygen
P	Phosphorus
Pb	Lead
Pr	Praseodymium
Rb	Rubidium
Sc	Scandium
Si	Silicon
Sm	Samarium
Sr	Strontium
Tb	Terbium
Ti	Titanium
Th	Thorium
Tm	Thulium
U	Uranium
V	Vanadium
Y	Yttrium
Yb	Ytterbium
Zn	Zinc

List of Symbols

a_i	Polynomial coefficients
a, b, B, C, D	Coefficients for temperature dependence, molar interaction (part I)
c	Concentration of dissolved gas
C_i	Concentration
C_P	Specific heat capacity
$\delta^{13}C$	Isotopic ratio of $^{13}\mathrm{C}/^{12}\mathrm{C}$
$\delta^{18}{}_\mathrm{VSMOW}$	Isotopic ratio of $^{18}\mathrm{O}/^{16}\mathrm{O}$
kH	Henry constant
K_sp	Solubility constant
m	Mass
M_i	Molecular weight
m_s	Solubility of a chemical compound
n	Number of moles of gas
p	Pressure
p	Thermal Power
pH	Potentia hydrogenii
Q	Flow rate
Q_c	Ratio of the ion product
R	Recovery rate (part IV)
R	Universal gas constant (part I)
rho_F	Density of the fluid
S	Supersaturation
T	Temperature
T_i	Production temperature
T_0	Reinjection temperature
V, v	Volume
x_{CO_2}	Solubility of CO_2
Z	Real gas factor, compressibility factor

Part I.

Fundamentals, motivation and objectives of the thesis

Chapter 1.

Introduction and fundamentals

1.1. Motivation

The European Commission set ambitious targets in 2019 to reach zero CO_2 emissions by 2050 and thus become the first green continent. The example of Germany shows that the transformation of the different consumption sectors occurs at different speeds. While avoidance of emissions in the electricity sector increases continuously, developments in the heating sector are not very dynamic (Lauf et al., 2021; Bracke et al., 2021). The heating sector in Germany has the largest share of final energy consumption at around 56%, of which, however, only 15.2% of the heating demand has so far been covered by renewable energies (Moeck and Weber, 2022).

Geothermal energy is a renewable energy technology and can support the world's energy transition to a more sustainable energy production. It offers high availability, dispatchability, and a temperature level suitable for industrial processes and district heating (Bosia et al., 2021). In 2019, the contribution of geothermal energy to the world's energy consumption amounted to 421 petajoules, approximately equally shared by electricity and heat (REN21, 2020). In Germany, the installed capacity of district heating by deep geothermal energy is approximately 417 MW_{th}, whereas the installed electrical capacity amounted to approximately 46 MW_{el} in 2022 (Bundesverband Geothermie e. V. and gec-co Global Engineering, 2021).

By being base load capable, geothermal energy can play a major role in decarbonising the power and heat sector in the future (Bundesministerium für Wirtschaft und Energie, 2021; Engelmann et al., 2021; Moeck and Weber, 2022). Modern binary deep geothermal energy systems have low emission factors compared with other renewable technologies (Pehnt, 2006; Frick et al., 2010; Pratiwi et al., 2018; Burkhardt et al., 2012) and offer at the same time high CO_2 savings (Lauf et al., 2021).

Moreover, compared with conventional heating technologies, such as heat pumps, it offers a high coefficient of performance defined by the ratio between the energy input (electricity) and the actual heat generated by the heating system (Bundesministerium für Wirtschaft und Energie, 2021; Günther et al., 2020; Francke, 2021; Wärmewende durch Geothermie, 2022).

The European Geothermal Energy Council (2022) announced the *geothermal decade* due to the recent energy crisis, because of the technology's wide application

possibilities as a renewable energy source for things such as buildings and industrial processes, but also potentially as part of a clean value chain for batteries in electric vehicles.

Clearly, there is a lot of high technical potential for deep geothermal energy to contribute to district heating in the future. In Germany, this potential is estimated for 2050 at 100 TWh per year (Sandrock et al., 2020; Engelmann et al., 2021; Bracke et al., 2021; Moeck and Weber, 2022) within the three most promising geothermal provinces (North German and Bavarian Molasse basins, Upper Rhine Graben). A listing of heat production costs of different generation options (Engelmann et al., 2021) shows that hydrothermal deep geothermal energy is already in competition with the reference option of natural gas combined heat and power (CHP). With the introduction of an effective CO_2 pricing system, the ratio would further improve in favour of renewables (Engelmann et al., 2021).

However, it is not only the initially very high investment costs for deep geothermal energy that prevent development from progressing as quickly as desired. The high exploration and the potential seismic risks also make investors cautious. Furthermore, public acceptance aspects could also cause delays during all project phases. Therefore, detailed communication formats are essential for geothermal projects. A large number of developments and optimisations are still necessary to advance deep hydrothermal geothermal energy. Keeping in mind the great potential of hydrothermal deep geothermal energy, it is important to promote this technology through funding instruments and detailed research.

The Strategic Energy Technology (SET) plan of the European Commission (SET Plan Secretariat, 2016) defines six targets to increase the share of geothermal energy in the European Union in order to realise its significant potential. These targets mainly focus on improving reservoir performance and therefore efficiency as well as cost reduction by technology development. This thesis aims at contributing to these targets in a threefold manner by focusing on the origin (part II), handling (part III) and utilisation of CO_2 (part IV) as part of the produced thermal water.

Non-condensable gases (NCG), in most regions mainly CO_2, are present in geothermal power plant systems worldwide (i.e., Ármannsson et al., 2005; Gokcen and

Yildirim (Özcan), 2008; Frondini et al., 2009; Seibt and Thorwart, 2011; DiPippo, 2012; Aksoy et al., 2015; Fridriksson et al., 2016; Bosia et al., 2021). These gases are called non-condensable gases as they do not condensate within the conditions of geothermal systems. When producing hot fluid, the gases flow as part of the fluid into the surface installations. The solubility of the gases decreases with lower pressure and higher salinity of the brine and may result in two phase flow (Markham and Kobe, 1941; Drummond, S.E., 1981; Nighswander et al., 1989; Rumpf et al., 1994; Seibt and Thorwart, 2011). This can cause problems like corrosion or scaling (Seibt and Thorwart, 2011) as well as decreasing heat exchange efficiency (Gokcen and Yildirim (Özcan), 2008).

Moreover, depending on local governmental regulations regarding carbon pricing and local resource conditions, the emission of those gases to the atmosphere is not rare (Aksoy, 2014; Kaya et al., 2011). According to Layman (2017), in 2017 all geothermal plant types installed in Turkey discharged CO_2 to the atmosphere. These emissions can even exceed the levels of thermal fossil-fueled power plants locally with emission factors up to 1300 g CO_2/kWh (Fridriksson et al., 2016). Furthermore, relatively high gas emission factors are reported for Italy, with an average of 330 g CO_2/kWh (Fridriksson et al., 2016). A global average emission factor is reported to 122 g CO_2/kWh (Fridriksson et al., 2016). Geothermal energy, as a form of renewable energy, is required to address the issue of greenhouse gas emissions in order to qualify for a zero-emission status. Several methods have been developed to tackle this challenge; however, these techniques entail relatively high operational expenses.

In a first step (part II), an extensive analysis is carried out on reservoir rocks within the Büyük Menderes Graben (western Turkey). This area is known for its relatively high levels of CO_2. The aim of this analysis is to investigate the CO_2 content. This study aims at contributing to the third and fourth SET plan targets (reducing production and exploration cost, respectively) by raising the possibility of a better understanding of the geothermal reservoir which supports the later stage exploration. Scientifically, the method of a multi-proxy approach will show how surface analogues can be used to retrieve an improved knowledge about the reservoir.

In a second study (part III), the motivation is led by reaching a reduction of NCG

emissions accompanied by optimising facility design and minimising operational costs. This supports the path towards the second and third objectives of the SET plan (improving efficiency and reducing production costs, respectively) by providing appropriate solutions for handling CO_2 in the surface installations.

The third study (part IV) accounts for the sixth SET plan target (demonstrating economic feasibility) by presenting a way to utilise the abundant CO_2 to precipitate lithium carbonate which is used for lithium ion battery production. Through further research, lithium, which is contained in geothermal brines in varying concentrations (up to 240 mg/L; Reich et al., 2022), could be separated via an appropriate extraction technology and subsequently precipitated by geothermal CO_2. In this way, lithium could be produced almost emission-free in association with geothermal plants.

1.2. Research Questions

Within the scope of this thesis, the following five research questions are addressed in the three scientific articles presented hereafter (part II, part III and part IV).

Research Question 1 *Can surface analogues be used to stratigraphically classify drilled intersections using a suitable multi-proxy approach?*

In part II, cutting samples of a geothermal exploration well of a mainly marble-gneiss-schist section, which are presumably the source of the CO_2 co-produced with the brine, are allocated to stratigraphically well-defined marble samples from surface outcrops. This raises the possibility of a better understanding of the geothermal reservoir which is important for the development of a geothermal field.

Research Question 2 *What are the major sensitive parameters for CO_2 handling in binary geothermal systems that influence plant performance?*

Research Question 3 *What is the ideal technical CO_2 handling in terms of avoiding CO_2 emissions and reaching the highest possible power output under different brine and operating conditions?*

In part III, we directly relate physio-chemical properties and the geothermal brine mass flow to the thermal and electrical output of the power plant. The objective of this surface installation simulation is to compare various technical options for CO_2 handling and operating conditions related to the Bruchsal brine. An essential knowledge gap is closed by answering the question of ideal technical CO_2 handling under different brine and operating conditions in the context of three simulated technical solutions which provide a first indication for identifying a technical solution in a future geothermal plant. However, a detailed simulation must be performed for any future plant after the primary cycle parameters (i.e., salinity, production temperature, gas composition and CO_2 content) are specified, as some primary cycle conditions could potentially fall in a transitional application range of the three technical solutions simulated here.

Research Question 4 *Is it possible to utilise the CO_2 of the feed line of a geothermal power plant in a sustainable way?*

Research Question 5 *Is the recovery and purity of the precipitated Li_2CO_3 using geothermal CO_2 sufficient for further processing steps?*

Part IV focuses on the utilisation of CO_2 related to geothermal plants. This study examines whether geothermal CO_2 can be utilised any further, and if so, under which conditions. A laboratory study tests the precipitation of lithium carbonate with geothermal CO_2 and aims at clarifying if the precipitate has sufficient purity for further processing steps.

1.3. Scientific approach

To answer research question 1, a field analysis of surface analogues was conducted in 2018 to potentially parallelise surface analogues of the northern and southern graben shoulders of the Büyük Menderes Graben (BMG) with two reservoir rock sections of a geothermal exploration well in western Anatolia (Turkey) (part II).

The field analysis was necessary to understand the characteristics of the reservoir rocks (marble-schist-gneiss intercalation) and allocate them to the surface analogues. This reveals a new understanding of the structural setting and new insights for the development of geothermal reservoirs in that region. The surface samples as well as the cutting samples were analysed by several petrographical (colouring with Alizarin-S, pattern, light transmission, pyrite-bearing, shape-preferred orientation, grain size distribution, maximum grain size, fractures, fissures, colour) and geochemical methods (ICP-OES, ICP-MS, SEM-EDX, C and O isotopic signature, Rb-Sr geochronology, Sr isotopic signature).

Evaluating all the gathered data, the shallower drilled section was allocated to the Paleozoic surface analogues of the Southern graben shoulder, whereas the deeper section is allocated to the younger Cretaceous surface samples of the Northern graben shoulder.

Research questions 2 and 3 were approached by a simulation and modelling study regarding CO_2 handling within the thermal water cycle of a geothermal plant (part III). Three different technical handling solutions were implemented as unit operations within the thermal water cycle of the simulation process scheme and evaluated regarding the lowest emission and highest thermal or power output. The simulation was conducted with ASPEN Plus and validated by operational data of the Bruchsal plant.

It is shown that the CO_2-solubility model implemented in ASPEN Plus overestimated the solubility and therefore another model was chosen with a better fit to the relevant range of parameters and implemented by a polynomial fit.

One result is that the major sensitive parameters for CO_2 handling within binary geothermal systems are gas composition and CO_2 content as well as brine composition (salinity), temperature and the resulting operating pressure. The publication lists recommendations for different brine and plant properties.

The last two research questions 4 and 5 are answered by an experimental study using (geothermal) CO_2 to precipitate lithium carbonate (Li_2CO_3) from a LiCl solution (part IV). The LiCl solution was synthetically prepared - but in future, the LiCl solution will be the result of lithium extraction from geothermal brine with sorbents. The

precipitation will represent one of the last steps making use of the lithium which is contained in most geothermal brines.

In the laboratory, different concentrated LiCl solutions were prepared and by injecting CO_2 into the solutions at defined temperature and starting pH of approximately 12 (adjusted by NaOH), a white powder of mainly Li_2CO_3 and NaCl as byproduct was precipitated.

1.4. Thesis structure

The thesis is cumulative and is structured in five parts. The first part describes the fundamentals that are required for this work, as well as a brief state of the art and the motivation for the development of the work. Furthermore, the methods are described in detail.

The three following parts are based on three publications that focus on the origin (part II: "Geothermal reservoir rocks of the Büyük Menderes Graben (Turkey): Stratigraphic correlation by a multi-proxy approach"), handling (part III: "CO_2 handling in binary geothermal systems - a modelling approach for different CO_2 contents, salinity, pressure and temperature conditions") and utilisation of CO_2 (part IV: "Lithium carbonate precipitation with carbon dioxide of a geothermal power plant") in geothermal systems.

The first article (part II) deals primarily with the origin of CO_2 in geothermal systems with a case study in western Anatolia (Turkey) including a comparison of reservoir rocks by applying a multi-proxy approach. It is published in the Turkish Journal of Earth Sciences 30 (2021) (Siefert et al., 2021). I was responsible for the selection of the outcrops and the fieldwork as such, for the mapping as well as for the selection of the samples to be analysed. Based on the detailed petrography of the samples, I decided on the appropriate geochemical and isotopic analytical programme. Markus Wolfgramm (GTN Geothermie Neubrandenburg GmbH) supported me in this task. I carried out the analysis and evaluation. With the support of Elisabeth Eiche (Karlsruhe Institute of Technology), I evaluated and interpreted the geochemical data. The Rb-Sr geochronology was done by Johannes Glodny (GFZ Helmholtz Centre Potsdam),

who interpreted the data with my input on the geological background. I was responsible for the drafting of the entire manuscript and for all figures, except for the Rb-Sr geochronology chapter. Jochen Kolb (Karlsruhe Institute of Technology) and Thomas Kölbel (EnBW AG) helped with identifying research questions in the discussion and proof reading the manuscript. All authors read, commented and approved the final manuscript.

The second article (part III) addresses the handling of CO_2 in geothermal systems and gives recommendations for action under different conditions by simulating different technical solutions. It is published in Renewable Energy 201 (2022) (Fechner et al., 2022). I identified the research questions, conducted the literature research and designed the overall concept for this study. I researched and chose the optimal software and created the framework parameters for the simulations. I was assisted by Milena Kondek (Karlsruhe Institute of Technology) in carrying out the simulation. The proposal to adapt a more appropriate solubility model for CO_2 in the software and the choice of it came from me, Milena Kondek was responsible for the implementation. I evaluated the simulation results, discussing them with Milena Kondek. I produced all the figures and the initial draft of the overall manuscript. Jochen Kolb and Thomas Kölbel provided assistance in designing the discussion chapter and editing the manuscript.

The third article (part IV) approaches the utilisation of CO_2, which occurs in relation to the geothermal system. Here, the heterogeneous precipitation of lithium carbonate (Li_2CO_3) out of a LiCl solution is considered to be a last step of lithium extraction out of geothermal brine. I drafted the concept and design of the laboratory and on-site study, and the final version was completed based on the input of all co-authors. I conducted the major laboratory work and on-site experiments supported by Laura Herrmann (Karlsruhe Institute of Technology) and Elif Kaymakci (EnBW AG). During laboratory work I was assisted by Thomas Kluge and Jochen Kolb. Laura Herrmann assisted me in creating the figures. I was supported by Laura Herrmann and Elif Kaymakci in writing the first draft of the manuscript. All the co-authors were supportive in proof reading the manuscript.

The last part (part V) summarises all findings and gives implications and perspec-

tives for the fields of research and industrial exploitation of deep geothermal systems. I wrote the first and last section.

1.5. Fundamentals

1.5.1. State of the art concepts of geothermal energy

Geothermal energy can be understood as the heat of the Earth (DiPippo, 2012), which, in terms of the Earth's crust, is mainly founded on the radioactive decay of natural isotopes (Bauer et al., 2014) (Table 1.1). This heat leads to an average global geothermal gradient of 30 K/km within the continental crust which is locally heterogeneous, reaching higher values depending on the tectonic regime (e. g. active volcanic regions). The geothermal potential worldwide is enormous and amounts to 100 million GWh in the course of a year (DiPippo, 2012). However, the variation of the heat flow in the Earth, different reservoir conditions as well as the locally varying demand, among other aspects, lead to the fact that the utilisation is diffuse so far and geothermal energy is not very much in focus in the overall energy picture (DiPippo, 2012).

Table 1.1.: Radioactive elements in common rocks in the Earth's crust based on DiPippo, 2012.

Rock	Concentration			Heat generation in 10-6 cal/g * yr		
	U in ppm	Th in ppm	K in %	U	Th	K
Granite	4.7	20	3.4	3.4	4	0.9
Basalt	0.6	2.7	0.8	0.44	0.54	0.23
Peridotite	0.016	0.004	0.0012	0.012	0.001	0.0003

The economic viability of a deep geothermal project relies on the temperature difference which can be used, the achieved flow rate and the heat capacity of the respective brine. The highest risk in geothermal energy is the so-called exploration risk: The exploration risk in geothermal wells is the risk of exploiting a geothermal reservoir with one (or more) wells of insufficient quantity or quality. The quantity is defined by the thermal power (P) that can be achieved by a well. The power is proportional to the flow rate (Q, in $m^3 s^{-1}$) and temperature (equation (1.1); Stober and Bucher, 2020).

In equation (1.1), ρ_F represents the density (kgm^{-3}), c_P is the specific heat capacity ($Jkg^{-1}K^{-1}$) of the liquid, T_i the production temperature and T_0 is the reinjection temperature. Furthermore, the injectivity of reinjection wells is important to not risk noticeable seismicity as this can pose an environmental and political risk. According to DiPippo (2012) five features exist which are essential in making a hydrothermal geothermal resource commercially viable:

- A large heat source
- A permeable reservoir
- A supply of water
- An overlying layer of impervious rock
- A reliable recharge mechanism

This leads to the conclusion, that without a fluid in the system, there is no heat transfer medium and the thermal energy cannot be exploited.

$$P = \rho_F \cdot c_P \cdot Q \cdot (T_i - T_0) \qquad [J/s] \tag{1.1}$$

The usage of geothermal energy can be subdivided according to different properties, such as the geological setting, drill hole depth, resource type, level of temperature and enthalpy, or the technology applied. Geothermal energy is used for heating, cooling or power generation. Deep geothermal energy (in general > 400 m to approximately 6,000 m) can be used for district heating or power generation, depending on the temperature of the pumped thermal brine. These systems can be differentiated by the utilisation of their reservoir: Hydrothermal systems utilise the existing natural reservoir as it is drilled and tested (Bracke et al., 2021: water-bearing rocks at depths of between 400-5,000 m; temperatures between 15 °C and 180 °C), whereas enhanced geothermal systems undergo enhancement processes after drilling, such as chemical or hydraulic stimulation (Bracke et al., 2021: petrothermal systems). A minimum of two wells are required to pump up the hot brine and reinject again after usage.

Nowadays, the wells are drilled from one drill pad and can be deviated allowing the utilisation of more wells than two from one site.

The technology installed above ground depends on the source of the deep geothermal reservoir, mainly on the result of testing regarding production temperature, flow rate and injectivity of the reinjection well. Depending on the source temperature, the fluid is water- or steam-based (Stober and Bucher, 2020). In regions with a resource temperature higher than 180-200 °C, the resource is mostly allocated to active plate boundaries and volcanic setting. These high-enthalpy systems (enthalpy > 800 $kJkg^{-1}$; Bauer et al., 2014) generate electricity directly from steam turbines. The conversion of heat from low-enthalpy systems (< 180 °C and enthalpy < 800 $kJkg^{-1}$; Bauer et al., 2014) into electricity with source temperature between 100-180 °C is only feasible with working fluids such as those used in ORC (Organic Rankine Cycle, working medium e.g. pentane) or Kalina cycles (working medium: ammonia-water mixture), named binary systems. Depending on the medium and temperature, the efficiency of such plants is between 10-15 % (Stober and Bucher, 2020). Another application of low-enthalpy and middle-enthalpy systems is direct use for district heating, fed into district heating grids. The energy of the thermal water is converted by a heat exchanger of the district heating water cycle.

Thermal water as a resource contains different amounts of dissolved solids and gas depending on its geological location and depth. Depending on these contents, different technologies exist regarding surface installations (materials and plant design) with respect to scaling, corrosion potential or heat exchange efficiency.

1.5.2. Deep geothermal energy in Turkey and Germany

Turkey

Geothermal energy in Turkey is mainly used for electricity generation by single flash steam plants (Layman, 2017) using a middle to high enthalpy source (> 150 °C). Due to its past and present tectonic situation, Turkey has regions with high heat flow and therefore high geothermal gradients (Baba and Chandrasekharam, 2022).

The major geothermal provinces of Turkey are located in the western Anatolian re-

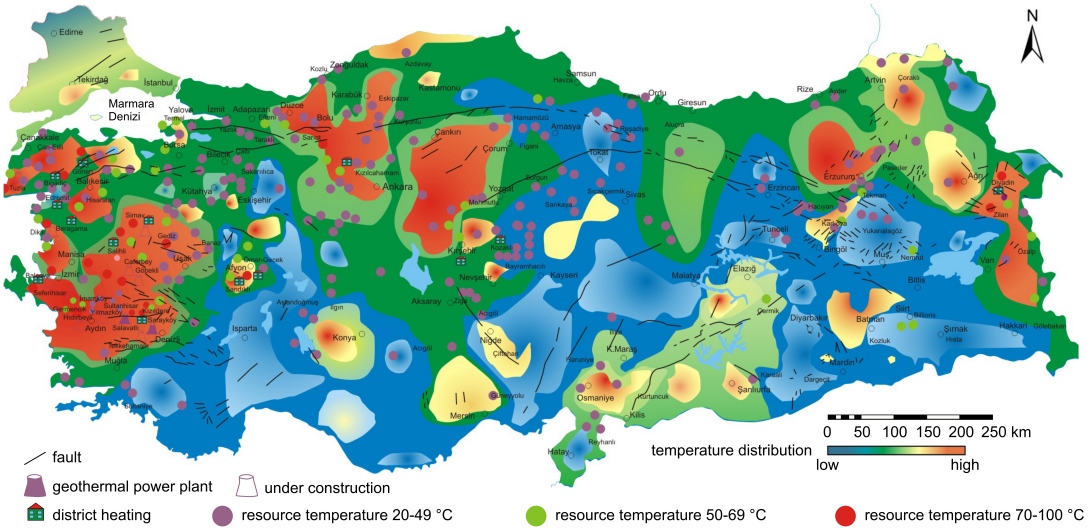


Figure 1.1.: Geothermal potential of Turkey according to General Directorate of Mineral Research and Exploration (MTA) (2015).

gion of Gediz and Büyük Menderes Graben, but significant potential is suspected in eastern parts of Turkey (Figure 1.1). In 1984, a geothermal energy program was established in Turkey, and in Kizildere 17 MW_{el} of electric capacity were installed. Today, the power generation from 60 geothermal power plants has an installed capacity of about 1,665 MW_{el}. In 2020, the gross power generation was about 13,100 GWh (Baba and Chandrasekharam, 2022). The major reservoir rocks are marble, (calc)schist, quartzite and gneiss (Haizlip et al., 2012; Aksoy, 2014).

The deep brine compositions are dominated by Na-Cl and Na-HCO_3 type waters, whereas the total dissolved solids vary between approximately 1-65 g/L (Vengosh et al., 2002). Due to the interaction between the carbonate reservoir rocks and the geothermal brines, moderate to high CO_2 contents are inherent. Therefore, the non-condensable gases of the Turkey fields are mainly comprised of CO_2 (96-99 % according to Layman, 2017). Additionally, notable amounts of hydrogen sulfide (H_2S) are present along with trace quantities of other gases (e.g. NH_3, H_2, N_2 and CH_4) (Kaya et al., 2017). The gas contents vary between approximately 2.4-4.2 wt-% which equals ca. 8-20 NL_{gas}/L_{fluid} (Haizlip et al., 2012).

Depending on the plant technology, such high gas contents can lead to gas emis-

sions (Aksoy, 2014; Aksoy et al., 2015; Layman, 2017; Fridriksson et al., 2017; Stober and Bucher, 2020), as it is not always possible to completely reinject the gas. Several publications exist considering and modelling gas removal or reinjection possibilities. Serpen and Aksoy (2005), Serpen and Aksoy (2010) and Serpen et al. (2015) point out difficulties of complete reinjection due to over-pressured reservoirs in Salavatli geothermal field (Turkey) and recommend detailed pressure, micro-seismic and tracer monitoring. Four different potential gas removal systems for flashed-steam geothermal power plants are considered and modelled (two-stage steam ejector system, two-stage hybrid system, two-stage compressor system and re-boiler system) by Yildirim Özcan (2010) and Yildirim (Özcan) and Gokcen (2015) validated on Kizildere geothermal power plant. They conclude that increasing the NCG content by 1 wt-% leads to a reduction in net power of up to 3 %, depending on the gas extraction system, with the compressor system being the most favourable option tested. Passarella et al. (2015) and Saldana et al. (2016) model and evaluate the effect of combined reinjection of brine and NCG on the reservoir rock aiming for an environmentally friendly way for the NCG disposal. In their research, Trimeric Corporation (2015) investigate the possibility of recovering CO_2 as a valuable product from a non-condensable gas stream in a geothermal plant. They propose potential process schemes and provide an estimate of the operational cost. The study identifies four potential products that could be obtained from the recovered CO_2, including a (1) low-pressure, low-purity CO_2 gas that could be transported via short, low-pressure pipelines to supplement CO_2 in greenhouses. Additionally, a (2) high-pressure, intermediate-purity CO_2 was identified as suitable for use in enhanced oil recovery, while a (3) high-purity, refrigerated liquid CO_2 was suggested for use in the beverage industry. Finally, (4) conducting reinjection of the non-condensable gas was identified as a potential strategy for receiving carbon capture credits.

In several publications since 2011, the researchers around Eylem Kaya study the effects of reinjection of NCG in geothermal fields in Turkey and worldwide which in their opinion is key to maintaining and managing geothermal resources in operation. They examine the challenges associated with successful reinjection, including pressure support, cooling mitigation, injectivity, scaling and solids deposition, mi-

croearthquakes, and tracer testing, and propose possible solutions to address them (Kaya et al., 2011; Kaya, 2016a; Kaya, 2016b; Kaya and Zarrouk, 2017; Kaya et al., 2017; Kaya et al., 2018; Kaya et al., 2019; Kamila et al., 2021). All this research is important to support geothermal energy systems regarding CO_2 handling and utilisation in Turkey.

Germany

Germany has three major provinces (Figure 1.2) which are favourable to utilise deep geothermal energy as low to medium enthalpy source. These are the North German and the Bavarian Molasse Basins, as well as the Upper Rhine Graben (Moeck and Weber, 2022). Currently, 41 geothermal plants exist which produce power (12) or heat (39) or combined heat and power (10) (Bundesverband Geothermie e. V. and gec-co Global Engineering, 2021). The installed heat capacity is 417 MW_{th} (Bundesverband Geothermie e. V. and gec-co Global Engineering, 2021). The installed electrical capacity amounts to 46 MW_{el} with a gross power generation in 2020 of 217 GWh (Bundesverband Geothermie e. V. and gec-co Global Engineering, 2021). The reservoir rocks are mainly sandstone (Sanjuan et al., 2016; Hettkamp, 2020). The projects covering district heating or power generation reach reservoir temperatures in the range of 37-165 °C and flow rates from 17 to 170 L/s (Bundesverband Geothermie e. V. and gec-co Global Engineering, 2021; Agemar et al., 2014).

Within the Upper Rhine Graben (Figure 1.2), the brine composition of different geothermal projects is similar, ranging from approximately 100 g/L to 130 g/L total dissolved solids (Stober et al., 2014; Sanjuan et al., 2016; Vidal and Genter, 2018; Hettkamp, 2020). The brines contain a high variety of different elements, but are mainly characterised by NaCl (Stober and Bucher, 2020). The origin of the brines is assumed to be a mixture of advanced seawater evaporation as well as meteoric water with contributions from halite dissolution being a result of marine transgression – regression cycles (Sanjuan et al., 2016). Helium isotopic signatures of gases dissolved in the brines reveal a crustal thermal anomaly of the Upper Rhine Graben which lead to a geothermal gradient up to 50-60 K/km (Sanjuan et al., 2016).

At reservoir conditions, gases are dissolved in the geothermal brines of the Upper Rhine Graben, which are mainly CO_2, CH_4, N_2 and some minor content of inert gases

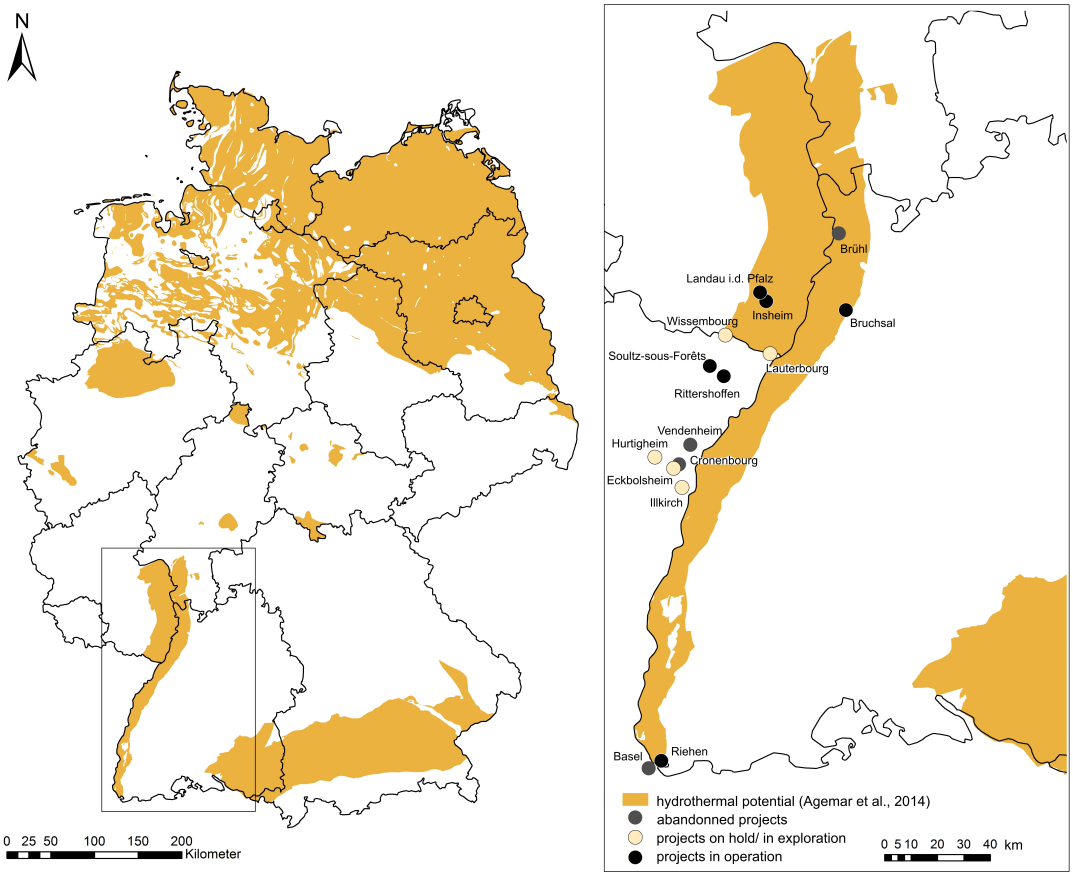


Figure 1.2.: Three major geothermal provinces of Germany and the projects of the Upper Rhine Graben (Agemar et al., 2014; Vidal and Genter, 2018; Bracke et al., 2021; Moeck and Weber, 2022).

which are typically He, Ar and H_2 (Hettkamp, 2020; Bosia et al., 2021). During the ascent of the fluid, decompression occurs, resulting in a two-phase flow of liquid brine and gas at surface depending on the gas breakout pressure of the system. The gas contents of the Upper Rhine Graben operating projects vary from 0.8-1.9 NL_{gas}/L_{fluid} which result in gas breakout pressures between 18 bar absolute (bar(a)) to more than 30 bar(a) (Hettkamp, 2020; Fechner et al., 2022).

1.5.3. Non-condensable gases in geothermal energy - focus on carbon dioxide

Non-condensable gases in geothermal energy

Non-condensable gases play a major role in most of the regions where geothermal energy is utilised. The majority of geothermal reservoirs contains a certain amount of non-condensable gases dominated by CO_2 (i.e., Ármannsson et al., 2005; Gokcen and Yildirim (Özcan), 2008; Frondini et al., 2009; Seibt and Thorwart, 2011; DiPippo, 2012; Aksoy et al., 2015; Fridriksson et al., 2016; Bosia et al., 2021). With respect to corrosion and precipitation effects as well as environmental friendliness and economic optimisation, the handling of these gases is challenging (Gokcen and Yildirim (Özcan), 2008; Aksoy, 2014; Seibt and Thorwart, 2011). These gases are typically dissolved in the brine and cannot be condensed solely by increasing the pressure at the geothermal systems' operation temperature. With increasing salt concentration (salinity) of the aqueous phase, the solubility of the gases decreases (Markham and Kobe, 1941;Drummond, S.E., 1981; Nighswander et al., 1989; Rumpf et al., 1994; Seibt and Thorwart, 2011), locally resulting in two-phase systems in the reservoir. With increasing pressure, the gas solubility increases (Seibt and Thorwart, 2011). The gas solubility decreases with increasing temperature (Seibt and Thorwart, 2011). In consequence, two-phase flow may evolve when decompression occurs at nearly constant temperatures, which may lead to problems depending on the power plant technology (direct use or binary power plants), such as potential CO_2 emission (Aksoy, 2014), decreasing efficiency of heat exchangers (Gokcen and Yildirim (Özcan), 2008), corrosion or scaling (Seibt and Thorwart, 2011).

Especially gaseous CO_2 lowers the efficiency of heat exchangers (Gokcen and Yildirim (Özcan), 2008). For example in Bruchsal (Germany), CO_2 accumulates within the plate heat exchangers. As a result, they are partly blocked for brine pathways (Schlagermann et al., 2014). Such a reduction of heat exchanger surface leads to the decrease of transferred thermal energy and therefore decreasing heat and electrical power output.

In addition, CO_2 in the gas phase enhances corrosion of the above-ground installa-

tions (Seibt and Thorwart, 2011; Seibt and Wolfgramm, 2012). In addition to gaseous CO_2, the high salt concentration enhances corrosion even further (Mundhenk et al., 2013). The mechanism of corrosion is attributed to the hydrogen corrosion induced by carbon dioxide (CO_2). Upon dissolution of CO_2 in brine, it undergoes dissociation to bicarbonate and subsequently to carbonate, which releases one H^+ ion. The H^+ ions then lead to hydrogen corrosion (Fischer and Siedlarek, 1977; Carneiro et al., 2003). Moreover, effervescence of CO_2 from the thermal water, caused by pressure drop, leads to an increase in pH in the liquid. This results in carbonate precipitation (scaling) in the pipelines, on top of scaling induced by decreasing salt solubility due to cooling (Seibt and Thorwart, 2011; Seibt et al., 1999).

This implies that NCG have to be considered in nearly all plant parts and status of a geothermal project, such as exploration, during testing, during plant design and operation at surface installations and during reinjection. State of the art plant designs vary depending on the source type, gas composition and gas content. During the exploration of a project, it is helpful to know the brine composition of other surrounding projects, especially in terms of gas content and gas composition. In addition, by getting a picture of the local geology by means of exploration, knowing the expected reservoir rock can already partly deduce how the gas composition is expected to be. If the carbonate content of the potential reservoir rock or its surface analogue is determined, a theoretical CO_2 content of the rock can be calculated. High carbonate contents may indicate an increased gas content. Afterwards, when testing a newly drilled well, it is important to thoroughly conduct a down hole sampling to determine the gas content and gas composition at reservoir conditions as exactly as possible. This is important for the plant design to decide on the handling possibility of the NCG (Bhatia, 2014). So far handling possibilities of gases are differentiated for direct or binary deep geothermal projects. Binary systems are usually closed loop systems where the operating pressure is kept above the gas breakout pressure (DiPippo, 2012) and the gas is reinjected along with the brine. If the operational pressure cannot be increased until the gas breakout pressure, difficulties can occur as mentioned above. For direct systems, depending on the gas content and composition, either the gas is vented to the atmosphere or it can be captured, compressed, reinjected and mineralised to

some extent (Vorum and Fritzler, 2000; Aradóttir and Gunnarsson, 2013; Bhatia, 2014; Aradóttir et al., 2015a; Aradóttir et al., 2015b; Gunnarsson et al., 2015; Júliusson et al., 2015; Berstad and Nord, 2016; Batini et al., 2016; Bonalumi et al., 2017b; Yücetaş et al., 2018; Kamila et al., 2021). So far utilisation possibilities for NCG, especially CO_2, are reported in DiPippo (2012), where CO_2 is further used for the beverage industry. Further utilisation possibilities are not known at this point.

CO_2 and its solubility in brines

Carbon dioxide is the reaction product of the combustion of carbon and carbon bonds. It is also formed during the decomposition of carbonates (equation (1.2)) when acids are added or during their thermal decomposition (equation (1.3); Mortimer and Müller, 2010). Carbon dioxide is a colourless and odourless gas. When cooled under atmospheric pressure, it becomes solid at -78 °C without first becoming liquid. Under pressure it liquefies easily (Figure 1.3).

$$CaCO_3(s) + 2H^+(aq) \rightarrow Ca^{2+}(aq) + CO_2(g) + H_2O \tag{1.2}$$

$$CaCO_3(s) \xrightarrow{900\,^\circ C} CaO(s) + CO_2(g) \tag{1.3}$$

The molecule is linear and non-polar and it is moderately soluble in water. It is the acid anhydride of carbonic acid, H_2CO_3. Solutions of carbon dioxide in water contain essentially dissolved CO_2 molecules; less than 1 % of it converts to H_2CO_3 depending on the physicochemical parameters. Carbonic acid is a weak, biprotonic acid (Mortimer and Müller, 2010). Due to salting out effect, CO_2 solubility decreases with increasing salinity (Setschenow, 1889). As mentioned before, the CO_2 solubility decreases with increasing temperature, which applies to most of the gases: According to the principle of least constraint, solubility decreases with increasing temperature in exothermic solution processes. Since gases usually dissolve exothermically, the solubility of gases decreases with an increase in temperature (Mortimer and Müller, 2010). When pressure is applied, the system conforms to the principle of least constraint through a process characterised by a reduction in volume. Increasing the pres-

sure will result in a greater amount of the gas being dissolved (Mortimer and Müller, 2010).

To be able to approximate this behaviour in the design of a power plant, a well-founded simulation must be carried out. Therefore, an exact down hole measurement serves as one input parameter for the simulation, in the form of the parameters total gas content and the CO_2 composition, which are determined in the laboratory after sampling. The simulations for plant design then require suitable gas solubility models. As most of the gas is comprised of CO_2, within the range of interest (p,T, salinity, gas content conditions) an appropriate CO_2 solubility model has to be chosen.

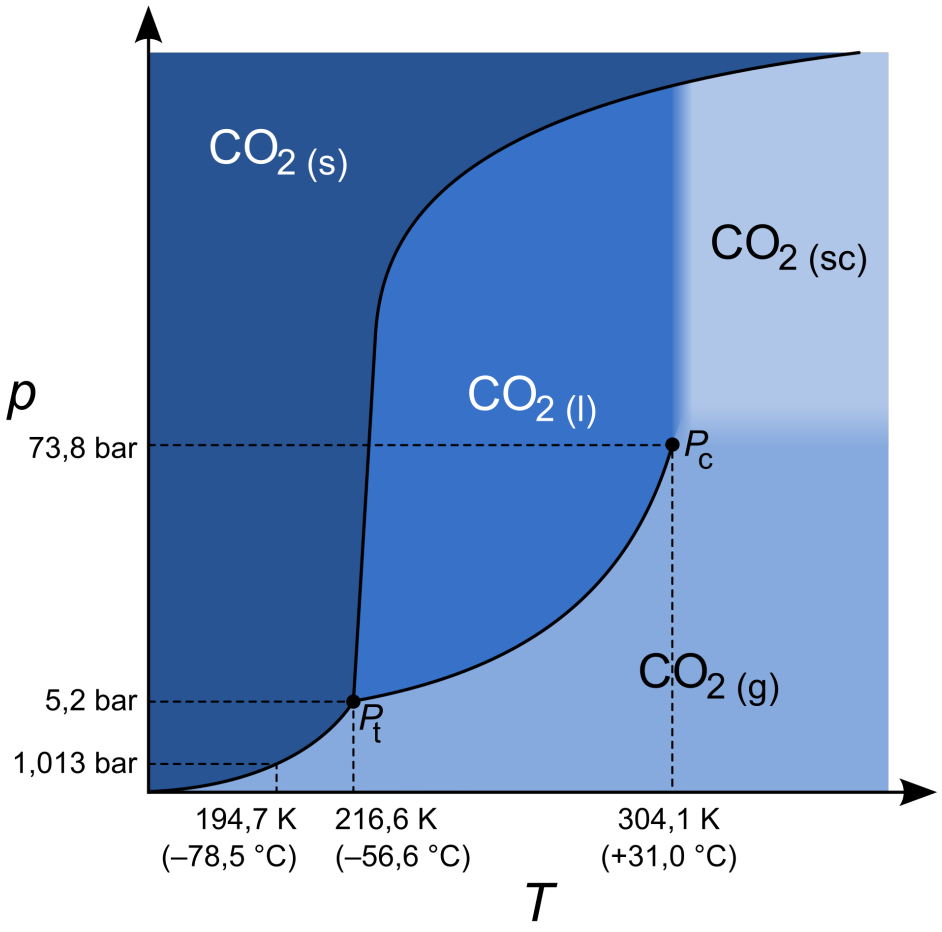


Figure 1.3.: Phase diagram of CO_2 adopted from Mortimer and Müller (2010).

Numerous CO_2 solubility models in electrolytes exist based on either an equation of

state (EOS) as deviation of the ideal gas law (equation (1.4) with p: pressure of the gas; v, V: volume of the gas; n: number of moles of gas; R: universal gas constant; T: absolute temperature of the gas) validated by experimental data, or on deviation of the Henry-Dalton-law (equation (1.5) with c: concentration of dissolved gas; kH: Henry constant) (Pfennig, 2004). According to the Henry-Dalton law, when a gas is dissolved in a liquid with which it does not react, its solubility is directly proportional to the partial pressure p of the gas present above the solution. However, this law only applies at low pressure regimes (i.e., below 5 bar(a); Mortimer and Müller, 2010). Therefore, in this study it was chosen to focus on applying an EOS.

$$\begin{aligned} pV &= NRT \\ pv &= RT \end{aligned} \tag{1.4}$$

$$p = kH * c \tag{1.5}$$

$$Z = pv/RT \tag{1.6}$$

To describe the pressure-, volume- and temperature-dependent behaviour of substances, it is useful to use EOS. Through this the fugacity coefficients and the real gas factor Z are calculated. The real gas factor describes the deviation of a real gas from its ideal behaviour by accounting the effects of intermolecular forces (Pfennig, 2004). As $Z = 1$ applies for ideal gases, the real gas factor allows the dimensionless representation and thus the deviation from the ideal gas can be well demonstrated (equation (1.6)). To be able to describe the real behaviour of gases more precisely, EOS are used which represent an adaptation of the ideal gas equation in different modes. EOS are valid for pure components and for mixtures. However, to describe the states of mixtures as well, some adaptations are required that depend on the type of EOS (Pfennig, 2004). Examples of adapted equations of state are the Virial equation (equation (1.7) in Leidenform; coefficients B, C, ... are temperature dependent and reflect the interaction of the molecules), the Van-der-Waals equation (equation (1.8) with coefficients a and b describing the molecular interactions and molar volume, respectively) and corresponding further developments, such as the Redlich-Kwong (equa-

tion (1.9)) or the Peng-Robinson equations (equation (1.10)) (Pfennig, 2004). The details and calculation of the respective coefficients can be accessed in Pfennig (2004).

$$\frac{pv}{RT} = Z = 1 + \frac{B(T)}{v} + \frac{C(T)}{v^2} + \frac{D(T)}{v^3} + \cdots \tag{1.7}$$

$$p = \frac{RT}{v-b} - \frac{a}{v^2} \tag{1.8}$$

These approaches or their adapted developments are typically applied in CO_2 solubility models (i.e., Duan et al., 1992a; Duan et al., 1992b; Duan and Sun, 2003; Duan et al., 2006; Spycher and Pruess, 2011 or Zhao et al., 2015). The difference of these solubility models and therefore the reason for different solubility models existing, is the need to describe the interaction of non-ideal gases with different electrolyte solutions. These models exhibit varying methodologies in approximating the interaction parameters and the equation of state utilised to describe the solubility in the electrolyte solution. Duan et al. (1992a; 1992b; 2003; 2006) use a modified EOS based on the Virial equation as the basis for their solubility calculations and models. Spycher and Pruess (2010; 2011) compute the solubility modifying the EOS according to Redlich-Kwong. Moreover, differences exist in the electrolytes under consideration and the computation of their interaction parameters based on Pitzer equations (Pitzer, 1991). These several authors have made additional advancements in their models regarding this matter by receiving additional experimental data with time and subsequently taking these into consideration.

$$p = \frac{RT}{v-b} - \frac{a}{T^{0.5}v(v+b)} \tag{1.9}$$

$$p = \frac{RT}{v-b} - \frac{a(T)}{v^2 - 2bv - b^2} \tag{1.10}$$

That gases, their handling and appropriate gas solubility models become more and more important, can be seen in further and new research developments (Lara Cruz et al., 2019; Chabab et al., 2021; Chabab et al., 2022; Merbecks et al., 2022; Lassin et al., 2022). Lara Cruz et al. (2019) and Lassin et al. (2022) generate new experimental

data fit to the requirements of some deep geothermal projects in the Upper Rhine valley which are implemented into a solubility model by Chabab et al. (2021), Chabab et al., 2022 and Lassin et al. (2022) covering different gases and electrolyte solutions. Merbecks et al. (2022) investigate the design of binary geothermal plants regarding different NCG. However, to fully understand the effects of CO_2 on the solubility of other gases, such as CH_4, will require extensive research and experimental data sets.

1.5.4. Gas breakout tests in Bruchsal (Germany)

In preparation of part III, gas breakout tests were performed in Bruchsal to determine the gas breakout pressure, also known as bubble point pressure. In former studies, the gas composition and content was defined by water and gas sampling at surface but also by down hole sampling and subsequent analysis. According to these investigations, a CO_2 content of only 0.3 wt-% is approximated (Table 1.2).

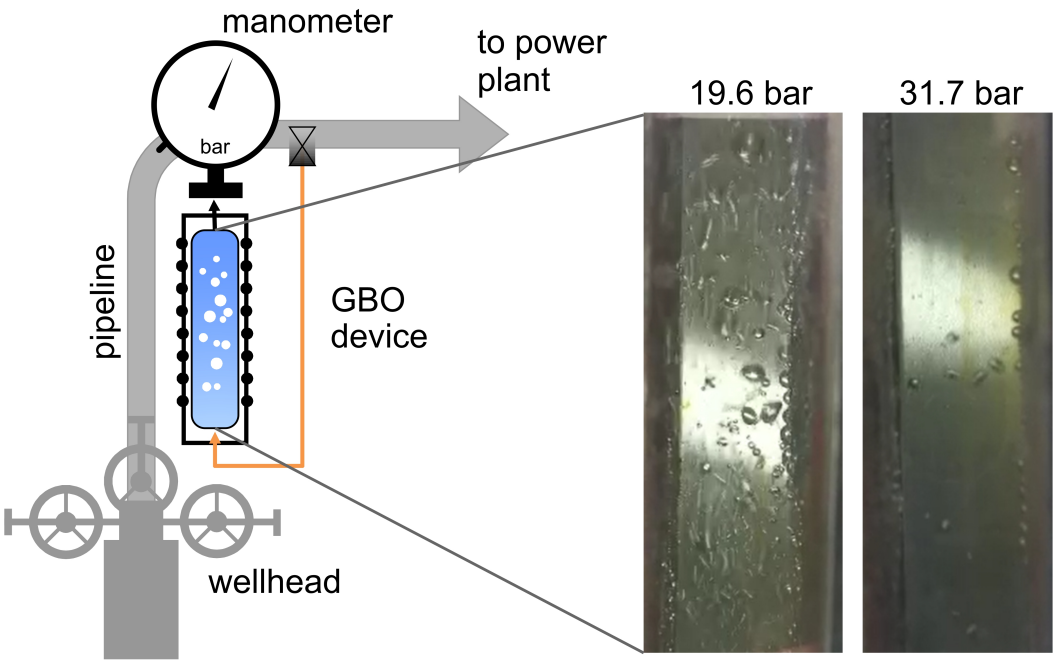


Figure 1.4.: Schematic illustration of the gas breakout (GBO) measurement device at the Bruchsal power plant and the situation shown by means of a picture at 19.6 and 31.7 bar(a). The picture at 31.7 bar(a) reveals less gas bubbles than at 19.6 bar(a).

Table 1.2.: List of down hole and surface gas measurement at Bruchsal production well of different sampling operators and at different years. Gas content into wt-% and g/L was recalculated with a density of 1.07 kg/L and based on Virial equation of state.

Year			**1985**	**2009**	**2009**	**2010**	**2010**
Sampling institution (1 or 2)			**1**	**2**	**2**	**2**	**2**
Depth		**m**	**1586 m**	**surface**	**surface**	**surface**	**surface**
Gas							
Carbon dioxide	CO_2	**vol-%**	89.31	93.6	94.7	94.91	94.78
Nitrogen	N_2	**vol-%**	5.36	4.01	3.29	3.13	3.31
Methane	CH_4	**vol-%**	4.17	2.09	1.8	1.73	1.67
Helium	**He**	**vol-%**	0.48	0.19	0.16	0.17	0.16
Hydrogen	H_2	**vol-%**	0.69	0	0.02	< 0.01	< 0.0001
Argon	**Ar**	**vol-%**		0.03	0.03	0.03	0.04
Further CHs (Ethane)		**vol-%**		0.04	0.04	0.04	0.04
Volume of gas (total) per L thermal water		**Nml**	**1819**	**1620**	**1592**	**1523**	**1520**
Gas content		**wt-%**	**0.33**	**0.29**	**0.29**	**0.27**	**0.27**
		g/L	**3.3**	**2.9**	**2.9**	**2.7**	**2.7**

Year			**2010**	**2010**	**2013**	**2013**	**2020**
Sampling institution (1 or 2)			**2**	**2**	**2**	**2**	**2**
Depth		**m**	**surface**	**surface**	**surface**	**surface**	**surface**
Gas							
Carbon dioxide	CO_2	**vol-%**	93.83	95.35	94.5	95.3	88.9
Nitrogen	N_2	**vol-%**	4.51	2.85	3.52	2.98	7.13
Methane	CH_4	**vol-%**	1.48	1.56	1.89	1.65	3.89
Helium	**He**	**vol-%**	0.14	0.15			
Hydrogen	H_2	**vol-%**	0.0062	0.0123	< 0.01	< 0.01	< 0.1
Argon	**Ar**	**vol-%**		0.15	< 0.01	< 0.01	< 0.1
Further CHs (Ethane)		**vol-%**		0.04	0.046	0.037	0.074
Volume of gas (total) per L thermal water		**Nml**	**1,513**	**1,503**	**1,726**	**1,712**	**1,900**
Gas content		**wt-%**	**0.27**	**0.27**	**0.31**	**0.31**	**0.34**
		g/L	**2.7**	**2.7**	**3.1**	**3.1**	**3.4**

The gas breakout measurement device (Figure 1.4) is typical for the determination of the approximate gas breakout pressure of the respective brine and was also used, for instance, in the Rittershoffen and Soultz-sous-Forêts projects (personal communication). To determine the gas content of a fluid, a pressure chamber with manometer is installed at the gathering pipe system close to the production well. The pressure within the system is increased to achieve single phase conditions by means of augmenting the pump frequency and regulating the valves subsequent to the connection of the gas breakout device. Single-phase conditions are characterised by the absence of gas bubbles in the system. In Bruchsal, the test started at a pressure of 19.6 bar(a) which is slightly lower than the typical operational pressure of 22 bar(a). The pressure was slowly increased and less gas bubbles were detected. However, due to pump

conditions, it was not possible to increase the pressure to more than 31.7 bar(a). At this pressure, still few gas bubbles are noticed (Figure 1.4). This pressure was used as the minimum gas breakout pressure as the actual gas breakout point could not be determined experimentally.

Recalculating the maximum reached pressure of 31.7 bar(a) by the model of Duan et al. (2006) with given salinity and temperature yields an approximate CO_2 content of 0.86 wt-%. This is in line with the observations made by simulating the thermal water cycle in part III.

Part II.

Geothermal reservoir rock characterisation and origin of Carbon dioxide

Summary to Part II

This paper focuses on the correlation of two different marble units from an approximately 3,900 m deep geothermal exploration well (GP-1) in western Turkey by petrographical and geochemical data. Future geothermal exploration drilling in that area will benefit from a better (tectono) stratigraphic correlation and a better definition of the reservoir geometry in the basin.

It is an innovative approximation in many settings to correctly correlate marble units without clear stratigraphic markers or fossil record, in particular when sample material is restricted to cuttings. The most distinctive petrographical and geochemical properties in this study are colour, light transmission along with rare-earth element + yttrium (REY) geochemistry, and stable carbon and oxygen isotope data.

Two stratigraphic correlations can be maintained for two different marble horizons of the GP-1 well to different stratigraphic horizons outcropping in the study area. Additional Rb-Sr geochronology yields an age of the last metamorphic overprint of the marbles of approximately 30 Ma. This study shows that a multi-proxy approach is required to yield a reliable stratigraphic correlation as an important component of geothermal exploration, which supports the conceptual geological model prior to further geothermal drilling.

Chapter 2.

Geothermal reservoir rocks of the Büyük Menderes Graben (Turkey): stratigraphic correlation by a multiproxy approach

2.1. Introduction and basics

Geothermal power production experienced a rapid development in Turkey in recent years with an installed electrical capacity of more than 1.5 GWel so far (REN21, 2020). The vast majority of the geothermal power plants are in the Büyük Menderes and Gediz Graben of the Menderes Massif in western Turkey (Figure 2.1).

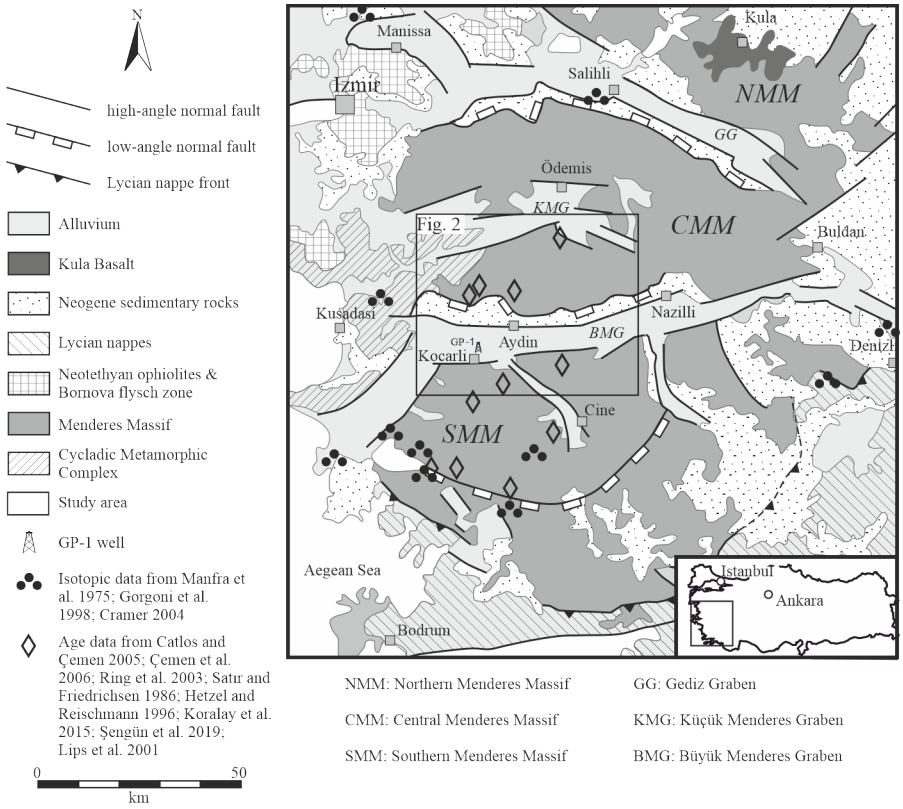


Figure 2.1.: Simplified geological map of the Menderes Massif with the location of the study area (Figure 2.2) (modified after Kaya, 2015). The central graben is the Büyük Menderes Graben (BMG). Marble outcrops studied by Manfra et al. (1975), Gorgoni et al. (1998) and Cramer (2004) are used for comparison. Locations with available geochronological data are shown.

The geological evolution of the Menderes Massif, starting in Neoproterozoic times, led to a complex geological architecture and a rich inventory of deformation structures. Detailed descriptions of the development of the Menderes Massif can be found in Bozkurt (2000), Bozkurt and Oberhänsli (2001) and Gessner et al. (2013). Since

the Miocene, crustal thinning resulted in the formation of East-West trending, extensional graben structures (Figure 2.1; Bozkurt and Oberhänsli, 2001; Gessner et al., 2001; Régnier et al., 2003; Reilinger et al., 2006). The basement rocks of the graben – consisting of metamorphic and igneous rocks – are overlain by sediments and sedimentary rocks with a thickness of several hundred meters (Figures 2.1 and 2.2; Gürer et al., 2009).

With a few exceptions, the geothermal reservoirs in the graben are located in schist and marble units and schist-marble intercalations (Şimşek, 1985). As marble may represent efficient geothermal reservoirs, the understanding of the local geological setting is key for expansion of existing geothermal sites and the overall development of geothermal power production from a regional perspective. Outcrops of these units are accessible at the southern and northern escarpments and were examined in detail in the past. Two different marble-bearing horizons are distinguishable within the area around the Büyük Menderes Graben: one of Paleozoic and another of Mesozoic (Cretaceous) age (Figure 2.2; Ring et al., 1999; Gessner et al., 2001; Özer and Sözbilir, 2003).

The composition of marble in general is controlled by (1) the composition of the precursor limestone; (2) metamorphism; (3) fluid-rock interaction and (4) weathering (Gorgoni et al., 1998). Characterisation of marble is usually based on multi-proxy approaches, covering different rock properties (Germann et al., 1980; Herz, 1987; Gorgoni et al., 1998; Cramer, 2004; Origlia et al., 2012; Ricca et al., 2015). Besides macroscopic features like mineral assemblage and colour, the maximum grain size of specific minerals can be a useful tool (e.g. Ricca et al., 2015). Furthermore, major, trace and rare-earth element (REE) data (e.g. Cramer, 2004) as well as C and O isotope data (e.g. Manfra et al., 1975; Satır and Friedrichsen, 1986) are important features for characterisation. Spry (1983) sets a petrographical characterisation of metamorphic rocks by analysing both texture and mineral assemblage as essential to an understanding of the rocks. In addition to the mineral assemblage and the purity of a marble (Fettes and Desmons, 2007), the appearance as well as the maximum grain size and the distribution of the carbonate minerals (calcite and dolomite) can be supportive when characterising a marble (Germann et al., 1980; Cramer, 2004; Ricca et al., 2015).

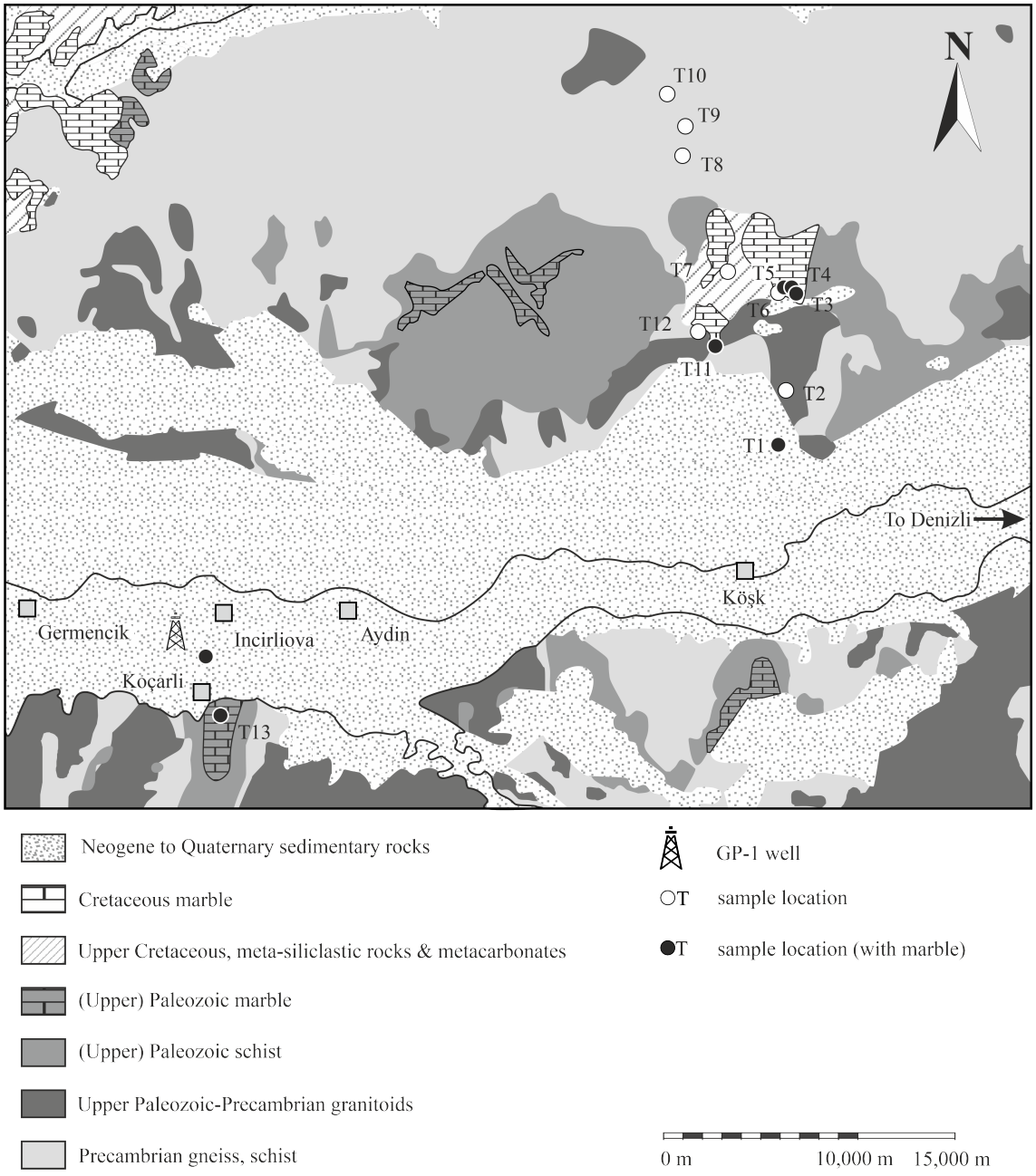


Figure 2.2.: Geological map of the study area with borehole GP-1 and outcrop locations (modified after General Directorate of Mineral Research and Exploration (MTA), 2015).

Several geochemical analytical methods were applied for provenance analysis of marbles (e.g. Germann et al., 1980) including mass spectrometry for determination of major and trace elements (e.g. Germann et al., 1980; Cramer, 2004; Ricca et al., 2015).

Existing positive or negative anomalies of REE and yttrium (REY) can be supportive when investigating redox conditions and evaluating freshwater or seawater origin. Cerium (Ce) anomaly variations are a function of variable redox potentials (Bau and Dulski, 1996) which are found in natural sedimentary environments. A negative Ce anomaly is indicative of oxic conditions in seawater (Bau and Dulski, 1996; Hua et al., 2013; Tostevin et al., 2016). Positive anomalies of Y can be separated into large (Y/Ho = 40-80), representing open marine settings, and small (Y/Ho = 33-40), being indicative of near shore settings (Tostevin et al., 2016). In addition, Webb and Kamber (2000) give a threshold for a Y/Ho mass ratio of > 44, which indicates a strong seawater influence. Positive Eu anomalies with values around 1.5 (Tostevin et al., 2016) can be observed when the seawater signal is overprinted by hydrothermal fluids (Meyer et al., 2012). Rubidium/strontium (Rb/Sr) geochronology may provide insights into the rock's age and metamorphic evolution (Satır and Friedrichsen, 1986).

Globally, marble $\delta^{13}C_{VPDB}$ values range from -5 to +5 ‰ and $\delta^{18}O_{VSMOW}$ from 18 to 34 ‰ (Rollinson, 1993). The primary isotopic signature acquired during limestone deposition and subsequent secondary processes, such as recrystallisation during metamorphism or fluid-rock interaction, lead to a characteristic isotopic fingerprint of different marble units. Therefore, C and O isotopes are commonly used to determine the marble origin (e.g. Craig and Craig, 1972; Manfra et al., 1975; Herz, 1987). Herz and Dean (1986) found that homogeneous isotopic composition in marbles can be perceived at a broad scale. However, in order to encounter a homogenous isotopic composition within a marble unit, the deposition and subsequent diagenesis of the limestone should occur under uniform physicochemical conditions and isotopic equilibrium must be attained and preserved during metamorphism (Herz and Dean, 1986). Furthermore, it is necessary that the marble unit is chemically homogeneous, has a significant thickness and underwent only a gentle metamorphic gradient (Herz and Dean, 1986).

During an exploration campaign in the vicinity of the Koçarli village, Büyük Menderes Graben (BMG), an approximately 3,900 m deep well (GP-1) was drilled in 2017 (Figure 2.2). The GP-1 well intersects two marble units at shallow depth and at bottom hole, separated by different metamorphic and igneous rocks of more than

2,000 m thickness. Cuttings from the two marble units have been examined along with marble samples from outcrops collected from the northern and southern escarpments of the BMG. Our multi-proxy approach characterises these marbles by their petrographical and geochemical features and their C and O isotope signatures. Furthermore, Rb-Sr geochronology is used to detect potentially contrasting metamorphic ages and initial Sr-isotopic ratios.

The aim of this publication is to demonstrate that surface analogues can be used to stratigraphically classify drilled intersections using a suitable multi-proxy approach. This methodology can also be applied to other locations related to graben systems. We compare cutting samples with different, stratigraphically well-defined marble samples from surface outcrops. We manage to allocate the two marble horizons of the cutting samples to the stratigraphically well-defined surface outcrops of marble of different age (Cretaceous and Paleozoic).

2.2. Regional geology

The Menderes Massif in western Anatolia consists of Proterozoic to Mesozoic, greenschist to amphibolite facies metamorphic rocks (Figure 2.1; cf. Bozkurt and Oberhänsli, 2001). They are mainly augengneiss, meta-granite, schist, marble, paragneiss and meta-gabbro (Satır and Friedrichsen, 1986; Gürer et al., 2009). Structural upper sections of this basal gneiss unit show an intercalation of quartzite and schist (Şimşek, 1985). This unit is overlain by the so-called mica schist unit. The stratigraphically uppermost unit of the metamorphic rocks is an intercalation of marble, calcareous schist, quartzite, and schist that is significantly fractured (Iğdecik Formation, Şimşek, 1985). The marbles are most likely of marine origin based on structural and tectonic observations, marine fossil findings and isotopic data (Şengör and Yilmaz, 1981; Özer and Sözbilir, 2003; Cramer, 2004).

The Neogene sedimentary cover (Figure2.1) consists of breccia, conglomerate, sandstone, clay stone, marl and in places coal seams, mainly deposited in shallow water environment (Satır and Friedrichsen, 1986; Gürer et al., 2009). This Lower Pliocene formation (Kızılburun Formation) represents the earliest continental to lacustrine

deposit above the Menderes Massif metamorphic rocks (Şimşek, 1985). On the Kızılburun Formation, there are yellowish to light brown sandstone, clay stone and clayey limestone (Kolankaya Formation, locally Sazak Formation). Fossil-bearing, clayey limestone, sandstone, clay stone and a poorly solidified conglomerate originate from the Pliocene to Quaternary (Tosunlar Formation). Alluvial sediments are represented by terrace deposits, travertine, alluvial debris fans and slope debris (Şimşek, 1985).

During the Alpine orogeny, the tectonic units of the Adriatic Plate and the continental fragments were stacked simultaneously to the subduction of the Neotethys. The evolution of the Menderes Massif is still a matter of debate. Either a "core-cover model" (Dürr et al., 1978; Bozkurt and Oberhänsli, 2001; Rimmelé, 2003; Rimmelé et al., 2003; Bozkurt, 2007; Candan et al., 2011) or a "nappe stacking model" (Dixon and Robertson, 1984; Ring et al., 2001; Gessner et al., 2001b; Gessner et al., 2002; Ring et al., 2003; Régnier et al., 2003; Erdoğan and Günğör, 2004; Gessner et al., 2004) are postulated. The "core-cover model" is based on large-scale correlation between Aegean and Anatolian units. Therefore, the model assumption is to parallelise units from the Greek Islands with units mapped in western Anatolia, Turkey. It separates the meta-sedimentary rocks and the metamorphic schist and gneiss into cover and core series. The contact between the core and the cover is either interpreted as a major unconformity (e.g. Schuiling, 1962) or as essentially intrusive reactivated as a major shear zone (e.g. Bozkurt and Park, 1994). The augengneiss, meta-granite and schist are allocated to the core facies, while the meta-sedimentary rocks (marble, paragneiss) represent an envelope-like cover (Table 2.1). Both units are assumed to be separated by a large fault system (Rimmelé et al., 2003; Bozkurt and Oberhänsli, 2001).

In the "nappe stacking model", the nappes are named Bayındır, Bozdağ, Çine and Selimiye nappes from bottom to top (e.g. Figure 2 of van Hinsbergen et al., 2010c). The Bayındır nappe consists predominantly of phyllite, quartzite, marble and greenschist, indicating a lower metamorphic grade compared to the other nappes. Alpine greenschist facies metamorphism is dated by Ar-Ar on white mica at >37 Ma (Lips et al., 2001). The Bozdağ nappe comprises mainly meta-pelite and meta-granite with some eclogite and amphibolite intercalations. The protolith age remains unknown. Gessner et al. (1998) suggest a Precambrian age based on the analysis of structural

data. The age determination of the granitic rocks by $^{207}Pb/^{206}Pb$ zircon dating indicates an intrusion age of 230-240 Ma (Ring et al., 2001). The Çine nappe consists mainly of orthogneiss, meta-granite and pelitic gneiss accompanied by eclogite and amphibolite lenses. The intrusion age of the orthogneiss protolith is dated at 560-540 Ma (U-Pb zircon age), with decreasing age from south to north (Ring et al., 2001). The age of the meta-granite protolith is determined at 530-540 Ma (U-Pb zircon age, Ring et al., 2001). The Selimiye nappe is subdivided into (1) the lower section consisting of meta-pelite and weakly-deformed meta-granite; and (2) the upper part composed of meta-pelite, meta-basite and marble. Uranium-Pb zircon ages of the meta-granite of the lower nappe section yield ca. 549 Ma indicating a Precambrian protolith age of the meta-pelite (Ring et al., 2001). An age from Devonian to Carboniferous is estimated for the upper nappe section supported by fossils (Schuiling, 1962; Cağlayan et al., 1980; Régnier et al., 2003; Table 2.1).

The Menderes Massif is crosscut by three roughly East-West striking graben systems into three submassifs (Figure 2.1). The Neogene BMG has a width of 8 to 12 km and a length of approximately 125 km. It separates the central and the southern Menderes Massif (CMM and SMM; Bozkurt, 2000). Bozkurt and Oberhänsli (2001) describe the graben systems as a result of "basin-and-range"-like extension of Neogene age. In the graben system, the geological units are divided into different compartments by antithetic faults.

2.3. Study area

The BMG graben filling consists of Neogene to Quaternary sedimentary rocks, whereas the graben shoulder comprises the metamorphic sequence of the Menderes Massif as described above. In the northern part, a Cretaceous marble is present along with a Paleozoic marble horizon and meta-carbonate rocks. Further north, a large area is covered by a Precambrian gneiss and schist sequence. The analogue stratigraphy is presented in the southern part of the rift system; however, the outcrops of the Cretaceous part are lacking.

Geothermal power generation in the BMG has a long history starting with a pilot

Table 2.1.: Comparison of the metamorphic rocks and the related nomenclature of the Menderes Massif (modified after Régnier et al., 2003; 2007).

Rock types	**Age**	**Classification**		**Reference**
		„core-cover-model “	„nappe-stacking model“	
phyllite quartzite marble (Iğdecik Formation)	Lower Cretaceous	cover	Bayındır	Ring et al., 1999, Gessner et al., 2001, Özer and Sözbilir, 2003, Şimşek, 1985
meta-pelite calcareous schist meta-marl marble-quartzite intercalation	Devonian-Carboniferous; meta-pelite protolith ≈ 549 Ma (Ring et al. 2001)	core, partly cover	Selimiye	Schuiling, 1962, Cağlayan et al., 1980 Satır and Friedrichsen, 1986, Hetzel and Reischmann, 1996, Régnier et al., 2003; 2007
augengneiss (meta-)granite intercalated mica schist paragneiss (containing eclogitic enclaves)	intrusion age of gneiss-protolith ≈ 560-540 Ma	core	Çine	Candan et al., 2001, Dora et al., 2001 Hetzel and Reischmann, 1996, Loos and Reischmann, 1999
meta-pelite and meta-psammite meta-granite amphibolite eclogite	amphibolite and eclogite precursor (Proterozoic)	core/cover facies	Bozdağ	Candan et al., 2001, Koralay et al., 2004

power plant constructed at the Kızıldere geothermal field close to Denizli in 1975 followed by the first commercial power plant in the same field with an electrical gross capacity of 15 MW (Aksoy, 2014). Additional plants in western Turkey that are located within the BMG increased the total capacity to 311 MW in 2013 (Aksoy, 2014). Most of the (more than 10) existing power plants in the BMG, a majority located at the northern escarpment in the Aydin and Denizli area, have an intercalation of marble, schist, and gneiss as reservoir rock. The marble horizons are described as the reason for the relatively high CO_2-contents of the produced geothermal fluid with an approximate average of 2.5 wt-% CO_2 (Aksoy, 2014).

2.4. Methods

2.4.1. General procedure and petrography

In total, 17 marble surface and cutting samples were analysed by different methods (Table 2.2). The study area is located in the BMG (Figure 2.1) including its northern and southern escarpment. The location of the 3,900 m deep geothermal exploration well GP-1 and the outcrops on the southern and northern escarpment of the graben are shown in Figure 2.2. All surface samples were collected from outcrops in 2018 and the cutting samples during drilling in 2017. While the first location is in Cretaceous marbles (northern escarpment), the latter location is underlain by marble and marble-schist intercalations of Paleozoic age (Régnier et al., 2007) (southern escarpment). The T1 sample originates from a small marble deposit which is not shown in the map due to scale reasons. A stratigraphical classification of T1 is not possible.

The samples from the southern escarpment are indicated with “Paleozoic” (T13-1 to 4; south of Koçarli village) and from the northern escarpment with “Cretaceous” (T3, T4, T5, T11; vicinity of Köşk village) based on the mapped geological formation (Figure 2.2). The cutting samples from the GP-1 well are differentiated in shallow (“well^S”, 1,050-1,325 m) and deep (“well^D”, 3,650-3,870 m) marble-bearing horizons based on intersection.

During drilling (rotary, direct circulation), composite samples of cuttings were taken in five-meter intervals. All samples were lag-time corrected and, after washing and drying, petrographical features were characterised with a binocular directly on site. Eight samples representative of the upper and lower marble-bearing intersections were selected for further analysis. Ricca et al. (2015) published a methodological approach to differentiate various marble types, originally named as provenance determination key. After sampling, the marbles were classified as pure or impure calcitic or dolomitic (Figure 2.3). Here the approach by Rosen et al. (2007) was applied where a pure calcitic marble is characterised by a modal $CaCO_3$ content of > 95 %. The calcite ($CaCO_3$) content of the total cutting sample in vol-% was first determined by point counting using a Novex RZB-SF binocular at drilling site.

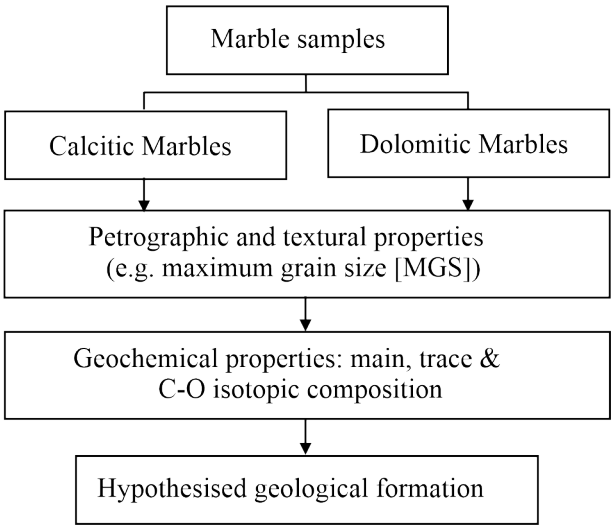


Figure 2.3.: Methodological diagram to differentiate various marble types (originally provenance determination key, modified after Ricca et al., 2015).

Furthermore, we employed a coupled scanning electron microscope and energy

Table 2.2.: List of methods applied to the different samples.

samples	#	1	2	3	4	5	6	7	8	9	10	11	12	13	14	15	16	17
	name	T1	T3	T4	T5-1	T11	T13-1	T13-2	T13-3	T13-4	1-1050	2-1065	3-1290	4-1325	5-3655	6-3680	7-3740	8-3865
	category	Cretaceous	Cretaceous	Cretaceous	Cretaceous	Cretaceous	Paleozoic	Paleozoic	Paleozoic	Paleozoic	well^S	well^S	well^S	well^S	well^D	well^D	well^D	well^D
geochemistry	C & O isotopic signature	X	X	X	X	X	X	X	X	X	X	X	X	X	X	X	X	X
	ICP-OES	X	X	X		X	X	X	X	X	X	X	X	X	X	X	X	X
	ICP-MS	X	X	X		X	X	X	X	X	X	X	X	X	X	X	X	X
	SEM-EDX	X	X		X	X	X	X	X	X	X	X		X		X	X	
	Rb-Sr geochronology								X		X		X	X	X		X	
	Sr isotopic signature	X	X				X			X								
petrography	colouring with Alizarin-S	X	X		X						X	X	X	X				
	pattern (calcite/dolomite)	X	X	X	X	X	X	X	X	X	X	X	X	X	X	X	X	X
	light transmission	X	X	X	X	X	X	X	X	X	X	X	X	X	X	X	X	X
	pyrite bearing	X	X	X	X	X	X	X	X	X	X	X	X	X	X	X	X	X
	shape-preferred orientation (calcite/dolomite)	X	X	X	X	X	X	X	X	X	X	X	X	X	X	X	X	X
	grain size distribution (calcite/dolomite)	X	X	X	X	X	X	X	X	X	X	X	X	X	X	X	X	X
	maximum grain size (calcite/dolomite)	X	X	X	X	X	X	X	X	X	X	X	X	X	X	X	X	X
	fractures, fissures	X	X	X	X	X	X	X	X	X		X						
	karst	X	X	X	X	X	X	X	X	X		X						
	colour	X	X	X	X	X	X	X	X	X	X	X	X	X	X	X	X	X

dispersive X-ray fluorescence analysis (SEM-EDX) to detect the type and purity of the samples in the Laboratory of the University of Greifswald, Germany. Hand specimens were crushed and attached to aluminium test plates with double side carbon adhesive pads to prevent charging of the sample. Additionally, the surfaces were vapour-coated with carbon. For the cutting samples, the same procedure was applied to 3 to 4 single calcareous grains previously identified under the binocular. A SEM Zeiss Evo 10 with an acceleration voltage of 20 kV was used. The EDX analysis was carried out using an element C2 detector.

A macroscopic characterisation of colour, rock texture including shape-preferred orientation, pattern, grain shape, grain structure, maximum grain size and grain size distribution of calcite and dolomite grains, open or sealed fissures and possible weathering features was done in the field and on hand specimens using a hand lens with millimetre scale. The odour while crushing the hand specimens or after reacting with hydrochloric acid (HCl) was determined indicating the presence of accessory pyrite. The light transmission was determined with a focused flashlight in the categories very low to high as described in Cramer (2004). For the cutting samples, these investigations were carried out using a binocular with the exception of fissure and karst features.

Microscopic features were analysed at the drilling site and the thin section analysis of both cuttings and surface samples (T1, T3, T5, 1-1050, 2-1065, 3-1290, 4-1325) with a polarizing microscope at the Karlsruhe Institute of Technology (KIT, Zeiss Axio Scope.A1, Axiocam 105 color). The colouring by Alizarin-S was done to distinguish calcite and dolomite. The thin section description focused on rock type and texture of the cuttings, including shape-preferred orientation and pattern of calcite and dolomite. The maximum grain size and grain size distribution of calcite and dolomite was determined by the conventional linear intercept method (Münzner and Schneiderhöhn, 1953). The average cutting size is in the range of 5 mm and that is why larger grain sizes cannot be investigated for these samples. The mineralogy was quantified by point counting with a binocular and colouring by Alizarin-S.

2.4.2. ICP-MS and ICP-OES analysis

For geochemical analyses, surface samples were crushed and pulverised in the Laboratory of Environmental and Raw Materials Analysis (LERA), Chair of Geochemistry and Economic Geology, Institute of Applied Geosciences (AGW) at KIT, while calcareous grains were picked from the cuttings using a binocular. In order to achieve complete digestion, the pulverised samples were dissolved in a combined HNO_3-HF-$HClO_4$ acid digestion. All samples were of suprapur (HNO_3, HF) or normapur ($HClO_4$) quality. The digests were analysed in LERA by inductively coupled plasma optical emission spectroscopy (ICP-OES, Varian 715ES, Agilent) (Ca, Fe, K, Mg, Na, Sr) and by inductively coupled plasma mass spectrometry (ICP-MS, XSeriesII, Thermo Fisher Scientific) with helium and hydrogen as collision gas (trace elements and REE). The collision gas was used to enable an accurate analysis of the interference-critical elements copper (Cu) and zinc (Zn). Quality control was secured by measuring the standard dolomite reference material "JDo-1" (SplitIO/Position 90) of the geological survey of Japan. Overall accuracy was better than ± 10 %; however, for some elements (e.g. Rb, Cs, Pb) the accuracy was lower mainly due to their extremely low concentration in carbonates.

REE concentrations including yttrium (REY) data were normalised to the Post Archean Australian Shale standard (PAAS, Piper and Bau, 2013; Y values from Condie, 1993). The calculation of the Ce anomaly is shown in equation (2.1) (Lawrence et al., 2006).

$$Ce/Ce^* = \frac{\frac{Ce_{sample}}{Ce_{PAAS}}}{((\frac{Pr_{sample}}{Pr_{PAAS}})^2 + \frac{Nd_{sample}}{Nd_{PAAS}})} \tag{2.1}$$

Furthermore, equation (2.2) introduces the Pr/Pr* parameter, which is useful to differentiate between apparent and real Ce anomalies (Bau and Dulski, 1996). If samples show a calculated Ce anomaly but Pr/Pr* yield values between 0.95 to 1.05, an apparent Ce anomaly is indicated.

$$Pr/Pr^* = \frac{2 * \frac{Pr_{sample}}{Pr_{PAAS}}}{(\frac{Ce_{sample}}{Ce_{PAAS}} + \frac{Nd_{sample}}{Nd_{PAAS}})} \tag{2.2}$$

Yttrium anomalies are indicated by calculating the ratio of Y to Ho without normalisation (Webb and Kamber, 2000; Tostevin et al., 2016). Europium anomalies are calculated with respect to its neighbours Sm and Gd as demonstrated in equation (2.3) (Meyer et al., 2012; Tostevin et al., 2016).

$$Eu/Eu^* = \frac{2 * \frac{Eu_{sample}}{Eu_{PAAS}}}{(\frac{Sm_{sample}}{Sm_{PAAS}} + \frac{Gd_{sample}}{Gd_{PAAS}})} \tag{2.3}$$

2.4.3. Stable carbon and oxygen isotopes

The C and O isotopic composition (δ^{13}C, δ^{18}O) of the marble carbonate minerals was determined by a Finnigan MAT 251 mass spectrometer in the laboratory of the University of Kiel, Germany. Samples reacted in 99 % H_3PO_4 to release gaseous CO_2 that was transferred into the mass spectrometer. The calibration was done using the carbonate isotope standard reference materials NBS 18, NBS 19 and 20. The C isotopic composition is given in the delta notation relative to the Vienna Pee Dee Belemnite (V-PDB) standard. O isotope data are given relative to the Vienna Standard Mean Ocean Water (V-SMOW). Measurement precision of repeated isotope measurements were within 0.1 to 0.5 ‰ for both O and C. To convert the δ^{18}O values from V-PDB to V-SMOW, equation (2.4) was used (Hoefs, 2015).

$$VSMOW\,in\,‰ = 1.03091 * VPDB\,in\,‰ + 30.91 \tag{2.4}$$

2.4.4. Rb-Sr geochronology

For Rb-Sr multimineral-based geochronology, we selected impure marble samples with significant amounts of muscovitic white mica and/or biotite. These were the surface sample T13-3 and the cuttings samples 1-1050, 3-1290, 4-1325, 5-3655 and 7-3740. In addition, the ^{87}Sr/^{86}Sr isotopic composition of pure marble samples T1, T3, T13-1 and T13-4 was measured. This was done to potentially determine the age of marble deposition from seawater based on Sr isotope stratigraphy (cf. McArthur et al., 2001). Sample preparation and analytical procedures followed the techniques

outlined in Glodny et al. (2008b). Isotopic data was measured at GFZ Potsdam on a Thermo Scientific TRITON thermal-ionisation mass spectrometer. Strontium data was generated in the dynamic multicollection mode, whereas Rb isotope dilution analysis was done in static multicollection mode. The value for $^{87}Sr/^{86}Sr$ in the NIST SRM 987 isotope standard, as obtained during the period of the analytical work, was 0.710242 ± 0.000020 (2σ, n= 16). Isochron parameters were calculated using standard uncertainties of 0.005 % for Sr isotopic ratios and of ± 1.5 % for Rb/Sr ratios. Individual analytical uncertainties were consistently smaller than these values. Uncertainties of isotope and age data are stated as 2σ throughout this work. The program ISOPLOT/EX3.71 (Ludwig, 2003) was used to calculate regression lines. The ^{87}Rb decay constant is adopted as suggested by Villa et al. (2015).

2.5. Results

2.5.1. Petrography

Paleozoic marble

The Paleozoic marble outcrops at the southern escarpment of the BMG (T13; Figure 2.2) are characterised by marble which is overlain by banded gneiss (Figure 2.4a). The marble is banded or has granoblastic structures (Figure 2.4c). At the contact of both units, an approximately 40 cm thick layer of very fine-grained marble is found, which shows less than 5 vol-% iron oxides (especially sample T13-3). The main marble horizon is massive, has a fine- to medium grain size and a mostly evenly distributed grain size but partly elongated calcite grains (T13-1, T13-4). Calcite (T13-2) is locally euhedral. Accessory pyrite explains the sulphuric odour while crushing the rocks. Typical for this marble is the light blueish-grey colour, a very low light transmission and a striated, partly mottled pattern. The marble is crosscut by fine carbonate fissures (approx. 1 mm thickness, N-S trending), covered with iron oxides.

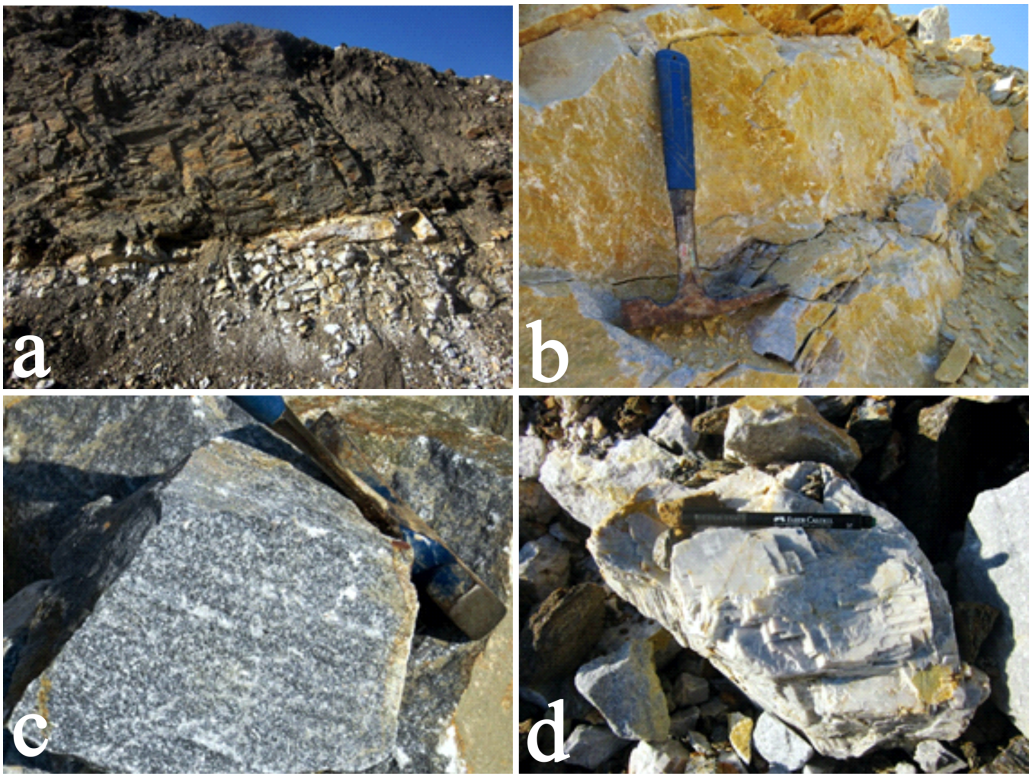


Figure 2.4.: Paleozoic marble: marble quarry SE of Koçarli village, southern escarpment of the BMG (Location T13): a) banded gneiss (dark colour) on top of marble (light colour) (image width: 6 m); b) light blueish-grey marble; c) light blueish-grey banded marble; d) light grey marble.

The SEM-EDX analysis of carbonate grains of this marble confirms calcite as the dominant carbonate mineral (Figure 2.5). The only exception is sample T13-3 with a nearly balanced Ca and Mg ratio pointing to an impure dolomitic marble. In the abandoned quarry of T13 location, the T13-3 sample is located very close to the transition to the overlying gneiss sequence (Figure 2.4a).

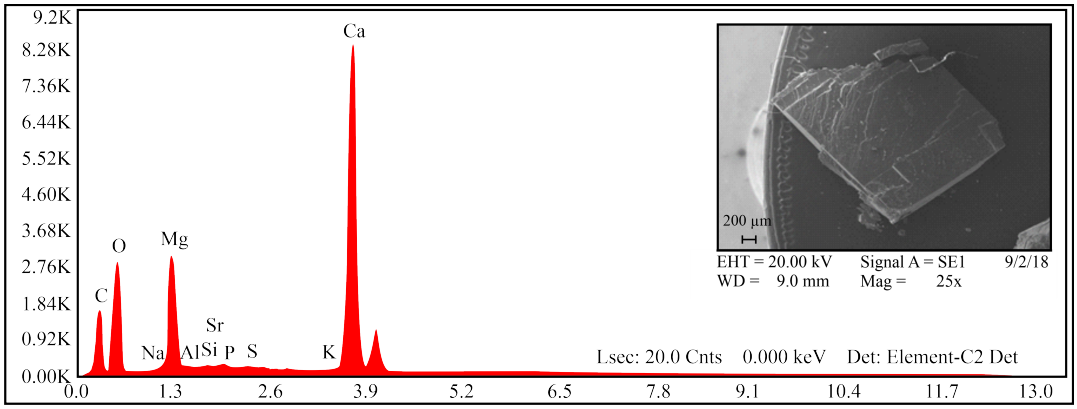


Figure 2.5.: SEM-EDX of sample T13-2. It shows that Ca is the main constituent of the sample.

Cretaceous marble

The Cretaceous marble is composed of a white marble (Figures 2.6a and b) at the footwall and alternating marble and meta-marl of approx. 3 m thickness in the hanging wall (Figure 2.6c). The white marble is predominantly very fine-grained, massive with fine fissures and frequent thin veins, both mainly composed of calcite (Figure 2.6a). The SEM-EDX analysis confirms calcite being the major carbonate mineral in the white marble. No foliation is observed. In thin section, the white marble has a homeoblastic structure with 75 vol-% calcite and 25 vol-% dolomite (Figure 2.7a). The grains are locally fractured with bulged grain boundaries (Figure 2.7b). The photomicrographs show a heteroblastic marble of mainly 90 vol-% calcite with some partly rounded and unoriented calcite grains that are embayed in a dark calcitic matrix (Figures 2.7c, d and f). The contact between the calcite grains is dentated. Thin, calcite-filled fissures and stylolites crosscut the calcite matrix (Figure 2.7e). Samples T1, T3 and T4 display a hematite coating along calcite grain boundaries.

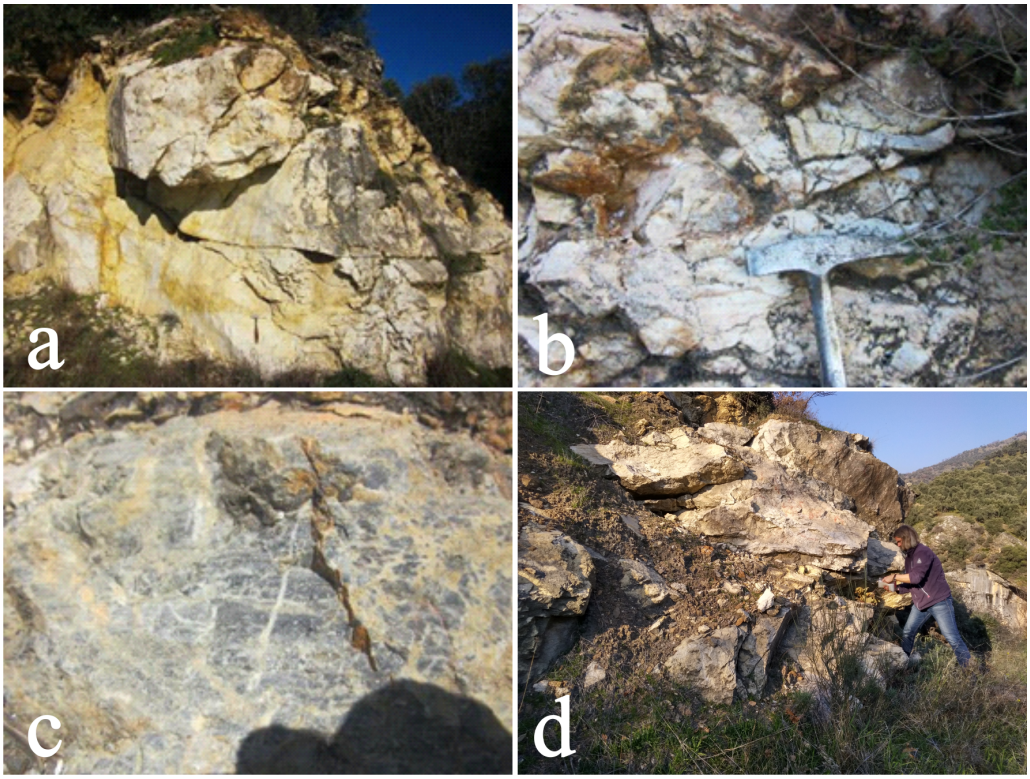


Figure 2.6.: Marble of three different outcrops at the northern escarpment of the BMG between Köşk and Eğrikavak (Figure 2.2): a) characteristic outcrop of the Cretaceous massive marble showing a light-coloured marble (T3) (image width: 10 m); b) detail of a) highlighting the characteristic white colour of the Cretaceous marble; c) typical metamorphosed marl of a Cretaceous unit showing the cross-hatched pattern of calcite veins (T5) (image width: 0.2 m); d) characteristic white marble of outcrop T11 with an overlying clay sequence.

GP-1 well

The GP-1 well intersected two marble horizons which were both sampled (Figure 2.8). Due to the drilling technology, all cutting samples are composite samples from a depth interval of 5 m. At bottom hole, orthogneiss with eclogite intercalations was drilled. Above this, the deepest carbonate-bearing rock section was sampled and further analysed (8-3865). It is a fault-related alteration zone having a significant calcite content (Figure 2.8) of 10 vol-% with also chips of orthogneiss and eclogite. The calcite content is rather low compared to the other cutting samples (Table 2.3). Above the fault, a mixed layer of predominantly banded gneiss and orthogneiss is present

with fault-controlled hydrothermal alteration zones in various intersections.

Table 2.3.: Calcite content as a result of point counting of the sampled cuttings. mTVD: meters in total vertical depth.

name	origin	depth in mTVD	calcite content in vol-%
1-1050	well^S	1050	75
2-1065	well^S	1065	56
3-1290	well^S	1290	34
4-1325	well^S	1325	39
5-3655	well^D	3655	39
6-3680	well^D	3680	32
7-3740	well^D	3740	41
8-3865	well^D	3865	10

The samples of the deep marble horizon show alternating layers of marble and banded gneiss at a decimetre scale, sometimes intercalated by feldspar-quartz veins. The calcite content is in the range of 32 to 41 vol-% (Table 2.3). The colour is white to light grey with a very low light transmission. The grain size is equally fine-grained. Calcite is characterised by partly elongated twin lamellae with dentated and sometimes lobate grain boundaries (Figure 2.9a). The EDX investigation yields more than 90 vol-% Ca content for the samples 6-3680 and 7-3740. This horizon is characterised as impure calcitic marble.

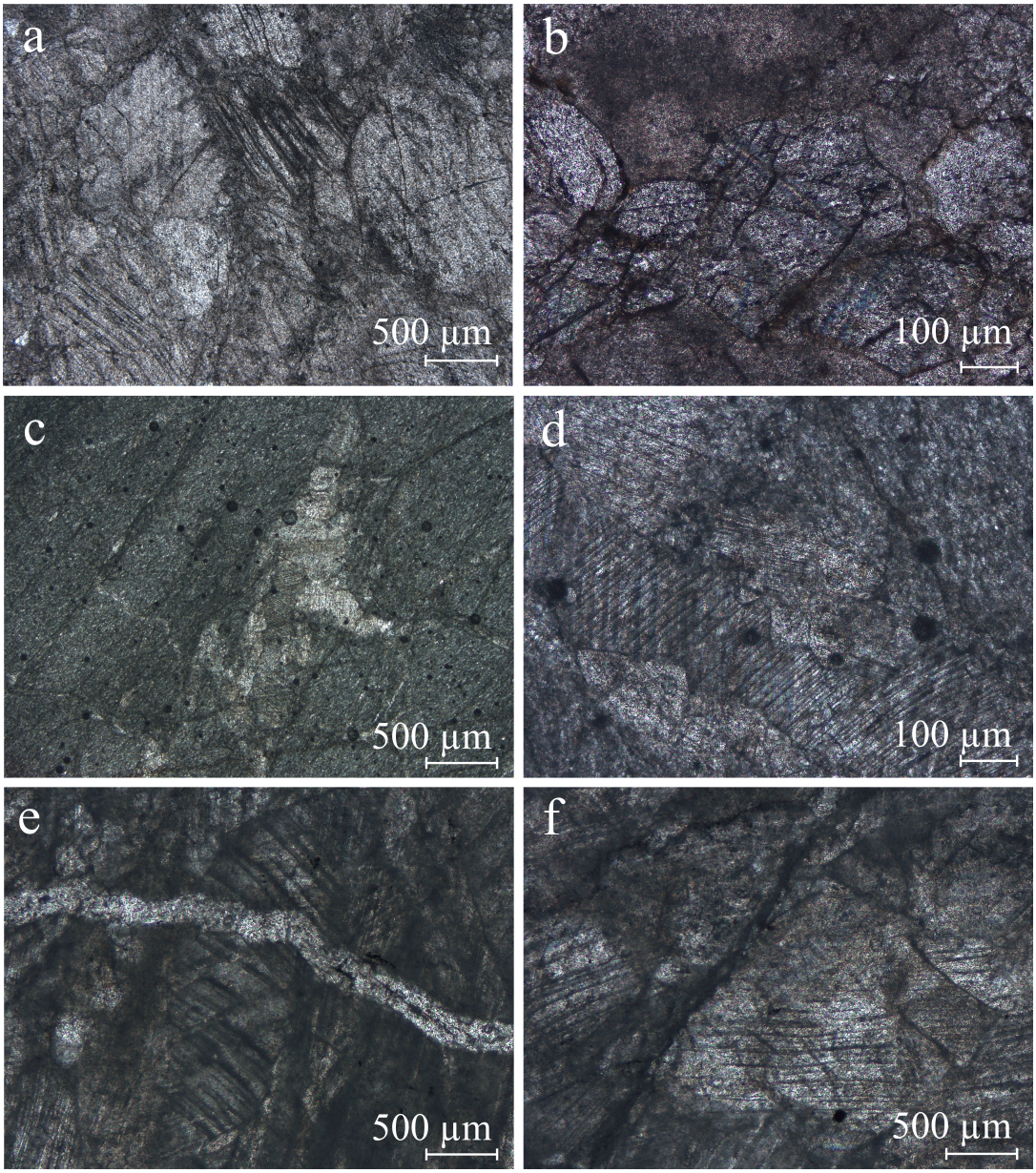


Figure 2.7.: Representative photomicrographs of Cretaceous marble (T1, T3 and T5). The dark and blurred appearance of thin sections is caused by poor polishing and a slightly higher thickness than standard. a) mainly homeoblastic calcite with twin lamellae parallel to the rhomb edges in plane polarised light (ppl). The sample consists of ca. 75 vol-% calcite and 25 vol-% dolomite (T1); b) fractured calcite of T1 in detail (ppl); c) calcite grains in calcite matrix with twin lamellae representing a heteroblastic marble of 90 vol-% calcite (ppl) (T3); d) fractured calcite with abundant twin lamellae (ppl) (T3); e) calcite fissure in calcite matrix showing twin lamellae (ppl) (T5); f) thin section with approximately 90 vol-% calcite and fractured calcite grains (ppl) (T5).

The shallow marble horizon above a fault-related alteration zone with greenish clay has a calcite content of 39 vol-% (sample 4-1325; Table 2.3). Shallower intersections (sample 3-1290) have similar characteristics with small interbedded layers of biotite gneiss. The marble consists of mainly calcite and little dolomite with bulged grain boundaries (Figure 2.9b).

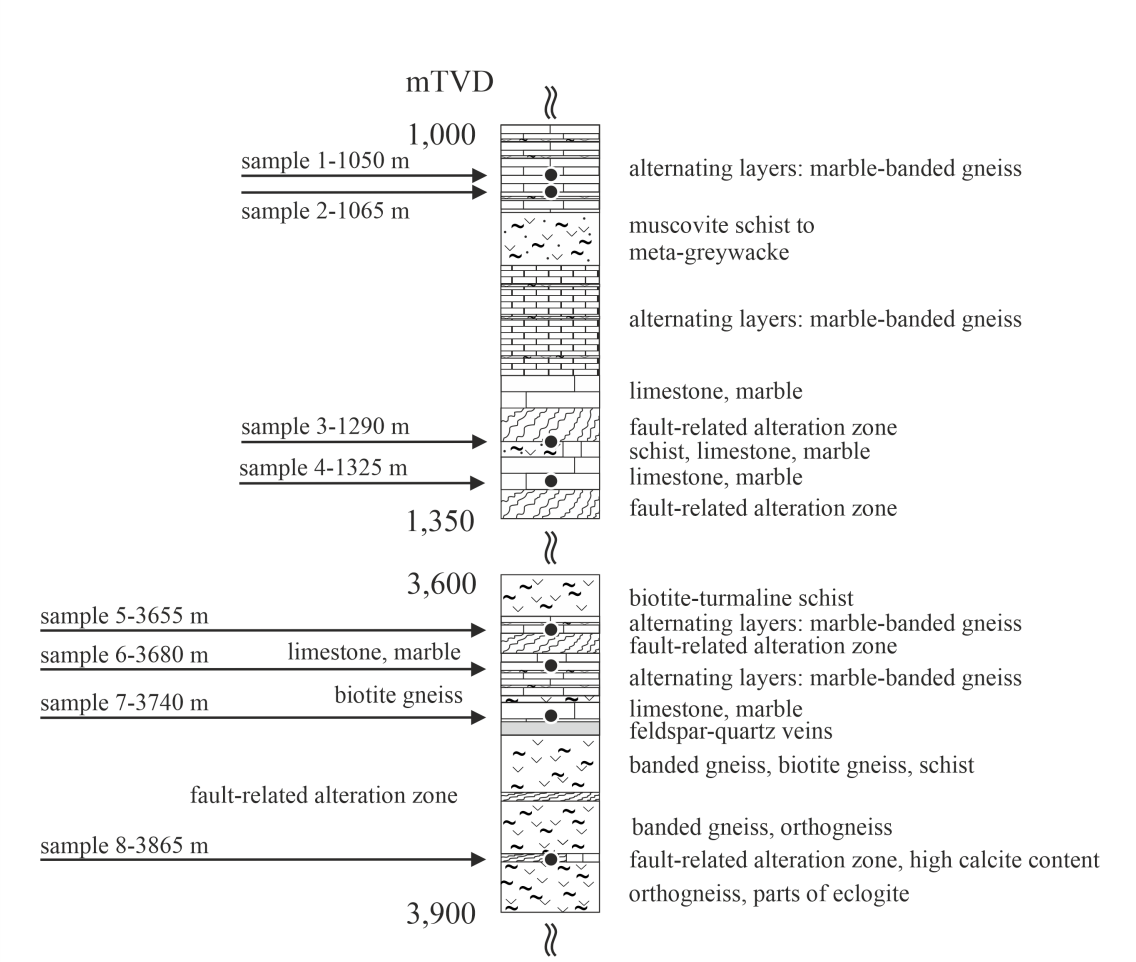


Figure 2.8.: Marble-bearing sections of the geothermal exploration well GP-1. Samples for detailed analysis are marked. Above 1,000 m, the sedimentary cover was drilled. In between the marble horizons gneiss and schist sequences were drilled, below 3,900 m a 50 m orthogneiss horizon was drilled until bottom hole. mTVD: meters in total vertical depth.

In the upper layer, a fault-related alteration zone is intersected, which is adjacent to

alternating layers of marble and banded gneiss. This section is followed by muscovite schist and meta-greywacke. At a depth of 1,065 m, a marble section with alternating layers of marble and banded gneiss is present. This marble has a blueish to light grey colour along with a low to medium light transmission and striated patterns. It has a calcite content of 56 to 75 vol-% (Table 2.3, 1-1050 and 2-1065) and a granoblastic-polygonal texture (Figure 2.9c) with fine-grained, elongated calcite grains. Compared to the other cutting samples, this marble has the highest calcite content. The sample 1-1050 has additional calcite fissures. Marble from the shallow intersection contains a small amount (< 5 %) of quartz and mica.

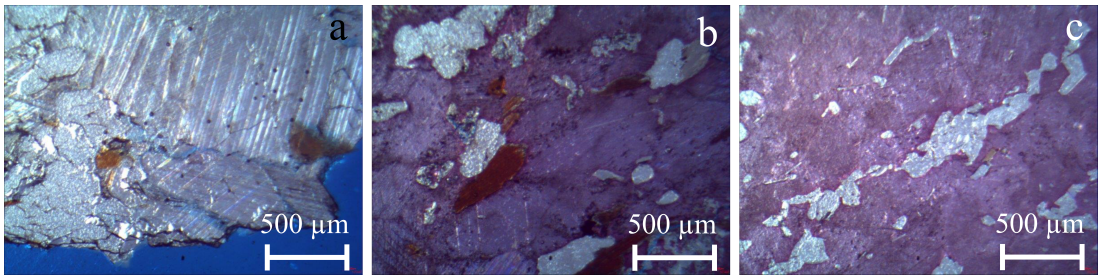


Figure 2.9.: Representative photomicrographs of cutting samples of the GP-1 well, b)-c) sections coloured by Alizarin-S: a) thin section of cuttings from 3,740 m with typical twin lamellae in partly elongated calcite with dentated and lobate grain boundaries (ppl); b) thin section of cuttings from 1,290 m containing mainly calcite and little dolomite (ppl); c) thin section of cuttings from 1,050 m with reddish calcite having a granoblastic-polygonal texture (ppl).

Maximum grain size of carbonate minerals in Paleozoic, Cretaceous and GP-1 samples

The maximum grain size (MGS) of the calcite and dolomite varies in a comparatively small range between 0.2 and 3.0 mm (Figure 2.10). One outlier is the Paleozoic outcrop sample T13-2 with an MGS > 10 mm (Table 2.4). The MGS of the well samples appears to be small compared to the surface samples, but no systematic difference is observed and the cutting size of 5 mm may have influenced the MGS determination of the well samples. The MGS of the samples analysed are small in comparison to data published from other sites worldwide ranging from 0.2 mm to 9.5 mm (Gorgoni et al., 1998; Ricca et al., 2015; Figure 2.10).

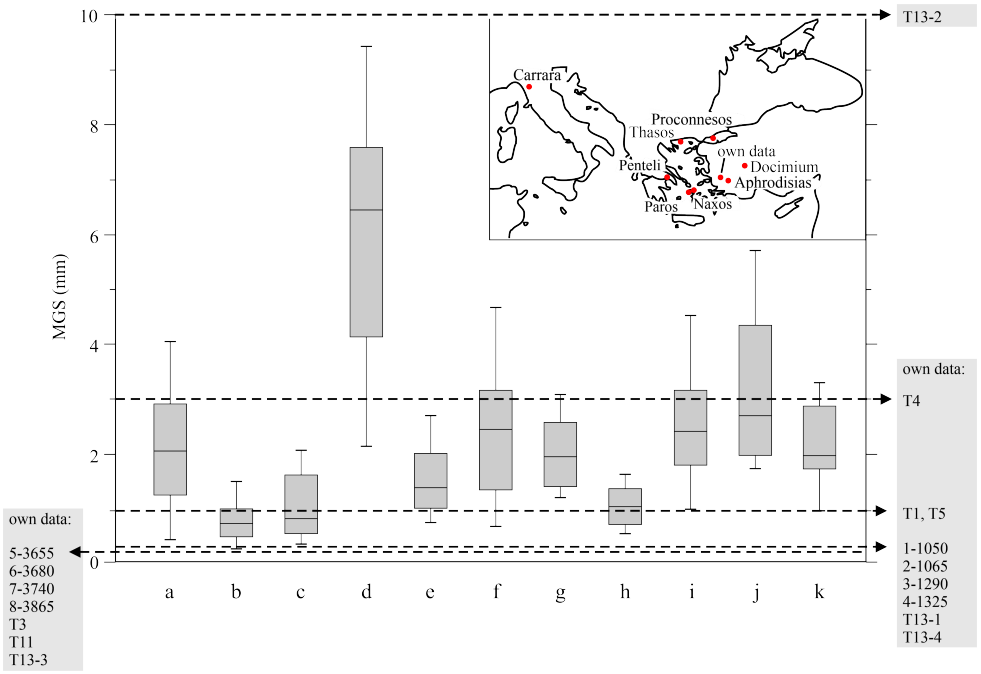


Figure 2.10.: Comparison of maximum grain size of various marbles (this study and Gorgoni et al., 1998). a) Aphrodisias, b) Carrara, c) Docimium, d) Naxos, e) Paros (1), f) Paros (2), g) Paros (4), h) Penteli, i) Proconnesos, j) Thasos (2), k) Thasos (3). The literature data is not from the same stratigraphy as the samples of this study.

2.5.2. Geochemistry

Major and trace elements

All samples collected at outcrops are dominated by a high CaO content of 33 to 59 wt-% (Table A.1). The Paleozoic marble has CaO contents in the range of 50 wt-%, however the T13-3 sample shows a lower CaO content of 33 wt-% along with a higher MgO content of 19 wt-%. The CaO content in the Cretaceous marble lies within the same range (Table A.1). Both, the Cretaceous and the Paleozoic samples show a similar pattern when comparing the concentrations of the major elements (Figure 2.11a). The Na_2O and K_2O contents are mostly below the detection limit (Figure 2.11a). All samples of the Paleozoic and Cretaceous marbles have similar Al_2O_3 (0.02-0.87 wt-%), $Fe_2O_{3\,tot}$ (0.07-1.34 wt-%) and MnO (0.01-0.15 wt-%) concentrations. The Sr concentration is below 1,000 mg/kg in the outcrop material.

Table 2.4.: Summary of petrographical observations. c: Cretaceous, p: Paleozoic.

	sample	origin	colour: white (w) or blueish light grey (bg)	calcitic (cc) or dolomitic (dol) marble; pure or impure (i)	maximum grain size [mm] (calcite/dolomite)	grain size distribution (calcite/dolomite) (eg: equally grained; ug: unequally grained)	shape-preferred orientation (calcite/dolomite	pattern (calcite/dolomite)	pyrite-bearing	light transmission
1	T-1	c	w	cc, pure	1	eg	no	no	no	low
2	T-3	c	w	cc, pure	0.2	eg	no	no	no	very low
3	T-4	c	w	cc, i	3	eg	no	no	no	very low
4	T-5	c	w	cc, pure	1	ug	no	stained	no	very low
5	T-11	c	w	cc, pure	0.2	eg	no	no	no	very low
6	T13-1	p	bg	cc, pure	0.3	eg	elongated	striated	yes	medium
7	T13-2	p	bg	cc, pure	>10	ug	no	striated,	yes	very low
8	T13-3	p	bg	dol, i	<0.2	eg	no	no	no	very low
9	T13-4	p	bg	cc, pure	0.3	eg	elongated	striated	yes	medium
10	1-1050	well^S	bg	cc, i	0.3	eg	elongated	striated	no	low
11	2-1065	well^S	bg	cc, i	0.3	eg	elongated	striated	no	medium
12	3-1290	well^S	bg	cc, i	0.3	eg	elongated	striated	no	low
13	4-1325	well^S	bg	cc, i	0.3	eg	elongated	striated	no	medium
14	5-3655	well^D	w	cc, i	0.2	eg	no	few dark points	no	very low
15	6-3680	well^D	w	cc, i	0.2	eg	no	no	no	very low
16	7-3740	well^D	w	cc, i	0.2	eg	elongated	streaks	no	very low
17	8-3865	well^D	w	cc, i	0.2	eg	no	no	no	very low

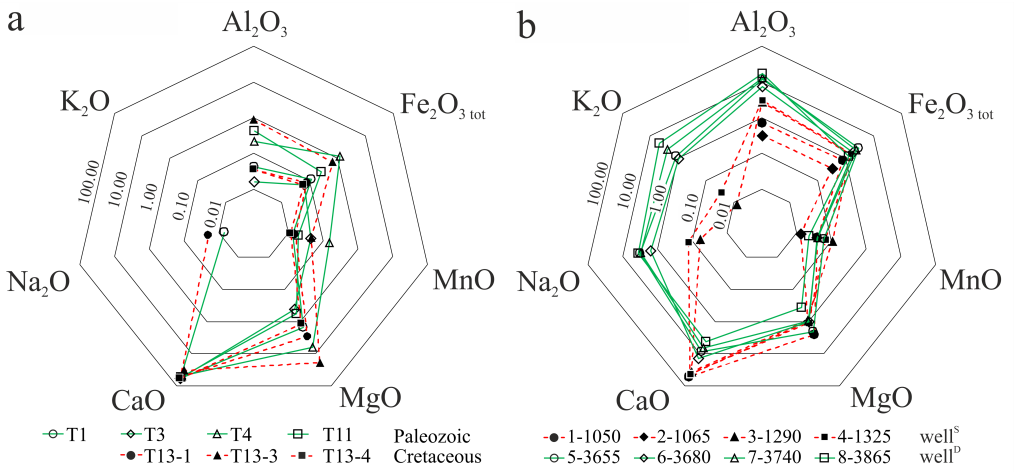


Figure 2.11.: Major oxide geochemistry in wt-%. a) surface samples (Paleozoic, Cretaceous); b) cutting samples (well^S; well^D).

The trace element concentrations of the Paleozoic and Cretaceous marble are rather low with a sum of below 460 mg/kg (Li to U, Table A.1). Beside Sr, Ba and P partly show higher concentrations in the range from 5 to 220 mg/kg. Based on the major and trace element concentrations, the Paleozoic and Cretaceous marbles are indistinguishable (Figure 2.11a).

The well^S samples of GP-1 have similar but lower CaO contents compared to the outcrop material with a slightly lower average content of 44 wt-%. Compared to the deeper section below 3,000 m depth, the well^S samples exhibit higher CaO contents (Figure 2.11b). The Al_2O_3, $Fe_2O_{3\,tot}$ and MnO concentrations of the well^S samples are also similar to the outcrop samples, whereas the Na_2O and K_2O concentrations reach partly 3-18 times higher concentrations than in the outcrop samples. The Sr concentrations reach up to 2,274 mg/kg. Besides Sr, the well^S samples have a sum of trace element contents of P, V, Cr, and Ba below 400 mg/kg. The total trace element content (Li to U, Table A.1) is higher than in the outcrop samples.

The well^D samples show a different major element pattern (Figure 2.11b) than the Paleozoic and Cretaceous outcrop samples and well^S samples. This is mainly related to Na_2O, K_2O and Al_2O_3 concentrations that are approximately one order of magnitude higher and within a range from 1 to 17 wt-%. The Sr concentrations are below 455 mg/kg. However, the total trace element content is relatively high with

1,265 mg/kg to nearly 3,000 mg/kg. In general, the cutting samples have higher trace element contents than the outcrop samples.

REY geochemistry

The Paleozoic marble samples tend to slightly lower REY contents (normalised to PAAS) compared to the Cretaceous samples (Figure 2.12). They lie within the range of the Menderes region with a negative Ce (0.68-0.71) and a positive Y anomaly (Y/Ho ratio: 39-48) (cf. Cramer, 2004). Each sample of Cretaceous marble has a negative Ce (0.55-0.80) and a positive Y anomaly (Y/Ho ratio: 44-51) (Figure 2.12). In addition, the T3 and T4 samples have a positive Eu anomaly (2.54 and 1.27) and also have higher normalised La to Tb values than reported for the Menderes region published by Cramer (2004). The GP-1 samples generally show higher absolute and normalised REY values in comparison with the surface samples (Figure 2.12). The well^{D} samples show higher absolute and normalised values than the well^{S} samples, which have normalised values below 0.6. The samples 1-1050 and 2-1065 have strong negative Ce anomalies with Ce/Ce* values of 0.73 and 0.56 and Y/Ho ratios of 39 and 46, respectively. The samples 3-1290 and 4-1325 have only a slight Ce anomaly (0.92-0.93) and no distinct Y anomaly (Y/Ho ratio: 29 and 30). The well^{D} cuttings have a flat PAAS-normalised pattern between La and Ho and neither a Ce nor a Y anomaly (Y/Ho ratio: 27-29) (Figure 2.12). Sample 8-3865 has a distinct positive Eu anomaly (1.62). In comparison to the cutting samples, the surface samples have a stronger Ce anomaly.

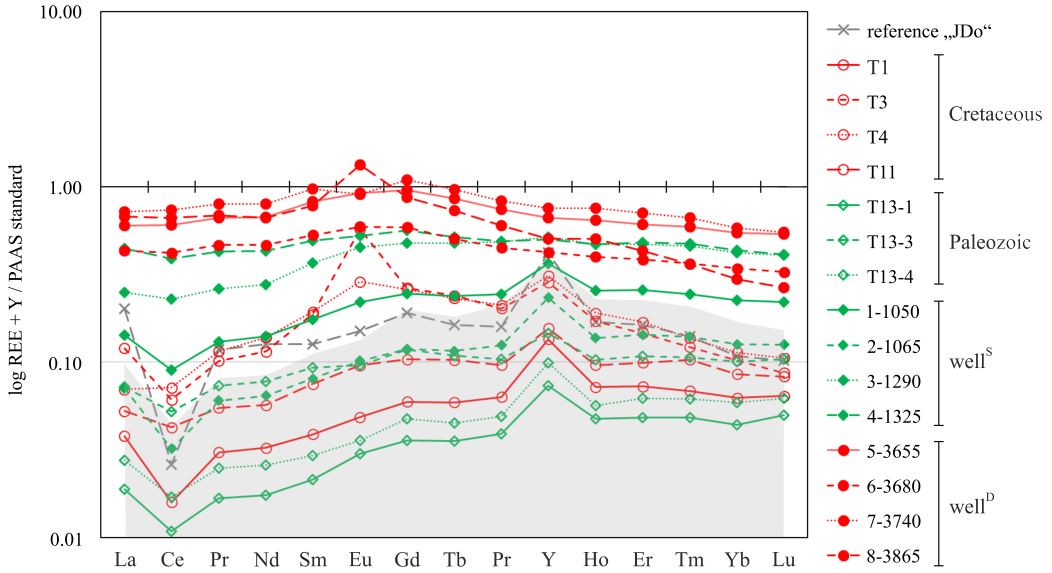


Figure 2.12.: PAAS-normalised Y and REE patterns for cutting and surface samples. The grey shaded area indicate maximum values reported for the Menderes region (Cramer, 2004). Minimum values of Cramer (2004) are lower than the shown normalised value of 0.01.

Regarding their absolute REY values, Paleozoic and well^S samples show lower REY contents than well^D samples and Cretaceous marble. In addition, the well^D and Cretaceous samples exhibit higher PAAS-normalised Gd_{PAAS}/Lu_{PAAS} (Lu: lutetium) ratios (Figure 2.13). The Paleozoic and the well^S samples have a lower Gd_{PAAS}/Lu_{PAAS} ratio indicating no significant HREE decrease.

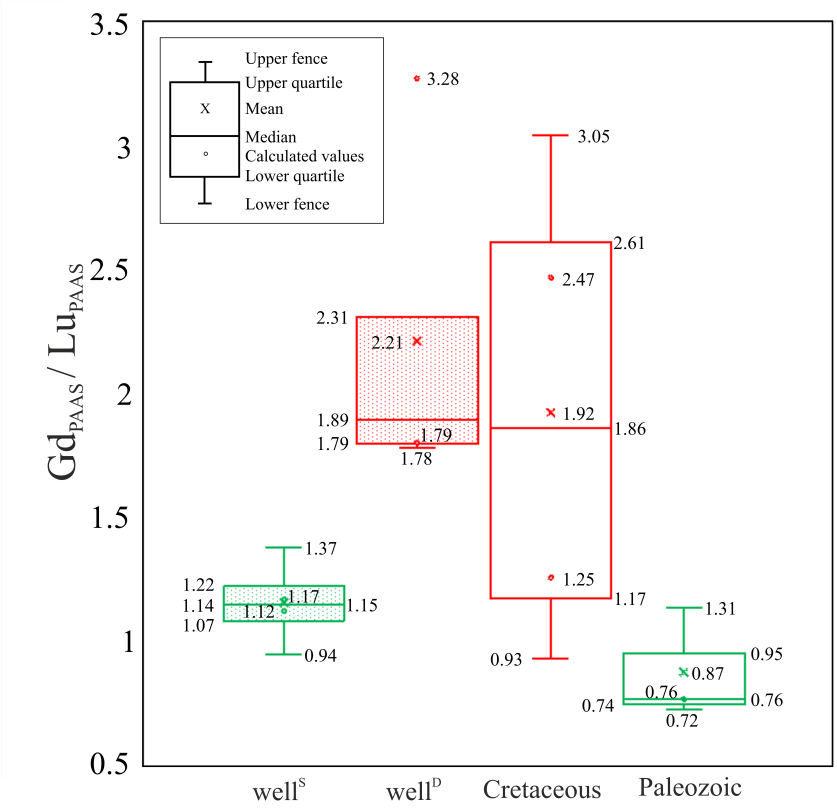


Figure 2.13.: Boxplot showing the PAAS-normalised values and quartiles of Gd_{PAAS} /Lu_{PAAS} ratios. The diagram displays the decrease of $HREE_{PAAS}$ in the well^D and Cretaceous samples.

Carbonate stable isotope composition: δ^{13}C and δ^{18}O

The δ^{13}C values show a range from 1.73 to 4.25 ‰ for the Paleozoic marble and -0.42 to 4.40 ‰ for the Cretaceous marble (Table 2.5). The well^S samples have δ^{13}C values from 1.76 to 3.00 ‰ and the well^D samples show negative values from -2.89 to -1.57 ‰. The δ^{18}O values in the Paleozoic samples are in the range of 19.62 and 23.84 ‰ and those of the Cretaceous samples in the range of 6.74 to 21.11 ‰. Well^S samples have δ^{18}O values between 18.17 to 20.07 ‰ and the well^D samples values between 13.05 and 15.28 ‰, respectively.

All Paleozoic and well^S samples show higher δ^{13}C values (1.73 to 4.00 ‰) relatively to well^D and Cretaceous samples (-2.89 to 1.60 ‰) (Figure 2.14). The only exception

Table 2.5.: Results of the $\delta^{13}C_{VPDB}$ and $\delta^{18}O_{VSMOW}$ stable isotope measurements.

#	name	origin	$\delta^{13}C_{VPDB}$	$\delta^{18}O_{VSMOW}$
surface samples			‰	‰
1	T1	Cretaceous	4.40	21.11
2	T3	Cretaceous	1.60	6.74
3	T4	Cretaceous	-0.42	13.45
4	T5-1	Cretaceous	-0.26	8.93
5	T11	Cretaceous	0.94	14.85
6	T13-1	Paleozoic	4.00	20.82
7	T13-2	Paleozoic	3.58	21.28
8	T13-3	Paleozoic	1.73	19.62
9	T13-4	Paleozoic	4.25	23.84
cutting samples				
10	1-1050	well^S	1.76	18.17
11	2-1065	well^S	2.11	18.52
12	3-1290	well^S	2.16	18.85
13	4-1325	well^S	3.00	20.07
14	5-3655	well^D	-2.20	13.05
15	6-3680	well^D	-2.83	13.74
16	7-3740	well^D	-2.89	13.66
17	8-3865	well^D	-1.57	15.28

is sample T1 (Cretaceous) with the highest $\delta^{13}C$ value of 4.40 ‰. The well^D and Cretaceous samples show lower $\delta^{18}O$ values (6.74 ‰ to 15.28 ‰) than the Paleozoic and the well^S samples (18.17 ‰ to 23.84 ‰) with values less than 15.28 ‰, except T1 sample (Cretaceous) which has a $\delta^{18}O$ value of 21.11 ‰ (Figure 2.14). The Cretaceous samples T3 and T5-1 show $\delta^{18}O$ values below 10 ‰. Both, cutting and surface samples of Paleozoic and well^S form one group regarding the ranges of the $\delta^{13}C$ and $\delta^{18}O$ values. Similarly, the Cretaceous and well^D samples can be grouped together (Figure 2.14). In general, the $\delta^{13}C$ values of this study are in a similar range compared to the samples from the Menderes region (from -6 to 5 ‰; Cramer, 2004; Manfra et al., 1975). The range of $\delta^{18}O$ values from the investigated well^S and Paleozoic samples are within the proposed range for limestone and marble (cf. Rollinson, 1993). The Cretaceous and well^D samples are significantly depleted in ^{18}O compared to the limestone-marble range specified by Rollinson (1993) (Figure 2.15a). The $\delta^{13}C$ signature of Cretaceous

and well^D samples plot within the field of freshwater as well as marine carbonate rocks, whereas Paleozoic and well^S samples show higher values within the freshwater carbonate rock region, some even exceeding towards higher values (esp. Paleozoic; Figure 2.15b). In contrast to δ^{13}C, the δ^{18}O values show a wider spread. The δ^{18}O values of all samples plot in the meteoric water region. They display relatively low values of δ^{18}O compared to other samples from the Menderes region (Cramer, 2004).

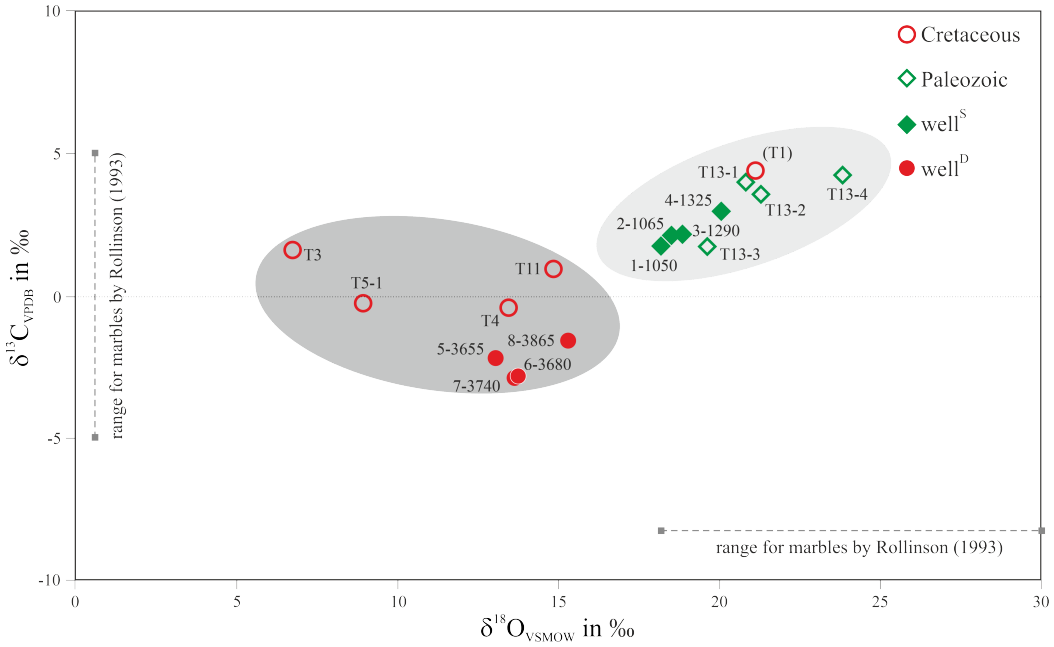


Figure 2.14.: Cross plot of δ^{18}O and δ^{13}C isotopic signatures. The grey ellipses indicate two groups according to the isotopic composition and define the well^D and the Cretaceous samples as one group and the Paleozoic and well^S samples, respectively.

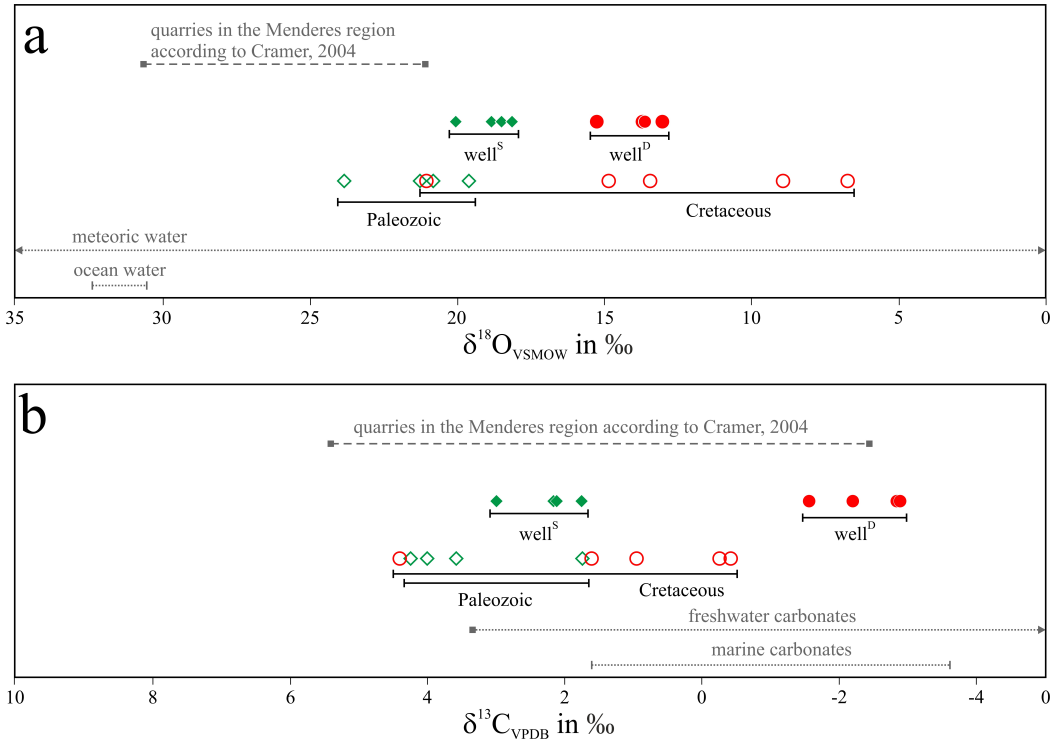


Figure 2.15.: a) $\delta^{18}O_{VSMOW}$ isotopic values and b) $\delta^{13}C_{VPDB}$ in ‰ from the samples in this study in comparison with common ranges of different rocks and waters (modified after Hoefs, 2015).

Rb-Sr geochronology and $^{87}Sr/^{86}Sr$ data

Six samples in total were analysed for Rb-Sr multimineral systematics (Figure 2.16; Table 2.6). Among the surface samples, only the fine-grained marble of sample T13-3 had sufficient mica to determine a Rb-Sr age (Figure 2.16a). The data for calcite and two muscovitic white mica fractions do not define an isochron; however, ages calculated for the two calcite-white mica pairs are close to 30 Ma (30.72 ± 0.46 Ma and 27.75 ± 0.47 Ma).

For the five cutting samples, the degree of overprint by ductile deformation was difficult to estimate. Nevertheless, all the samples show indications for a preferred orientation of mica, indicating that the rocks experienced ductile shear. For all these samples, we analysed calcite, two grain size fractions of white mica, and carefully selected, well preserved biotite without any evidence of bleaching or chloritisation. A striking

Table 2.6.: Rb-Sr data. n.d.: not determined.

sample #	material	Rb in mg/kg	Sr in mg/kg	$^{87}Rb/^{86}Sr$	$^{87}Sr/^{86}Sr$	$^{87}Sr/^{86}Sr\ 2\sigma_m$
analysis						
T13-3						
PS3449	white mica > 250 µm	307	55.2	16.1	0.719112	0.0011
PS3450	white mica < 250 µm	323	12.6	74.4	0.744796	0.0014
PS3451	calcite	2.68	109	0.0709	0.712901	0.002
1-1050						
PS3460	white mica > 250 µm	351	155	6.54	0.715878	0.0016
PS3461	white mica < 250 µm	310	211	4.25	0.714283	0.0016
PS3462	calcite	0.87	616	0.0041	0.71022	0.0019
PS3463	biotite < 250 µm	490	21.7	65.5	0.738503	0.003
3-1290						
PS3456	biotite > 250 µm	436	93.1	13.6	0.714216	0.0022
PS3457	white mica > 250 µm	335	356	2.72	0.709947	0.0031
PS3458	white mica < 250 µm	321	400	2.32	0.709731	0.0028
PS3459	calcite	0.73	2369	0.00089	0.708584	0.0012
4-1325						
PS3464	biotite > 250 µm	416	42.2	28.5	0.720779	0.0021
PS3465	white mica < 250 µm	310	482	1.86	0.708938	0.0022
PS3466	white mica > 250 µm	341	407	2.43	0.709293	0.0018
PS3467	calcite	3.58	1592	0.00652	0.707675	0.0014
5-3655						
PS3445	biotite > 250 µm	260	14.3	53	0.736219	0.0022
PS3446	white mica > 250 µm	232	115	5.83	0.720568	0.0024
PS3447	white mica < 250 µm	209	120	5.06	0.719794	0.0016
PS3448	calcite	39.4	146	0.782	0.71533	0.0028
7-3740						
PS3452	biotite > 250 µm	346	27.8	36.1	0.730156	0.0024
PS3453	white mica > 250 µm	270	143	5.46	0.722326	0.002
PS3454	white mica < 250 µm	263	161	4.73	0.722	0.0021
PS3455	calcite	9.86	881	0.0324	0.709463	0.0013
Calcite from marble						
PS3468	calcite T1	n.d.	n.d.	n.d.	0.70838	0.0014
PS3469	calcite T3	n.d.	n.d.	n.d.	0.712295	0.0017
PS3470	calcite T13-1	n.d.	n.d.	n.d.	0.709222	0.0033
PS3471	calcite T13-4	n.d.	n.d.	n.d.	0.7093	0.0012

similarity between the samples 1-1050, 3-1290, 4-1325 and 5-3655 (Figure 2.16b, c, d, e) is that calcite-biotite pairs consistently yield apparent ages near 30 Ma, whereas white mica-calcite apparent ages are unsystematically higher, with age values between 36 and 75 Ma (Figure 6). In sample 7-3740 (Figure 2.16f), the biotite-calcite age is, with 41 ± 0.6 Ma, apparently older than in the other cutting samples. In this sample, the apparent ages for calcite-white mica pairs are near 170 Ma, being the oldest in the entire set of samples. The $^{87}Sr/^{86}Sr$ isotopic composition of four samples of pure marble from surface outcrops do not show a consistent cluster but show variable values between 0.7083 and 0.7123 (Table 2.6). A similar variability is seen in the initial Sr isotopic composition of the samples characterised by Rb-Sr geochronology. Here, the initial Sr isotopic composition (as approximated by the Sr isotopic composition of the low-Rb/Sr phase calcite) is between 0.7077 (sample 4-1325) and 0.7153 (sample 5-3655) (Figure 2.16; Table 2.6). It is important to note that the majority of these initial Sr isotopic ratios are considerably higher than the $^{87}Sr/^{86}Sr$ ratio of seawater in Paleozoic to Mesozoic times (cf. McArthur et al., 2001).

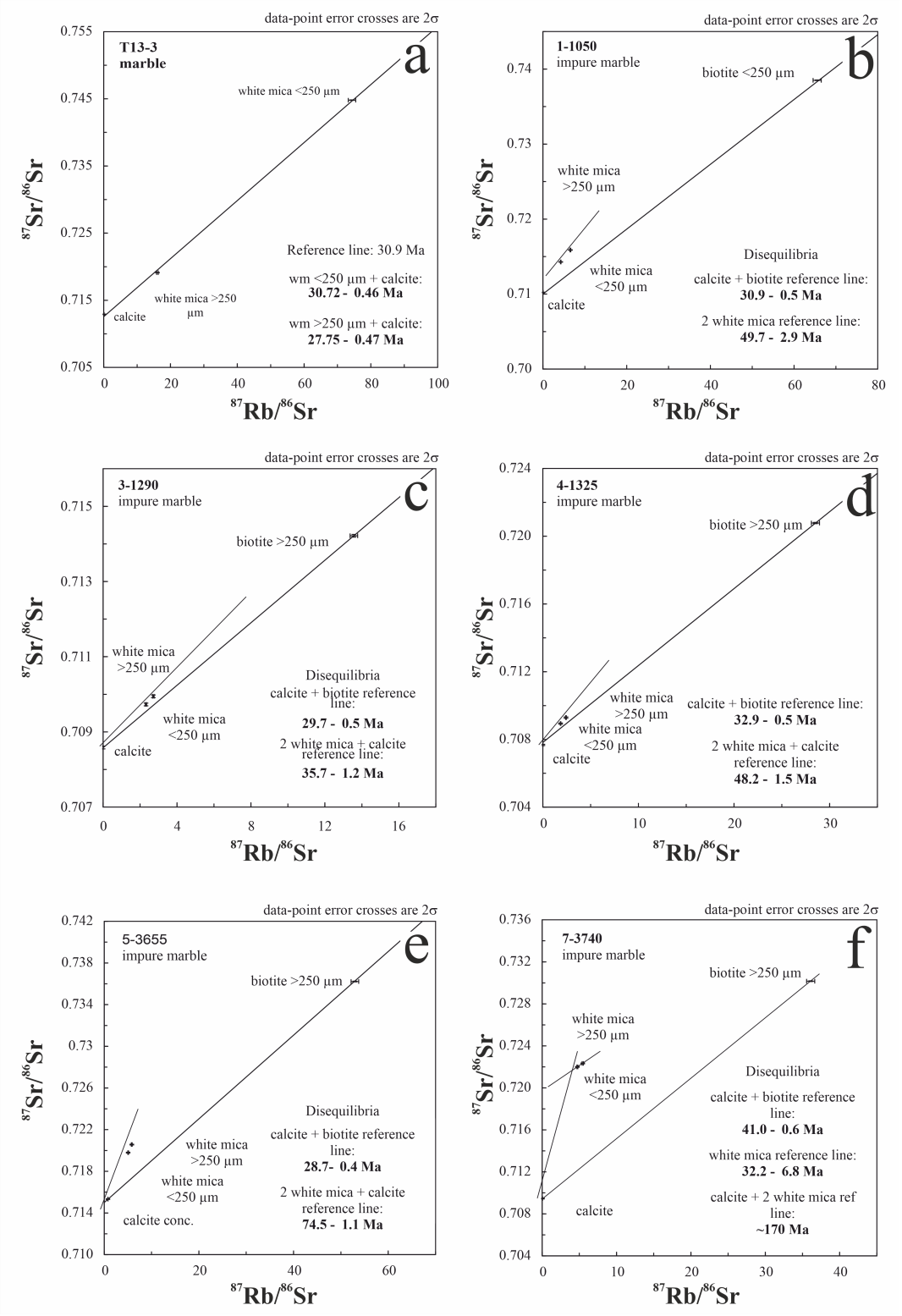


Figure 2.16.: Rb-Sr isochrons. Age results by calcite-biotite and white mica-calcite reference lines of the samples a) T13-3; b) 1-1050; c) 3-1290; d) 4-1325; e) 5-3655; f) 7-3740.

2.6. Discussion

2.6.1. Comparison and stratigraphic correlation of cuttings with Paleozoic and Cretaceous marble from outcrops

A synthesis of all investigated petrographical properties (Table 2.4) of the samples reveals that the colour of the marbles is a characteristic macroscopic feature which allows a subdivision of the examined marbles into two different groups: (1) the marbles from the outcrop south of Koçarli village (Paleozoic) and from the shallow marble-bearing section in the exploration well GP-1 (well^S) which are predominantly white; in contrast, (2) the marbles from the outcrops of the northern escarpment of the BMG (Cretaceous) and from the deeper section of the well (well^D) are characterised by blueish light grey colour (Tables 2.4 and 2.7). The light transmission and different patterns indicate the same two groups and confirm the correlation of cutting and surface samples based on a characteristic colour.

The major elements of all samples except well^D samples are similar and characterise the marbles as calcitic (Figure 2.11). Only in the Paleozoic marble, an approximately 0.4 m thick layer of dolomitic marble occurs (Table 2.7). All well^D samples plot in a group, which is separated from all other samples by their relatively high $Fe_2O_{3\,tot}$, Al_2O_3, Na_2O and K_2O content in combination with relatively low CaO concentration (Table 2.8). This is explained by a contamination of the cutting samples by schist or gneiss fragments. The geochemistry of the samples from well^S is more widely scattered than that of the other marble units (Figure 2.11; Table A.1).

A mixture of marble with silicate rocks in the deep section of GP-1 is likely since the stratigraphy in the deeper parts is much more variable than in the 1,050-1,325 m section (Figure 2.8). The deeper reservoir of the geothermal sites in the BMG is mostly an intercalation of marble, schist, and gneiss (Aksoy, 2014; Karamanderesi, 2013). The Cretaceous marble is located at the contact of the shallow south-dipping Büyük Menderes detachment and can occur as intercalation of marble, schist and gneiss sequences (Özer and Sözbilir, 2003).

The well^D and Cretaceous samples show highest absolute REY and Σ REY values and a high Gd_{PAAS}/Lu_{PAAS} ratio (Figure 2.13). Additionally, these samples exhibit

Table 2.7.: Characterisation of samples by petrographical properties. The investigation on calcitic and dolomitic marble uses SEM-EDX measurements and petrographical description of hand specimens as well as thin sections and point counting of cuttings.

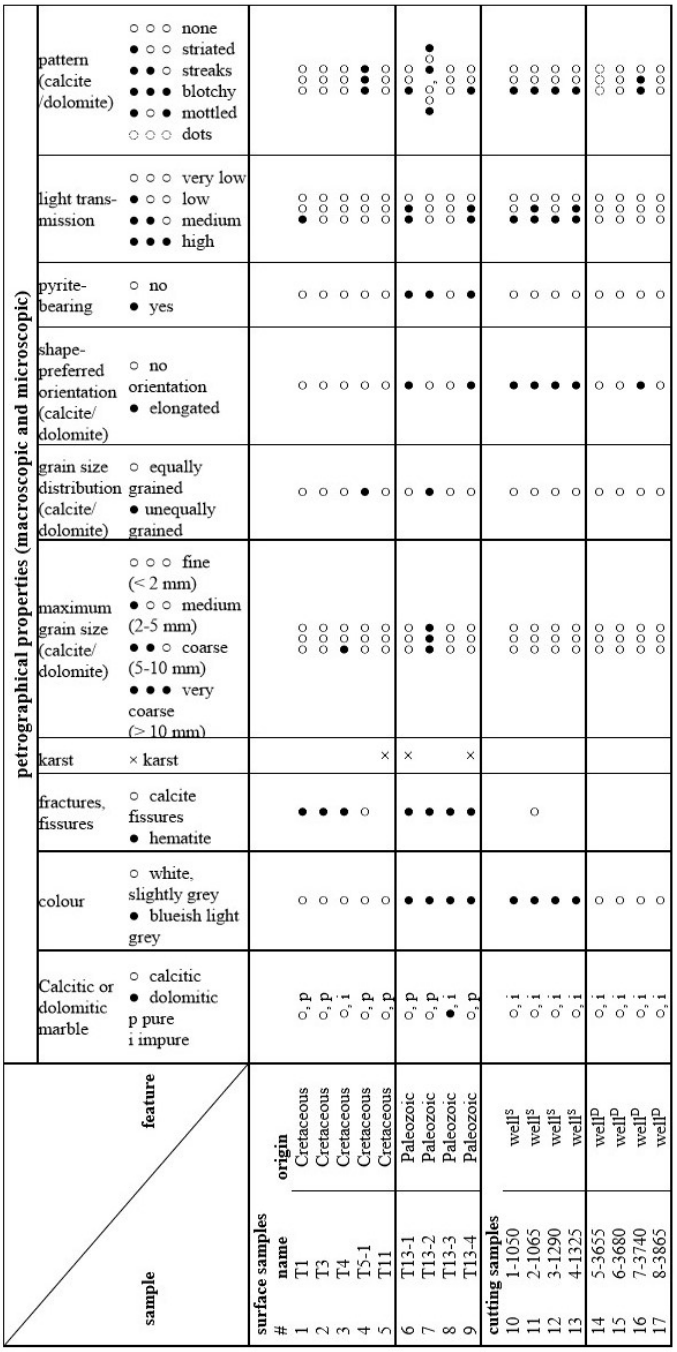


Table 2.8.: Characterisation of samples by geochemical properties. c: Cretaceous, p: Paleozoic.

sample	feature		geochemical properties (selected features)																
			Al_2O_3	$Fe_2O_{3\,tot}$	MnO	MgO	CaO	Na_2O	K_2O	P_2O_5	$\delta^{13}C$ VPDB	$\delta^{18}O$ VSMOW	Sr	Y/Ho	Ce/Ce* (PAAS)	Pr/Pr* (PAAS)	Eu/Eu* (PAAS)
#	name	category															
surface samples																	
1	T1	c	○○○	○○○	○○○	●●○	●●●	○○○	×	○○○	●●●	●●●	●○○	●●○	●	●	●
2	T3	c	○○○	○○○	●●○	○○○	●●●	×	×	○○○	●○○	○○○	●○○	●●○	●	●	○
3	T4	c	●○○	●●○	●●●	●●●	●●○	×	×	●○○	●○○	○○○	●●○	●●○	●	●	●
4	T5-1	c									●○○	○○○					
5	T11	c	●○○	●○○	●○○	○○○	●●○	×	×	○○○	●○○	○○○	●●○	●●○	●	●	●
6	T13-1	p	○○○	○○○	○○○	●●○	●●○	●○○	×	●●○	●●●	●●○	○○○	●●○	●	●	●
7	T13-2	p									●●○	●●●					
8	T13-3	p	●●○	●○○	●●○	●●●	●●○	×	×	●●○	●●○	●●○	○○○	●○○	●	●	●
9	T13-4	p	○○○	○○○	○○○	●●○	●●●	×	×	●●○	●●●	●●●	●○○	●●○	●	●	●
cutting samples																	
10	1-1050	well^S	●●○	●○○	●●○	●●○	●●○	×	×	●○○	●●○	●○○	●●●	●○○	●	●	●
11	2-1065	well^S	●○○	●○○	○○○	●○○	●●○	×	×	○○○	●●○	●○○	●●○	●●○	●	●	●
12	3-1290	well^S	●●○	●●○	●●○	●○○	●●○	●○○	○○○	●○○	●●○	●○○	●●●	○○○	●	×	●
13	4-1325	well^S	●●○	●●●	●●●	●○○	●●○	●○○	●○○	●●●	●●○	●●○	●●●	○○○	●	×	●
14	5-3655	well^D	●●●	●●●	●●●	●●○	●○○	●●●	●●○	●●●	○○○	○○○	●○○	○○○	●	×	●
15	6-3680	well^D	●●●	●●●	●○○	●○○	●○○	●●○	●○○	●●○	○○○	○○○	●●●	○○○	●	×	●
16	7-3740	well^D	●●●	●●●	●●○	●○○	●○○	●●○	●●○	●●●	○○○	○○○	○○○	○○○	●	×	●
17	8-3865	well^D	●●●	●●○	○○○	○○○	●○○	●●●	●●●	●●●	○○○	○○○	●●○	○○○	●	×	○
			wt-%	wt-%	wt-%	wt-%	wt-%	wt-%	wt-%	wt-%	‰	‰	mg/kg	-	-	-	-
	minimum value		0.017	0.067	0.011	0.362	4.207	0.007	0.008	0.003	-2.89	6.74	114	27.3	0.55	1.03	0.87
	first quartile		0.132	0.205	0.017	0.920	23.157	0.050	0.267	0.011	-0.99	15.28	218	28.9	0.68	1.04	0.99
	median		0.718	0.870	0.039	1.084	43.813	0.874	1.109	0.019	1.73	18.85	261	38.8	0.74	1.10	1.05
	third quartile		5.402	1.709	0.052	2.282	52.933	3.117	2.200	0.072	3.29	20.44	455	45.4	0.92	1.16	1.07
	maximum value		17.231	3.190	0.148	18.943	58.975	3.603	4.776	0.201	4.40	23.84	2275	51.1	0.94	1.27	2.54

element contents: × not present, ○○○ very low [< first quartile], ●○○ scarce / low [first quartile to < median], ●●○ abundant / medium [median to < third quartile], ●●● very abundant / high [≥ third quartile]; **isotopic values**: from low to high values; **Y/Ho ratio**: ○○○ < 33, ●○○ 33-40, ●●○ 40-80, ●●● > 80; **Ce/Ce*$_{(PAAS)}$**: ● ≤ 0.95, ○ > 0.95; **Pr/Pr*$_{(PAAS)}$**: ● oxic (> 1.05), ○ anoxic (< 0.95), × 0.95-1.05; **Eu/Eu*$_{(PAAS)}$**: ● ≤ 1.5, ○ > 1.5
(geochemical values originally in wt.-%, δ-values in ‰)

higher absolute HREE values but with a decreasing trend towards higher masses, which can be explained by pronounced weathering (Pereira et al., 2019). The Paleozoic and well^S samples do not show this characteristic REY pattern. Due to contamination, a direct comparison of the absolute REY values of the well^D samples with the other marble horizons can only be made with restrictions. The normalised REY pattern (Figure 2.12), and Gd/Lu ratio (Figure 2.13) can be used as indications allowing a distinction between Paleozoic and well^S samples relative to the Cretaceous and well^D samples.

All the δ^{13}C values of this study lie within the general range of marble values (Rollinson, 1993; Cramer, 2004), whereas the δ^{18}O values are in the lower range of marbles in general (Figures 2.14 and 2.15). The Paleozoic and well^S samples have both higher δ^{18}O and δ^{13}C values in comparison to the Cretaceous and well^D samples. A pronounced CO_2 degassing during metamorphic processes such as decarbonation reactions can explain this difference (Cramer, 2004; Hoefs, 2015). During metamorphic volatilisation reactions, the lost CO_2, and additionally H_2O, are enriched in ^{16}O compared to the bulk rock (Valley and O'Neil, 1986; Hoefs, 2015). The well^S samples have slightly lower δ^{13}C and δ^{18}O values than the surface samples, which may be explained by hydrothermal alteration as metamorphic or meteoric fluids lead to decrease of the heavy isotope (Cramer, 2004; Craig and Craig, 1972).

The Cretaceous marble and well^D samples show in general lower values for both δ^{18}O and δ^{13}C. They may have been influenced by meteoric water in addition to marine water, so that the limestone protolith had a lighter pre-metamorphic isotope ratio (Valley and O'Neil, 1986). McCrea (1950) and Kim and O'Neil (1997) investigated the temperature dependence of Ca-carbonate formation on O-isotope composition, yielding decreasing δ^{18}O values in Ca-carbonate with increasing temperatures. Again, subsequent fluid-rock interaction can be one reason for the lower δ^{18}O values as explained above. Therefore, no clear correlation of the metamorphic grade and isotopic signature can be made. Combining the δ^{18}O and δ^{13}C values (Figure 2.14; grey ellipses), two groups of marble (Paleozoic and well^S; Cretaceous and well^D) are distinguished (Figure 2.14; Table 2.8). The difference between the two groups is caused by their different metamorphic overprint resulting in different C and O isotopic fin-

gerprint just discussed.

Based on the detailed petrographical and geochemical data (Tables 2.7 and 2.8), a stratigraphic correlation of cuttings and outcrop samples is suggested. The critical parameters are colour, transparency (light transmission), the REY pattern and stable C and O isotopic composition. The well^{S} and the Paleozoic marble are associated to each other, thus both belonging to the Selimiye nappe. Accordingly, the well^{D} and the Cretaceous samples are interrelated, belonging to the Bayındır nappe. This implies that the younger Bayındır nappe (e.g. Lips et al., 2001) lies structurally below the older Selimiye nappe (cf. Régnier et al., 2003) intersected by the GP-1 well in the graben structure.

Implications on marble genesis

The Paleozoic marble shows negative Ce anomalies pointing to a seawater origin and oxic conditions during formation (Figure 2.17). The positive Y anomalies of the Paleozoic samples indicate a seawater influence (Bau et al., 1997; Tostevin et al., 2016). The negative Ce anomalies and Pr/Pr* indication of the well^{S} samples point to a near shore (3-1290 and 4-1325 with Y/Ho ratios around 30) to open marine setting (1-1050 and 2-1065 with Y/Ho of 39 and 46). In contrast, the C and O isotopic signatures of the Paleozoic marble samples postulate a meteoric origin of the limestone precursor (Table 2.9). As subsequent fluid-rock interactions affected the original isotopic signature, the presumed meteoric origin may be biased.

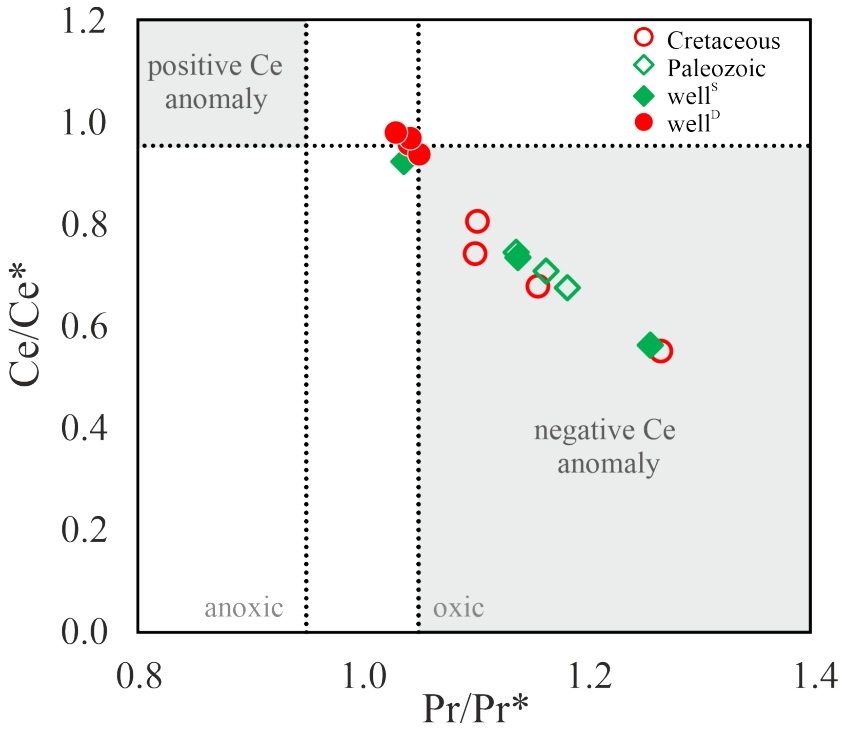


Figure 2.17.: Ce/Ce* vs. Pr/Pr* with Ce anomalies indicated in grey including the marked fields of positive and negative Ce anomalies as described in Bau and Dulski (1996).

The Cretaceous marble has a positive Y anomaly with highest Y/Ho ratios between 44 and 51 suggesting seawater origin (Bau et al., 1997; Tostevin et al., 2016). The $\delta^{13}C$ values are consistent with both, a seawater, and a freshwater origin (Table 2.9). The Ce/Ce* values around 0.9, and Pr/Pr* values around 1.0 of well^D samples indicate oxic conditions during formation of the marble (Bau and Dulski, 1996) (Figure 2.17).

As the Cretaceous and Paleozoic limestone protoliths formed on the shelf of the Neotethys, they must be marine (Şengör and Yilmaz, 1981; Cramer, 2004; van Hinsbergen et al., 2010c; Gessner et al., 2013). Özer and Sözbilir (2003) find Cretaceous reef-forming rudist species which confirm a shallow ocean setting at least for the Cretaceous marble. Thus, the C and O isotopic signatures indicative of meteoric influence, must result from processes that took place during diagenesis or metamorphism. A strong post-depositional metamorphic overprint is indicated by metamorphic phases within the impure marbles, including biotite and muscovitic white mica.

Table 2.9.: Information gained by applying REY and C and O isotopic signatures regarding formation environment.

geochemical parameter	**Ce/Ce* and Y/Ho**	$\delta^{18}\mathbf{O}_{VSMOW}$	$\delta^{13}\mathbf{C}_{VPDB}$
reference:	Bau and Dulski, 1996; Webb and Kamber, 2000; Tostevin et al., 2016	Hoefs, 2015	Hoefs, 2015
Paleozoic	oxic, near shore to open marine setting	meteoric water	higher values than freshwater carbonates
well^{S}	oxic, near shore to open marine setting	meteoric water	freshwater carbonates
Cretaceous	oxic, seawater	meteoric water	freshwater carbonates and marine carbonates
well^{D}	oxic, near shore setting	meteoric water	freshwater carbonates and marine carbonates

The calcite-biotite Rb-Sr ages clustering around the 30 Ma metamorphic age indicate metamorphic isotope re-equilibration. The C and O isotopic composition may also be influenced by equilibration during metamorphism or interaction with hydrothermal fluids as indicated by abundant veins.

Structure and evolution of the BMG

The results of this study indicate the location of Cretaceous marble below Paleozoic rocks at the location of the exploration well GP-1 (Figure 2.2). This is explained by nappe stacking as also suggested by various researchers for the Menderes Massif (Lips et al., 2001; Gessner et al., 2013; Régnier et al., 2003; van Hinsbergen et al., 2010c). The two different marble horizons in GP-1 belong to the Bayındır nappe (Cretaceous marble, 3,650-3,870 m) and the Selimiye nappe (Paleozoic marble, 1,050-1,325 m) according to our results from petrographical and geochemical analyses. Consequently, the BMG can be considered as a half-graben structure as already suggested by van Hinsbergen et al. (2010c) (Figure 2.18). In the northern escarpment of the BMG, the four nappes are north-vergent and in the south, the nappes are south-vergent and, separated in blocks dipping northwards due to the antithetic normal faults of the graben structure. During graben development, the blocks of Selimiye, Çine and Boz-

dağ nappes subsided in the southern graben structure. The deeper marble of the Bayındır nappe is separated by the low-angle, southward dipping Büyük Menderes detachment and represents the deeper (well^D) marble horizon (Figure 2.18).

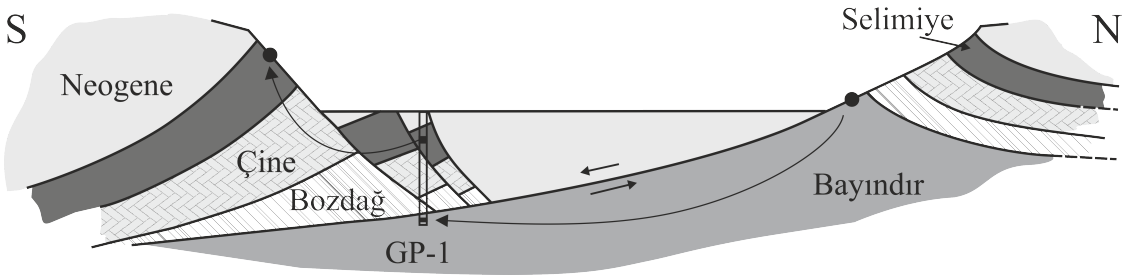


Figure 2.18.: Simplified cross-section of the BMG as half-graben structure with allocated nappes and the exploration well GP-1. The two different marble horizons are marked. The straight arrows indicate the shear sense along the low-angle Büyük Menderes detachment. Complemented and redrawn according to van Hinsbergen et al. (2010c).

Constraints on the timing of the regional tectonic evolution come from the Rb-Sr and Sr isotopic data which reveal a conspicuously tight cluster of calcite-biotite and calcite-muscovite-based apparent ages around 30 Ma (27.3 to 33.4 Ma; Figure 2.16). Studies of the correlation between deformation textures and Sr-isotopic signatures show that synkinematic recrystallisation of coexisting minerals in a deforming rock is usually accompanied by isotopic re-equilibration (Müller et al., 1999; Müller et al., 2000; Cliff and Meffan-Main, 2003; Glodny et al., 2008b). Sr-isotopic re-equilibration between minerals is equivalent to a complete reset of the Rb-Sr geochronological system. Most of the dated samples show clear indications for ductile deformation, like foliation-defining preferred orientation of mica. This is particularly true for sample T13-3, which is from a fine-grained, strongly sheared impure marble domain at the contact between a marble and a gneiss body (Figure 2.4a) and resembles part of a mylonite. In this sample, white mica-calcite pairs point to an age near 30 Ma, which therefore can be interpreted as the deformation age. For a synkinematic reset of the Rb-Sr system in white mica, temperatures of at least 350 °C are required (Müller et al., 1999; Müller et al., 2000). With incomplete dynamic recrystallisation or at static conditions, temperatures required to reset the Rb-Sr system of muscovitic white mica are much higher (near 600 °C, Glodny et al., 2008a). In consequence, the age cluster

around 30 Ma is best explained as dating the waning stages of ductile deformation in both, the Bayındır and Selimiye nappes at temperatures near or in excess of 350 °C. In such a scenario, the higher apparent ages for biotite in sample 7-3740 (41 Ma; Figure 2.16) and the consistently higher but incoherent apparent ages for calcite-white mica pairs in all investigated samples except T13-3 (between 36 and 170 Ma; Figure 2.16) would reflect incompletely reset age signatures from previous metamorphic events, with no direct geological significance. As mentioned above, metamorphic temperatures at 30 Ma were at least near 350 °C, and potentially considerably higher, as indicated by the stability of muscovite ± biotite ± epidote ± garnet in the silicate sub assemblage. Therefore, the 30 Ma ductile deformation event occurred contemporaneously in both nappes, at mid-crustal temperatures and at considerable depth. We infer that this 30 Ma event most likely dates the late stages of nappe stacking within a compressional tectonic regime. Incipient formation of the graben structure therefore must post-date this deformation and is inferred to be Late Oligocene to Miocene in age.

The above scenario is well in line with pre-existing geochronological data and interpretations. Ring et al. (2003) proposed, based on $^{40}Ar/^{39}Ar$ muscovite ages and fission track ages for zircon and apatite, incipient extension-related cooling from the Late Oligocene onwards. An end of ductile deformation within the nappe stack roughly near 30 Ma is also in line with the presence of post-tectonic auriferous veins, formed at temperatures near 350 to 360 °C, and dated by in-situ analysis of K-feldspar and muscovite at 31.3 ± 4.7 Ma (Şengün et al., 2019). Regionally, youngest biotite and muscovite ages near 30 Ma were also reported elsewhere (Hetzel and Reischmann, 1996; Satır and Friedrichsen, 1986). Older Rb/Sr and Ar/Ar mica apparent ages (> 35 Ma), as detected here for Rb-Sr in muscovitic white mica and as reported from elsewhere in gneissic rocks and schists of the Menderes Massif (Hetzel and Reischmann, 1996; Satır and Friedrichsen, 1986; Koralay, 2015), may reflect earlier cessation of deformation in rocks of higher shear strength compared to the impure marbles of the present study. They may also be mixed ages with partial inheritance from earlier metamorphic stages as hypothesised for most of the here studied muscovite fractions.

Analysis of different samples of pure marble was undertaken to potentially con-

strain the deposition age of the marbles by means of Sr isotope stratigraphy (cf. McArthur et al., 2001). The observed variability of initial Sr isotopic ratios (between 0.7083 and 0.7123 for pure marbles, and between 0.7077 and 0.7153 for calcite from impure marbles, Table 2.6) precludes a clear distinction between different marble units, as well as direct dating of depositional ages. Furthermore, the majority of the initial Sr isotopic ratios are higher than $^{87}Sr/^{86}Sr$ of Paleozoic or Mesozoic seawater (cf. McArthur et al., 2001). Therefore, marbles either were formed in non-oceanic basins or, more likely, there was a significant metasomatic overprint of the marbles with synmetamorphic exchange of Sr between the marine carbonate rocks and nearby silicate-rich rocks with their potentially much more radiogenic $^{87}Sr/^{86}Sr$ signatures.

The $^{87}Sr/^{86}Sr$ isotopic composition of four of the samples of pure marbles from surface outcrops do not show a consistent cluster but show rather variable values between 0.7083 and 0.7123 (Table 2.6). A similar variability is seen in the initial Sr isotopic composition for the samples characterised by Rb-Sr geochronology. Here, the initial Sr isotopic composition (as approximated by the Sr isotopic composition of the low-Rb/Sr phase calcite) is between 0.7077 (sample 4-1325) and 0.7153 (sample 5-3655) (Figure 2.16; Table 2.6). The majority of these initial Sr isotopic ratios are considerably higher than the $^{87}Sr/^{86}Sr$ ratio of seawater in Paleozoic to Mesozoic times (cf. McArthur et al., 2001).

To enhance the development of geothermal energy, detailed studies on the reservoir rocks are important. By the stratigraphic correlation of the GP-1 marble horizons, an improvement of the structural model was achieved. For future exploration drillings, the presence of the deeper, and because of the presumably higher temperature, more promising marble reservoir horizon was confirmed. Therefore, when investigating surface analogues and cuttings of an exploration well, a multi-proxy approach is supportive by enhancing the geological model of the area for the determination of future well target zones. This leads to synergies and cost-effective development of new geothermal projects.

2.7. Conclusion of part II

Two different marble horizons were drilled by the GP-1 geothermal exploration well near Koçarli (Büyük Menderes Graben, Turkey). Cuttings and stratigraphically well-defined surface samples allow correlation of cuttings to regional stratigraphic units by detailed comparison of their petrographical, geochemical and isotope properties. Several independent methods (macroscopic and microscopic petrography, major, trace and REY geochemistry, C, O and Sr stable isotopic composition, Rb-Sr geochronology) were combined in order to establish a geological model for the GP-1 well in the BMG.

The marble horizon at the bottom of GP-1 relates to the Cretaceous Bayındır nappe. In contrast, the shallow marble intersection is related to the Paleozoic Selimiye nappe. By this stratigraphic correlation, we were able to prove the nappe geometry of the BMG below the younger cover in the graben (from bottom to top: Bayındır, Bozdağ, Çine and Selimiye). Ductile deformation in both the Bayındır and Selimiye nappes at upper-crustal temperatures and considerable depth is estimated at 30 Ma. The extensional graben structure must have formed < 30 Ma. Both, stable (C, O and Sr) and radiogenic (Rb-Sr) isotope data are modified by hydrothermal alteration.

We securely identified a second deeper reservoir in the graben with the Cretaceous marble, which promises higher reservoir temperatures (unpublished temperature logs by Borusan EnBW Enerji) and therefore a potentially higher economic efficiency for geothermal energy projects. Reservoir-specific characteristics can now be easily studied in representative surface analogues. The existence of two separate marble-dominated units at different depths in the Aydin-Koçarli area has thus an important impact on future exploration and drilling campaigns as well as upscaling of existing geothermal sites in the vicinity. Accepting a lower reservoir temperature accompanied by reasonable drilling cost may lead to target the shallow marble reservoir. On the other hand, accepting higher total drilling cost, the deeper marble reservoir with higher temperature may become the focus of future project developers.

Part III.

CO_2 handling in binary geothermal systems

Summary to Part III

The decarbonisation of power and heat production is recently one of the major challenges in the Energy sector. Among other technologies, deep geothermal energy is an interesting option, because source temperature, plant capacity, low environmental footprint and high availability allow the application in district heating grids. The majority of geothermal reservoirs contains a certain amount of non-condensable gases dominated by CO_2. With respect to corrosion and precipitation effects as well as environmental friendliness and economic optimisation, the handling of these gases is challenging.

In this study three different technical options – a gas bypass system, a certain pressure regime and a secondary gas turbine – are investigated to overcome this challenge. The geothermal plant at Bruchsal/Germany was selected as case example for process simulation and further analyses.

The major outcome shows that a gas bypass excluding CO_2 from the power plant results to be the best option for the existing plant in terms of avoiding CO_2 emissions and reaching highest possible power output. Furthermore, the study results recommend the best CO_2 handling solution for different conditions within the simulated range (temperatures from 100 to 160 °C, salinity from 0–200 g/L, CO_2 content from 0–20 g/L, pressures from 15–135 bar, and flow rates until 100 kg/s) as an essential contribution to the field.

Chapter 3.

CO_2 handling in binary geothermal systems: A modelling approach for different CO_2 contents, salinity, pressure and temperature conditions

3.1. Introduction and basics

With respect to the global climate change, the reduction of carbon emissions in several sectors becomes a major objective. The recent energy mix will be the subject to a redesign with the aim decarbonising power and heat supply. Geothermal energy is a renewable energy resource and its contribution to the world's energy consumption amounted to 421 petajoules in 2019, approximately equally shared by electricity and heat (REN21, 2020). The major characteristics of geothermal energy are high availability, dispatchability, and a temperature level suitable for industrial processes and district heating (Bosia et al., 2021).

Geothermal energy can be utilised from different reservoir types, e.g. volcanic and (meta-)sedimentary basins. Caused by magmatic exhalation or water-rock interaction, the geothermal brine is often accompanied by non-condensable gases (NCG) such as carbon dioxide (CO_2), methane (CH_4), and hydrogen sulfide (H_2S). These gases are typically dissolved in the brine and cannot be condensed solely by increasing the pressure at the geothermal systems' operation temperature. With increasing salt concentration (salinity) of the aqueous phase, the solubility of the gases decreases (Markham and Kobe, 1941;Drummond, S.E., 1981; Nighswander et al., 1989; Rumpf et al., 1994; Seibt and Thorwart, 2011), locally resulting in two-phase systems in the reservoir. With increasing pressure, the gas solubility increases (Seibt and Thorwart, 2011). The gas solubility decreases with increasing temperature (Seibt and Thorwart, 2011). In consequence, two-phase flow may evolve when decompression occurs at nearly constant temperatures, which may lead to problems depending on the power plant technology (direct use or binary power plants), such as potential CO_2 emission (Aksoy, 2014), decreasing efficiency of heat exchangers (Gokcen and Yildirim (Özcan), 2008), corrosion or scaling (Seibt and Thorwart, 2011).

Especially gaseous CO_2 lowers the efficiency of heat exchangers (Gokcen and Yildirim (Özcan), 2008). For example in Bruchsal (Germany), CO_2 accumulates within the plate heat exchangers. As a result, they are partly blocked for brine pathways (Schlagermann et al., 2014). Such a reduction of heat exchanger surface leads to the decrease of transferred thermal energy and therefore decreasing heat and electrical power output.

In addition, CO_2 in the gas phase enhances corrosion of the above-ground installations (Seibt and Thorwart, 2011; Seibt and Wolfgramm, 2012). In addition to gaseous CO_2, the high salt concentration enhances corrosion even further (Mundhenk et al., 2013). The corrosion mechanism is the CO_2 induced hydrogen corrosion. When CO_2 dissolves in the brine, it dissociates to bicarbonate and further to carbonate with the release of one H^+ ion each, which then leads to hydrogen corrosion by the H^+ ions. (Fischer and Siedlarek, 1977; Carneiro et al., 2003). Moreover, effervescence of CO_2 from the thermal water, caused by pressure loss, leads to an increase in pH in the liquid. This results in carbonate precipitation (scaling) in the pipelines, on top of scaling induced by decreasing salt solubility due to cooling the power plant (Seibt and Thorwart, 2011; Seibt et al., 1999).

There are different solutions for gas handling during geothermal power plant operation that depend on power plant type, geographical location and therefore geological situation of the geothermal plant, gas content and composition, temperature, pressure, and salinity (Bhatia, 2014). Exemplary technical solutions for flashed-steam power plants are gas-removal systems using steam jet ejectors, turbo-compressors or hybrid systems of both (Vorum and Fritzler, 2000). In binary power plants, the gas phase is (1) removed and transmitted by a gas bypass (Bruchsal, Hettkamp, 2020); (2) kept in solution by pressure maintenance (Soultz-sous-Forêts, Bosia et al., 2021); and (3) a proposed closed-loop solution simulated with non-toxic and non-flammable working fluid with an installed turboexpander where the plant is fed by geothermal steam (Tuscany, Vaccaro et al. (2016)).

More published simulated technical solutions are described by the authors Bonalumi et al., 2017a and Ghasemi et al. (2013) who present different solutions for an Organic-Rankine-Cycle (ORC) plant and optimised systems for air-cooled working media. Bonalumi et al. (2017a) apply the ELECNRTL thermodynamic model in ASPEN Plus to simulate a zero-emission flash plant and a basic process of a binary ORC plant which in our application range not sufficiently pictures the system H_2O - NaCl - CO_2. Ghasemi et al. (2013) propose a thermodynamic model of an ORC for a low temperature geothermal source in ASPEN Plus focusing on power plant parameter optimisation in which the gas handling is not considered.

A common method for describing and optimising technical solutions is simulation. Most studies on geothermal processes focus on either the reservoir performance, wellbore simulation, reinjection technologies (Kaya et al., 2018; Battistelli, 2010) or the power plant systems. None of the known studies focus on the handling of gases. In comparison with this study, most simulated processes within geothermal energy represent an ORC or a flash system (Bonalumi et al., 2017a; Ghasemi et al., 2013; Vetter et al., 2013). The Kalina power plant simulations by Ogriseck (2009) are performed considering a waste heat power generating system. To our knowledge, no geothermal in general and no Kalina plant in particular has been simulated so far with ASPEN Plus in terms of gas handling.

In simulation, we face three major challenges: (1) choosing the relevant code and software; (2) defining technical solutions in advance that can be implemented into simulation; and (3) defining the thermodynamic parameters that are applicable to the system. For simulation of a geothermal power plant, several simulation programs are commonly used. Common software are Ebsilon (Ogriseck, 2009), ASPEN Hysys (Vaccaro et al., 2016) or Plus (Bonalumi et al., 2017a; Ghasemi et al., 2013), Thermoflow (Mergner and Weimer, 2015) or specially written codes (Vetter et al., 2013; Liu et al., 2017; Borsukiewicz-Gozdur and Nowak, 2007). We use ASPEN Plus to thoroughly describe the gas flow throughout a Kalina binary geothermal plant by simulation and propose three different CO_2 handling options. In addition to two technical solutions which are already used (gas bypass and pressure maintenance), we implement an additional CO_2 turbine which so far has never been applied in a geothermal plant simulation.

In order to realise a simulation in which the impact of the thermal water cycle on power plant performance is considered, it is necessary to provide a well-fitting solubility model for CO_2 in aqueous salt solutions. There are numerous thermodynamic calculation models for the ternary system of CO_2-solubility in water and brine containing different salts (phase equilibria system H_2O – CO_2 - salts) for different applications (e.g., Tödheide and Franck, 1963; Hu et al., 2007; Duan and Sun, 2003; Duan et al., 2006; Spycher and Pruess, 2010), which are based on experimental data (e.g., Nighswander et al., 1989; Ellis and Golding, 1963; He and Morse, 1993; Kiepe et al.,

2002; Koschel et al., 2006; Liu et al., 2011; Lucile et al., 2012; Gilbert et al., 2016; Lara Cruz et al., 2019). Representative models are the calculation models of Duan et al. (2006), Spycher and Pruess (2011) or Zhao et al. (2015). Compared to Vaccaro et al. (2016) who used the existing thermodynamic models of ASPEN Hysys in their simulation, we compared the thermodynamic models to existing operational data and implemented an improved model.

Our simulation focuses on the Bruchsal geothermal plant located in the Upper Rhine Graben in the southwest of Germany. The reservoir type (sedimentary basin) and the related geothermal brine composition (ca. 120 g/L salinity and 1.9 NL_{gas}/L_{fluid}) can be compared to a certain number of low enthalpy geothermal sites in Central Europe and worldwide (Bosia et al., 2021). Furthermore, the Bruchsal plant deals with both, providing power via a binary cycle process as well as supplying heat to local facilities (Bosia et al., 2021). As the critical parameters are salinity, gas content and temperature and pressure, Bruchsal is an appropriate example to examine different CO_2 treatment measures in detail and the related results can be – with a few restrictions – transferred to other geothermal sites.

In our study, we directly relate physio-chemical properties and the geothermal brine mass flow to the thermal and electrical output of the power plant. This simulation of surface installations aims the comparison of different technical solutions for CO_2 handling of the Bruchsal brine and operating conditions. We close an essential knowledge gap by answering the question of ideal technical CO_2 handling (in terms of avoiding CO_2 emissions and reaching highest possible power output) under different brine and operating conditions in the context of three simulated technical solutions which provide a first indication for identifying a technical solution in a future geothermal plant. However, a detailed simulation must be performed for any future plant after the primary cycle parameters (i.e., salinity, production temperature, gas composition and CO_2 content) are specified, as some primary cycle conditions could potentially fall in a transitional application range of the three technical solutions simulated here. So far, only at specific operational parameters simulations were performed regarding CO_2 handling, without recommending application ranges. A further novel technical solution approach is proposed by simulating a further tur-

bine which additionally uses the gaseous CO_2. The results of this unique simulation contribute to increased energy efficiency by increasing the performance of the plant while minimising emissions. A further knowledge gap is closed by quantitatively express the effect of CO_2 handling on energy efficiency.

Furthermore, with just a few modifications, it is achievable to redesign the simulation model into an ORC system. For this purpose, only the part of the simulation concerning the power plant cycle should be adapted regarding the working medium and the system points used. Besides, existing operational parameters of a plant should be used to calibrate the new power plant cycle. Moreover, the model could be used to understand and optimise other geothermal power plant systems regarding CO_2 handling.

3.2. Bruchsal geothermal power plant

Bruchsal in West Germany is located at the eastern margin of the Upper Rhine Graben, approximately 120 km south of Frankfurt. The Bruchsal power plant consists of two wells with a production well of approximately 2,500 m depth and a ca. 1,900 m deep reinjection well. The bottom hole temperature of 135 °C corresponds to a geothermal gradient of 49 K/km (Kölbel et al., 2020). The geothermal water contains 120 g/L of total dissolved solids (Table B.2), which is within the typical range of geothermal water from the Upper Rhine Graben (Sanjuan et al., 2016).

The geothermal water has a wellhead temperature of 124 °C and is fed to the power plant at an operational pressure of 22 bar absolute (bar(a)) (Mergner and Schaber, 2018). The heat transfer is conducted in two parallel plate heat exchangers. The power plant is a Kalina cycle plant and the working media consists of an ammonia/water mixture (ca. 90 wt-% ammonia, 10 wt-% water, Mergner and Schaber, 2018). Following the heat transfer, the geothermal water is reinjected at a temperature of approx. 60 °C. The design power output of Bruchsal is 560 kW_{el}. In addition, 1200 kW_{th} heat is extracted to the local heating network. At operational conditions, two-phase flow of geothermal water and mainly CO_2 (in Bruchsal 93 to 96 vol-% CO_2 of total gas content, Table B.2) is observed. The total gas content measured at surface is 1.9 NL_{gas}/L_{fluid}.

To minimise NCG accumulation in the heat exchanger a specially designed gas bypass (Figure 3.1) is installed. Upstream of the power plant feed, the gas from the thermal water pipeline is separated by expanding the pipeline diameter in the bypass, a pressure drop is created, and the gas is reinjected into the pipeline at the cold side of the plant. Redissolution of the gas at the injection side is efficient due to lower temperatures.

In the Kalina power plant the heat of the thermal water is used to evaporate the zeotropic working media, a mixture of ammonia and water, partly in two parallel heat exchangers. Downstream of the heat exchangers, a high pressure separator separates the ammonia-rich vapor and the ammonia-lean liquid phase in the secondary cycle. A valve in the bypass of the turbine reduces the pressure of the liquid stream to the same pressure of the vapour stream after the turbine. The liquid and the vapour working media are mixed inside the preheater again, which is an internal heat exchanger. A low pressure separator is followed by the internal heat exchanger. From this low pressure separator the working media is pumped into the condenser, fed by water from a wet cooling tower to completely condensate the working media. Afterwards, the working media is led into a tank from which it is brought back to the pressure of 22 bar(a) before it flows to the preheater. After the internal heat exchanger, the ammonia mixture returns to the evaporators. The Bruchsal secondary cycle is described in detail in Mergner and Schaber (2018).

3.3. Methodological approach

3.3.1. ASPEN Plus

The software ASPEN Plus (Aspen Technology Inc., 2017) is a simulation tool for chemical process design and simulation. For the simulations of this study, version 10 of ASPEN Plus is used (Aspen Technology Inc., 2017). The software's calculations are based on different thermodynamic models and refer to a variety of thermodynamic databases. Details can be accessed from the software (Aspen Technology Inc., 2017). Furthermore, ASPEN Plus (Aspen Technology Inc., 2017) has implemented different

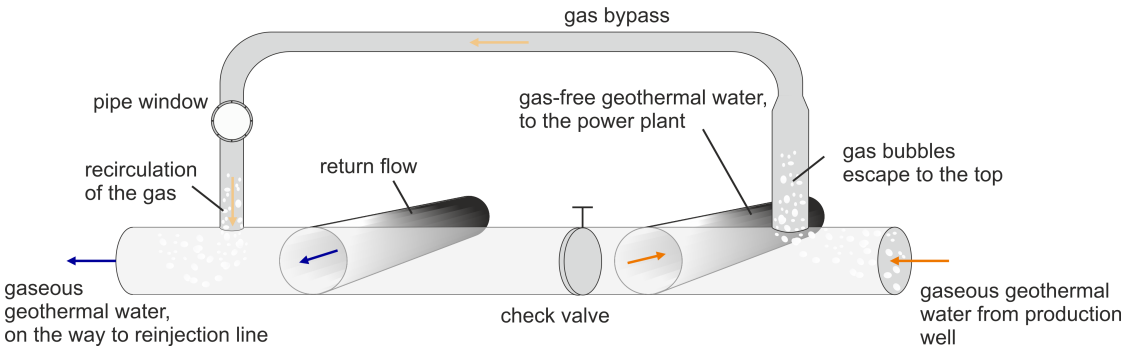


Figure 3.1.: Gas bypass installed in Bruchsal to handle the CO_2 not dissolved in the brine at operational conditions. By expanding the pipeline diameter, a pressure drop is created intentionally, and the gas bubbles escape to the top before entering the power plant section. After heat transfer, the cooled brine is fed back to the pipeline after the check valve. The gas is recirculated in this brine.

templates for several unit operations. Three technical options (options 1, 2 and 3) to handle the CO_2 are simulated based on three different process schemes (Figures 3.2a, 3.2b, and 3.2c). The different options are presented in detail in section 3.3.5.

The selection of the thermodynamic base method was made by specifying the component type, which is the type "Special" in ASPEN Plus. The special component type includes electrolyte systems, for which the implemented properties base method of ELECNRTL is proposed. For the simulation of this study, this method is chosen due to the high salt concentration of the brine. Experimental data for the specific heat capacity at a temperature of 124 °C (c_p=3.88 J/(g K)) in comparison with calculated data by ELECNRTL (c_p=3.83 J/(g K)) show a good agreement with a mean absolute error (MAE) of only 1.2 %. At 60 °C (outlet temperature of the evaporator), the deviation (MAE) is only 0.6 %. This is important for the estimation of the transferred heat in the heat exchangers. Regarding the working media properties (density, specific heat capacity, vapour liquid equilibrium), the ELECNRTL model similarly shows a good consistency, when compared with operational data from the existing plant (MAE < 7.0 %).

The calculation of the pressure increase in the pump before the heat exchanger leads to a mismatch between modelled and measured temperature. In order to overwrite the overestimated temperature, the pipe component was used to define the out-

let temperature and at the same time to simulate the pressure loss in the plant which can be derived from the operating data.

3.3.2. Model setup

A flow scheme of the thermal water cycle was implemented using specific unit operations (Table 3.1). The process schemes start at the wellhead. Therefore, the production and reinjection wells are not considered in detail with regard to pressure and heat loss. The ASPEN Plus unit operations pipe and pipeline are used to calculate the pressure drop and the heat loss from the wellhead to the power plant entrance. Additionally, one valve is implemented which simulates the pressure maintaining valve controlling the pressure in the pipelines. A split unit separates the CO_2 stream from the liquid brine stream, which flows to the power plant (Figures 3.2a and 3.2c). A mixer unit combines the separated stream again when the cooled brine leaves the power plant cycle after the heat exchanger (Figures 3.2a and 3.2c).

The power plant cycle consists of various unit operations, such as a flash operator, a compressor that is set as turbine, heat exchangers, a pump, a split and several mixing points, a valve and a pipe (Table 3.1). In addition to Figures 3.2a, 3.2b, and 3.2c, the details of the different design of the three simulated options are explained in section 3.3.5.

The flash operator is used to calculate the separation of the working fluid into a liquid and a vapour phase prior to the turbine at thermodynamic equilibrium. To calculate the electrical power output, the compressor block is set as turbine. The pressure reduction in the power plant turbine is set to the fixed value of 12 bar(a), as it corresponds to the design case of the power plant in Bruchsal. For each calculation in each technical solution the fixed value of 12 bar(a) is held constant to give a better comparability of the different options. The isentropic efficiency of the turbine in the power cycle is constantly set to 0.9 (Rönsch, 2015) and the mechanical efficiency is set to 0.89, due to the loss through friction and heat inside the turbine and additionally the loss caused by the coupling machine and generator (Sigloch, 2013). In the simulation of the third technical solution (option 3 shown in Figure 3.2c) the isentropic efficiency of the gas turbine is set to 0.95 and the mechanical efficiency is set

to 0.9. The higher efficiency is assumed due to the lower mass flow and the therefore lower friction caused by the media (Sigloch, 2013). In total, four heat exchangers were installed. Two of them are installed for the vaporisation of the working media heated by the thermal water ("HEX1" and "HEX2" in Figures 3.2a, 3.2b and 3.2c). In addition to that, one preheater and one condenser are present ("PREHEATER" and "CONDENSER" in Figures 3.2a, 3.2b and 3.2c). The design of the two heat exchangers for vaporisation in the simulation is based on the existing plant. The data of the existing heat exchangers is implemented to the model by two exchanger design and rating files (EDR). "HEX1" consists of 240 titanium-plates with an effective surface area of 407.15 m^2 and "HEX2" consists of 280 Stainless steel plates with an area of 475.15 m^2. This sums up to a total heat transfer area of 882.3 m^2 for vaporisation. The other two heat exchangers ("PREHEATER", "CONDENSER") were simulated as shortcut models with each 400 m^2 heat exchanger surface.

The valve within the process scheme of the power plant (Figures 3.2a, 3.2b and 3.2c) was installed to reduce the pressure of the remaining liquid fraction of the working media, so the relaxed gas stream and the liquid stream can be mixed at the same pressure conditions.

The pump brings the working fluid back to the operating pressure before the heat exchangers "HEX1" and "HEX2". It is implemented with the specification of the efficiency of 0.9. The temperature at the pump outlet is calculated incorrectly as it increases the temperature up to a difference of 25 K. Therefore, the pipe in the power cycle is implemented as a correction unit to invalidate the incorrectly calculated temperature after the pump.

3.3.3. Thermal water composition

The simulated thermal water compositions were simplistically assumed to be mixtures of water, sodium chloride (NaCl) and CO_2. Usually, geothermal brine consists of a number of additional salt ions like potassium, calcium, magnesium, sulphate (e.g., Sanjuan et al. (2016)). Within our condition range of interest, the solubility calculations of CO_2 in a brine with Bruchsal salt composition (Table B.2) compared to the calculation in a solution with corresponding sodium chloride equivalent ($NaCl_{eq}$; ac-

Table 3.1.: List of unit operations. [*] The simulation of the third technical solution (option 3) is designed with two turbines.

unit operation	No.	description
Pipe	3	calculates pressure loss, has defined outlet temperatures
FSplit	4	separates streams by specified fractions
Mixer	3	calculates thermodynamic mixing conditions
HeatX	4	vaporiser, the preheater and the condenser
Flash2	1	calculates thermodynamic liquid - vapor conditions
Compr	1*	turbine for electrical power output
Valve	2	pressure reduction
Pump	1	pressure increase

cording to the model of Duan and Sun (2003) do not differ by more than 0.2 % MAE. Consequently, the following calculations are performed with $NaCl_{eq}$ as the single salt. The calculation of the specific heat capacity of the thermal water in ASPEN Plus, using the same simplification, results in a MAE of only 0.6–1.2 % compared to the experimental data (Table B.2).

The gas analysis of the Bruchsal brine shows that the main gas is CO_2 (94.5 vol-%, Table B.2). Further gases are nitrogen (N_2, 3.5 vol-%), CH_4 (1.9 vol-%) and other hydrocarbons. Comparative calculations of the fugacity coefficients for the gas mixture and pure CO_2 show minor deviations (MAE 0.2 %) in the range of interest, so the assumption is made that the gas solely consists of CO_2. The composition applied in the simulation resulting from these assumptions are listed in Table B.3.

3.3.4. Solubility calculation

To calculate the solubility of CO_2 in brine an appropriate solubility model has to be chosen. Various CO_2-solubility models are compared and finally in the following section it is described and explained in detail which model was used and how it was implemented into simulation. This calculation is applied at two specific positions within the simulations of options 1 and 3. The first calculation point is located after the first pipeline before the heat transfer (split after TW0; Figures 3.2a and 3.2c). The second calculation point to calculate the CO_2-solubility is set after the heat transfer. For option 2 (Figure 3.2b), the gas breakout pressure was calculated directly according

to the chosen CO_2-solubility model. Referring to this calculation, the system pressure for the specific simulation runs was adjusted.

3.3.5. Technical solutions for CO_2 handling (options 1, 2 and 3)

Three different technical solutions to handle the CO_2 within a binary geothermal power plant are simulated. The first technical solution (Figure 3.2a) , simulates the existing solution in Bruchsal (option 1). The second and third handling options (option 2 and option 3; Figures 3.2b and 3.2c) are selected as they represent evident and relatively easy-to-implement optimisation.

The simulation of option 1 differs from the original installation in the Bruchsal power plant in a few minor points. The low pressure separator and the second pump after the low pressure separator are not considered for simulation. These two components are important for stable plant operation, since they are relevant for adjusting the correct working fluid composition as well as for maintaining the pressure of the system, but have no thermodynamic influence on the simulation, since ideally the mixing ratio of water to ammonia can be assumed to be constant and pressure loss between preheater and condenser are neglected. The installed gas bypass, in which the degassed CO_2 is separated from the brine flow led to the power plant, is simulated as an ideal CO_2-separator. To validate the simulation results in ASPEN Plus, they were compared to measured and operational data of the power plant. The 27 data points which were used to fit the simulation to the existing plant are all measuring points for pressure, temperature or flow that display real data.

To simulate the second technical solution (Figure 3.2 b), a single phase flow is assumed by setting the operational pressure above the gas breakout pressure to simulate the influence of the operational pressure on the performance of the power plant. For each brine composition the gas breakout pressure is calculated by the model of Duan et al. (2006) and is set to operational pressure, after adding one bar to compensate pressure loss. The pressure on the working media side is set to the operational pressure of the thermal water cycle, in order to reduce large pressure difference between the plates of the heat exchangers. Because the operational pressure is above the gas break out pressure, no bypass is needed and no split with solubility calculation is

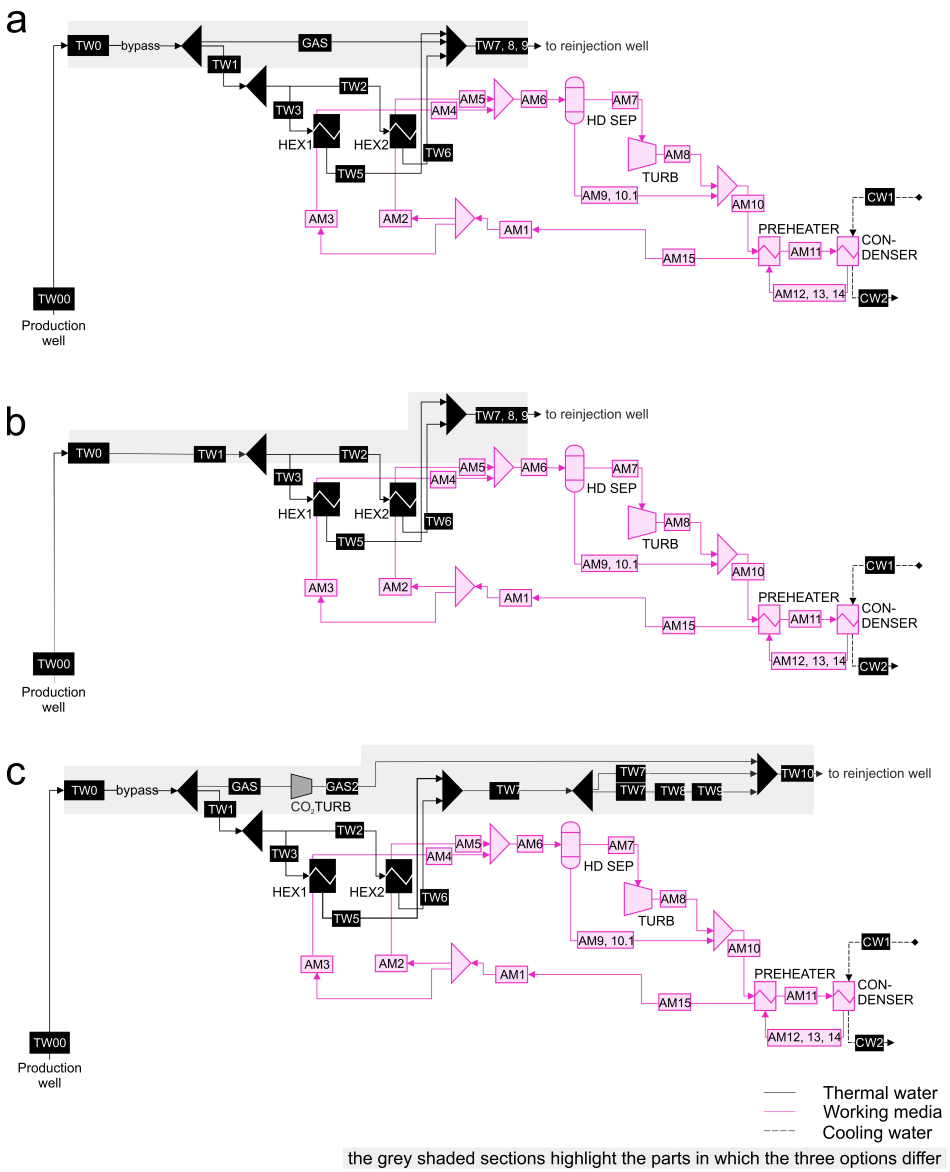


Figure 3.2.: Schematic process schemes a) Option 1: Existing solution in Bruchsal including the gas bypass. b) Option 2: Pressure maintenance and thereby prevention of free gas in the thermal water cycle. In comparison to option 1 (Figure 3.2a), separation of the gas phase is not included in this scheme. c) Option 3: An additional CO_2-turbine is implemented. The redissolution of the gas is performed directly prior to the reinjection well. In comparison to option 1 (Figure 3.2a) and option 2 (Figure 3.2b), option 3 (Figure 3.2c) leads the gas stream to the second turbine. TW: system points simulated within thermal water cycle; AM: system points simulated within the secondary cycle with ammonia-water mixture as working media; CW: system points within cooling cycle.

implemented.

In the third simulation (Figure 3.2c), a second turbine is inserted which is fed by the CO_2 stream. In the turbine the CO_2 stream is reduced to the reinjection pressure of 5 bar(a) and is mixed with the brine stream after the pressure regulating valve right before the reinjection.

3.4. CO_2 solubility models

In order to simulate the thermal water cycle of Bruchsal with its special components and the specific water-gas-mixture, an appropriate CO_2-solubility model has to be chosen. We examined different models (Rumpf et al., 1994; Tödheide and Franck, 1963; Duan and Sun, 2003; Duan et al., 2006; He and Morse, 1993; Spycher and Pruess, 2011; Zhao et al., 2015; Dubacq et al., 2013; Enick and Klara, 1990; Gehrig et al., 1986; Zhou, 2013; Jiang et al., 2016; Portier and Rochelle, 2005; Duan et al., 1992a; Diamond and Akinfiev, 2003; Upton and Santoyo, 2003) before testing three (electrolyte non-random two-liquid model (ELECNRTL) implemented in ASPEN Plus, Upton and Santoyo (2003) and Duan et al. (2006)) and compared them to experimental data (Markham and Kobe, 1941; Ellis and Golding, 1963; He and Morse, 1993; Gilbert et al., 2016; Zhao et al., 2015; Malinin and Savelyeya, 1972; Malinin and Kurorskaya, 1975; Savary et al., 2012) within our specific range of interest. The most important factors are: (1) The model must represent the parameter range of our area of interest and should be fitted to a high number of experimental data in this range; (2) the model must be easily accessible and convenient to implement in ASPEN Plus; and (3) the model must be able to implement different approaches (deviation of Henry's constant and a modified Virial equation of state).

Finally, we compared the ELECNRTL model already implemented in ASPEN Plus and the model of Duan et al. (2006). The ELECNRTL model did not match the experimental data sufficiently in our specific range of interest. Modelling of CO_2-solubility by the two different solubility models yields different results with significantly higher CO_2-solubility predicted by ELECNRTL compared to Duan et al. (2006) (Figure 3.3) and therefore overestimates CO_2-solubility as it can be observed by comparison with

experimental data.

The solubility calculation of ELECNRTL is based on Henry's law and the main data source for solution chemistry is the study by Drummond, S.E. (1981). The two models differ in terms of their calculation method (deviation of Henry's constant and a modified Virial equation of state) and the fit to experimental data. At lower temperatures, the CO_2-solubility is strongly overestimated by the modified Henry approach in the ELECNRTL model. This overestimation decreases with increasing temperature, but the fit to the available experimental data is still superior in the model of Duan et al. (2006) which presents the best fit compared to experimental data with acceptable deviations (MAE of 3.5 %) within the relevant temperature, pressure and salinity ranges (0–225 °C, 1–200 bar(a), 0.1–4.5 mol/kg), so it is chosen to be implemented for further calculations.

The polynomial fit on this model was executed at different temperature and pressure ranges. The polynomial equations for six different salt concentrations ($NaCl_{eq}$ of 0 g/L, 50 g/L, 100 g/L, 120 g/L, 150 g/L, 200 g/L) and two different temperature ranges (20–100 °C and 100–220 °C) for each concentration (Table B.3) with the variables temperature and pressure (equations (B.1) and (B.2)). Furthermore, the polynomial coefficients are listed (Table B.1). The calculation block in ASPEN Plus is set after the split named "bypass". It calculates the maximum solubility of CO_2 in the thermal water at the specific outlet conditions (p, T) of the production pipe. The CO_2 which is not dissolved in the brine is separated as gas stream from the thermal water (options 1 and 3). The values calculated by the implemented polynomial differ by 1.0 – 7.9 % MAE from those calculated with Duan et al. (2006). The gas break out pressure applied in option 2 was calculated directly by the model of Duan et al. (2006).

3.5. Simulation results of three different CO_2 handling technical solutions

The Bruchsal location conditions with its existing CO_2 handling solution with implemented gas bypass (Figure 3.1) were simulated and compared to two other possible operational schemes (Table 3.2). The chosen input parameters are listed in Ta-

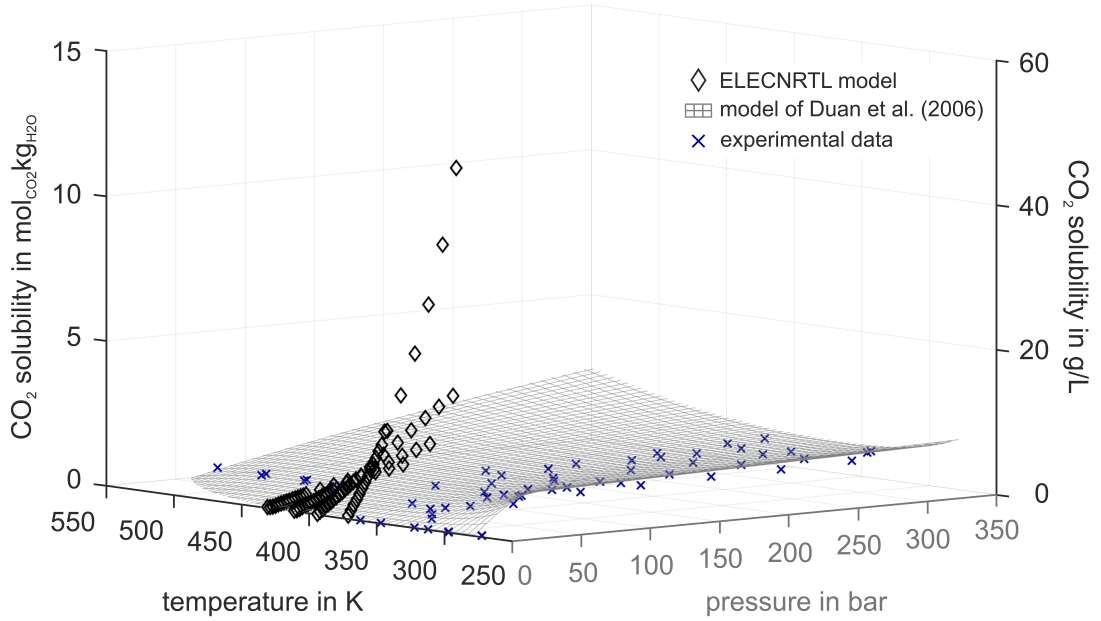


Figure 3.3.: CO_2 solubility in the H_2O - NaCl - CO_2 system calculated with ELECNRTL model and the model of Duan et al. (2006) at a salinity of 120 g/L in comparison with experimental data (Markham and Kobe, 1941; Ellis and Golding, 1963; He and Morse, 1993; Gilbert et al., 2016; Zhao et al., 2015; Malinin and Savelyeya, 1972; Malinin and Kurorskaya, 1975; Savary et al., 2012). It can be seen that the ELECNRTL model overestimates the CO_2 solubility compared to experimental data within the relevant ranges of this study.

ble 3.3. The comparison of the three simulated technical solutions was evaluated by the resulting specific heat capacity, thermal output, and gross power output (Tables B.4, B.5, B.6, B.7). When comparing the different options, the existing option 1 gives good results with a similar specific heat capacity between all options (around 3832 J/(kg K)), a thermal output of 5,902.8 kW_{th}, and an electrical output of 556.2 kW_{el} (Tables B.4, B.5, B.6 and B.7). Option 3 yields a slightly higher electrical output of 560.2 kW_{el} (Table B.4). Because of the required pressure maintenance, the power output is reduced to 206.7 kW_{el} for option 2 (Table B.4) as the pressure on the working media side is set to operational pressure of the thermal water cycle to reduce pressure differences between the heat exchanger plates and therefore less vapour is formed.

As a further step, all three options were simulated with input parameters deviat-

ing from the existing Bruchsal conditions to make the results transferable to other geothermal plants' conditions. When altering one of the parameters to evaluate its influence, all the other parameters were held constant at standard composition (Table 3.3).

Table 3.2.: List of different simulated technical solutions.

option 1	bypassing the free gas using a gas bridge with re-dissolution directly downstream of the power plant (existing CO_2 handling strategy of Bruchsal)
option 2	pressure maintenance and thereby prevention of free gas in the thermal water cycle
option 3	bypassing the free gas using a CO_2-turbine; re-dissolution of the gas after the choke and directly before the reinjection well

Several simulation runs were performed by altering the input parameters CO_2 content (0–20 g/L), amount of total dissolved salts (0–200 g/L $NaCl_{eq}$), pressure (especially for the application of option 2, 15–135 bar(a)), production temperature (100–160 °C), brine (9–100 kg/s) and working media flow rate (3–30 kg/s) (Tables B.4, B.5, B.6 and B.7). The range of both, CO_2 contents and totally dissolved solids represent typical low and high gas contents and salinity brines of binary power plants e.g. in Turkey, Germany, or France (Bosia et al., 2021; Sanjuan et al., 2016; Aksoy et al., 2015; Seibt and Wolfgramm, 2012). Furthermore, the brine temperature and flow rate are typical for low to middle enthalpy binary geothermal power plants (Mergner and Schaber, 2018; Hettkamp, 2020). The range of working media flow rate results from the brine flow rate range and was adjusted accordingly.

The results of each simulation run are presented in Tables B.4, B.5, B.6 and B.7. For option 2, the minimum required pressure for single-phase conditions is given in Table B.4 and illustrated in Figure 3.4 considering different CO_2 content and salinity. The highest theoretically calculated pressure is 135 bar(a) which would be required for single-phase conditions at the highest salinity (200 g/L $NaCl_{eq}$) and CO_2 content (20 g/L) simulated in this study. The lowest system pressure for simulation at a salinity of 0 g/L and no gas content was set at 15 bar(a).

Figure 3.5a illustrates the simulation results comparing all three options by power output when altering the production temperature. The power output of all three options varies between 154 and 730 kW_{el} with the lowest output being logically at the

Table 3.3.: The standard composition of input parameters for the simulation (Bruchsal power plant conditions).

parameter	unit	value
salinity	g/L	120
CO_2	g/L	8.5
CO_2	g/kg	7.9
density	kg/L	1.07
pressure	bar(a)	22
temperature	°C	124
working media flow rate	kg/s	5.6
brine flow rate	kg/s	25

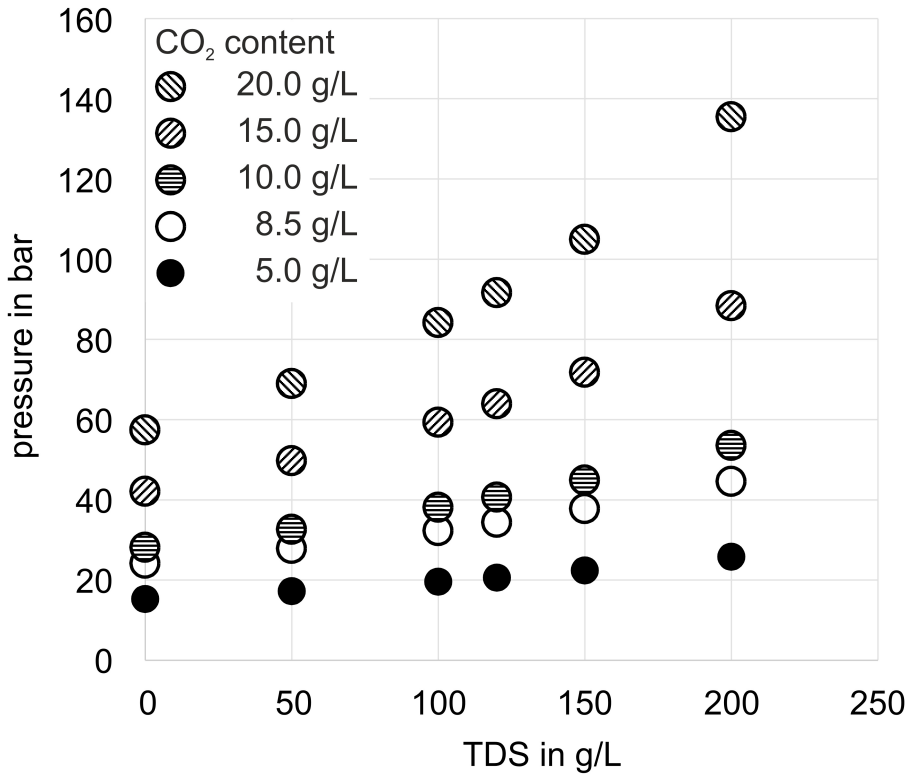


Figure 3.4.: Theoretically minimum required pressures for single-phase conditions at different salinity (total dissolved solids, TDS) and various CO_2 contents, calculated using the equations of Duan et al. (2006). One bar was added for potential pressure loss within the piping system. To reach single-phase at Bruchsal power plant conditions, a theoretical minimum pressure of 34.3 bar(a) was calculated.

lowest production temperature of 100 °C and highest at the highest temperature of 160 °C (Table B.7). All three options have comparable power output, but with option 2 representing the lowest value. The highest output is the result of option 3 at 160 °C production temperature, with a slightly additional output of ca. 29 kW_{el} caused by the implemented CO_2 turbine in the simulation scheme.

In Figure 3.5b, the simulation results of varying brine flow rate are compared. Here, all three options have highest power output at the highest simulated brine flow rate of 100 kg/s. At the simulated brine flow rates of higher than 25 to 100 kg/s, also the working media flow rate was adjusted to 10 kg/s. This was necessary in order to be able to carry out the simulation runs without error reports. The power output ranges from 73 (option 2) to 1,051 kW_{el} (option 3; Table B.7). The simulated case of 100 kg/s brine flow rate yields a power output of 79 % (option 2), and 188 % (option 3) compared to the design power of Bruchsal (560 kW_{el}). The working media flow rate was

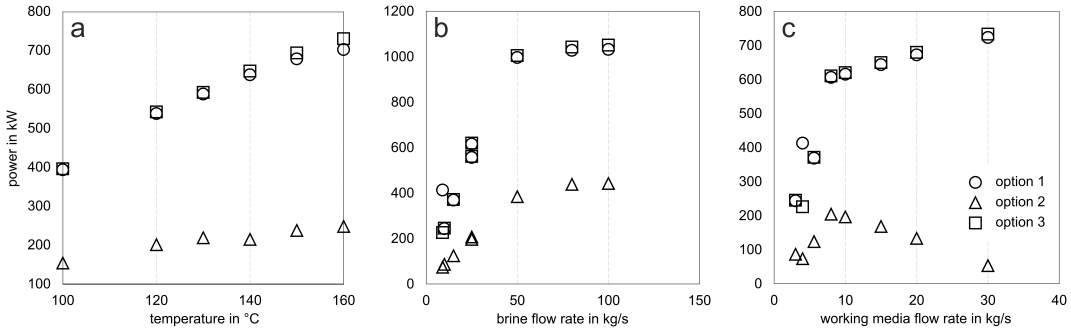


Figure 3.5.: Simulation results of options 1, 2 and 3 for variations of the (a) production temperature, the (b) brine mass flow rate and the (c) working media mass flow rate.

simulated in a range from 3 to 30 kg/s (Figure 3.5c), where 5.6 kg/s is the design working media flow rate of Bruchsal. At a working media flow rate of 3, 4 and 5.6 kg/s, the brine flow rate was 10, 9 and 15 kg/s, respectively. This is caused by technical simulation reasons to prevent simulation errors and highest possible brine flow rates were chosen for each case. The simulation runs for 8–30 kg/s working media flow rate are comparable as simulated with a constant brine flow rate of 25 kg/s. As expected, at the highest flow rate, the highest power output is displayed for options 1 (723 kW_{el}) and 3 (733 kW_{el}; Figure 3.5c). The opposite is evident with option 2 which shows the

lowest output at the highest working media flow rate of 53 kW_{el} and represents less than 10 % of the design power output of the existing power plant in Bruchsal.

The results of option 1 vary between 531 and 572 kW_{el} (Figure 3.6a), option 2 simulation results give a range from 0 to 1,055 kW_{el} power output (Figure 3.6b), and option 3 yields simulated power outputs between 536–588 kW_{el} (Figure 3.6c) which represent the influence of salinity and CO_2 contents on power output. The simulated highest power output is dedicated to option 2 and can be reached when neither gas nor salinity is measured. All options show decreasing power output with increasing salinity. For options 1 and 2 it can be seen additionally, that with increasing CO_2 content, the simulated power output decreases (Figure 3.6a and b). This strongly applies for option 2: at a salinity of at least 150 g/L and a CO_2 content 15 g/L, the simulated process no longer shows any power output within the process simulation of option 2. Option 3 simulation results first show a decrease of power output with increasing CO_2 content until 5 g/L, then an increase due to additional power generated by the implemented CO_2 turbine within this process scheme (Figure 3.6c).

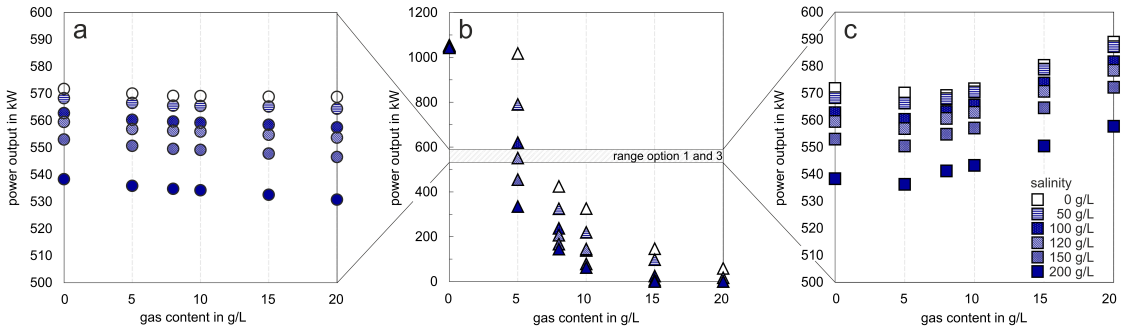


Figure 3.6.: Simulation results of (a) option 1, (b) option 2 and (c) option 3 in terms of the power output according to various CO_2 contents and salinity.

3.6. Interpretation of simulation results

By implementing a polynomial fit to the CO_2-solubility model of Duan et al. (2006) in the simulation software to calculate the CO_2-solubility in the system H_2O – NaCl – CO_2 (condition range 0–225 °C, 1–200 bar(a) and 0.1–4.5 mol/kg NaCl), a closer fit to

experimental data was achieved. We validate the simulation of the Bruchsal power plant at different system points of simulation by comparing with operational and measured data. This reveals that the simulation has a good agreement with operational data. This is also proven by the electrical gross power output of the standard process (option 1) with gas bypass which was 556 kW_{el} in comparison of design gross power output (Table B.4). This is a MAE of only 0.7 %. Furthermore, the calculated value of specific heat capacity for the standard process (3,832 J/(kg K); Table B.4) deviates only about 1.2 % (MAE) to the measured value of 3,880 J/(kg K) at 124 °C.

So far, the technical solutions of gas bypass (option 1) and pressure maintenance (option 2) were not compared regarding the performance of the plant. In our simulation, we show that the existing technology has a higher performance than option 2. The gross power and the thermal output of option 2 only reach 37 % and 84 % of option 1, respectively (Table B.4). This is due to the required pressure maintenance at these conditions to keep the thermal brine in single-phase. The pressure maintenance of 34.3 bar(a) in the primary cycle (thermal water cycle) determines the pressure maintenance in the secondary cycle (working media cycle). The higher pressure within the heat exchangers on the working media side leads to a lower vapour fraction and therefore results in a lower power output. The simulated option 2 is not economically viable at the Bruchsal conditions.

The thermal output of option 1 and option 3 is similar as the process scheme of both options is comparable apart from the additionally implemented CO_2 turbine. However, the CO_2 turbine has a supplementary power output of 4.4 kW_{el} (Table B.4) with a simulated gas mass flow of 0.06 kg/s at the Bruchsal conditions. However, when considering this low additional input, we would recommend implementing a CO_2 turbine with a minimum gas mass flow of 0.1 kg/s. To evaluate this in more detail, a careful economic analysis of capital and operational costs would be necessary.

Due to the reservoir temperature at the Bruchsal production well and the characteristics of the installed down hole pump, the production temperature and thermal water flow rate can only be adjusted within a limited range of a few Kelvin and about 2–6 L/s. Therefore, among these three sensitive parameters, the working media flow rate is identified as the adjusting screw (Figure 3.5c and Table B.7). According to our

simulation, a higher working media flow rate of 30 kg/s in combination with the actual thermal water flow rate of 25 kg/s leads to an additional power output of approximately 160 kW_{el} (in sum 723 kW_{el}; Table B.7), if the technical implementation is feasible.

A further investigation of the performance of all three simulated options is performed by evaluating the energy conversion process using the gross electrical utilisation efficiency (Figure B.3) calculated by the electrical power divided by the supplied heat amount (Mergner and Schaber, 2018). The term gross efficiency indicates that self-consumption, such as the electricity consumption of the production pump, are not subtracted. The highest possible efficiency for the illustrated cycle is the Carnot efficiency which represents the thermodynamically ideal cycle operating between a heat source at the temperature T_H (Bruchsal case: 124 °C) and a heat sink at the temperature T_L (DiPippo (2012)) (Bruchsal case: 61 °C). The ideal efficiency for the Bruchsal cycle amounts to 15.9 %. The design case reveals a utilisation efficiency of 9.5 %. This is also represented by the simulation of option 1 with a similar calculated efficiency of 9.4 % (Figure B.3a).

Options 1 and 3 have comparable calculated efficiencies at salinities below 150 g/L and CO_2 contents below 10 g/L. Besides, option 3 shows a higher efficiency up to 0.5 % more than option 1 (Figure B.3a and c). Similar to the thermal and electrical power output, the efficiency of option 2 is highly variable. At TDS = 0-120 g/L and CO_2 content of 0–5 g/L option 2 is more efficient than options 1 and 3 by ca. 30 %. This confirms the previous analysis that the gas development in the heat exchangers reduces the efficiency at higher salt and CO_2 contents and option 2 is not a suitable solution for these condition ranges for geothermal plants.

3.7. Investigation of influencing parameters - different CO_2 contents, salinity and p-T conditions

In the following, we discuss the variation of different sensitive thermodynamic parameters during different simulation runs. The parameters which influence the CO_2-solubility in the system H_2O – NaCl – CO_2 are system pressure, production tempera-

ture, salinity, and CO_2 content (Seibt et al., 1999; Duan et al., 2006; Zhao et al., 2015; Jacob and Saylor, 2016). In addition to these sensitive parameters, operational parameters such as production temperature (100–160 °C), brine (9–100 kg/s) and working media flow rate (3–30 kg/s) are varied in order to be able to transfer the simulation to other geothermal plant conditions and thus cover a wider application field reaching optimised performance. Qualitatively, Figure 3.7 illustrates the interconnection between the relevant parameters which influence the turbine power output. The arrows represent the relations between the different parameters conditioned by reservoir characteristics as well as the secondary cycle parameters. The black arrows illustrate interconnections which are valid for all simulated options. In addition, specific option 2 and option 3 connections are coloured pink and blue, respectively. Brine properties such as salinity and gas content (Table B.2), as well as the temperature and mass flow (within the pump design specification) are conditioned by the reservoir. These parameters have an influence on the parameters which link the primary cycle with the secondary cycle. These are the system pressure, the bypassed gas quantity (options 1 and 3) and the transferred heat. Exemplary, the temperature and the salinity influence the specific heat capacity. The specific heat capacity has an impact on the amount of transferred heat which of course effects the temperature after the heat transfer and the vapour fraction on the working media side. These two parameters directly affect turbine output. The working media mass flow is given by process design and has a direct impact on the vapour fraction and the temperature after heat transfer.

Similarly, the gas content conditions the system pressure and the bypassed gas quantity for options 1 and 3. In addition, the brine mass flow influences the amount of gas bypassed and the transferred heat. Higher system pressure causes less vapour fraction within the secondary cycle and thus decreases the turbine output. For option 2, the direct influence additionally exists between salinity, temperature and mass flow, and the system pressure, as no gas is bypassed within this process scheme. Furthermore, within the option 3 scheme, pressure, temperature and the bypassed gas quantity directly affect the turbine output of the CO_2 turbine. Here, the Kalina and CO_2 turbine output are summed up to obtain the total power.

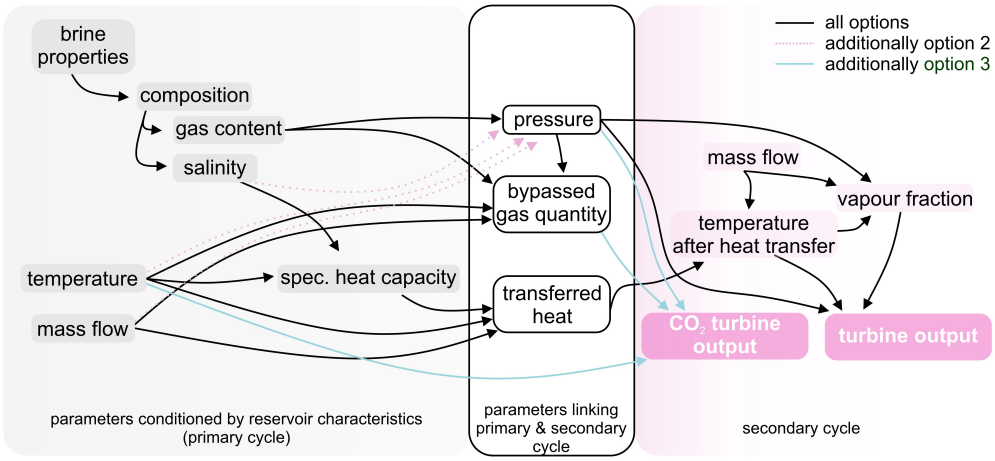


Figure 3.7.: Results of sensitivity analysis: The sensitive parameters which influence the gross power output, separated into two categories, are marked according to the different simulated options.

Quantitatively, the sensitive parameters are varied regarding different gas handling solutions and their impact is evaluated in two different ways. First, we proof that CO_2 has an impact on power plant performance at all and CO_2 handling, in this regard, is necessary in an economical point of view. To demonstrate this, we compare the option 1 simulation with a simulation run in which all CO_2 is channelled through the heat exchangers without further CO_2 handling at option 1 pressure conditions. Secondly, we compare the simulation results of all three options and suggest the most suitable of all three options at specific conditions within the simulated ranges of CO_2 content, salinity, temperature and system pressure. The most suitable technical option is chosen referring to the highest power output according to simulation. To quantify the economic effect of all gas taking part in the heat transfer, the gaseous CO_2 volume flow was calculated by simulation. For this approach, it was assumed that 50 % of the heat transfer area is blocked by the gas. This assumption was derived based on findings from Schlagermann et al. (2014). From this, the economic loss is quantified, depending on the lower heat capacity of CO_2 blocking the heat exchanger surface partly. Therefore, 50 % of the heat exchanger area will be blocked constantly, while additional gas flows into the heat exchanger and only partly leaves the heat exchanger again. Comparing the process without gas handling solution to

option 1 at Bruchsal conditions, 16 kW_{el} are lost due to gas evolving within the heat exchangers. Considering one year (7,000 h production), this yields a reduction from 3893 MWh_{el} to 3,808 MWh_{el} of annual production (at 8.5 g/L). This is equal to 3 % loss of electricity production. At higher CO_2 content of 20 g/L and a salinity of e.g. 200 g/L, the loss due to this effect is 268 MWh_{el} within one year compared to the simulated option 3 with highest performance at these conditions (3904 MWh_{el}) which equals 7 % loss of performance. This loss can be effectively prevented by adding one of the proposed technical solutions (option 1–3). Comparing the simulation results of

Table 3.4.: Recommendation of different simulated options 1, 2 and 3 depending on different simulated ranges of sensitive parameters (CO_2 content, salinity, production temperature, brine and working media flow rate). The recommendation considers the most suitable technical solution with respect to gross power output according to simulation.

sensitive parameters	CO_2 content	salinity	production temperature	flow rate		option		
				brine	working media	1	2	3
unit	g/L	g/L	°C	kg/s	kg/s			
composition	0–5	0–100	124	25	5.6		×	
	5–20	0–150	124	25	5.6	×		
	5–20	150–200	124	25	5.6			×
production temperature	8.5	120	100–130	25	5.6	×		
	8.5	120	140–160	25	5.6			×
flow rate	8.5	120	124	9–25	3–10	×		
	8.5	120	124	25–100	10–30			×

options 1–3 under different conditions, a recommendation for a technical handling option can be expressed for a defined range of values of the sensitive parameters (Table 3.4). When the production temperature is varied, at lowest temperature simulated (100 °C), the lowest power output for all options is reached (Figure 3.5a). In addition, option 2 yields the lowest output (154 kW_{el}) at 100 °C production temperature. This is because under these conditions, only a small amount of vapour fraction is generated in the secondary cycle to be able to drive the turbine. At the highest simulated production temperature of 160 °C, the option 3 layout can be recommended (Table 3.4). Due to higher temperature in the system, a greater amount of CO_2 is generated, which additionally drives the CO_2 turbine. Furthermore, the temperature is the reason for the higher vapour fraction which drives the Kalina turbine in the secondary cycle. For

higher temperature systems at a salinity of 120 g/L and a moderate CO_2 content comparable to the Upper Rhine Graben brines, it is an option to add a well-designed CO_2 turbine. When increasing the brine flow rate during simulation runs to maximum 100 kg/s (Figure 3.5b), a higher increase in power output can be seen in comparison to a production temperature increase to 160 °C. At 100 kg/s brine flow rate, 10 kg/s working media flow rate and other parameters representing Bruchsal conditions, the simulated option 3 yields a power output of even 1,051 kW_{el} (188 % of Bruchsal design power). By doubling the brine flow rate of Bruchsal power plant (50 kg/s), one already achieves an immense increase in performance of 179 % (1,005 kW_{el}) of Bruchsal design power. Option 1 yields an increase of 178 % at 50 kg/s brine flow rate (996 kW_{el} and 10.6 MW_{th}). Bruchsal performance will be increased immensely if changes could be made to the design of the well casing and a pump with a higher capacity is installed to reach higher brine flow rates. To be able to obtain higher mass flow, the well performance of both production and injection wells has to be ensured (sufficient productivity and injectivity). In line with that, the production temperature will increase, and an even higher performance will be gained at Upper Rhine Graben conditions comparable to Bruchsal. Similarly, a production temperature of 112 °C would be enough to generate the 10.6 MW_{th} thermal power at same conditions.

If plant operation allows a higher working media flow rate, this can also influence the performance positively (options 1 and 3), but also negatively (option 2; Figure 3.5c). If option 1 working media flow rate would be increased to 8 or even 30 kg/s, the electrical performance would increase to 606 kW_{el} and 723 kW_{el} (Figure 3.5c; Table 3.4), respectively. However, the working media flow rate cannot be increased without a detailed look and adjustment on design and layout of other related power plant components such as pumps and tanks. This could limit the positive impact of increasing the working media flow rate and an optimum between different plant design parameters has to be found for each plant individually. For option 2, the increase of the working media flow rate leads to a decrease in performance (Figure 3.5c; Table 3.4) because the amount of mass of working media cannot be heated properly at heat transfer, which leads to less vapour fraction and therefore lower performance.

When varying the CO_2 content and the salinity of the brine (Figure 3.6a-c), option 2

(Figure 3.6b) shows the most extreme variation in electrical power output. This is due to the requirement of maintaining the single-phase conditions and therefore the influence of salinity and gas content is very high. The other solutions do not require single-phase conditions, and therefore the pressure has not the same important influence on the process schemes of option 1 and 3. If pressure is very high in the system, the same pressure has to be also kept on secondary cycle. The high pressure leads to lower vapour fraction and yields less to even zero power output (Figure 3.6b). Due to the gas bypass in option 1 (Figure 3.6a), the gaseous CO_2 is assumed to not disturb the process and in option 3 (Figure 3.6c) the gas turbine even makes use of the additional gas.

With increasing salinity, all options show a decrease of performance due to the influence of salts on specific heat capacity and CO_2-solubility. This can be explained by the lower specific heat capacity of salts than water. Furthermore, the higher the salinity, the lower the CO_2-solubility. Due to these reasons, option 2 solution is proposed as technical solution for low CO_2 and low salinity brine. The systems can be run at low pressure to keep the single-phase brine within the system and this is also beneficial for the vapour fraction on the secondary cycle to produce power (Table 3.4). For high salinity systems ($\geq$ 150 g/L), option 3 is suggested as optimal solution (Table 3.4) as it uses the CO_2 additionally when comparing to option 1 and 2. Similarly, it would also be the option of choice at moderate to high gas content and higher flow rate (Table 3.4).

With increasing salinity, the electrical output of option 3 is first decreasing and the more gas is exsolved from the brine, the more suitable option 3 gets: at lower salinity, the additional implementation of a CO_2 turbine would not be beneficial. Therefore, option 1 is the most suitable solution at low to moderate salinity and low to high CO_2 content. For equal reasons, option 1 is proposed at low to moderate brine and working media flow rates (Table 3.4). Option 1 is the technical CO_2 handling solution of choice if the primary system has low to intermediate production temperatures (100–130 °C; Table 3.4). At higher production temperature and intermediate CO_2 content and salinity (8.5 g/L CO_2; 120 g/L salinity), option 3 gets more economically viable again in comparison to option 1 (Table 3.4).

In general, if option 1 or option 3 are proposed at certain CO_2 content, salinity, flow rate, pressure and temperature conditions, it has to be considered that detailed modelling of flow regime of the gas bypass and CO_2 turbine is needed to match the required design (e.g., length, height and diameter of pipes and turbine specifications) at specific conditions. The planning, design, and installation costs are not within the scope of this work and would be required to estimate if a realisation comes into play.

If the simulated CO_2 handling technical solutions options 1 and 3 could be also applied to handle the gases for non-binary geothermal plants, could be another aspect to focus on in the future and should be assessed in detail according to the specific location. At this point, it also has to be mentioned that within this process only $NaCl_{eq}$ as representative for salinity and CO_2 representative for the gas phase of the system are simulated. If there is a considerable amount of other non-condensable gases (e.g. CH_4 which is less soluble than CO_2) inherent, the impact or application of other gas solubility models could be assessed in the future. A further possible step would be the application of the simulation on ORC geothermal power plants.

3.8. Conclusion of part III

By analysing the influence of CO_2 in a geothermal power plant, this work aims to answer the question, which technical solution for CO_2 handling suits best to various outer circumstances, such as salinity, gas amount, temperature and flow rate of the brine. Despite the economic benefit, which is provided by optimised plant performance, the release of CO_2 into the atmosphere has to be minimised for ecological reasons. We simulate three different variations of operational schemes with technical gas handling solutions that have been selected since already applied which are a gas bypass to exclude gas from the heat exchanger (option 1), and the increase in operational pressure above the bubble point pressure (option 2). The installation of a second gas turbine after the gas bypass (option 3) is chosen to additionally benefit from the present CO_2. The simulations are validated against operational data from an existing geothermal power plant located in Bruchsal (Germany) and show a mean absolute error of less than 1 %.

Table 3.4 summarises the recommendation for different operational conditions when optimising CO_2 handling in terms of avoiding CO_2 emissions and reaching highest possible thermal or power output. At moderate to high gas content (5–20 g/L) and medium production temperature (around 120 °C), option 1 (gas bypass) is the most suitable option with a higher power output of 268 % compared to option 2 and similar to option 3 at Bruchsal conditions (99 % of option 3). At low gas contents (0–5 g/L) and low salinity (0–100 g/L) of the brine system, option 2 (pressure maintenance) is proposed to be the most preferable solution for electrical power production with an output of up to 187 % compared to options 1 and 3. At moderate to high gas contents (5–20 g/L) and higher production temperature (140–160 °C), option 3 (gas bypass and CO_2 turbine) is a valid solution with a power output of up to more than 8.5 times higher in comparison to options 1 and 2. The higher CO_2 content and production temperature result in a larger proportion of gas that is not dissolved and thus generates additional electricity by means of the CO_2 turbine. These recommendations for technical gas handling options can be used as an indication for other binary geothermal plants. The use of a simulation tool with implemented appropriate CO_2-solubility model can also be supportive for different applications, such as carbon capture and storage technology.

Part IV.

Utilisation of geothermal brine related carbon dioxide

Summary to Part IV

Lithium carbonate (Li_2CO_3) is conventionally produced from brines via solar evaporation and precipitation by adding sodium carbonate (Na_2CO_3). In this study, heterogeneous lithium carbonate precipitation from LiCl solution with using CO_2 uptake is investigated. In a commercial process the CO_2 could be sourced directly from the geothermal system itself or the carbonate precipitation may present a sink for industrial CO_2 of other origin. The results are compared with the homogeneous precipitation reaction by using Na_2CO_3. The precipitation is conducted in a stirred reactor at 25 °C and 50 °C. Furthermore, tests are conducted at 50 °C with natural CO_2 from a geothermal reservoir at the power plant in Bruchsal, Germany.

Precipitated lithium carbonate is crystalline with halite byproduct for all experiments. Li_2CO_3 with a purity of 98.7 % has been obtained by homogeneous precipitation at 3 g/L initial Li concentration and 50 °C reaching near technical grade purity. A recovery rate of 53.4 % is reached by homogeneous precipitation at 8 g/L initial Li concentration and 50 °C. Heterogeneous and homogeneous precipitation as well as on-site experiments show comparable purity and recovery.

The findings of this study demonstrate the feasibility of employing carbon dioxide (CO_2) from geothermal power plants or other industrial sources for the purpose of precipitating lithium carbonate. Such a strategy for recovering lithium using captured CO_2 would be environmentally sustainable by preventing its release into the atmosphere. Further purification steps have to be investigated along with optimising the recovery, such as by adjusting the precipitation temperature or recycling the residual LiCl solution.

Chapter 4.

Utilisation of geothermal brine related carbon dioxide: Lithium carbonate precipitation with carbon dioxide of a geothermal power plant

4.1. Introduction

The European Union has set ambitious targets to become the first green continent and to reduce CO_2 emissions to zero by 2050 (European Commission, 2019). The decarbonisation of the heating sector is a major challenge of the energy transition (REN21, 2020; Bracke et al., 2021; Moeck and Weber, 2022). Geothermal energy offers great potential as base-load-capable renewable energy in this regard (Stober and Bucher, 2020; Vivas et al., 2020; Bosia et al., 2021). In a binary geothermal plant (e.g., Bruchsal plant) hot brine is pumped to the Earth's surface and used at a production temperature between 120-180 °C (Bauer et al., 2014; in Bruchsal ca. 124 °C) for heating and power generation (Figure 4.1a). The cooled brine at a temperature of around 60 °C is reinjected into the subsurface (Fechner et al., 2022). Geothermal brine usually has a high content of a wide variety of salts and contains dissolved gases, whereby the composition of the brine depends on reservoir rocks and their interaction with the brine (Pauwels et al., 1993; Sanjuan et al., 2016; Stober and Bucher, 2020; Sanjuan et al., 2022). During ascent of the geothermal fluid, decompression occurs and a two-phase flow can evolve. Depending on the gas content, it requires different CO_2 handling techniques to keep a closed-loop system with zero emissions (Fechner et al., 2022). A further strategy could be to utilise the gas as raw material. Additionally, among other salts, the brines contain intermediate to high lithium (Li) contents (20-1,750 mg/L; Reich et al., 2022; Sanjuan et al., 2022). Both the natural CO_2 and the contained lithium allocated to the geothermal resource can be used for an innovative lithium extraction process. This offers a great opportunity to use geothermal energy as a renewable energy source, while at the same time enabling an environmentally friendly and local production of lithium as a low-emission byproduct.

In the automotive industry, electrification has increased dramatically in recent years. Great numbers of car manufacturers have already set a timeline for fully phasing out the combustion engine automobile production (Wittmann, 2017; Yawger, 2022). This development leads to a significant increase in global demand for lithium (Schmidt, 2017; Marscheider-Weidemann et al., 2022; Warren, 2021; Schmidt, 2022), making lithium one of the most important raw materials in the world today. According to expert prediction, demand for lithium will increase (An et al., 2012; Grosjean

et al., 2012; Stringfellow and Dobson, 2021b; U.S. Geological Survey, 2021; Reich et al., 2022) to ca. 320,000 t lithium by 2030 and there will be a shortage in lithium supply (Schmidt, 2022). Lithium is commonly extracted by solar evaporation from salar brines, such as in Chile and Argentina (Wanger, 2011; An et al., 2012), and from hard rock, such as in Australia (U.S. Geological Survey, 2021; Warren, 2021). These processes have a high CO_2 footprint or negative impact on the environment in a very sensitive desert (Agusdinata et al., 2018; Wanger, 2011: Kaunda, 2020; Kelly et al., 2021; Flexer et al., 2018). After the extraction of lithium, purification and conversion steps are required to obtain battery-grade Li-salts (e.g LiOH, Li_2CO_3) (Warren, 2021; Stringfellow and Dobson, 2021b; Reich et al., 2022). Li_2CO_3 is conventionally precipitated by mixing soda ash (Na_2CO_3) with purified LiCl solution (Peerawattuk and Bobicki, 2018; Han et al., 2020; Warren, 2021).

Several direct lithium extraction (DLE) technologies were investigated for recovery of lithium from geothermal brine or seawater, such as liquid-liquid extraction (LLE), precipitation and adsorption (Shi et al., 2017; Slunitschek et al., 2021; Warren, 2021; Reich et al., 2022). DLE is already applied in salars in Argentinia using aluminium hydroxide (Grant, 2020; Fries et al., 2022). Among these processes, adsorption with MnO_x-sorbents also seems to be promising to develop further (Shi et al., 2011; Shi et al., 2017; Slunitschek et al., 2021). Geothermal brine at 60 °C is pumped into a reactor in which lithium is selectively sorbed on the sorbent (Figure 4.1a). The lithium depleted brine is reinjected into the subsurface. In a second step the sorbent is regenerated by adding a desorption agent (i.e., HCl) in order to release Li ions and to obtain a LiCl solution (Slunitschek et al., 2021; Herrmann et al., 2022). In conventional processes this Li-rich solution has to be concentrated, purified and crystallised to obtain Li_2CO_3 (Stringfellow and Dobson, 2021a; Stringfellow and Dobson, 2021b).

Several studies and industrial applications deal with homogeneous reactions of precipitating Li_2CO_3 using soda ash (An et al., 2012; Peerawattuk and Bobicki, 2018). However, recent studies (Han et al., 2020; Anwar Ul Haq, 2019; Battaglia et al., 2022) show that heterogeneous precipitation using CO_2 can be a viable option to recover lithium as Li_2CO_3 from Li_2SO_4 solution. Moreover, Zhou et al. (2014) produce Li_2CO_3 from a LiCl solution with CO_2 via a coupled reaction and a solvent extraction process

using an organic reactant. Sun et al. (2012) study Li_2CO_3 production by gas-liquid reactive crystallisation of LiOH and CO_2.

In this study, we test precipitation of Li_2CO_3 in a heterogeneous reaction by the injection of CO_2 into a LiCl solution. Our results are compared with homogeneous precipitation (conventional method with soda ash) in terms of purity and recovery. Two main scientific questions are answered: (1) Is it possible to utilise the natural CO_2 at the geothermal power plant for heterogeneous precipitation of Li-carbonate and (2) are the recovery and the purity of the precipitate sufficient for further processing steps in obtaining battery-grade lithium salts?

Precipitation with CO_2 from geothermal fluids allows the entire geothermal lithium recovery process to reach a negative CO_2 balance of the overall geothermal process and to reduce the amount of additional chemicals such as soda ash to convert the lithium solution into lithium salts. Also, additional CO_2 from CO_2-intensive processes such as cement, steel or combustion processes may be used and captured in the solid product.

4.2. Materials and methods

4.2.1. Materials

The materials used in this study for precipitation of lithium carbonate in the heterogeneous system are synthetically prepared LiCl (anhydrous LiCl, 99 %, Alfa Aesar), NaOH (NaOH, ≥ 99 %, pellets, CAS-number: 1310-73-2, VWR Chemicals) and CO_2 (CO_2, UN 1013, DIN EN ISO 14175-C1-C, Air Liquide Deutschland GmbH). Five different LiCl solutions with initial Li concentrations of 3, 5, 8, 10, 12.3 g/L were investigated in the laboratory experiments and two different LiCl solutions with Li concentrations of 5 and 10 g/L were examined in the on-site experiments at the Bruchsal geothermal power plant using the natural gas.

To prepare LiCl solutions, analytical-grade lithium chloride was mixed with milli-Q water. The pH was adjusted using 100 mL of 5 M sodium hydroxide (NaOH, ≥ 99 %, pellets, CAS-number: 1310-73-2, VWR Chemicals). Lithium carbonate (Li_2CO_3) was

produced by mixing the solution with carbon dioxide gas. For the on-site experiments at 5 and 10 g/L Li concentration at 50 °C, the natural gas pumped along with the geothermal brine at the Bruchsal geothermal power plant was used (Table 4.1). After pumping the geothermal fluid, the decompression results in a two-phase flow. The gas stream is separated from the brine before the heat exchanger, and after that fed to the reinjection line. At this process step, part of the natural gas can be branched off to be used in the on-site experiments.

Similarly, synthetically prepared LiCl was used for the precipitation of lithium carbonate in the homogeneous system. Sodium carbonate (Na_2CO_3, 99 %, Merck KGaA) was used instead of sodium hydroxide and carbon dioxide to precipitate lithium carbonate.

Table 4.1.: Composition of geothermal gas sampled from gas bypass at Bruchsal geothermal power plant (Fechner et al., 2022).

CO_2	N_2	CH_4
94.5 vol-%	3.5 vol-%	1.89 vol-%

4.2.2. Precipitation method

Experimental setup

Precipitation of lithium carbonate by homogeneous and heterogeneous reactions (reaction partners of different states of aggregation are involved; Pfennig, 2004) were conducted in an open, 1 L stirred-tank reactor at 25 °C and 50 °C. The reactor was equipped with a magnetic stirrer at 250 rpm to ensure good dispersion and regulate the temperature. Over the course of the experiments, a WTW pH Meter 330 was used to monitor temperature and pH.

In the heterogeneous precipitation, CO_2 gas at 0.1 bar was fed into the solution with initial Li concentrations of 3, 5, 8, 10 and 12.3 g/L (18.3, 30.5, 48.9, 61.1 and 75 g/L LiCl concentration) by a glass tube with a diameter of 0.5 cm (Figure 4.1b). At the start of the experiments the pH was set approximately to 12 by addition of 5 M NaOH. To reach the target temperatures of 25 °C and 50 °C, the solution was heated. Subsequently, the pH was slowly lowered to 8 by the constant addition of CO_2 gas and the

experiment was stopped at this point to prevent dissolution of the precipitate. This was done by turning off the injection of the CO_2 gas, the magnetic stirrer and heating plate. The supernate was separated from the precipitate after centrifuging. The experimental setup is based on Zhou et al. (2014) and Han et al. (2020) who also recommended to stop the experiments at a pH of 8.

For the homogeneous precipitation, the LiCl solutions with identical initial Li concentrations as for heterogeneous precipitation were heated slowly to 50 °C and then mixed with soda ash (Na_2CO_3) in stoichiometric proportion (16.0, 26.6, 42.6, 53.2 and 65.3 g of soda ash). After mixing, an increase in temperature was observed. With increasing temperature, the formation of crystalline particles was noticed, proving that precipitation took place. Crystalline substances were separated from the solution by centrifuging, washing with milli-Q water and drying in an oven at 60 °C for approximately 48 hours. A portion of each sample was not washed to investigate a possible effect of washing.

On-site setup

An experimental set-up was established to utilise CO_2 contained in geothermal brine for heterogeneous precipitation (Figure 4.1a). The experiments were performed with a starting pH of approximately 12 in an open, 1 L stirred-tank reactor. LiCl solutions with a Li concentration of 5 g/l and 10 g/l were heated slowly to 50 °C. Once the target temperature was reached, gas (mainly CO_2; Table 4.1) extracted from a bypass of the geothermal plant's brine feed line (Figure 4.1a) was constantly fed into the LiCl solution at approximately 0.1 bar. The experiment was retained until the pH of the solution dropped to 8, after which the CO_2 supply was stopped. The precipitates were processed and examined analogously to the laboratory experiments.

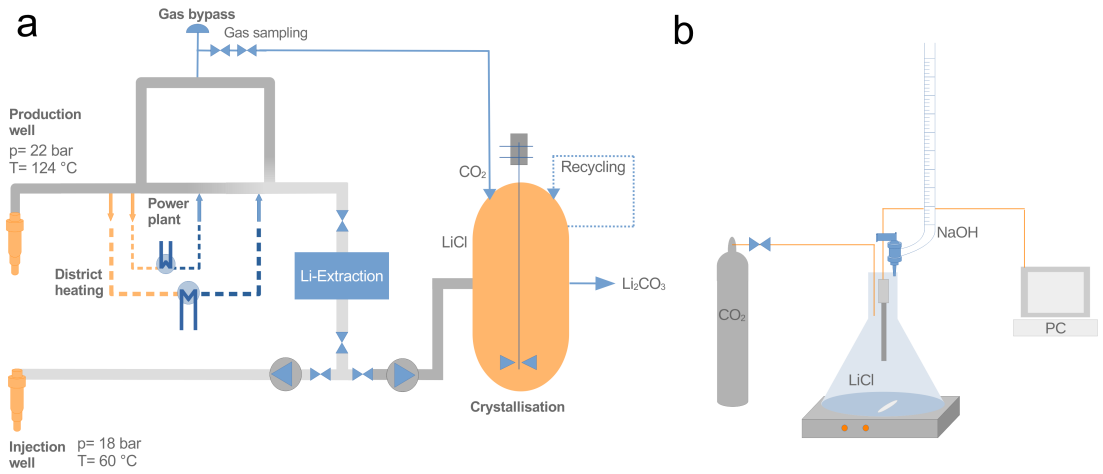


Figure 4.1.: a) On-site experimental set-up at the Bruchsal geothermal power plant with implemented Li-extraction; b) set-up for heterogeneous precipitation with CO_2.

4.2.3. Mineralogical and geochemical characterisation

The precipitates were analysed by XRD and SEM to determine the crystallinity, morphology and the particle size. Inductively coupled plasma spectroscopy (ICP-OES) was used to analyse the elemental composition of the substances and the purity of the precipitated Li_2CO_3 was calculated accordingly.

The concentrations in solution were analysed by ICP-OES (Varian 715ES, Agilent) in the Laboratory of Environmental and Raw Materials Analysis (LERA; AGW) of Karlsruhe Institute of Technology. For the laboratory experiments, Li and Na were analysed. For the on-site experiments, the elements Li, Na, As, Ba, Ca, Fe, K, Mg, Mn, Si, Sr and Zn were analysed. Quality control was secured by measuring standards. The standard deviation was calculated on the base of two measurements of the samples. Overall accuracy was better than ± 6 %. Structural analysis was carried out using the X-ray diffractometer (XRD, Bruker D8 Discover) with Cu K_α radiation (λ = 0.154056 nm) at 40 kV, 40 mA, 0.4 sec/step scanning speed and 0.02 ° step size in the 2θ range from 2 ° to 82 ° (sample diameter: 20 mm). The morphology of Li_2CO_3 was studied using scanning electron microscopy (SEM, Zeiss Sigma VP 03-88 at 15 Pa and acceleration voltage of 15 kV) at the EnBW Kernkraft GmbH (EnKK) laboratory in Philippsburg.

4.2.4. Theoretical considerations

Precipitation occurs when super saturation is reached and a solid is formed by the combination of certain anions and cations in a solution. Accordingly, precipitation of Li_2CO_3 begins when the concentration of CO_3^{2-}(aq) along with Li^+ in solution reaches supersaturation of Li_2CO_3. The supersaturation of Li_2CO_3 can be defined using equation (4.1) (Gondesen, 2020). The solubility product K_{sp} indicates how much salt can be dissolved in a given volume of water. According to equation (4.1), supersaturation (S) is given as the ratio of the ion activity product Q_c to the solubility product K_{sp}.

$$S = \frac{Q_c}{K_{sp}} = \frac{(Li^+)^2 \cdot (CO_3^{2-})}{[Li^+]^2 \cdot [CO_3^{2-}]} \tag{4.1}$$

When CO_2 gas is fed into an aqueous solution, the gas partially dissolves in water and reacts with water to form carbonic acid as shown in equations (4.2) and (4.3).

$$CO_{2(g)} \rightleftharpoons CO_{2(aq)} \tag{4.2}$$

The Erlenmeyer rule (Buddrus and Schmidt, 2014) describes the instability of molecules with two hydroxyl groups on one carbon atom. This instability is explained by dissociation in equations (4.3), (4.4) and (4.5). The equilibrium state of the reactions varies according to temperature and pH. In an acidic environment the equilibrium shifts to the reactant CO_2, while it shifts to the product CO_3^{2-} in an alkaline environment (Zeebe and Wolf-Gladrow, 2001) and in between, the system is dominated by HCO_3^- (Figure 4.2). In this study, pH was set at a minimum of 8 to ensure the formation of a sufficiently high amount of carbonate ions.

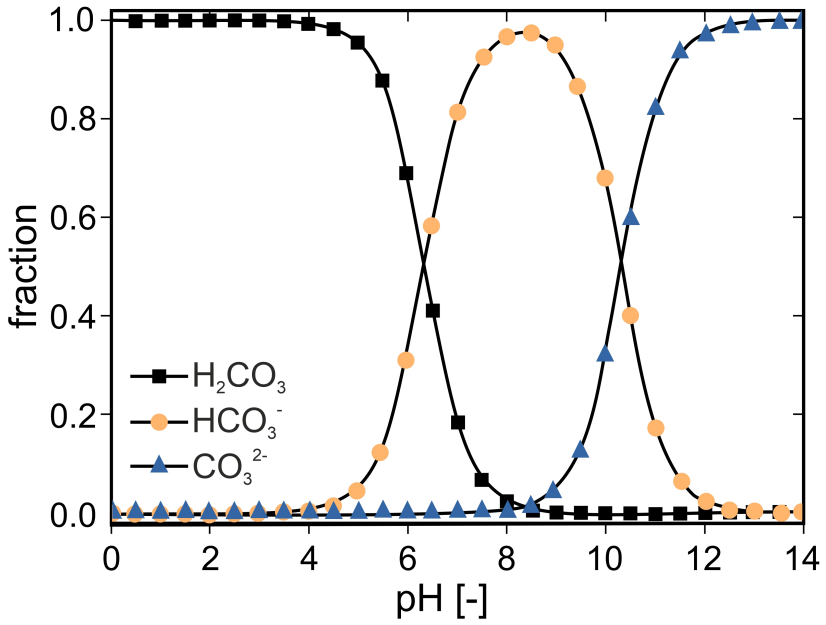


Figure 4.2.: Fraction of carbonic acid (H_2CO_3), hydrogen carbonate (HCO_3^-) and of carbonate (CO_3^{2-}) in water as a function of the pH. Modified after Wisotzky (2011).

$$CO_2 + H_2O \rightleftharpoons H_2CO_3 \tag{4.3}$$

$$H_2CO_3 + H_2O \rightleftharpoons H_3O^+ + HCO_3^- \tag{4.4}$$

$$HCO_3^- + H_2O \rightleftharpoons CO_3^{2-} + H_3O^+ \tag{4.5}$$

In the homogeneous precipitation experiments of our study, carbonate ions are formed by dissociation of Na_2CO_3, equation (4.6).

$$Na_2CO_3 \rightleftharpoons 2Na^+ + CO_3^{2-} \tag{4.6}$$

To precipitate Li_2CO_3 the supersaturation S must be greater than 1 ($S > 1$). This is only achieved when the Li concentration is sufficiently high and an adequate amount of carbonate ions is present in the solution (equation (4.7)).

$$2Li^+ + CO_3^{2-} \rightleftharpoons Li_2CO_3 \downarrow \tag{4.7}$$

The precipitated mass m of Li_2CO_3 ($m_{Li_2CO_3}$) is calculated by equation (4.8), where M_i is the molecular weight of Li and Li_2CO_3, c_{Li} the concentration of Li, and V the volume of the solution. The purity is calculated after equation (4.9) with $m_{precipitate}$ as the sum of the mass of all measured compounds measured by ICP-OES.
The recovery rate $R_{Li_2CO_3}$ of lithium carbonate is defined by equation (4.10). m_s is the solubility of lithium carbonate in a LiCl brine (Cheng et al., 2013) of the five relevant initial Li concentrations at a certain temperature T. $m_{t(Li_2CO_3)}$ is the theoretical mass of Li_2CO_3 following equation (4.8).

$$m_{Li_2CO_3} = (c_{Li} \cdot V)\frac{M_{Li_2CO_3}}{M_{Li} \cdot 2} \tag{4.8}$$

$$purity = \frac{m_{Li_2CO_3}}{m_{precipitate}} \tag{4.9}$$

$$R_{Li_2CO_3} = \frac{m_{Li_2CO_3}}{m_{t(Li_2CO_3)} - m_s} \tag{4.10}$$

4.3. Results

4.3.1. Heterogeneous precipitation experiments in the laboratory and on-site

After heating the LiCl solution to 25°C or 50°C CO_2 was fed into the solution until a pH of 8 was reached. At the start of the reaction, the temperature increased by 5.4-7.7 K depending on starting composition (3, 5, 8, 10 and 12.3 g/L initial Li concentration; Figure 4.3a). This means that the reaction is exothermic. The temperature was subsequently adjusted to starting conditions while CO_2 feeding was continued. The pH drop was small during temperature increase after CO_2 feed was started. With decreasing temperatures, a sharp pH drop followed and then the pH stabilised (Figure 4.3a). In low Li concentration solutions (3 g/l and 5 g/l), precipitation is not spontaneous,

but starts after approximately 15-20 minutes. Precipitation is spontaneous as soon as CO_2 is added at higher initial Li concentrations (8-12.3 g/L). Experiments with low initial Li concentration (3–8 g/l) at 25 °C required twice as much time (up to 123 min) to reach pH 8 than experiments with high initial Li concentration (10–12.3 g/L) at 25 °C (Figure 4.3a).

4.3.2. Homogeneous precipitation experiments in the laboratory

During homogeneous precipitation, a white precipitate was obtained in all experiments as soon as Na_2CO_3 was added, regardless of the initial Li concentration. Similar to the heterogeneous precipitation experiments, an increase in temperature (4.8-7.1 K) was detected for homogeneous precipitation depending on starting composition (3, 5, 8, 10 and 12.3 g/L initial Li concentration). Therefore, both homogeneous and heterogeneous precipitation are exothermic reactions. During homogeneous precipitation experiments, pH was not recorded. The reaction time was less than 5 minutes and no kinetic difference regarding initial Li concentration is observed, as the stochiometric amount of Na_2CO_3 added to the LiCl solution is adjusted to the Li concentration in each solution.

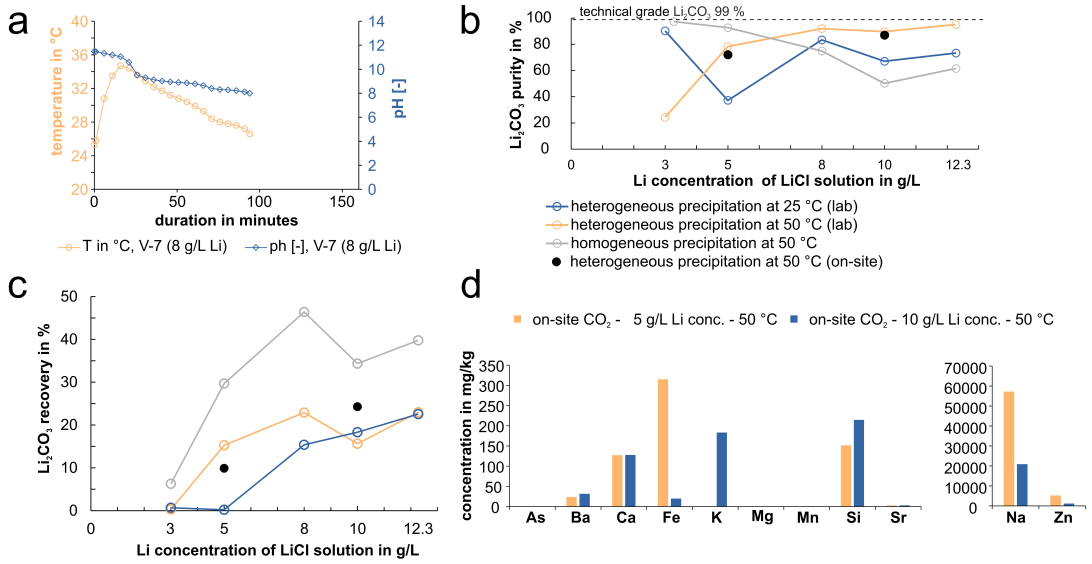


Figure 4.3.: a) Diagram (at 8 g/L Li concentration and 25 °C) showing the duration of heterogeneous precipitation with CO_2 until pH of 8 was reached. At the start of the CO_2 supply, the temperature rises to 35 °C; b) Li_2CO_3 purity of heterogeneous and homogeneous precipitation (laboratory and on-site); c) Li_2CO_3 recovery of heterogeneous and homogeneous precipitation (laboratory and on-site). Legend is given in b); d) Composition of precipitate of on-site experiments.

4.3.3. Composition, purity and recovery of the precipitates

The precipitates mainly consist of lithium (as lithium carbonate, Li_2CO_3) and sodium (as sodium chloride, NaCl) (Tables 4.2 and 4.3). A few additional elements (mainly Zn, Fe, Si, Ca) were detected in the on-site experiments.

In laboratory experiments, the purity of the precipitate obtained from heterogeneous precipitation varied from 37.2 to 90.2 % at 25 °C and from 24.2 to 95.1 % at 50 °C. At 25 °C with Li concentration of 5 g/L and at 50 °C with Li concentration of 3 g/L precipitates with the lowest Li_2CO_3 purity were recovered. Among the experiments at 25 °C, the experiment with the lowest Li concentration of 3 g/L reached the highest Li_2CO_3 purity. Contrary to this, the highest Li_2CO_3 purity at 50 °C was obtained with the highest Li concentration of 12.3 g/L. In the heterogeneous precipitation experiments at 50 °C, the Li_2CO_3 purity is significantly enhanced with increased Li concentration. This trend is not reproduced for either heterogeneous precipitation at 25 °C

Table 4.2.: Results of ICP-OES analysis of all experiments V-1 to V-15 including standard deviation. The precipitation method (homogeneous/heterogeneous) is specified. Furthermore, purity and recovery of laboratory experiments are listed for washed (w) and non-washed samples (see Figure 4.4) calculated according to equations (4.9) and (4.10), respectively.

experiment code			**V-1**	**V-1 (w)**	**V-2**	**V-2 (w)**	**V-3**	**V-3 (w)**	
initial Li concentration	g/L		**12.3**	**12.3**	**12.3**	**12.3**	**10**	**10**	
precipitation method			**CO_2**	**CO_2**	**CO_2**	**CO_2**	**CO_2**	**CO_2**	
temperature in °C			**25**	**25**	**50**	**50**	**25**	**25**	
		detection limit							
Li	mg/kg	0.008	139,252	139,303	151,149	173,397	147,556	146,099	
standard deviation (n=2)	mg/kg		3,330	705	188	2,232	395	1,977	
Na	mg/kg	0.009	66,339	50,809	49,890	8,983	73,705	72,008	
standard deviation (n=2)	mg/kg		261	293	325	139	163	119	
Li/Na	-		2.1	2.7	3.0	19.3	2.0	2.0	
Li_2CO_3 (purity)	wt-%		81.5	85.2	86.4	97.6	80.7	80.9	
NaCl	wt-%		18.5	14.8	13.6	2.4	19.3	19.1	
recovery	%		31.1	26.4	31.8	23.7	26.3	22.4	

experiment code			**V-4**	**V-4 (w)**	**V-5**	**V-5 (w)**	**V-6**	**V-6 (w)**	
initial Li concentration	g/L		**10**	**10**	**8**	**8**	**8**	**8**	
precipitation method			**CO_2**	**CO_2**	**CO_2**	**CO_2**	**CO_2**	**CO_2**	
temperature in °C			**50**	**50**	**25**	**25**	**50**	**50**	
		detection limit							
Li	mg/kg	0.008	157,747	167,238	165,013	173,242	165,245	166,438	
standard deviation (n=2)	mg/kg		1,876	3,187	2,461	2,495	1,725	3,122	
Na	mg/kg	0.009	61,275	19,341	48,724	34,788	41,430	14,518	
standard deviation (n=2)	mg/kg		314	188	320	6	129	166	
Li/Na	-		2.6	8.6	3.4	5.0	4.0	11.5	
Li_2CO_3 (purity)	wt-%		84.4	94.8	87.6	91.2	89.3	96.0	
NaCl	wt-%		15.6	5.2	12.4	8.8	10.7	4.0	
recovery	%		20.8	16.6	23.4	17.1	28.6	24.2	

experiment code			**V-7**	**V-7 (w)**	**V-8**	**V-8 (w)**	**V-9**	**V-9 (w)**	
initial Li concentration	g/L		**5**	**5**	**5**	**5**	**3**	**3**	
precipitation method			**CO_2**	**CO_2**	**CO_2**	**CO_2**	**CO_2**	**CO_2**	
temperature in °C			**25**	**25**	**50**	**50**	**25**	**25**	
		detection limit							
Li	mg/kg	0.008	41,957	101,585	164,120	134,813	31,552	160,246	
standard deviation (n=2)	mg/kg		173	308	1,343	1,078	654	4,540	
Na	mg/kg	0.009	309,410	171,788	54,290	37,466	353,073	17,489	
standard deviation (n=2)	mg/kg		3,379	105	323	6	86	952	
Li/Na	-		0.1	0.6	3.0	3.6	0.1	9.2	
Li_2CO_3 (purity)	wt-%		22.1	55.3	86.4	88.3	15.8	95.0	
NaCl	wt-%		77.9	44.7	13.6	11.7	84.2	5.0	
recovery	%		0.5	0.3	17.9	18.0	0.4	0.9	

experiment code			**V-10**	**V-10 (w)**	**V-11 (w)**	**V-12 (w)**	**V-13 (w)**	**V-14 (w)**	**V-15 (w)**
initial Li concentration	g/L		**3**	**3**	**12.3**	**10**	**8**	**5**	**3**
precipitation method			**CO_2**	**CO_2**	**Na_2CO_3**	**Na_2CO_3**	**Na_2CO_3**	**Na_2CO_3**	**Na_2CO_3**
temperature in °C			**50**	**50**	**50**	**50**	**50**	**50**	**50**
		detection limit							
Li	mg/kg	0.008	24,840	70,406	135,489	109,128	147,169	166,379	170,734
standard deviation (n=2)	mg/kg		566	129	1,927	1,713	1,634	2,161	326
Na	mg/kg	0.009	340,559	220,089	84,805	108,502	49,664	13,247	4,810
standard deviation (n=2)	mg/kg		1,084	72	32	34	110	157	125
Li/Na	-		0.1	0.3	1.6	1.0	3.0	12.6	35.5
Li_2CO_3	wt-%		13.2	40.1	77.0	67.8	86.1	96.3	98.7
NaCl	wt-%		86.8	59.9	23.0	32.2	13.9	3.7	1.3
recovery	%		0.2	0.5	49.8	46.4	53.4	30.9	6.4

(w) - washed

or homogeneous precipitation. The Li_2CO_3 purity rather decreased with increasing Li concentration at 25 °C (Figure 4.3b; Table 4.2).

In on-site experiments a purity of 84.3 % was achieved with the Li concentration of 5 g/L (50 °C) and a purity of 93.3 % was obtained with 10 g/L (50 °C) Li concentration. The major elements detected were Na (at 5 g/L Li concentration: 57,205 mg/kg; at 10 g/L Li concentration: 20,877 mg/kg), followed by Zn (at 5 g/L: 5,211 mg/kg; at 10 g/L: 1,153 mg/kg), Fe (at 5 g/L: 315 mg/kg; at 10 g/L: 20 mg/kg), K (at 5 g/L: n.d. ; at 10 g/L: 183 mg/kg), Si (at 5 g/L: 152 mg/kg; at 10 g/L: 215 mg/kg), Ca (at 5 g/L: 127 mg/kg; at 10 g/L: 128 mg/kg), and trace amounts of Ba (at 5 g/L: 23 mg/kg; at 10 g/L: 31 mg/kg). The elements Mg, As and Mn were below detection limit (Figure 4.3c; Table 4.3).

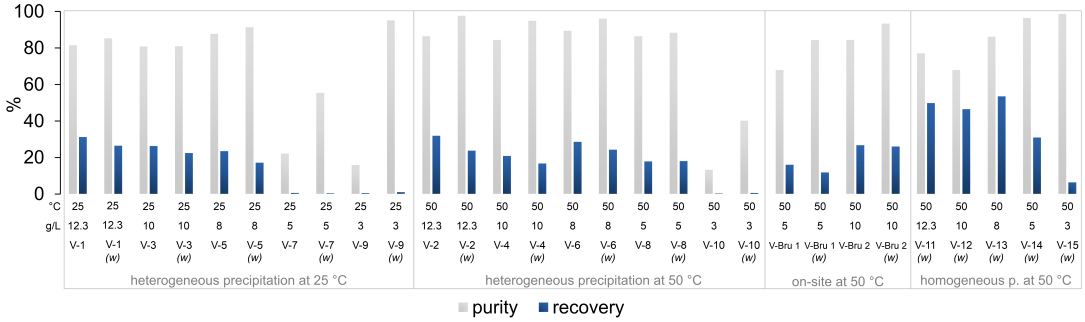


Figure 4.4.: Evaluation of homogeneous and heterogeneous precipitates with and without washing step regarding recovery and purity. *(w) - washed.*

The Li_2CO_3 recovery varied from 0.3 to 53.4 % for all experiments (Figure 4.3c). The highest recovery was obtained by homogeneous precipitation with 8 g/L Li concentration, while the lowest recovery by heterogeneous precipitation was revealed with 3 and 5 g/L (25 °C). The on-site experiment recovery varied from 11.8 % at 5 g/L to 26.0 % at 10 g/L Li concentration (Table 4.3). These results of the on-site experiments are comparable with the laboratory results under similar conditions (5 and 10 g/L Li concentration at 50 °C with a recovery of 18.0 % and 16.6 %, respectively). With 5 g/L Li concentration, 6.2 percentage points less recovery was achieved in on-site experiments, while with 10 g/L Li concentration the on-site experiment yielded 9.4 percentage points higher performance in comparison with the laboratory results

(Tables 4.2 and 4.3).

Table 4.3.: Results of ICP-OES analysis with purity and recovery of on-site experiments. The precipitation method (homogeneous/heterogeneous) is specified. Furthermore, purity and recovery of laboratory experiments are listed for washed (w) and non-washed samples (see Figure 4.4) calculated according to equations (4.9) and (4.10), respectively.

experiment code			**V-Bru 1**	**V-Bru 1 (w)**	**V-Bru 2**	**V-Bru 2 (w)**
initial Li concentration	g/L		**5**	**5**	**10**	**10**
precipitation method			**CO_2**	**CO_2**	**CO_2**	**CO_2**
temperature in °C			**50**	**50**	**50**	**50**
		detection limit				
Li	mg/kg	0.008	127,289	161,176	160,663	150,808
Na	mg/kg	0.009	120,761	57,205	59,935	20,877
Li/Na	-		1.1	2.8	2.7	7.2
Li_2CO_3 (purity)	wt-%		67.9	84.3	84.4	93.3
NaCl	wt-%		31.2	14.5	15.1	6.2
others	wt-%		1.0	1.2	0.5	0.5
recovery	%		16.0	11.8	26.6	26.0
As	mg/kg	0.0011	<0.0011	<0.0011	<0.0011	<0.0011
Ba	mg/kg	0.0001	20	23	34	31
Ca	mg/kg	0.0096	204	127	201	128
Fe	mg/kg	0.0004	319	315	20	20
K	mg/kg	0.0154	272	<0.0154	659	183
Mg	mg/kg	0.0013	<0.0013	<0.0013	<0.0013	<0.0013
Mn	mg/kg	0.0005	<0.0005	<0.0005	<0.0005	<0.0005
Si	mg/kg	0.0035	129	152	219	215
Sr	mg/kg	0.0001	3	3	4	3
Zn	mg/kg	0.0002	4,500	5,211	1,289	1,153

(w) - washed

4.3.4. Mineralogy of the precipitate

The precipitates are dominated by lithium carbonate (reference ICDD 00-022-1141). All precipitation products have a high crystallinity, no amorphous phases were detected (Figure 4.5a). Halite is co-precipitated in homogeneous precipitation experiments. While the intensities of the lithium carbonate peaks were higher at experiments of 5 g/L initial Li concentration than of 10 g/L at 25 °C, the contrary was found at 50 °C. A similar trend is noticed for the samples precipitated with CO_2 in on-site

experiments. The peak intensities of the lithium carbonate precipitated during on-site experiments both with initial 5 g/L and 10 g/L Li concentration were higher than during heterogeneous laboratory experiments. The peaks of NaCl were less intense at 50 °C during heterogeneous laboratory experiments with 10 g/L Li concentration. The most significant NaCl peaks are noticed at 25 °C with 5 g/L Li concentration.

The SEM images show flake like, sometimes radial particles with wide particle size between 1 µm to 55 µm (Figure 4.5b-f). Most particles of the lithium carbonate obtained during heterogeneous precipitation on-site with 5 g/L Li concentration were in the range of 5-10 µm, but smaller than 15 µm (Figure 4.5c). The lithium carbonate precipitated during homogeneous precipitation with 5 g/L Li concentration at 50 °C (Figure 4.5d) shows similar particles in both shape and sitze to the ones from on-site experiments with 5 g/L Li concentration. The shape and particle size of lithium carbonate precipitated during heterogeneous precipitation in the laboratory with 10 g/L Li concentration at 50 °C (Figure 4.5e) was remarkably similar to that obtained by heterogeneous precipitation in the laboratory with 5 g/l Li concentration (Figure 4.5b). The Li_2CO_3 obtained by heterogeneous precipitation on-site with 10 g/L Li concentration at 50 °C shows inhomogeneous, needle- and flake-shaped particles (Figure 4.5f) with a wide particle size range between 1 µm to 30 µm. The particles obtained by homogeneous precipitation with 10 g/L Li concentration at 50 °C are homogeneous and show a narrow particle size < 5 µm (Figure 4.5g).

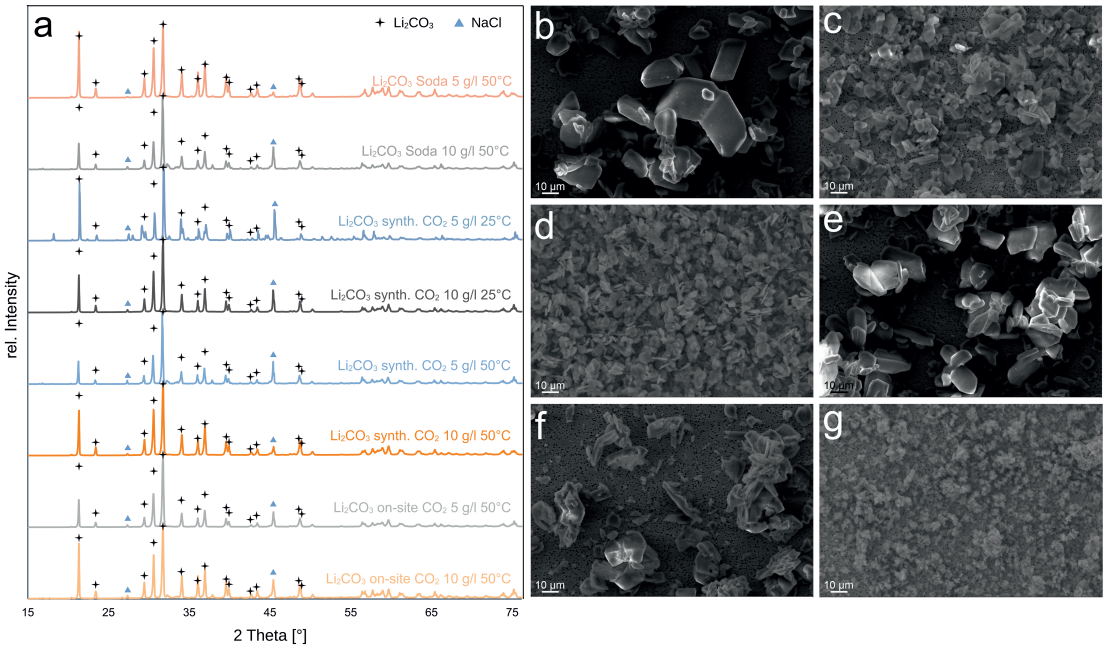


Figure 4.5.: XRD patterns of precipitates (laboratory and on-site experiments) precipitated with Na_2CO_3 and CO_2 at different temperatures and initial Li concentrations (a). (b) SEM image of precipitates at 5 g/l Li concentration and 50 °C precipitated with synthetic CO_2; (c) precipitated on-site with natural CO_2 at 5 g/l Li concentration and 50 °C; (d) precipitated with Na_2CO_3 at 5 g/l Li concentration and 50 °C; (e) precipitated with synthetic CO_2 at 10 g/l Li concentration and 50 °C; (f) precipitated on-site with natural CO_2 at 10 g/l Li concentration and 50 °C; (g) precipitated with Na_2CO_3 at 10 g/l Li concentration and 50 °C.

4.4. Discussion

4.4.1. Precipitation performance: comparison of homogeneous and heterogeneous precipitation

Reaction process

Both the homogeneous and heterogeneous precipitation reactions are exothermic. This was expected from theory, as gases usually dissolve exothermically (Mortimer and Müller, 2010). At both temperature levels during the heterogeneous precipitation experiments, the characteristic of the pH decrease is similar. At 50 °C, the target pH of

8 is reached faster at the same CO_2 flow rate compared with the experiments at 25 °C, which means that the reaction kinetics is faster at higher temperatures. Furthermore, at higher initial Li concentration, precipitation occurs immediately when CO_2 is fed to the reactor due to faster kinetics at higher reactant concentration. Accordingly, at lower initial Li concentration, precipitation is slightly delayed.

These observations indicate that the heterogeneous precipitation at 50 °C and higher initial Li concentration have a better performance in terms of reaction time compared with the experiments at 25 °C. Han et al. (2020) confirm supersaturation and precipitation kinetics being enhanced at higher reaction temperatures. Furthermore, Han et al. (2020) state that higher temperatures can enhance the collision probability between different ions and the number of active molecules. This in turn explains why more molecules in the starting solution imply that precipitation is more likely to occur. At higher temperatures, the Li_2CO_3 solubility decreases, so that supersaturation is higher at 50 °C (Han et al., 2020). Also, the pH reduction is faster, due to CO_3^- ion consumption. During homogeneous precipitation, the reaction time is much shorter (less than 5 minutes) and no kinetic difference regarding initial Li concentration is observed, as the stochiometric amount of Na_2CO_3 added to the LiCl solution is adjusted to the Li concentration in each solution. Compared with the heterogeneous precipitation experiments, the $[OH]/[Li]$ ratio is kept constant.

Mineralogy and chemistry

The precipitates are lithium carbonate and halite (Figure 4.5a) formed due to buffering with NaOH and the addition of soda ash. The shape of the XRD peaks indicates a high degree of crystallinity of the formed lithium carbonate. There is no clear indication that the initial Li concentration or temperature influences the peak height of the NaCl peaks, but there is a slight tendency towards a higher intensity of the NaCl peaks at lower temperatures. This is rationalised by a reduced solubility of NaCl at lower temperatures and slower growth of the carbonate crystals. The comparison between the lithium carbonate peak intensities of washed (Figure 4.5a) and non-washed samples (Figure C.1) precipitated with CO_2 reveal higher Li peak intensity for washed samples and lower NaCl peak intensity, which proves that the washing significantly

improves the quality of the final product.

The XRD of lithium carbonate heterogeneously precipitated at 25 °C and low initial Li concentration (3-5 g/L; laboratory) reveal higher intensities than those of lithium carbonate obtained from high initial Li concentration (8-12.3 g/L). At high temperature a higher initial Li concentration is needed to obtain a crystalline product. Although halite is identified by XRD in all the precipitates, no halite is observed in the SEM, indicating that (1) the grains are too small to be observed; (2) the halite content is so small that this phase is overlooked; or (3) halite was dissolved during sample preparation.

It is known that the size and the shape of precipitated lithium carbonate crystals are affected by the stirring speed, reaction temperature, the grade of supersaturation and by the CO_2 flow rate (Sun et al., 2012; Zhou et al., 2014; Han et al., 2020). By keeping both the CO_2 flow rate and the stirring speed constant we are able to evaluate the effect of temperature and the initial Li concentration. In general, flake-like crystals are found (Figure 4.5b-g) in line with smaller particles of less than 5 µm, whereas heterogeneous precipitation leads to fewer bigger particles up to 30 µm (Figure 4.5) at 50 °C. Han et al. (2020) find that higher reaction temperatures favour larger particles as the nucleation takes place earlier promoting crystal growth which is confirmed by our results. With increasing precipitation temperature, the crystal size increases significantly (Han et al., 2020) from a maximum particle size of ≈ 25 µm at 25 °C to ≈ 55 µm at 50 °C at 10 g/L Li concentration, similar to the inhomogeneity of the size distribution. The smaller particles are more homogeneously distributed which is also confirmed by findings of Zhou et al. (2014). The washing step has no influence on crystal size (Figure C.2). With increasing Li concentration, a slight increase in particle size is detected during heterogeneous precipitation. At high Li concentration, the particle size distribution appears more inhomogeneous in both laboratory and on-site experiments. For homogeneous precipitation, a slight decrease in particle size is found from an average crystal size of ≈ 15 µm at 5 g/L to ≈ 8-10 µm at 10 g/L (50 °C).

Purity and recovery

The highest purity of nearly technical grade (99 %) Li_2CO_3 was reached with homogeneous precipitation at 3 g/L Li concentration. This is the result of adding the stochiometric amount of soda ash to the starting solution (with a ratio of $[CO_3]/[Li] = 0.5$). In contrast, the $[OH]/[Li]$ ratio for heterogeneous precipitation varied from 1.7 (12.3 g/L Li concentration) to 7.1 (3 g/L Li concentration) due to NaOH buffering. This means that the solution is in excess of NaOH and therefore more halite is precipitated (Figure 4.4). Battaglia et al. (2022) report purity values near 100 % with a similar approach at 50 and 80 °C and 4 g/L Li and $[OH]/[Li]$ ratios between 1 and 4. We attribute this to the centrifuging processing step which was applied in this study instead of filtering. During centrifuging, the supernate is removed manually. If the centrifuging step is not sufficient, precipitate loss could occur by removing the supernate. Moreover, at higher temperatures, the lithium carbonate solubility is decreased which is clearly one reason for reaching higher purity at 50 °C experiments (Figure 4.4). At low initial Li concentration (3 and 5 g/L Li at 25 °C and 3 g/L at 50 °C, respectively), the initial Li concentration has an effect on purity which in these cases does not exceed 55 %. This indicates that the temperature (and therefore solubility of lithium carbonate) has less effect on purity than the initial Li concentration.

The washing step with milli-Q water increases the purity (Figure 4.4) as halite is partly dissolved. This results in an average increase in Li_2CO_3 purity of ≈10 percentage points from washed to non-washed samples. Similar findings are reported by Battaglia et al. (2022), where the washing step is conducted with ethanol. The increase in purity due to washing is higher than the effect of increasing temperature and initial Li concentration. However, as also noticed by Battaglia et al. (2022), the washing step causes a loss of Li_2CO_3 recovery between 0.2-8.1 percentage points by dissolution.

The recovery is the highest during homogeneous precipitation at 8-12.3 g/L initial Li concentration reaching a value of up to 53.4 %. This is significantly lower than the recovery in experiments by Han et al. (2020) who reached more than 70 % recovery, at an initial Li concentration of 20 g/L. However, our results are in line with those of Battaglia et al. (2022), who reached around 60 % at a comparable initial Li concentra-

tion of 4 g/L at 50 °C. For both homogeneous and heterogeneous precipitation, there is a slight trend towards decreasing recovery with decreasing Li concentration: When more Li is present, the reaction leads to a higher recovery of up to 32 % at 12.3 g/L Li concentration and 50 °C. These values are slightly lower than the recovery of Han et al. (2020), who reached up to 45 %, but at a much higher Li concentration of 20 g/L. This could be attributed to either the grade of supersaturation of Li ions within the initial solution or to differences in the experimental arrangement when utilising centrifugation rather than filtration. Some precipitate may have been lost during manual removal of the supernate.

According to Sun et al. (2012) and Battaglia et al. (2022), temperature is the most significant variable affecting recovery. However, as the solubility of CO_2 in aqueous salt solutions decreases with increasing temperature, and as the process presented in this study is intended to be implemented within the reinjection line of a geothermal power plant (which is typically at around 60 °C; Fechner et al., 2022), the temperatures were chosen accordingly. Clearly, for the potential implementation of such a system at a later stage, a trade-off between initial purity and recovery needs to be found and thus temperature and Li concentration adjusted in such a way that further purification steps could be introduced at a later stage.

4.4.2. Assessment of the utilisation of geothermal CO_2 for the precipitation of lithium carbonate

The precipitates in the on-site experiments have the same composition, grain shape, grain size and grain size distribution as precipitates in the laboratory experiments (Figure 4.5). The recovery efficiency of the on-site experiments (Table 4.3) is similar to the experiments under the same conditions in the laboratory (Table 4.2). The purity of the precipitates from the on-site experiments with 84.4 and 93.3 % at 5 g/L and 10 g/L Li concentration, respectively, are only slightly lower than the results obtained with the laboratory set-up (88.3 and 94.8 %) (Figures 4.3b and 4.4). Other components besides NaCl (Table 4.3) amount to a maximum of 1.2 wt-%. Zinc and Fe originate at least partly from corrosion of the tubing (Eggeling et al., 2018). It is noticeable that the

level of the two elements is elevated in the experiment at 5 g/L Li concentration (V-Bru-1) carried out before V-Bru-2 (Table 4.3). At this point there were still more rust particles in the pipeline outlet at the gas bypass, which were flushed into the solution along with the CO_2. The implementation of a filter could offer a suitable solution for this issue. The other elements are from the brine, which are in the gas most likely due to slugs of brine sometimes passing the bypass. With the implementation of filters, at least the amount of the rust particles could be diminished. The other components could be reduced when optimising the gas bypass to have fewer brine slugs passing through.

The on-site experiments show that the natural gas stream from the Bruchsal power plant (containing mainly CO_2; Table 4.1) can be used in the same way as pure CO_2 used in the laboratory. Utilising the abundant, natural CO_2 instead of soda ash to precipitate lithium carbonate could be a viable option. Moreover, no need for gas purification opens up the possibility of utilising CO_2 from other industrial processes as well and provide a new sink for anthropogenic CO_2. One advantage would be the reduction of the CO_2 footprint and the positive impact on the environment for both the product and the industrial process as the source of the CO_2 used. However, a realistic assessment of transportation options and associated costs would be necessary to evaluate the feasibility of the proposed approach, as transport expenses may potentially offset the benefits of the strategy.

Further enhancement of the process will be automatising the addition of LiCl solution, NaOH and also CO_2, which can possibly be injected by an appropriate sparger system. The addition of NaOH will be adjusted by continuous addition rather than varying the volume of added NaOH when monitoring the pH, and therefore the recovery could be potentially increased. In that case as well as in the case of this study, further purification of the lithium carbonate is needed. A further step to be investigated is the addition of a different hydroxide to the LiCl solution for pH adjustment having the potential to impede the formation of chloride (i.e., LiOH with negligible additional impurities and no impact of NaCl). This will partly solve the purification problem. However, this could lead to a considerable increase in the cost of the process, as LiOH currently accounts to 80 times the cost of NaOH. In addition to that,

conventional purification steps, such as are listed in Yi et al. (2007) can be applied to the process, where the precipitated lithium carbonate is purified by a CO_2-water solution. In this case, further natural CO_2 can be utilised.

4.5. Conclusion of part IV

The precipitated lithium carbonate has a crystalline structure for both the heterogeneous and homogeneous precipitation. Grain shape and size of precipitates from laboratory and on-site experiments are similar. Nevertheless, a slight increase in particle size is observed when increasing temperature and Li concentration. For homogeneous precipitation, a slight decrease in grain size is noticed at a higher initial Li concentration.

The heterogeneous precipitation is strongly pH dependent. Therefore, it is crucial to precisely monitor the proton concentration in the solution. Higher temperature and Li concentration promote the reaction progress, as the lithium carbonate solubility is reduced along with higher collision possibility as more Li ions are abundant to react. The results show that highest purity values are attained for homogeneous precipitation with an almost technical purity for Li_2CO_3 of ≈ 99 % at 50 °C. The purity of heterogeneous precipitation increases with an increasing temperature and higher initial LiCl concentration. Applying a washing step further enhances purity as contaminants are partially dissolved. However, recovery is decreased slightly as minor amounts of lithium carbonate are also dissolved. A high recovery is reached for homogeneous and heterogeneous precipitation experiments at high initial Li concentration. For heterogeneous precipitation experiments, additionally to the aforementioned, a high temperature improves the recovery.

The experiments of this study reveal that CO_2 of a geothermal power plant or other industrial CO_2 can be used to precipitate lithium carbonate. The heat of the geothermal plant can be used to additionally heat the initial LiCl solution. Further purification steps have to be investigated along with optimising the recovery. To enhance the purity, the washing step could be improved as well as other hydroxides could be used to impede halite precipitation. Recycling of the residual LiCl solution could be one

option, to increase recovery. Utilising CO_2 to recover lithium would be sustainable since CO_2 is captured, which otherwise may be released to the atmosphere. By using CO_2 from other industrial processes, an improvement of the CO_2 footprint could be achieved, whereby realistic considerations of the potential transport, its CO_2 impact and transport costs should be considered in detail.

Part V.

Implications and perspectives

Chapter 5.

Major outcomes, conclusion and perspectives

5.1. Major outcome for research

Part II One origin of CO_2 in reservoir rocks is the decomposition of carbonate rocks (Berner and Caldeira, 1997; Mortimer and Müller, 2010). An intensive investigation in carbonate bearing reservoir rocks of the Büyük Menderes Graben (Turkey) proves the local nappe geometry which can be applied to the geological model of future geothermal projects. This multi-proxy approach may be applicable to all graben structure-related systems and can serve as a means of comprehending the graben setting and integrating it into a conceptual model. Regarding the investigated setting of the Büyük Menderes Graben, from bottom to top these nappes are named Bayındır, Bozdağ, Çine and Selimiye.

According to geochronological investigation (Rb-Sr data) ductile deformation in both the Bayındır and Selimiye nappes at upper-crustal temperatures and considerable depth is estimated at 30 Ma. Furthermore, the formation of the extensional graben structure is deduced to < 30 Ma. Both, stable (C, O and Sr) and radiogenic (Rb-Sr) isotope data are modified by hydrothermal alteration. An intense multi-proxy approach of petrographical and geochemical features can be applied to better characterise reservoir rocks by comparing them to well-known surface analogues.

Part III For CO_2 handling in binary geothermal systems, three different options were simulated and recommended to be used at different brine properties and operational conditions at the surface. These are (1) a gas bypass to minimise accumulation of non-condensable gases in the heat exchanger, (2) pressure maintenance to keep the gases dissolved in the brine above the gas breakout pressure, and (3) in addition to (2) an implemented CO_2 turbine to generate power with the bypassed CO_2.

For a simulation of surface installations, it is of major importance to very well fit the thermodynamic models on experimental data at condition ranges of interest, especially for CO_2 solubility models. If the simulation is to be performed at operational pressures much higher than at atmospheric pressure (i.e., higher than five bar(a)), then a usual calculation for CO_2-solubility based on Henry's law is not sufficient anymore. It is suggested to use an (derivative of) equation of state and fit the CO_2 model on sufficient experimental data within the relevant condition ranges. The model ELECNRTL often used and implemented in the software ASPEN Plus, overestimates the CO_2 solubility because of a poor model fit to an insufficient amount of experimental data and thus should be checked before its use. Therefore, a best practice suggestion is using the model of Duan et al. (2006) or later derivatives to calculate basic gas breakout pressure estimations. For more detailed calculations, a verification of respective model constraints and the quantity and quality of its data base is recommended.

When determining the solubility of gases in brine, it is adequate to perform calculations based on the solubility of CO_2 if the concentration of CO_2 represents more than 90 vol-% of the total gas amount. Furthermore, if NaCl is the major component of the total dissolved solids in the brine, NaCl equivalents ($NaCl_{eq}$) can be used for thermodynamic and solubility calculation. To simulate CO_2 handling in geothermal systems the sensitive parameters system pressure, (production) temperature, gas content and gas composition, salinity, as well as brine and working media flow rate are identified.

Part IV The precipitation experiments demonstrate that CO_2 of a geothermal power plant can be used to precipitate lithium carbonate. If using NaOH for pH buffering, a by-product is halite. As CO_2 is abundant within most geothermal brines, the recovery

of lithium (in several process steps before being extracted from the geothermal brine) would be sustainable since CO_2 is captured and nearly no further chemicals are used. Since the rate at which CO_2 is injected into the LiCl solution is slow, it is assumed that capturing only a portion of the CO_2 stream will not significantly affect the primary geothermal reservoir conditions at Bruchsal (Germany). Additionally, the heat of the geothermal plant can be used to heat the initial LiCl solution. Despite the fact that the gas used in the geothermal power plant is not pure CO_2, the amount of other components in the precipitate are small.

A further finding is that the heterogeneous precipitation with CO_2 is dependent on pH, temperature and the initial lithium concentration of the LiCl solution. If a washing step is applied the purity increases but the recovery decreases because of partial loss of precipitated Li_2CO_3. These different sensitive parameters have to be studied in detail to optimise the laboratory study and as a further step implement a pilot plant on-site.

5.2. Major outcome for industrial exploitation

Part II In part II, a second deeper reservoir is identified within the Büyük Menderes Graben that is made of Cretaceous marble, which has the potential to provide higher reservoir temperatures for geothermal energy projects and improve their economic efficiency. A better understanding of the characteristics of the reservoir has been gained by applying a multi-proxy approach to compare drilled reservoir sections to surface analogues of graben structures. This new knowledge has the potential to significantly impact the future industrial exploitation of geothermal energy in the area, both in terms of drilling campaigns and the upscaling of existing sites. There is a trade-off to consider when it comes to geothermal energy projects in this area: higher drilling costs may result in higher reservoir temperatures, but lower drilling costs could result in lower reservoir temperatures at the same flow rate.

Part III Managing CO_2 in binary geothermal systems at surface installations is crucial for achieving nearly zero emissions and maximising thermal or power output.

To select an appropriate technical CO_2 handling solution, it is important to conduct down hole sampling of the future production well to determine the nearly undisturbed gas content, composition, and salinity of the brine. Intense hydraulic testing is also necessary to determine potential flow rates and production temperatures for plant design. For binary geothermal systems, technical CO_2 handling solutions are recommended at the planning stage of a plant (such as a district heating or power plant) when all wells have been drilled and the properties of the brine (such as total dissolved solids/salinity, gas composition, and gas/fluid ratio), potential production temperature and flow rate are known.

Based on these recommendations, a suitable technical handling solution can be chosen, although it must be validated and simulated for specific plant conditions and future plant design. At moderate to high gas content (5-20 g/L) and medium production temperature (around 120°C), a gas bypass installed at the feedline that bypasses the heat exchangers is the most suitable option. At low gas content (0-5 g/L) and low salinity (0-100 g/L) of the brine system, pressure maintenance is the preferred solution for heat or power production. In situations where the gas content is moderate to high (5-20 g/L) and the production temperature is higher (140-160°C), incorporating a gas bypass with an additional CO_2 turbine can be a viable option. This approach can yield a power output that is more than 8.5 times higher than that of pressure maintenance or a gas bypass by itself.

Part IV Geothermal energy utilisation can potentially be enhanced and its economic viability increased by implementing a lithium extraction plant, depending on the lithium content of the brine and the future developments of lithium extraction technology. Using geothermal CO_2 to precipitate Li_2CO_3 out of a lithium-rich solution is one option to further exploit the favourable conditions at a geothermal plant. Further research on sorbents is necessary, as well as the development of specialised processes for each type of brine, as it has been demonstrated that sorbents that work for South American brines may not be effective for geothermal brines with lower salinity (Stringfellow and Dobson, 2021a; Stringfellow and Dobson, 2021b). Moreover, the precipitation step must be optimised regarding purity and recovery of the product.

The next step in this research would be a more detailed laboratory study, followed by the construction of a pilot plant. Despite the challenges that need to be overcome, this is a topic that is worth pursuing for industrial players in the geothermal industry.

5.3. Conclusion and perspectives

To decarbonise the energy and heat sector, a remarkable increase in geothermal power and heat generation is needed (Bracke et al., 2021). With its exceptional potential, the expansion of geothermal energy utilisation must be greatly intensified to reach the ambitious goals set by the European Commission until 2050 (European Commission, 2019).

The development of a geothermal project requires a strong combination of different multidisciplinary expertise. During the first phase of a project, it is essential to minimise the exploration risk. This is achieved by combining various exploration techniques. Besides geophysical exploration methods (i.e., seismic, gravity or magnetic surveys), it is important to include existing and new structural geological data combined with geochemical data of reservoir rocks. Integrating all these techniques into a joint interpretation leads to the development of a preliminary conceptual model, which can be refined into a reservoir model. Based on this, the first drilling can be planned and carried out. The previously collected data and subsequently established models can be calibrated and validated by additional information gained through the drilling process. In this study, part II demonstrates that a detailed structural understanding of local geology is indispensable. Geochronological aspects are useful to better understand the structural geological situation which is important for further geothermal field development. Standard petrographical features and geochemical investigation (major and trace geochemistry) as well as the C and O stable isotopic signature can represent a useful tool comparing well-known surface analogues and reservoir rock samples.

By expanding the applied methodological multi-proxy approach, i.e. throughout further petrographical or geochemical features, unforeseen opportunities open up when characterising new reservoirs. A theoretical CO_2 content can be calculated

based on the geochemical investigation on carbonate content of the reservoir rock assuming the fluid is CO_2 saturated. This will support estimating the CO_2 content of the future brine which can be used as a working basis for geothermal exploration.

A further important step for a geothermal project is the design of a plant, based on a secured reservoir, a well and the brine properties. For the design, an appropriate simulation is mandatory to secure a long-term operation with few incidents. In part III of this study this aspect is supported by recommending different technical solutions to handle various gas contents in binary geothermal systems, focused on the gas CO_2. An option can be chosen according to simulation results for each potential plant design, depending on the input parameters, brine flow rate, production temperature, salinity, gas content and composition of the brine. It is fundamental to know the brine properties beforehand after conducting and evaluating a down hole sampling and hydraulic testing. It is shown that it is crucial to select a suitable CO_2 solubility model for simulation, which can be applied to the relevant condition ranges.

Perspectively, any geothermal project under development should consider the gas content in terms of optimising the operational pressure to be selected for the plant. As different geothermal brines contain different amounts and types of gases, it is important that further fundamental research is performed on the solubility of gases in different brines to gain more experimental data on CO_2 solubility within the relevant condition ranges of pressure, temperature, salinity and CO_2 content. This experimental data archive should be extended by studying more complex systems than only CO_2-NaCl-H_2O but more different complex salt systems and various gases, such as CH_4 and CO_2 - as rare modelling and even less experimental data exist on combined CH_4-CO_2 solubility in complex brine systems at relevant condition ranges. Relevant data ranges would be represented by higher salinity than seawater conditions at suitable intervals, temperatures between 100-180 °C, low pressures up to 50 bar(a) at suitable intervals and different gas contents between 5-25 g/L of the two gases CH_4-CO_2.

In addition, to handle the CO_2 of geothermal brines, it is also possible to utilise part of the gas. This side-product could raise the economic viability of a geothermal plant. It is already applied at some plants by extracting the gas for the beverage industry (DiPippo, 2012) or by mineralisation (Carbfix and Sulfix projects; Aradóttir et al.,

2015a; Aradóttir et al., 2015b; Gunnarsson et al., 2015; Júliusson et al., 2015). In part IV of this study, a totally novel possibility to use the CO_2 of geothermal brines was tested.

In combination with lithium extraction of geothermal brine, this process can represent one of the last steps within the whole lithium extraction process. After selectively extracting the lithium, it is tested, to precipitate lithium carbonate with geothermal CO_2 out of a synthetically prepared LiCl solution. This heterogeneous precipitation is possible, however, optimisation steps should be performed.

It is crucial to precisely monitor the pH. Besides higher temperatures than 50 °C, different initial Li concentration, and other hydroxides for pH buffering should be tested in future works to increase the purity and recovery of the process. A washing step with milli-Q water was applied and revealed higher purity, but at the same time decreased the recovery. Enhancing this washing step by applying another washing solution or modifying this process step could optimise the overall process. As a synthetically prepared LiCl solution was used in these experiments, a further step would be to heterogeneously precipitate lithium carbonate out of a LiCl solution actually coming from a lithium extraction process from geothermal brine - which means it should function as one of the last steps in a lot of process steps to extract the lithium inherent in the natural brine system and produce it in a usable form.

Appendices

Appendix to part II

Table A.1.: Results of major, trace and REE elements (ICP-MS/OES). c: Cretaceous; p: Paleozoic.

#		1	2	3	5	6	8	9	10	11	12	13	14	15	16	17
name		T1	T3	T4	T11	T13-1	T13-3	T13-4	1-1050	2-1065	3-1290	4-1325	5-3655	6-3680	7-3740	8-3865
category		c	c	c	c	p	p	p	well^S	well^S	well^S	well^S	well^D	well^D	well^D	well^D
oxides of major elements																
SiO_2		n.a.	n.a.	n.a.	n.a.	n.a.	n.a.	n.a.	n.a.	n.a.	n.a.	n.a.	n.a.	n.a.	n.a.	n.a.
TiO_2		n.a.	n.a.	n.a.	n.a.	n.a.	n.a.	n.a.	n.a.	n.a.	n.a.	n.a.	n.a.	n.a.	n.a.	n.a.
Al_2O_3	wt-%	0.043	0.017	0.221	0.440	0.036	0.871	0.035	0.718	0.325	2.782	3.160	12.104	7.644	13.073	17.231
$Fe_2O_{3\,tot}$	wt-%	0.126	0.073	1.340	0.283	0.090	0.743	0.067	0.870	0.374	1.665	1.753	3.190	2.036	2.569	1.389
MnO	wt-%	0.013	0.042	0.148	0.019	0.016	0.045	0.011	0.039	0.013	0.104	0.067	0.058	0.039	0.040	0.023
MgO	wt-%	1.520	0.402	6.201	0.555	2.949	18.943	1.184	2.500	0.979	0.904	1.084	2.063	1.013	0.936	0.362
CaO	wt-%	56.458	57.319	47.216	52.317	53.340	32.843	58.975	52.526	43.813	36.346	42.176	8.278	13.470	6.521	4.207
Na_2O	wt-%	0.007	<0.0027	<0.0027	<0.0027	0.020	<0.0027	<0.0027	<0.0027	<0.0027	0.061	0.129	3.233	1.619	3.079	3.603
K_2O	wt-%	<0.0024	<0.0024	<0.0024	<0.0024	<0.0024	<0.0024	<0.0024	<0.0024	<0.0024	0.008	0.029	1.239	0.979	2.520	4.776
P_2O_5	wt-%	0.0035	0.0050	0.0180	0.0030	0.0193	0.0505	0.0267	0.0150	0.0095	0.0133	0.0761	0.1662	0.0671	0.2007	0.1416
CO_{2-calc}	wt-%	45.968	45.422	43.826	41.664	45.081	46.459	47.576	43.953	35.454	29.511	34.283	8.749	11.677	6.140	3.697
totals	wt-%	104.138	103.280	98.970	95.281	101.551	99.955	107.876	100.621	80.967	71.394	82.759	39.081	38.544	35.078	35.429
trace elements																
Li	mg/kg	0.52	0.86	1.01	0.52	1.06	17.82	0.28	5.77	2.56	14.77	11.03	24.61	17.64	12.80	12.12
B	mg/kg	<0.43	<0.43	<0.43	<0.43	<0.43	<0.43	<0.43	0.84	2.03	<0.43	<0.43	<0.43	<0.43	<0.43	<0.43
P	mg/kg	15.22	21.83	78.68	13.11	84.17	220.26	116.62	65.30	41.64	58.15	332.08	725.31	292.80	875.71	617.96
Sc	mg/kg	0.27	0.35	0.30	0.68	0.11	0.79	0.14	1.35	0.82	3.71	5.05	6.96	4.76	5.54	3.39
V	mg/kg	3.29	0.58	2.60	4.07	1.32	13.04	1.48	5.30	3.02	20.87	34.93	56.23	35.04	38.43	21.46
Cr	mg/kg	2.02	0.87	1.72	13.54	0.57	9.05	0.98	4.52	1.93	15.56	38.39	44.58	29.00	25.87	9.70
Co	mg/kg	0.40	0.34	1.16	0.55	0.36	2.69	0.31	0.80	0.88	2.44	2.25	7.26	5.66	7.27	3.41
Ni	mg/kg	1.11	0.52	2.39	1.38	0.50	3.49	0.77	3.20	1.55	4.91	5.39	18.79	16.45	18.19	5.84
Cu	mg/kg	<0.03	<0.03	<0.03	<0.03	<0.03	<0.03	<0.03	0.51	0.88	2.75	31.83	45.42	8.84	11.88	10.69
Zn	mg/kg	<0.29	<0.29	<0.29	<0.29	<0.29	6.61	<0.29	4.51	11.19	5.39	12.73	35.46	22.27	21.51	40.03
As	mg/kg	1.72	0.35	0.39	0.97	0.29	1.19	0.76	1.16	0.42	0.43	1.01	0.99	0.54	0.67	1.15
Rb	mg/kg	0.282	0.111	1.647	3.947	<0.003	7.906	0.078	3.484	2.158	18.226	18.220	64.651	53.232	76.129	84.484
Sr	mg/kg	237.719	217.882	281.209	351.189	177.977	113.918	243.060	776.135	453.790	1808.443	2274.601	239.123	455.105	208.214	261.329
Y	mg/kg	3.641	7.707	8.405	4.198	1.982	3.937	2.680	9.833	6.291	13.988	13.567	17.939	11.426	20.421	13.644
Cd	mg/kg	0.199	0.234	0.178	0.271	0.132	0.150	0.159	0.583	0.353	0.065	0.050	0.092	0.066	0.035	0.204
Cs	mg/kg	0.021	0.021	0.156	0.303	0.046	0.281	0.034	0.181	0.135	0.714	0.602	3.865	1.708	2.268	1.444
Ba	mg/kg	4.41	17.79	55.63	13.37	7.29	57.02	5.68	26.34	10.00	36.76	31.84	1011.61	292.89	627.09	1844.69
Pb	mg/kg	1.60	0.65	3.15	2.75	0.58	0.97	0.85	3.48	1.71	6.74	4.77	8.50	7.61	13.34	42.36
Th	mg/kg	0.11	0.07	0.29	0.55	0.07	1.08	0.08	0.71	0.27	2.24	3.11	9.10	8.58	12.50	10.71
U	mg/kg	3.817	0.110	1.953	0.363	1.632	0.662	1.697	0.631	0.244	1.108	1.900	1.941	1.471	1.260	0.798
rare-earth elements																
La	mg/kg	1.45	4.58	2.67	2.01	0.72	2.76	1.05	5.44	2.71	9.51	17.01	22.88	16.48	27.50	25.82
Ce	mg/kg	1.26	4.86	5.69	3.37	0.86	4.14	1.36	7.15	2.55	18.25	30.99	48.01	33.40	58.55	53.05
Pr	mg/kg	0.270	0.898	1.020	0.484	0.148	0.650	0.220	1.157	0.534	2.313	3.763	5.853	4.103	7.062	6.050
Nd	mg/kg	1.099	3.891	4.696	1.930	0.592	2.624	0.875	4.758	2.175	9.357	14.632	22.711	15.762	27.071	22.527
Sm	mg/kg	0.215	1.042	1.073	0.417	0.119	0.517	0.163	0.971	0.446	2.034	2.724	4.576	2.946	5.409	4.313
Eu	mg/kg	0.052	0.620	0.310	0.103	0.032	0.104	0.039	0.238	0.110	0.486	0.567	0.993	0.639	0.975	1.441
Gd	mg/kg	0.277	1.231	1.214	0.482	0.167	0.549	0.221	1.147	0.552	2.218	2.629	4.465	2.738	5.082	4.065
Tb	mg/kg	0.046	0.186	0.179	0.080	0.027	0.084	0.035	0.184	0.089	0.369	0.401	0.664	0.391	0.747	0.565
Dy	mg/kg	0.297	0.944	0.988	0.451	0.182	0.488	0.229	1.142	0.583	2.264	2.290	3.471	2.098	3.877	2.819
Ho	mg/kg	0.071	0.170	0.189	0.095	0.047	0.102	0.056	0.253	0.136	0.464	0.466	0.641	0.395	0.749	0.499
Er	mg/kg	0.207	0.417	0.482	0.283	0.137	0.309	0.177	0.737	0.409	1.338	1.375	1.737	1.095	2.025	1.228
Tm	mg/kg	0.028	0.049	0.056	0.042	0.020	0.043	0.025	0.099	0.056	0.186	0.192	0.239	0.147	0.269	0.147
Yb	mg/kg	0.176	0.289	0.320	0.241	0.124	0.284	0.166	0.638	0.356	1.184	1.227	1.536	0.963	1.636	0.835
Lu	mg/kg	0.028	0.038	0.046	0.036	0.022	0.045	0.027	0.095	0.054	0.177	0.178	0.233	0.141	0.238	0.115
rare-earth elements ratios and anomalies																
Y/Ho	-	51.1	45.4	44.5	44.0	42.1	38.6	48.0	38.8	46.2	30.1	29.1	28.0	28.9	27.3	27.3
Ce/Ce*	-	0.55	0.68	0.74	0.80	0.68	0.74	0.71	0.73	0.56	0.92	0.93	0.92	0.90	0.92	0.94
Pr/Pr*	-	1.27	1.16	1.10	1.10	1.18	1.14	1.16	1.14	1.26	1.04	1.04	1.04	1.05	1.04	1.03
Eu/Eu*	-	0.99	2.54	1.27	1.07	1.05	0.91	0.93	1.05	1.02	1.07	1.00	1.03	1.06	0.87	1.62

Appendix to part III

Solubility calculation

The formulae (B.1) and (B.2) represent the polynomial equations for six different salt concentrations ($NaCl_{eq}$ of 0 g/L, 50 g/L, 100 g/L, 120 g/L, 150 g/L, 200 g/L) and two different temperature ranges (20-100 °C and 100-220 °C) for each concentration (Table B.3), with the variables temperature and pressure. Table B.1 shows the polynomial coefficients of the solubility calculation. The temperature range is from 20 °C to 220 °C and the pressure range extends from 2 bar(a) to 50 bar(a). For option 2 the simulation points which are outside the pressure range were calculated directly by Duan et al. (2006) and were implemented as value.

$$x_{CO_2} = (a_1 + a_2 * p + a_3 * T + a_4 * p^2 + a_5 * p * T + a_6 + T^2 + a_7 * T * p^2 + a_8 * p * T^2 + a_9 * T^3) * m_{total} \tag{B.1}$$

$$x_{CO_2} = (a_1 + a_2 * p + a_3 * T + a_4 * p^2 + a_5 * p * T + a_6 * T^2 + a_7 * T * p^2 + a_8 * p * T^2 + a_9 * T^3 + a_{10} * T^2 * p^2 + a_{11} * p * T^3 + a_{12} * T^4) * m_{total} \tag{B.2}$$

Thermal water composition

The Table B.2 shows the composition of thermal water according to analyses of recent samplings.

The varied compositions which were used for every option in the simulation are listed in the Table B.3. The density for the calculation of wt-% from g/L was set to

Table B.1.: Polynomial coefficients of equations B.1 and B.2 for the solubility calculation of various salt concentrations and temperature ranges. *was calculated with equation B.2.

Salt	T	a_1	a_2	a_3	a_4	a_5	a_6
0	20-100	9.714	0.08926	-0.07338	$-9.624 * 10^{-5}$	-0.000374	0.000186
0	100-200	39.32	0.4305	-0.3511	-0.0007839	-0.002175	0.001042
50	20-100	9.327	0.07131	-0.06979	$-6.197 * 10^{-5}$	-0.0002942	0.0001752
50	100-220	31.4	0.3497	-0.2802	-0.0006585	-0.001758	0.000831
100	20-100	7.65	0.05933	-0.05727	$-4.309 * 10^{-5}$	-0.000244	0.000144
100	100-220	25.04	0.2839	-0.2232	-0.0005528	-0.00142	0.0006615
120	100-200	22.86	0.261	-0.2037	-0.0005153	-0.001303	0.0006035
150	20-100	6.26	0.0494	-0.0469	$-2.871 * 10^{-5}$	-0.0002024	0.0001181
150	100-220	19.93	0.2301	-0.1775	-0.0004637	-0.001144	0.0005256
200	20-100	5.11	0.04115	-0.03832	$-1.787 * 10^{-5}$	-0.000168	$9.666 * 10^{-5}$
200	100-220	15.83	0.1863	-0.1408	-0.0003887	-0.0009211	0.0004167
120*	20-100	0.08313	0.1291	0.007207	-0.0003758	$-7.052 * 10^{-5}$	$-5.967 * 10^{-5}$

		a_7	a_8	a_9	a_{10}	a_{11}	a_{12}
0	20-100	$1.74 * 10^{-7}$	$4.358 * 10^{-7}$	$-1.586 * 10^{-7}$			
0	100-200	$2.085 * 10^{-6}$	$2.812 * 10^{-6}$	$1.028 * 10^{-6}$			
50	20-100	$9.394 * 10^{-8}$	$3.442 * 10^{-7}$	$-1.48 * 10^{-7}$			
50	100-220	$1.744 * 10^{-6}$	$2.265 * 10^{-6}$	$-8.195 * 10^{-7}$			
100	20-100	$5.121 * 10^{-8}$	$2.861 * 10^{-7}$	$-1.219 * 10^{-7}$			
100	100-220	$1.458 * 10^{-6}$	$1.822 * 10^{-6}$	$-6.519 * 10^{-7}$			
120	100-200	$1.357 * 10^{-6}$	$1.669 * 10^{-6}$	$-5.946 * 10^{-7}$			
150	20-100	$1.97 * 10^{-8}$	$2.379 * 10^{-7}$	$-1.002 * 10^{-7}$			
150	100-220	$1.217 * 10^{-6}$	$1.462 * 10^{-6}$	$-5.176 * 10^{-7}$			
200	20-100	$3.068 * 10^{-9}$	$1.98 * 10^{-7}$	$-8.22 * 10^{-8}$			
200	100-220	$1.016 * 10^{-6}$	$1.172 * 10^{-6}$	$-4.10 * 10^{-7}$			
120*	20-100	$1.615 * 10^{-6}$	$1.289 * 10^{-6}$	$1.6 * 10^{-6}$	$-1.825 * 10^{-9}$	$-7.215 * 10^{-10}$	$1.436 * 10^{-10}$

1.07 kg/L according to measurements in Bruchsal brine system.

Table B.2.: Measured values for the thermal water in Bruchsal including major salts and gas composition, total gas content and specific heat capacity.

Salt ion		mg/L
Chloride	[Cl]	72,500
Sodium	[Na]	36,800
Potassium	[K]	3,220
Lithium	[Li]	155
Calcium	[Ca]	7,250
Magnesium	[Mg]	340
Strontium	[Sr]	380
Hydrogen carbonate	[HCO_3]	363
Salinity		121,852
Gas		Vol-%
carbon dioxide	[CO_2]	94.5
Nitrogen	[N_2]	3.52
methane	[CH_4]	1.89
Total gas content	NL_{gas}/L_{fluid}	1.9
Specific heat capacity		J/(kgK)
at 124 °C		3.88

Results

Tables B.4 - B.7 show the calculated values for each simulation of each option.

Further visualisation of the results for the specific heat capacity and the thermal power output for the simulated temperatures, flow rates, salinity's and gas contents (Figures B.1 and B.2).

Table B.3.: The different calculated mass compositions in wt-% as simulation input for different simulation runs are listed. With a density of 1.07 kg/L the calculation from g/L to wt-% was performed according to measurements in Bruchsal brine system.

	gas content g/L						wt-%
salt content	0	5	8.5	10	15	20	
0 g/L	0.00	0.00	0.00	0.00	0.00	0.00	salt
	0.00	0.47	0.79	0.93	1.40	1.87	CO_2
	100.00	99.53	99.21	99.07	98.60	98.13	water
50 g/L	4.67	4.67	4.67	4.67	4.67	4.67	salt
	0.00	0.47	0.79	0.93	1.40	1.87	CO_2
	95.33	94.86	94.53	94.39	93.93	93.46	water
100 g/L	9.35	9.35	9.35	9.35	9.35	9.35	salt
	0.00	0.47	0.79	0.93	1.40	1.87	CO_2
	90.65	90.19	89.86	89.72	89.25	88.79	water
120 g/L	11.21	11.21	11.21	11.21	11.21	11.21	salt
	0.00	0.47	0.79	0.93	1.40	1.87	CO_2
	88.79	88.32	87.99	87.85	87.38	86.92	water
150 g/L	14.02	14.02	14.02	14.02	14.02	14.02	salt
	0.00	0.47	0.79	0.93	1.40	1.87	CO_2
	85.98	85.51	85.19	85.05	84.58	84.11	water
200 g/L	18.69	18.69	18.69	18.69	18.69	18.69	salt
	0.00	0.47	0.79	0.93	1.40	1.87	CO_2
	81.31	80.84	80.51	80.37	79.91	79.44	water

Table B.4.: Listing the specific heat capacity, thermal output and power output as results of the simulations of options 1-3. During these simulation runs the parameters salinity and gas content were varied. For all simulations the production temperature, brine and working media flow rate were constant (124 °C, 25 kg/s, 5.6 kg/s). *option 2: calculated minimum pressure for single-phase conditions.

			spec. heat capacity			thermal output			power output		
			option 1	option 2	option 3	option 1	option 2	option 3	option 1	option 2	option 3
salinity	CO_2	pressure	J/(kg K)			kW_{th}			kW_{el}		
g/L	g/L	bar(a)									
0	0	22 (15.00*)	4,239.3	4,242.8	4,239.3	6,084.4	3,564.3	6,084.4	571.7	1,054.8	571.7
50	0	22 (15.00*)	4,072.2	4,073.9	4,072.2	6,046.9	3,546.1	6,046.9	568.3	1,052.4	568.3
100	0	22 (15.00*)	3,903.0	3,904.6	3,903.0	5,981.6	3,525.2	5,981.6	562.7	1,049.6	562.7
120	0	22 (15.00*)	3,835.7	3,837.3	3,835.7	5,943.5	3,516.3	5,943.5	559.5	1,048.4	559.5
150	0	22 (15.00*)	3,734.1	3,735.6	3,734.1	5,867.3	3,501.4	5,867.3	552.9	1,046.4	552.9
200	0	22 (15.00*)	3,563.8	3,566.7	3,563.8	5,694.0	3,472.9	5,694.0	538.3	1,042.6	538.3
0	5	22 (15.23*)	4,237.6	4,240.9	4,239.2	6,067.3	3,576.4	6,067.3	570.0	1,017.5	570.0
50	5	22 (17.19*)	4,069.2	4,070.4	4,070.7	6,027.5	3,920.1	6,023.4	566.5	790.1	566.3
100	5	22 (19.54*)	3,900.8	3,900.2	3,901.8	5,953.0	5,023.7	5,952.7	560.3	619.7	560.2
120	5	22 (20.60*)	3,833.4	3,835.1	3,834.7	5,912.7	5,983.0	5,912.7	556.8	550.8	556.8
150	5	22 (22.36*)	3,732.0	3,731.9	3,733.3	5,837.5	5,854.7	5,837.5	550.6	454.8	550.4
200	5	22 (25.77*)	3,731.9	3,561.6	3,564.8	5,668.2	5,293.9	5,668.2	535.8	334.4	536.2
0	8.5	22 (20.46*)	4,236.5	4,237.4	4,238.0	6,056.7	6,091.1	6,056.7	569.1	424.2	569.1
50	8.5	22 (23.66*)	4,068.5	4,068.7	4,069.7	6,014.2	5,686.2	6,014.4	565.5	324.7	567.9
100	8.5	22 (32.27*)	3,899.5	3,897.5	3,899.5	5,946.8	5,161.2	5,942.8	559.6	237.1	563.1
120	8.5	22 (34.32*)	3,832.2	3,830.1	3,832.2	5,902.8	4,951.2	5,902.4	556.2	206.7	560.6
150	8.5	22 (32.34*)	3,730.5	3,728.3	3,732.9	5,827.0	4,661.6	5,827.0	549.5	166.8	554.8
200	8.5	22 (38.26*)	3,561.2	3,547.9	3,564.5	5,655.2	5,060.6	5,655.5	534.7	144.6	541.1
0	10	22 (28.12*)	4,236.5	4,235.9	4,237.4	6,055.6	5,777.6	6,055.7	569.0	325.3	571.6
50	10	22 (34.20*)	4,069.3	4,066.4	4,069.3	6,012.8	5,171.9	6,012.8	565.4	219.1	570.4
100	10	22 (41.70*)	3,900.8	3,896.4	3,900.8	5,940.1	4,555.5	5,940.1	559.2	138.6	565.6
120	10	22 (40.63*)	3,831.7	3,828.5	3,831.7	5,899.2	4,568.4	5,899.0	555.9	144.9	562.9
150	10	22 (50.80*)	3,732.7	3,726.5	3,732.7	5,822.7	4,015.2	5,822.7	549.1	78.7	557.0
200	10	22 (53.50*)	3,560.2	3,558.0	3,564.1	5,648.8	3,808.9	5,648.7	534.2	62.4	543.2
0	15	22 (42.09*)	4,236.5	4,230.8	4,235.8	6,053.2	4,786.7	6,053.1	568.8	146.4	580.2
50	15	22 (49.69*)	4,067.5	4,060.6	4,076.5	6,011.8	4,306.5	6,007.6	565.2	97.4	578.9
100	15	22 (65.80*)	3,899.9	3,890.1	3,899.9	5,931.6	3,675.0	5,931.6	558.4	24.7	573.7
120	15	22 (72.10*)	3,833.0	3,822.1	3,832.9	5,888.2	3,623.5	5,888.1	554.7	6.6	570.6
150	15	22 (82.80*)	3,732.0	3,719.2	3,732.0	5,806.9	3,400.6	5,806.9	547.8	0.0	564.5
200	15	22 (88.35*)	3,557.1	3,550.9	3,564.1	5,629.4	3,353.0	5,629.4	532.5	0.0	550.4
0	20	22 (57.38*)	4,236.5	4,224.5	4,234.2	6,049.6	4,017.1	6,049.6	568.7	58.7	588.8
50	20	22 (68.93*)	4,066.6	4,055.9	4,066.8	6,001.0	3,677.0	6,001.0	564.4	16.7	587.2
100	20	22 (84.11*)	3,895.9	3,885.4	3,899.0	5,920.2	3,430.8	5,920.0	557.5	0.0	581.6
120	20	22 (91.60*)	3,827.8	3,817.3	3,832.3	5,875.7	3,413.2	5,875.8	553.7	0.0	578.4
150	20	22 (104.91*)	3,725.0	3,714.3	3,731.5	5,791.7	3,386.1	5,791.8	546.5	0.0	572.1
200	20	22 (135.45*)	3,560.2	3,553.7	3,567.0	5,609.0	3,338.9	5,613.2	530.7	0.0	557.7

Table B.5.: Listing the specific heat capacity as a result of the simulations of options 1-3. During these simulation runs the parameters production temperature, brine flow rate and working media flow rate were varied. For all simulations the same composition was used (salinity of 120 g/L, CO_2 content of 8.5 g/L). *option 2: calculated minimum pressure for single-phase conditions.

			flow rate		option 1	option 2	option 3
	pressure bar(a)	temperature °C	brine kg/s	working media kg/s	spec. heat capacity J/(kg K)		
production temperature [°C]							
100	22		25	5.6	3,807.1	3,807.3	3,807.1
120 (124)	22		25	5.6	3,827.4	3,825.7	3,827.4
130	22		25	5.6	3,841.8	3,838.8	3,841.8
140	22		25	5.6	3,859.4	3,854.9	3,859.4
150	22		25	5.6	3,880.4	3,874.2	3,880.4
160	22		25	5.6	3,904.8	3,896.6	3,904.8
brine flow rate [kg/s]							
9	22	124		4	3,832.2	3,830.1	3,832.2
10	22	124		3	3,832.2	3,830.1	3,832.2
15	22	124		5.6	3,832.2	3,830.1	3,832.2
25	22	124		10	3,832.2	3,830.1	3,832.2
50	22	124		10	3,832.1	3,830.2	3,832.2
80	22	124		10	3,832.4	3,830.3	3,832.2
100	22	124		10	3,832.1	3,830.4	3,832.2
25	22(34.32*)	124		5.6	3,832.2	3,830.1	3,832.2
working media flow rate [kg/s]							
3	22	124	10		3,832.2	3,830.1	3,832.2
4	22	124	9		3,832.2	3,830.1	3,832.2
5.6	22	124	15		3,832.2	3,830.1	3,832.2
8	22	124	25		3,832.2	3,830.1	3,832.2
10	22	124	25		3,832.2	3,830.1	3,832.2
15	22	124	25		3,832.2	3,830.1	3,832.2
20	22	124	25		3,832.2	3,830.1	3,832.2
30	22	124	25		3,832.2	3,830.1	3,832.2

Table B.6.: Listing the thermal output as a result of the simulations of options 1-3. During these simulation runs the parameters production temperature, brine flow rate and working media flow rate were varied. For all simulations the same composition was used (salinity of 120 g/L, CO_2 content of 8.5 g/L). *option 2: calculated minimum pressure for single-phase conditions.

			flow rate		option 1	option 2	option 3
	pressure bar(a)	temperature °C	brine kg/s	working media kg/s	thermal output kW_{th}		
production temperature [°C]							
100	22		25	5.6	4,094.4	3,214.5	4,075.1
120 (124)	22		25	5.6	5,705.3	4,705.5	5,684.5
130	22		25	5.6	6,331.7	5,378.6	6,272.4
140	22		25	5.6	6,948.7	5,929.4	6,853.1
150	22		25	5.6	7,334.7	6,498.7	7,207.1
160	22		25	5.6	7,520.8	6,902.1	7,351.6
brine flow rate [kg/s]							
9	22	124		4	2,286.3	2,104.7	2,286.3
10	22	124		3	2,539.2	2,178.4	2,537.4
15	22	124		5.6	3,806.0	3,346.0	3,803.3
25	22	124		10	6,322.1	5,503.0	6,322.1
50	22	124		10	10,575.1	9,122.5	10,567.5
80	22	124		10	10,938.1	10,228.7	10,929.8
100	22	124		10	10,986.5	10,314.9	10,978.7
25	22(34.32*)	124		5.6	5,902.4	4,951.2	5,902.4
working media flow rate [kg/s]							
3	22	124	10		2,539.2	2,178.4	2,537.4
4	22	124	9		2,286.3	2,104.7	2,286.3
5.6	22	124	15		3,806.0	3,345.9	3,803.3
8	22	124	25		6,305.2	5,312.1	6,305.2
10	22	124	25		6,322.1	5,503.0	6,322.1
15	22	124	25		6,331.4	5,829.2	6,331.4
20	22	124	25		6,334.8	6,014.8	6,334.8
30	22	124	25		6,339.0	6,199.2	6,339.0

Table B.7.: Listing the power output as a result of the simulations of options 1-3. During these simulation runs the parameters production temperature, brine flow rate and working media flow rate were varied. For all simulations the same composition was used (salinity of 120 g/L, CO_2 content of 8.5 g/L). *option 2: calculated minimum pressure for single-phase conditions.

			flow rate		option 1	option 2	option 3
	pressure bar(a)	temperature °C	brine kg/s	working media kg/s	power output kW_{el}		
production temperature [°C]							
100	22		25	5.6	393.0	153.7	395.3
120 (124)	22		25	5.6	537.4	200.7	541.5
130	22		25	5.6	587.6	218.5	591.9
140	22		25	5.6	637.1	214.5	646.6
150	22		25	5.6	677.8	237.4	693.2
160	22		25	5.6	701.7	247.6	729.9
brine flow rate [kg/s]							
9	22	124		4	412.7	73.4	225.9
10	22	124		3	243.1	86.3	244.9
15	22	124		5.6	368.6	123.6	371.1
25	22	124		10	615.1	196.0	619.3
50	22	124		10	996.0	383.7	1,004.8
80	22	124		10	1,027.6	438.0	1,041.9
100	22	124		10	1,031.8	442.1	1,050.6
25	22(34.32*)	124		5.6	556.2	206.7	560.6
working media flow rate [kg/s]							
3	22	124	10		243.1	86.3	244.9
4	22	124	9		412.7	73.4	225.9
5.6	22	124	15		368.6	123.6	371.1
8	22	124	25		605.7	204.3	610.3
10	22	124	25		615.1	196.1	619.9
15	22	124	25		643.2	168.1	649.4
20	22	124	25		672.0	133.0	679.4
30	22	124	25		723.0	53.0	732.9

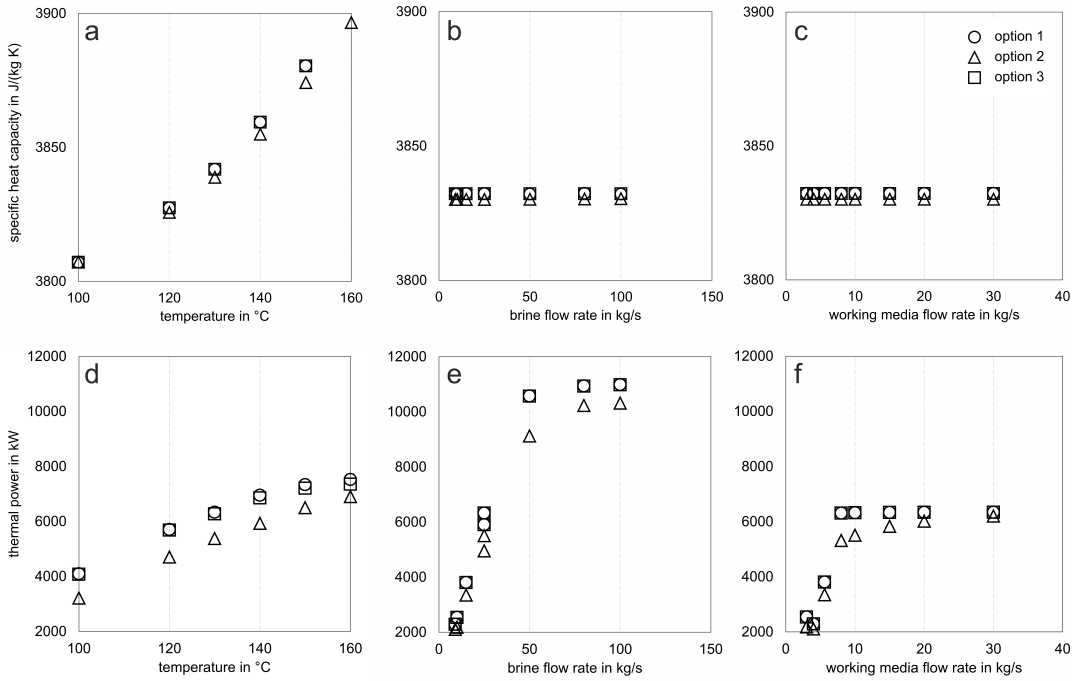


Figure B.1.: Depiction of the simulation results for the specific heat capacity and thermal power of options 1, 2 and 3 (Tables B.5 and B.6). The results for specific heat capacity are shown in a-c by variation of the (a) production temperature, the (b) brine flow rate and the (c) working media flow rate. The results for thermal power are shown in d-f for variations of the (d) production temperature, the (e) brine flow rate and the (f) working media flow rate.

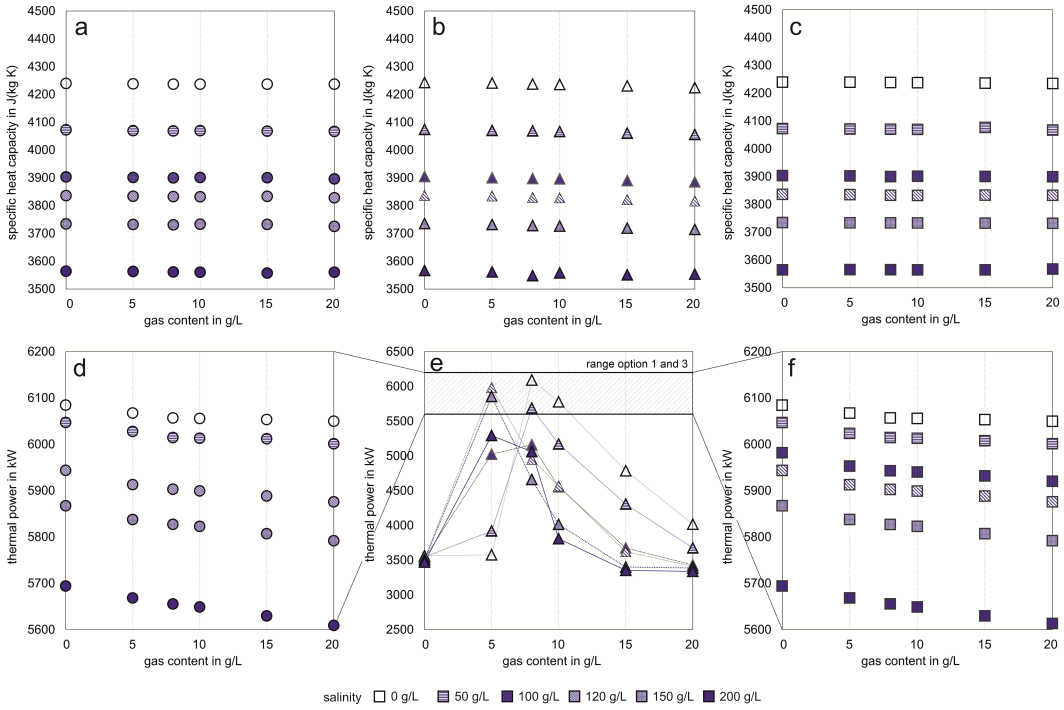


Figure B.2.: Depiction of the simulation results for the specific heat capacity and thermal power of options 1, 2 and 3 at different salinity and gas content (Table B.4). The results for specific heat capacity are shown in (a) option 1, (b) option 2 and (c) option 3. The results for thermal power are shown in (d) option 1, (e) option 2 and (f) option 3.

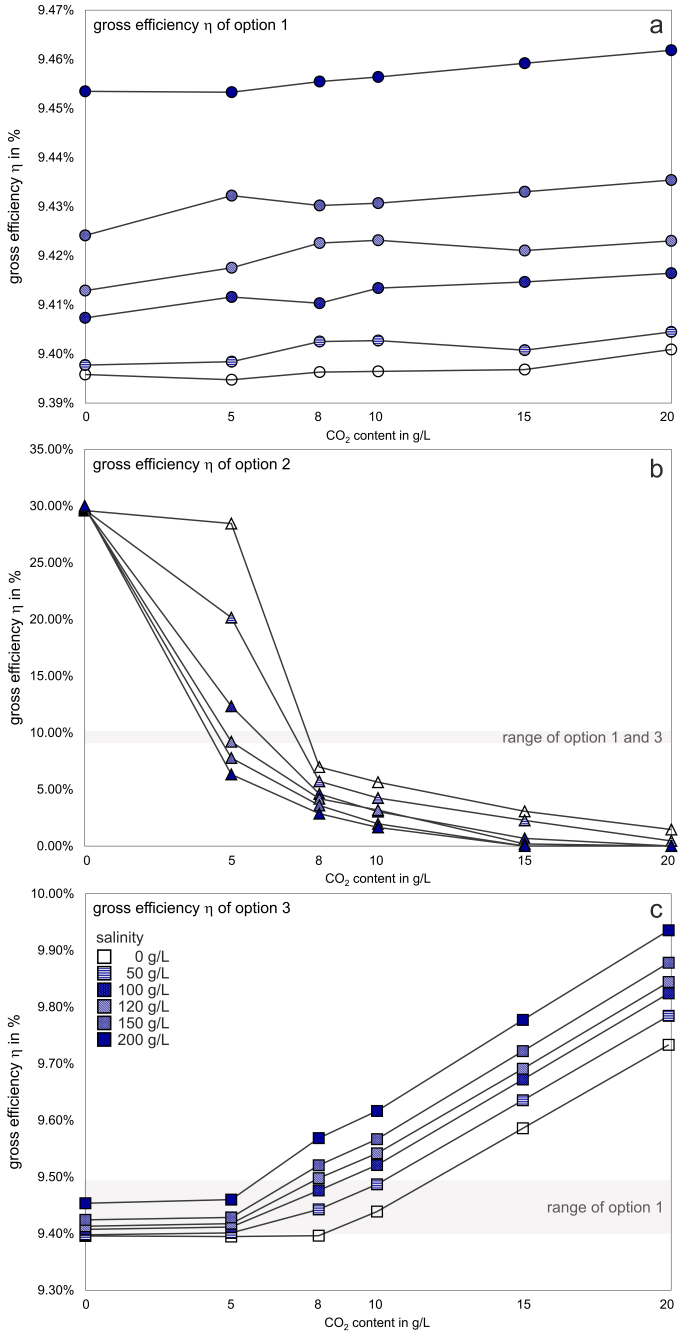


Figure B.3.: Comparison of electrical gross efficiency of (a) option 1, (b) option 2 and (c) option 3.

Appendix to part IV

XRD patterns and SEM images of precipitates

In addition to Figure 4.5a, the XRD patterns as well as the SEM images of precipitates from further experiments are shown in Figures C.1 and C.2.

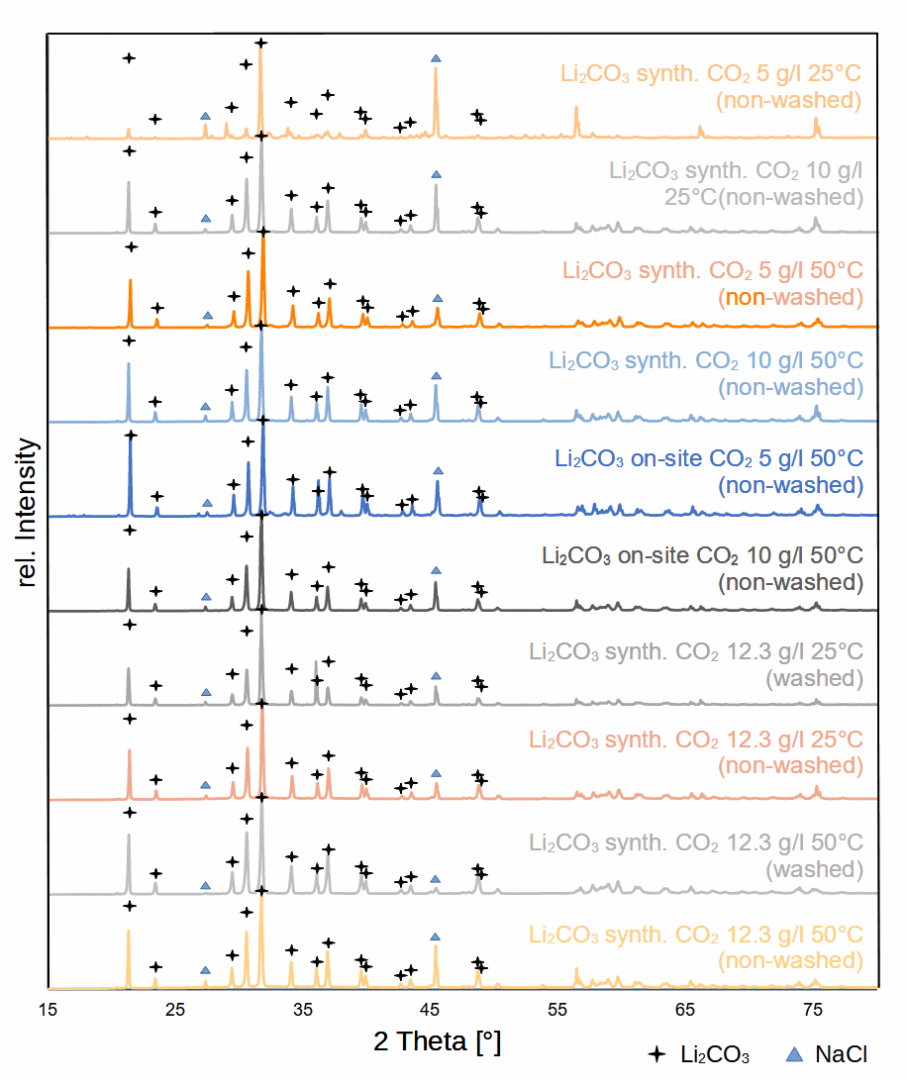


Figure C.1.: Supplementary XRD patterns of (partly washed and non-washed) precipitates (laboratory and on-site experiments) precipitated with CO_2 at different temperatures and Li concentrations.

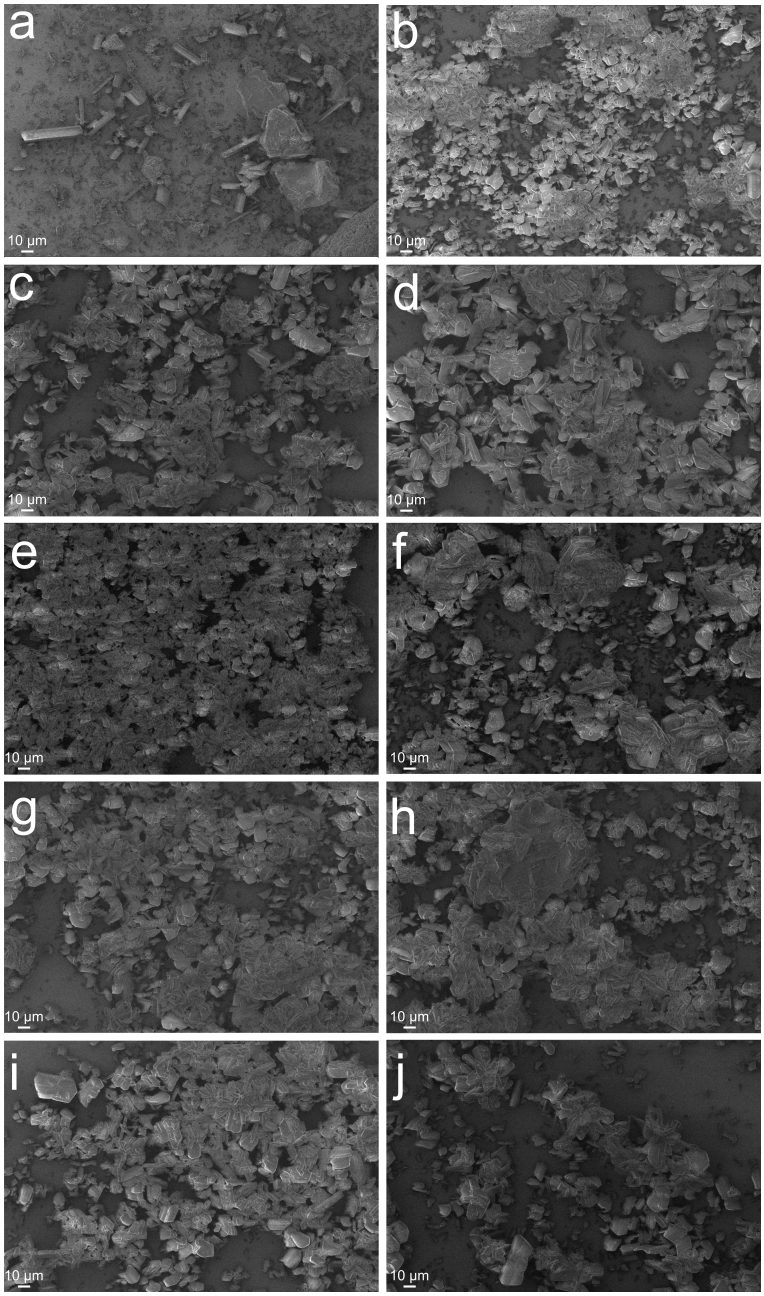


Figure C.2.: SEM image of precipitates at 5 g/l Li concentration at 25 °C using synthetic CO_2 (non-washed) (a); at 10 g/l Li concentration at 25 °C using synthetic CO_2 (non-washed) (b); at 5 g/l Li concentration at 50 °C using synthetic CO_2 (non-washed) (c); at 10 g/l Li concentration at 50 °C using synthetic CO_2 (non-washed) (d); using geothermal CO_2 on-site at 5 g/l Li concentration at 50 °C (non-washed) (e); using geothermal CO_2 on-site at 10 g/l Li concentration at 50 °C (non-washed) (f); using synthetic CO_2 at 12.3 g/l Li concentration at 25 °C (washed) (g); using synthetic CO_2 at 12.3 g/l Li concentration at 25 °C (non-washed) (h); using synthetic CO_2 at 12.3 g/l Li concentration at 50 °C (washed) (i); using synthetic CO_2 at 12.3 g/l Li concentration at 50 °C (non-washed) (j).

Bibliography

Agemar, T., Alten, J.A., Ganz, B., Kuder, J., Kühne, K., Schumacher, S., Schulz, R., 2014. The geothermal information system for germany – geotis. Zeitschrift der Deutschen Gesellschaft für Geowissenschaften 165, 129–144. URL: http://dx.doi.org/10.1127/1860-1804/2014/0060, doi:10.1127/1860-1804/2014/0060.

Agusdinata, D.B., Liu, W., Eakin, H., Romero, H., 2018. Socio-environmental impacts of lithium mineral extraction: towards a research agenda. Environmental Research Letters 13, 123001. doi:10.1088/1748-9326/aae9b1.

Aksoy, N., 2014. Power generation from geothermal resources in turkey. Renewable Energy 68, 595–601. doi:10.1016/j.renene.2014.02.049.

Aksoy, N., Gok, O.S., Mutlu, H., Kılınc, G., 2015. CO_2 Emission from Geothermal Power Plants, in: International Geothermal Association (Ed.), World Geothermal Congress, pp. 1–7.

An, J.W., Kang, D.J., Tran, K.T., Kim, M.J., Lim, T., Tran, T., 2012. Recovery of lithium from Uyuni salar brine. Hydrometallurgy 117-118, 64–70. doi:10.1016/j.hydromet.2012.02.008.

Anwar Ul Haq, R., 2019. Thermodynamics and Precipitation Kinetics of Lithium Carbonate (Li_2CO_3). Master thesis. Aalto University - School of Chemical Technology. Espoo.

Aradóttir, E.S.P., Gunnarsson, I., 2013. Carbfix and sulfix sequestration projects.

Aradóttir, E.S.P., Gunnarsson, I., Sigfússon, B., Gíslason, S.R., Oelkers, E.H., Stute, M., Matter, J.M., Snaebjörnsdottir, S.O., Mesfin, K.G., Alfredsson, H.A., Hall, J. Arnars-

son, M. Th., Dideriksen, K., Juliusson, B.M., Broecker, W.S., Gunnlaugsson, E., 2015a. Towards cleaner geothermal energy: Subsurface sequestration of sour gas emissions from geothermal power plants, in: International Geothermal Association (Ed.), World Geothermal Congress, pp. 1–12.

Aradóttir, E.S.P., Gunnarsson, I., Sigfússon, B., Gunnarsson, G., Júliusson, B.M., Gunnlaugsson, E., Sigurdardóttir, H., Arnarson, M.T., Sonnenthal, E., 2015b. Toward Cleaner Geothermal Energy Utilization: Capturing and Sequestering CO_2 and H_2S Emissions from Geothermal Power Plants. Transport in Porous Media 108, 61–84. doi:10.1007/s11242-014-0316-5.

Ármannsson, H., Fridriksson, T., Kristjánsson, B.R., 2005. CO_2 emissions from geothermal power plants and natural geothermal activity in Iceland. Geothermics 34, 286–296. doi:10.1016/j.geothermics.2004.11.005.

Aspen Technology Inc., 2017. Aspen plus. URL: https://www.aspentech.com/en/products/engineering/aspen-plus.

Baba, A., Chandrasekharam, D., 2022. Geothermal resources for sustainable development: A case study. International Journal of Energy Research 46, 20501–20518. doi:10.1002/er.7778.

Batini, F., Lisi, S., Guglielmetti, L., Bellini, F., Trinciarelli, V., Pucci, M., 2016. Well engineering and simulation for non-condensable gases total reinjection systems, in: European Geothermal Energy Council (Ed.), European Geothermal Congress, pp. 1–4.

Battaglia, G., Berkemeyer, L., Cipollina, A., Cortina, J.L., Fernandez de Labastida, M., Lopez Rodriguez, J., Winter, D., 2022. Recovery of Lithium Carbonate from Dilute Li-Rich Brine via Homogenous and Heterogeneous Precipitation. Industrial & engineering chemistry research 61, 13589–13602. doi:10.1021/acs.iecr.2c01397.

Battistelli, A., 2010. PROFILI wellbore flow simulator: from geothermal wells to GHG and acid gas injection wells: poster.

Bau, M., Dulski, P., 1996. Distribution of yttrium and rare-earth elements in the Penge and Kuruman iron-formations, Transvaal Supergroup, South Africa. Precambrian Research 79, 37–55. doi:10.1016/0301-9268(95)00087-9.

Bau, M., Möller, P., Dulski, P., 1997. Yttrium and lanthanides in eastern mediterranean seawater and their fractionation during redox-cycling. Marine Chemistry 56, 123–131. doi:10.1016/S0304-4203(96)00091-6.

Bauer, M., Freeden, W., Jacobi, H., Neu, T., 2014. Handbuch Tiefe Geothermie. Springer Berlin Heidelberg, Berlin, Heidelberg. doi:10.1007/978-3-642-54511-5.

Berner, R.A., Caldeira, K., 1997. The need for mass balance and feedback in the geochemical carbon cycle. Geology 25, 955–956.

Berstad, D., Nord, L.O., 2016. Acid gas removal in geothermal power plant in iceland. Energy Procedia 86, 32–40. doi:10.1016/j.egypro.2016.01.004.

Bhatia, S.C., 2014. Advanced renewable energy systems. Woodhead publishing India in energy, Woodhead, New Delhi.

Bonalumi, D., Bombarda, P., Invernizzi, C., 2017a. Potential performance of environmental friendly application of ORC and Flash technology in geothermal power plants. Energy Procedia 129, 621–628. doi:10.1016/j.egypro.2017.09.114.

Bonalumi, D., Bombarda, P., Invernizzi, C., 2017b. Zero emission geothermal flash power plant. Energy Procedia 126, 698–705. doi:10.1016/j.egypro.2017.08.302.

Borsukiewicz-Gozdur, A., Nowak, W., 2007. Maximising the working fluid flow as a way of increasing power output of geothermal power plant. Applied Thermal Engineering , 2074–2078doi:10.1016/j.applthermaleng.2006.11.013.

Bosia, C., Mouchot, J., Ravier, G., Seibel, O., Genter, A., 2021. Evolution of Brine Geochemical Composition During Operation of EGS Geothermal Plants (Alsace, France). Proceedings, 46th Workshop on Geothermal Reservoir Engineering .

Bozkurt, E., 2000. Timing of extension on the büyük menderes graben, western turkey, and its tectonic implications. Geological Society, London, Special Publications , 385–403doi:10.1144/GSL.SP.2000.173.01.18.

Bozkurt, E., 2007. Extensional v. contractional origin for the southern Menderes shear zone, SW Turkey: Tectonic and metamorphic implications. Geological Magazine , 1–20doi:10.1017/S0016756806002664.

Bozkurt, E., Oberhänsli, R., 2001. Menderes Massif (Western Turkey): Structural, metamorphic and magmatic evolution - a synthesis. International Journal of Earth Sciences , 679–708doi:10.1007/s005310000173.

Bozkurt, E., Park, L., 1994. Southern Menderes Massif: an incipient metamorphic core complex in western Anatolia, Turkey. Journal of the Geological Society 151, 213–216. doi:10.1144/gsjgs.151.2.0213.

Bracke, R., Huenges, E., Acksel, D., Amann, F., Bremer, J., Bruhn, D., Budt, M., Bussmann, G., Görke, J.U., Grün, G., Hahn, F., Hanßke, A., Kohl, T., Kolditz, O., Regenspurg, S., Reinsch, T., Rink, K., Sass, I., Schill, E., Schneider, C., Shao, H., Teza, D., Thien, L., Utri, M., Will, H., 2021. Roadmap Tiefengeothermie für Deutschland. doi:10.24406/IEG-N-645792.

Buddrus, J., Schmidt, B., 2014. Grundlagen der Organischen Chemie. De Gruyter Studium, De Gruyter. URL: https://books.google.de/books?id=LzV1BgAAQBAJ.

Bundesministerium für Wirtschaft und Energie, 2021. Dialog Klimaneutrale Wärme: Zielbild, Bausteine und Weichenstellungen 2030/2050.

Bundesverband Geothermie e. V. and gec-co Global Engineering, 2021. Tiefe Geothermie - Projekte in Deutschland 2021/22.

Burkhardt, J.J., Heath, G., Cohen, E., 2012. Life Cycle Greenhouse Gas Emissions from Electricity Generation: Update. doi:10.1111/j.1530-9290.2012.00474.x.

Caglayan, M.A. and Ötztürk, E.M. and Ötztürk, S. and Sav, H. and Akat, U., 1980. Some new data for southern Menderes Massif structural interpretation. Geological Engineering 10, 9–19.

Candan, O., Dora, O.Ö., Oberhänsli, R., Çetinkaplan, M., Partzsch, J., Warkus, F., Dürr, S., 2001. Pan-African high-pressure metamorphism in the Precambrian basement of the Menderes Massif, western Anatolia, Turkey. International Journal of Earth Sciences 89, 793–811. doi:10.1007/s005310000097.

Candan, O., Dora, O.Ö., Oberhänsli, R., Koralay, O.E., Çetinkaplan, M., Akal, C., Satır, M., Chen, F., Kaya, O., 2011. Stratigraphy of the Pan-African basement of the Menderes Massif and the relationship with Late Neoproterozoic/Cambrian evolution of the Gondwana. Bulletin of the Mineral Research and Exploration 142, 25–68.

Carneiro, R.A., Ratnapuli, R.C., de Freitas Cunha Lins, V., 2003. The influence of chemical composition and microstructure of API linepipe steels on hydrogen induced cracking and sulfide stress corrosion cracking. Materials Science and Engineering: A 357, 104–110. doi:10.1016/S0921-5093(03)00217-X.

Chabab, S., Cruz, J.L., Poulain, M., Ducousso, M., Contamine, F., Serin, J.P., Cézac, P., 2021. Thermodynamic Modeling of Mutual Solubilities in Gas-Laden Brines Systems Containing CO_2, CH_4, N_2, O_2, H_2, H_2O, NaCl, $CaCl_2$, and KCl: Application to Degassing in Geothermal Processes. Energies 14, 5239. doi:10.3390/en14175239.

Chabab, S., Poulain, M., Ducousso, M., Cézac, P., 2022. A thermodynamic modelling to predict the bubble-point pressure from available information (T, GLR) from geothermal processes to prevent degassing: Congress paper, in: European Geothermal Energy Council (Ed.), European Geothermal Congress, pp. 1–6.

Cheng, W., Li, Z., Cheng, F., 2013. Solubility of Li_2CO_3 in Na–K–Li–Cl brines from 20 to 90 °C. The Journal of Chemical Thermodynamics 67, 74–82. doi:10.1016/j.jct.2013.07.024.

Cliff, R., Meffan-Main, S., 2003. Evidence from Rb-Sr microsampling geochronology

for the timing of Alpine deformation in the Sonnblick Dome, SE Tauern Window, Austria. Geological Society, London, Special Publications 220, 159–172.

Condie, K.C., 1993. Chemical composition and evolution of the upper continental crust: Contrasting results from surface samples and shales. Chemical Geology 104, 1–37. doi:10.1016/0009-2541(93)90140-E.

Craig, H., Craig, V., 1972. Greek marbles: determination of provenance by isotopic analysis. Science (New York, N.Y.) 176, 401–403. doi:10.1126/science.176.4033.401.

Cramer, T., 2004. Multivariate Herkunftsanalyse von Marmor auf petrographischer und geochemischer Basis: Das Beispiel kleinasiatischer archaischer, hellenistischer und römischer Marmorobjekte der Berliner Antikensammlung und ihre Zuordnung zu mediterranen und anatolischen Marmorlagerstätten: Dissertation.

Diamond, L.W., Akinfiev, N.N., 2003. Solubility of CO_2 in water from −1.5 to 100 °C and from 0.1 to 100 MPa: evaluation of literature data and thermodynamic modelling. Fluid Phase Equilibria 208, 265–290. doi:10.1016/S0378-3812(03)00041-4.

DiPippo, R., 2012. Geothermal power plants: Principles, applications, case studies, and environmental impact. 3rd ed. ed., Butterworth-Heinemann, Amsterdam and Boston.

Dixon, J.E., Robertson, A.H.F. (Eds.), 1984. The Geological Evolution of the Eastern Mediterranean. Blackwell Scientific, Oxford, London, Edinburgh, Boston, Palo Alto, Melbourne.

Dora, O.Ö., Candan, O., Kaya, O., Koralay, O.E., Dürr, S., 2001. Revision of "Leptite-gneisses" in the Menderes Massif: A supracrustal metasedimentary origin. International Journal of Earth Sciences , 836–851doi:10.1007/s005310000102.

Drummond, S.E., 1981. Boiling and mixing of hydrothermal fluids: Chemical effects of mineral precipitation. Ph.D. Thesis. Pennsylvania State University. Pennsylvania.

Duan, Z., Møller, N., Weare, J.H., 1992a. An equation of state for the CH_4-CO_2-H_2O system: I. Pure systems from 0 to 1000°C and 0 to 8000 bar. Geochimica et Cosmochimica Acta 56, 2605–2617.

Duan, Z., Møller, N., Weare, J.H., 1992b. An equation of state for the CH_4-CO_2-H_2O system: II. Mixtures from 50 to 1000°C and 0 to 1000 bar. Geochimica et Cosmochimica Acta 56, 2619–2631. doi:10.1016/0016-7037(92)90348-M.

Duan, Z., Sun, R., 2003. An improved model calculating CO_2 solubility in pure water and aqueous NaCl solutions from 273 to 533 K and from 0 to 2000 bar. Chemical Geology 193, 257–271.

Duan, Z., Sun, R., Zhu, C., Chou, I.M., 2006. An improved model for the calculation of CO_2 solubility in aqueous solutions containing Na^+, K^+, Ca^{2+}, Mg^{2+}, Cl^-, and $SO_4{}^{2-}$. Marine Chemistry 98, 131–139.

Dubacq, B., Bickle, M.J., Evans, K.A., 2013. An activity model for phase equilibria in the H_2O–CO_2–NaCl system. Geochimica et Cosmochimica Acta 110, 229–252. doi:10.1016/j.gca.2013.02.008.

Dürr, S., Altherr, R., Keller, J., Okrusch, M., Seidel, E., 1978. The Median Aegean crystalline belt: Stratigraphy, structure, metamorphism and magmatism.

Eggeling, L., Herr, K., Goldberg, V., Siefert, D., Köhler, J., Kölbel, T., Reith, S., 2018. Schlussbericht zum Verbundprojekt ANEMONA. Anlagenmonitoring als Schlüsseltechnologie für den erfolgreichen Betrieb von Geothermiekraftwerken in Deutschland.

Ellis, A.J., Golding, R.M., 1963. The solubility of carbon dioxide above 100 °C in water and in sodium chloride solutions. American Journal of Science 261 (1963).

Engelmann, P., Köhler, B., Meyer, R., Dengler, J., Herkel, S., Bürger, V., Braungardt, S., Hesse, T., Sandrock, M., Maaß, C., Strodel, N., 2021. Systemische Herausforderung der Wärmewende: Abschlussbericht.

Enick, R.M., Klara, S.M., 1990. CO_2 solubility in water and brine under reservoir conditions. Chemical Engineering Communications 90, 23–33. doi:10.1080/00986449008940574.

Erdoğan, B., Günğör, T., 2004. The problem of the core-cover boundary of the Menderes Massif and an emplacement mechanism for regionally extensive gneissic granites, Western Anatolia (Turkey). Turkish Journal of Earth Sciences , 15–36.

European Commission, 2019. Communication from the Commission to the European Parliament, the European Council, the Council, the European economic and social Committee and the committee of the regions: The European Green Deal.

European Geothermal Energy Council, 2022. Geothermal Decade. URL: https://www.egec.org/geothermal-decade-2/.

Fechner, D., Kondek, M., Kölbel, T., Kolb, J., 2022. CO_2 handling in binary geothermal systems — A modelling approach for different CO_2 contents, salinity, pressure and temperature conditions. Renewable Energy 201, 780–791. doi:10.1016/j.renene.2022.10.127.

Fettes, D., Desmons, J. (Eds.), 2007. Metamorphic rocks: A classification and glossary of terms, recommendations of the International Union of Geological Sciences Subcommission on the Systematics of Metamorphic Rocks. Cambridge Univ. Press, Cambridge. URL: http://www.loc.gov/catdir/enhancements/fy0805/2007281854-b.html.

Fischer, W., Siedlarek, W., 1977. Wasserstoffentwicklung aus CO_2–haltigen wäßrigen Elektrolyten. Werkstoffe und Korrosion , 822–827.

Flexer, V., Baspineiro, C.F., Galli, C.I., 2018. Lithium recovery from brines: A vital raw material for green energies with a potential environmental impact in its mining and processing. Science of the Total Environment 639, 1188–1204.

Francke, H., 2021. Energy/exergy conversion factors of low enthalpy geothermal plants.

Frick, S., Kaltschmitt, M., Schröder, G., 2010. Life cycle assessment of geothermal binary power plants using enhanced low-temperature reservoirs. Energy 35, 2281–2294. doi:10.1016/j.energy.2010.02.016.

Fridriksson, T., Mateos, A., Audinet, P., Orucu, Y.E., 2016. Greenhouse gases from geothermal power production. doi:10.1596/24691.

Fridriksson, T., Mateos Merino, A., Orucu, A.Y., Audient, P., 2017. Greenhouse gas emissions from geothermal power production, in: Stanford Earth (Ed.), Workshop on Geothermal Reservoir Engineering, pp. 1–12.

Fries, D., Lebouil, S., Martin, C., Baujard, C., Ravier, G., Boguais, R., Amari, S., 2022. Lithium extraction through pilot scale tests under real geothermal conditions of the Upper Rhine Graben: Congress paper, in: European Geothermal Energy Council (Ed.), European Geothermal Congress, pp. 1–7.

Frondini, F., Caliro, S., Cardellini, C., Chiodini, G., Morgantini, N., 2009. Carbon dioxide degassing and thermal energy release in the Monte Amiata volcanic-geothermal area (Italy). Applied Geochemistry 24, 860–875. doi:10.1016/j.apgeochem.2009.01.010.

Gehrig, M., Lentz, H., Franck, E.U., 1986. The System Water-Carbon Dioxide-Sodium Chloride to 773 K and 300 MPa. Berichte der Bunsengesellschaft für physikalische Chemie 90, 525–533. doi:10.1002/bbpc.19860900606.

General Directorate of Mineral Research and Exploration (MTA), 2015. Geoscience map viewer and drawing editor. URL: http://yerbilimleri.mta.gov.tr/anasayfa.aspx.

Germann, K., Holzmann, G., Winkler, F.J., 1980. Determination of marble provenance: Limits of isotopic analyses. Archaeometry 22, 99–106.

Gessner, K., Collins, A.S., Ring, U., Güngör, T., 2004. Structural and thermal history of poly-orogenic basement: U-Pb geochronology of granitoid rocks in the southern Menderes Massif, Western Turkey. Journal of the Geological Society 161, 93–101. doi:10.1144/0016-764902-166.

Gessner, K., Gallardo, L.A., Markwitz, V., Ring, U., Thomson, S.N., 2013. What caused the denudation of the Menderes Massif: Review of crustal evolution, lithosphere structure, and dynamic topography in southwest Turkey. Gondwana Research 24, 243–274. doi:10.1016/j.gr.2013.01.005.

Gessner, K., Piazolo, S., Günğör, T., Ring, U., Kröner, A., Passchier, C.W., 2001. Tectonic significance of deformation patterns in granitoid rocks of the Menderes nappes, Anatolide belt, southwest Turkey. International Journal of Earth Sciences 89, 766–780. doi:10.1007/s005310000106.

Gessner, K., Ring, U., Johnson, C., Hetzel, R., Passchier, C.W., Günğör, T., 2001b. An active bivergent rolling-hinge detachment system: Central Menderes metamorphic complex in Western Turkey. Geology 29, 611–614.

Gessner, K., Ring, U., Lackmann, W., Passchier, C.W., Güngör, T., Anonymous, 1998. Structure and crustal thickening of the Menderes Massif, southwest Turkey, and consequences for large-scale correlations between Greece and Turkey. Bulletin of the Geological Society of Greece 32, 145–152.

Gessner, K., Ring, U., Passchier, C.W., Hetzel, R., 2002. Discussion on "Stratigraphic and metamorphic inversions in the central Menderes Massif: A new structural model", by Aral I. Okay. International Journal of Earth Sciences 91, 168–172. doi:10.1007/s005310100223.

Ghasemi, H., Paci, M., Tizzanini, A., Mitsos, A., 2013. Modeling and optimization of a binary geothermal power plant. Energy 50, 412–428. doi:10.1016/j.energy.2012.10.039.

Gilbert, K., Bennett, P.C., Wolfe, W., Zhang, T., Romanak, K.D., 2016. CO_2 solubility in aqueous solutions containing Na^+, Ca^{2+}, Cl^-, $SO_4{}^{2-}$ and $HCO_3{}^-$: The effects of electrostricted water and ion hydration thermodynamics. Applied Geochemistry 67, 59–67. doi:10.1016/j.apgeochem.2016.02.002.

Glodny, J., Kühn, A., Austrheim, H., 2008a. Geochronology of fluid-induced eclogite

and amphibolite facies metamorphic reactions in a subduction–collision system, bergen arcs, norway. Contributions to Mineralogy and Petrology 156, 27–48.

Glodny, J., Ring, U., Kühn, A., 2008b. Coeval high-pressure metamorphism, thrusting, strike-slip, and extensional shearing in the Tauern Window, Eastern Alps. Tectonics 27.

Gokcen, G., Yildirim (Özcan), N., 2008. Effect of Non-Condensable Gases on geothermal power plant performance. Case study: Kizildere Geothermal Power Plant-Turkey. International Journal of Exergy 5, 684. doi:10.1504/IJEX.2008.020832.

Gondesen, B., 2020. Säuren und Basen, Löslichkeitsprodukt, Komplexgleichgewichte, Elektrochemie. Chemie, Springer. URL: https://books.google.de/books?id=J1vlzQEACAAJ.

Gorgoni, C., Lazzarini, L., Pallante, P., Turi, B., 1998. An updated and detailed mineropetrographic and C-O stable isotopic reference database for the main Mediterranean marbles used in antiquity, in: Herrmann, J., Herz, N., Newman, R. (Eds.), ASMOSIA 5. London, pp. 1–25.

Grant, A., 2020. From Catamarca to Qinghai: the commercial scale direct lithium extraction operations. Jade Cove Partners: San Francisco, CA, USA .

Grosjean, C., Herrera Miranda, P., Perrin, M., Poggi, P., 2012. Assessment of world lithium resources and consequences of their geographic distribution on the expected development of the electric vehicle industry. Renewable and Sustainable Energy Reviews 16, 1735–1744. URL: https://www.sciencedirect.com/science/article/pii/S1364032111005594, doi:https://doi.org/10.1016/j.rser.2011.11.023.

Gunnarsson, I., Júliusson, B.M., Aradóttir, E.S.P., Sigfússon, B., Arnarson, M.T., 2015. Pilot scale geothermal gas separation, hellisheiði power plant, iceland, in: International Geothermal Association (Ed.), World Geothermal Congress, pp. 1–8.

Günther, D., Wapler, J., Langner, R., Helmling, S., Miara, M., Fischer, D., Zimmermann, D., Wolf, T., Wille-Hausmann, B., 2020. Wärmepumpen in Bestandsgebäuden: Ergebnisse aus dem Forschungsprojekt "WPsmart im Bestand" (Abschlussbericht).

Gürer, Ö.F., Sarica-Filoreau, N., Özburan, M., Sangu, E., Dogan, B., 2009. Progressive development of the Büyük Menderes Graben based on new data, Western Turkey. Geological Magazine 146, 652–673. doi:10.1017/S0016756809006359.

Haizlip, J.R., Güney, A., Tut Haklidir, F.S., Garg, S.K., 2012. The impact of high noncondensible gas concentration on well performance: Kizildere geothermal reservoir, turkey, in: Stanford Earth (Ed.), Workshop on Geothermal Reservoir Engineering, pp. 1–6.

Han, B., Anwar UI Haq, R., Louhi-Kultanen, M., 2020. Lithium carbonate precipitation by homogeneous and heterogeneous reactive crystallization. Hydrometallurgy 195, 105386. doi:10.1016/j.hydromet.2020.105386.

He, S., Morse, J.W., 1993. The carbonic acid system and calcite solubility in aqueous Na-K-Ca-Mg-Cl-SO_4 solutions from 0 to 90°C. Geochimica et Cosmochimica Acta 57, 3533–3554. doi:10.1016/0016-7037(93)90137-L.

Herrmann, L., Ehrenberg, H., Graczyk-Zajac, M., Kaymakci, E., Kölbel, T., Kölbel, L., Tübke, J., 2022. Lithium recovery from geothermal brine – an investigation into the desorption of lithium ions using manganese oxide adsorbents. Energy Advances doi:10.1039/D2YA00099G.

Herz, N., 1987. Carbon and oxygen isotopic ratios: a data base for classical greek and roman marble. Archaeometry 29, 35–43. doi:10.1111/j.1475-4754.1987.tb00395.x.

Herz, N., Dean, N.E., 1986. Stable isotopes and archaeological geology: the Carrara marble, northern Italy. Applied Geochemistry 1, 139–151. doi:10.1016/0883-2927(86)90045-4.

Hettkamp, T., 2020. Industrial Experiences with Downhole Geothermal Line-Shaft Production Pumps in Hostile Environment in the Upper Rhine Valley. Proceedings World Geothermal Congress, Reykjavik, Iceland, 2020 .

Hetzel, R., Reischmann, T., 1996. Intrusion age of pan-african augen gneisses in the southern menderes massif and the age of cooling after alpine ductile extensional deformation. Geological Magazine 133, 565–572. doi:10.1017/S0016756800007846.

Hoefs, J., 2015. Stable Isotope Geochemistry. Springer International Publishing, Cham. doi:10.1007/978-3-319-19716-6.

Hu, J., Duan, Z., Zhu, C., Chou, I.M., 2007. PVTx properties of the CO_2–H_2O and CO_2–H_2O–NaCl systems below 647 K: Assessment of experimental data and thermodynamic models. Chemical Geology 238, 249–267. doi:10.1016/j.chemgeo.2006.11.011.

Hua, G., Yuansheng, D., Lian, Z., Jianghai, Y., Hu, H., Min, L., Yuan, W., 2013. Trace and rare earth elemental geochemistry of carbonate succession in the middle gaoyuzhuang formation, pingquan section: Implications for early mesoproterozoic ocean redox conditions. Journal of Palaeogeography 2, 209–221.

Jacob, R., Saylor, B.Z., 2016. CO_2 solubility in multi-component brines containing NaCl, KCl, $CaCl_2$ and $MgCl_2$ at 297 K and 1–14 MPa. Chemical Geology 424, 86–95. doi:10.1016/j.chemgeo.2016.01.013.

Jiang, H., Panagiotopoulos, A.Z., Economou, I.G., 2016. Modeling of CO_2 solubility in single and mixed electrolyte solutions using statistical associating fluid theory. Geochimica et Cosmochimica Acta 176, 185–197. doi:10.1016/j.gca.2015.12.023.

Júliusson, B.M., Gunnarsson, I., Matthiasdottir, K.V., Markusson, S.H., Bjarnason, B., Sveinsson, O.G., Gíslason, T., Thorsteinsson, H.H., 2015. Tackling the Challenge of H_2S Emissions, in: International Geothermal Association (Ed.), World Geothermal Congress, pp. 1–5.

Kamila, Z., Kaya, E., Zarrouk, S.J., 2021. Reinjection in geothermal fields: An updated worldwide review 2020. Geothermics 89, 101970. doi:10.1016/j.geothermics.2020.101970.

Karamanderesi, İ.H., 2013. Characteristics of Geothermal Reservoirs in Turkey.

Kaunda, R.B., 2020. Potential environmental impacts of lithium mining. Journal of energy & natural resources law 38, 237–244.

Kaya, A., 2015. The effects of extensional structures on the heat transport mechanism: An example from the Ortakçı geothermal field (Büyük Menderes Graben, SW Turkey). Journal of African Earth Sciences 108. doi:10.1016/j.jafrearsci.2015.05.002.

Kaya, E., 2016a. Modelling reinjection into vapour-dominated two-phase systems: Part 1—experiments on model design. Geothermics 60, 175–195. doi:10.1016/j.geothermics.2015.12.005.

Kaya, E., 2016b. Modelling reinjection into vapour-dominated two-phase systems: Part 2- reinjection experiments on the 3d model. Geothermics 60, 196–217. doi:10.1016/j.geothermics.2015.12.006.

Kaya, E., Adityatama, D., Zarrouk, S.J., 2019. Investigation of pressure transient analysis methods for single-phase and CO_2-rich geothermal reservoirs. Renewable Energy 141, 162–180. doi:10.1016/j.renene.2019.03.140.

Kaya, E., Callos, V., Mannington, W., 2018. CO_2 –water mixture reinjection into two-phase liquid dominated geothermal reservoirs. Renewable Energy 126, 652–667. doi:10.1016/j.renene.2018.03.067.

Kaya, E., Zarrouk, S.J., 2017. Simulation of reinjection of non-condensable gas-water mixture into geothermal reservoirs, in: Stanford Earth (Ed.), Workshop on Geothermal Reservoir Engineering, pp. 1–14.

Kaya, E., Zarrouk, S.J., Kaya, 2017. Reinjection of greenhouse gases into geothermal reservoirs. International Journal of Greenhouse Gas Control 67, 111–129. doi:10.1016/j.ijggc.2017.10.015.

Kaya, E., Zarrouk, S.J., O'Sullivan, M.J., 2011. Reinjection in geothermal fields: A review of worldwide experience. Renewable and Sustainable Energy Reviews 15, 47–68. doi:10.1016/j.rser.2010.07.032.

Kelly, J.C., Wang, M., Dai, Q., Winjobi, O., 2021. Energy, greenhouse gas, and water life cycle analysis of lithium carbonate and lithium hydroxide monohydrate from brine and ore resources and their use in lithium ion battery cathodes and lithium ion batteries. Resources, Conservation and Recycling 174, 105762. doi:10.1016/j.resconrec.2021.105762.

Kiepe, J., Horstmann, S., Fischer, K., Gmehling, J., 2002. Experimental Determination and Prediction of Gas Solubility Data for CO_2 + H_2O Mixtures containing NaCl or KCl at Temperatures between 313 and 393 K and Pressures up to 10 MPa. Industrial & Engineering Chemistry Research 41, 4393–4398. doi:10.1021/ie020154i.

Kim, S.T., O'Neil, J.R., 1997. Equilibrium and nonequilibrium oxygen isotope effects in synthetic carbonates. Geochimica et Cosmochimica Acta 61, 3461–3475. doi:10.1016/S0016-7037(97)00169-5.

Kölbel, L., Kölbel, T., Sauter, M., Schäfer, T., Siefert, D., Wiegand, B., 2020. Identification of fracture zones in geothermal reservoirs in sedimentary basins: A radionuclide-based approach. Geothermics 85, 101764. doi:10.1016/j.geothermics.2019.101764.

Koralay, O.E., 2015. Late Neoproterozoic granulite facies metamorphism in the Menderes Massif, Western Anatolia/Turkey: implication for the assembly of Gondwana. Geodinamica Acta 27, 244–266. doi:10.1080/09853111.2015.1014987.

Koralay, O.E., Dora, O.Ö., Chen, F., Satır, M., Candan, O., 2004. Geochemistry and Geochonology of Orthogneisses in the Derbent (Alaşehir) Area, Eastern part of the

Ödemiş-Kiraz Submassif, Menderes Massif: Pan-African Magmatic Activity. Turkish Journal of Earth Sciences 13, 37–61.

Koschel, D., Coxam, J.Y., Rodier, L., Majer, V., 2006. Enthalpy and solubility data of CO_2 in water and $NaCl_{(aq)}$ at conditions of interest for geological sequestration. Fluid Phase Equilibria 247, 107–120. doi:10.1016/j.fluid.2006.06.006.

Lara Cruz, J.L., Contamine, F., Cézac, P., 2019. Experimental study of CO_2 solubility on NaCl and $CaCl_2$ solutions at 333.15 K and pressures up to 40.0 MPa. European Geothermal Congress, Den Haag, The Netherlands, 2019 .

Lassin, A., dos Santos, P.F., Ducousso, M., Cézac, P., André, L., 2022. Experimental measurements and modelling of thermodynamic properties of NaCl-$CaCl_2$ aqueous solutions up to high temperatures and CO_2 pressures: Congress paper, in: European Geothermal Energy Council (Ed.), European Geothermal Congress, pp. 1–7.

Lauf, T., Memmler, M., Schneider, S., 2021. Emissionsbilanz erneuerbarer Energieträger.

Lawrence, M.G., Greig, A., Collerson, K.D., Kamber, B.S., 2006. Rare earth element and yttrium variability in south east queensland waterways. Aquatic Geochemistry 12, 39–72. doi:10.1007/s10498-005-4471-8.

Layman, E.B., 2017. Geothermal Projects in Turkey: Extreme Greenhouse Gas Emission Rates Comparable to or Exceeding Those from Coal-fired Plants, in: Stanford Earth (Ed.), Workshop on Geothermal Reservoir Engineering, pp. 1–16.

Lips, A.L.W., Cassard, D., Sözbilir, H., Yilmaz, H., Wijbrans, J.R., 2001. Multistage exhumation of the Menderes Massif, western Anatolia (Turkey). International Journal of Earth Sciences 89, 781–792. doi:10.1007/s005310000101.

Liu, X., Zhang, Y., Shen, J., 2017. System performance optimization of ORC-based geoplant with R245fa under different geothermal water inlet temperatures. Geothermics 66, 134–142. doi:10.1016/j.geothermics.2016.12.004.

Liu, Y., Hou, M., Yang, G., Han, B., 2011. Solubility of CO_2 in aqueous solutions of NaCl, KCl, $CaCl_2$ and their mixed salts at different temperatures and pressures. The Journal of Supercritical Fluids 56, 125–129. doi:10.1016/j.supflu.2010.12.003.

Loos, S., Reischmann, T., 1999. The evolution of the southern Menderes Massif in SW Turkey as revealed by zircon dating. Journal of the Geological Society 156, 1021–1030.

Lucile, F., Cézac, P., Contamine, F., Serin, J.P., Houssin, D., Arpentinier, P., 2012. Solubility of Carbon Dioxide in Water and Aqueous Solution Containing Sodium Hydroxide at Temperatures from (293.15 to 393.15) K and Pressure up to 5 MPa: Experimental Measurements. Journal of Chemical & Engineering Data 57, 784–789. doi:10.1021/je200991x.

Ludwig, K., 2003. User's manual for isoplot 3.00, a geochronlogical toolkit for Microsoft Excel. Berkeley Geochronl. Cent. Spec. Publ. 4, 25–32.

Malinin, S.D., Kurorskaya, N.A., 1975. Investigation of CO_2 solubility in a solution of chlorides at elevated temperatures and pressures of CO_2. Geokhimiya , 547–551.

Malinin, S.D., Savelyeya, N., 1972. The solubility of CO_2 in NaCl and $CaCl_2$ solutions at 25, 50, and 75 °C under elevated CO_2 pressures. Geokhimiya , 643–653.

Manfra, L., Masi, U., Turi, B., 1975. Carbon and oxygen isotope ratios of marbles from some ancient quarries of western anatolia and their archaeological significance. Archaeometry 17, 215–221.

Markham, A.E., Kobe, K.A., 1941. The Solubility of Carbon Dioxide and Nitrous Oxide in Aqueous Salt Solutions. Journal of the American Chemical Society 63, 449–454. doi:10.1021/ja01847a027.

Marscheider-Weidemann, F., Langkau, S., Eberling, E., Erdmann, L., Haendel, M., Krail, M., Loibl, A., Neef, C., Neuwirth, M., Rostek, L., et al., 2022. Raw materials for emerging technologies 2021. DERA Rohstoffinformationen .

McArthur, J.M., Howarth, R., Bailey, T., 2001. Strontium isotope stratigraphy: LOWESS version 3: best fit to the marine Sr-isotope curve for 0–509 Ma and accompanying look-up table for deriving numerical age. The Journal of Geology 109, 155–170.

McCrea, J.M., 1950. On the isotopic chemistry of carbonates and a paleotemperature scale. The Journal of Chemical Physics 18, 849–857. doi:10.1063/1.1747785.

Merbecks, T., Bombarda, P., Saar, M.O., Silva, P., Alfani, D., 2022. Investigating the design of ORC heat introduction for singe- and two-phase geofluid brines with and without non-condensable gases: Congress paper, in: European Geothermal Energy Council (Ed.), European Geothermal Congress, pp. 1–4.

Mergner, H., Schaber, K., 2018. Performance analysis of an evaporation process of plate heat exchangers installed in a Kalina power plant. Energy 145, 105–115. doi:10.1016/j.energy.2017.12.105.

Mergner, H., Weimer, T., 2015. Performance of ammonia–water based cycles for power generation from low enthalpy heat sources. Energy 88, 93–100. doi:10.1016/j.energy.2015.04.084.

Meyer, E.E., Quicksall, A.N., Landis, J.D., Link, P.K., Bostick, B.C., 2012. Trace and rare earth elemental investigation of a Sturtian cap carbonate, Pocatello, Idaho: Evidence for ocean redox conditions before and during carbonate deposition. Precambrian Research 192-195, 89–106. doi:10.1016/j.precamres.2011.09.015.

Moeck, I., Weber, J., 2022. Metastudie zur nationalen Erdwärmestrategie: Ersatz fossiler Brennstoffe im Bereich Raumwärme und Warmwasser durch Geothermie als unverzichtbarer Bestandteil im Energiesektor Ökowärme bis 2045.

Mortimer, C.E., Müller, U., 2010. Chemie: Das Basiswissen der Chemie. 10., überarb. Aufl. ed., Thieme, Stuttgart.

Müller, W., Dallmeyer, R.D., Neubauer, F., Thöni, M., 1999. Deformation-induced resetting of Rb/Sr and ^{4}0Ar/^{3}9Ar mineral systems in a low-grade, polymetamorphic terrane (Eastern Alps, Austria). Journal of the Geological Society 156, 261–278.

Müller, W., Mancktelow, N.S., Meier, M., 2000. Rb–Sr microchrons of synkinematic mica in mylonites: an example from the DAV fault of the Eastern Alps. Earth and Planetary Science Letters 180, 385–397.

Mundhenk, N., Huttenloch, P., Kohl, T., Steger, H., Zorn, R., 2013. Metal corrosion in geothermal brine environments of the Upper Rhine Graben – Laboratory and on-site studies. Geothermics 46, 14–21. doi:10.1016/j.geothermics.2012.10.006.

Münzner, H., Schneiderhöhn, P., 1953. Das Sehnenschnittverfahren. Heidelberger Beiträge zur Mineralogie und Petrographie 3, 456–471. doi:10.1007/BF01129198.

Nighswander, J.A., Kalogerakis, N., Mehrotra, A.K., 1989. Solubilites of Carbon Dioxide in Water and in 1 wt% NaCl Solution at Pressures up to 10 MPa and Temperatures from 80 to 200 °C. Journal of Chemical and Engineering Data 34 (3) (1989).

Ogriseck, S., 2009. Integration of Kalina cycle in a combined heat and power plant, a case study. Applied Thermal Engineering 29, 2843–2848. doi:10.1016/j.applthermaleng.2009.02.006.

Origlia, F., Gliozzo, E., Gandin, A., Meccheri, M., Spangenberg, J.E., Memmi, I.T., 2012. Marbles and carbonate rocks from central Morocco: a petrographic, mineralogical and geochemical study. Environmental Earth Sciences 66, 209–222. doi:10.1007/s12665-011-1224-4.

Özer, S., Sözbilir, H., 2003. Presence and tectonic significance of Cretaceous rudist species in the so-called Permo-Carboniferous Göktepe Formation, central Menderes metamorphic massif, western Turkey. International Journal of Earth Sciences 92, 397–404. doi:10.1007/s00531-003-0333-z.

Passarella, M., Mountain, B.W., Zarrouk, S.J., Burnell, J., 2015. Experimental Simulation of Re-Injection of Non-Condensable Gases into Geothermal Reservoirs: Greywacke-Fluid Interaction, in: University of Auckland (Ed.), New Zealand Geothermal Workshop, pp. 1–7.

Pauwels, H., Fouillac, C., Fouillac, A., 1993. Chemistry and isotopes of deep geothermal saline fluids in the Upper Rhine Graben: Origin of compounds and water-rock interactions. Geochimica et Cosmochimica Acta 57, 2737–2749.

Peerawattuk, I., Bobicki, E.R., 2018. Lithium Extraction and Utilization: A Historical Perspective, in: Davis, B.R., Moats, M.S., Wang, S., Gregurek, D., Kapusta, J., Battle, T.P., Schlesinger, M.E., Alvear F., G.R., Jak, E., Goodall, G., Free, M.L., Asselin, E., Chagnes, A., Dreisinger, D., Jeffrey, M., Lee, J., Miller, G., Petersen, J., Ciminelli, V.S.T., Xu, Q., Molnar, R., Adams, J., Liu, W., Verbaan, N., Goode, J., London, I.M., Azimi, G., Forstner, A., Kappes, R., Bhambhani, T. (Eds.), Extraction 2018. Springer International Publishing, Cham. The Minerals, Metals & Materials Series, pp. 2209–2224. doi:10.1007/978-3-319-95022-8{\textunderscore}186.

Pehnt, M., 2006. Dynamic life cycle assessment (LCA) of renewable energy technologies. Renewable Energy 31, 55–71. doi:10.1016/j.renene.2005.03.002.

Pereira, H.A., Mironuk Frescura, L., Menezes de Brumelhaus, B., Duarte, R., Villetti, M.A., Hilgemann, M., Barcellos da Rosa, M., 2019. A multivariate approach at the thermodynamic properties of rare earth elements. Thermochimica Acta 678, 178315. doi:10.1016/j.tca.2019.178315.

Pfennig, A., 2004. Thermodynamik der Gemische. Springer Berlin Heidelberg, Berlin, Heidelberg. doi:10.1007/978-3-642-18923-4.

Piper, D.Z., Bau, M., 2013. Normalized rare earth elements in water, sediments, and wine: Identifying sources and environmental redox conditions. American Journal of Analytical Chemistry 04, 69–83. doi:10.4236/ajac.2013.410A1009.

Pitzer, K.S. (Ed.), 1991. Activity coefficients in electrolyte solutions. 2. ed. ed., CRC Press, Boca Raton.

Portier, S., Rochelle, C., 2005. Modelling CO_2 solubility in pure water and NaCl-type waters from 0 to 300 °C and from 1 to 300 bar. Chemical Geology 217, 187–199. doi:10.1016/j.chemgeo.2004.12.007.

Pratiwi, A., Ravier, G., Genter, A., 2018. Life-cycle climate-change impact assessment of enhanced geothermal system plants in the Upper Rhine Valley. Geothermics 75, 26–39. doi:10.1016/j.geothermics.2018.03.012.

Régnier, J.L., Mezger, J.E., Passchier, C.W., 2007. Metamorphism of Precambrian–Palaeozoic schists of the Menderes core series and contact relationships with Proterozoic orthogneisses of the western Çine Massif, Anatolide belt, western Turkey. Geological Magazine 144, 1–38. doi:10.1017/S0016756806002640.

Régnier, J.L., Ring, U., Passchier, C.W., Gessner, K., Günğör, T., 2003. Contrasting metamorphic evolution of metasedimentary rocks from the Çine and Selimiye nappes in the Anatolide belt, western Turkey. Journal of Metamorphic Geology 21, 699–721.

Reich, R., Slunitschek, K., Danisi, R.M., Eiche, E., Kolb, J., 2022. Lithium Extraction Techniques and the Application Potential of Different Sorbents for Lithium Recovery from Brines. Mineral Processing and Extractive Metallurgy Review 1, 1–20. doi:10.1080/08827508.2022.2047041.

Reilinger, R., McClusky, S., Vernant, P., Lawrence, S., Ergintav, S., Cakmak, R., Ozener, H., Kadirov, F., Guliev, I., Stepanyan, R., Nadariya, M., Hahubia, G., Mahmoud, S., Sakr, K., ArRajehi, A., Paradissis, D., Al-Aydrus, A., Prilepin, M., Guseva, T., Evren, E., Dmitrotsa, A., Filikov, S.V., Gomez, F., Al-Ghazzi, R., Karam, G., 2006. GPS constraints on continental deformation in the Africa-Arabia-Eurasia continental collision zone and implications for the dynamics of plate interactions. Journal of Geophysical Research: Solid Earth 111, 1–26. doi:10.1029/2005JB004051.

REN21, 2020. Renewables 2020 Global Status Report.

Ricca, M., Belfiore, C.M., Ruffolo, S.A., Barca, D., Buergo, M.A.d., Crisci, G.M., La Russa, M.F., 2015. Multi-analytical approach applied to the provenance study of marbles used as covering slabs in the archaeological submerged site of baia (naples, italy): The case of the “villa con ingresso a protiro”. Applied Surface Science 357, 1369–1379. doi:10.1016/j.apsusc.2015.10.002.

Rimmelé, G., 2003. Structural and metamorphic evolution of the Lycian nappes and the Menderes Massif (Southwest Turkey): Geodynamic implications and correlations with the Aegean domain: Dissertation.

Rimmelé, G., Jolivet, L., Oberhänsli, R., Goffé, B., 2003. Deformation history of the high-pressure Lycian Nappes and implications for tectonic evolution of SW Turkey. Tectonics 22, 1–21. doi:10.1029/2001TC901041.

Ring, U., Gessner, K., Güngör, T., Passchier, C.W., 1999. The Menderes Massif of western Turkey and the Cycladic Massif in the Aegean—do they really correlate? Journal of the Geological Society 156, 3–6. doi:10.1144/gsjgs.156.1.0003.

Ring, U., Johnson, C., Hetzel, R., Gessner, K., 2003. Tectonic denudation of a Late Cretaceous Tertiary collisional belt: Regionally symmetric cooling patterns and their relation to extensional faults in the Anatolide belt of western Turkey. Geological Magazine 140, 421–441. doi:10.1017/S0016756803007878.

Ring, U., Willner, A.P., Lackmann, W., 2001. Stacking of nappes with different pressure-temperature paths: An example from the Menderes nappes of western Turkey. American Journal of Science 301, 912–944. doi:10.2475/ajs.301.10.912.

Rollinson, H.R., 1993. Using Geochemical Data: Evaluation, Presentation, Interpretation. Taylor & Francis Ltd.

Rönsch, S., 2015. Anlagenbilanzierung in der Energietechnik: Grundlagen, Gleichungen und Modelle für die Ingenieurpraxis. Springer Vieweg, Wiesbaden. URL: http://dx.doi.org/10.1007/978-3-658-07824-9, doi:10.1007/978-3-658-07824-9.

Rumpf, B., Nicolaisen, H., Öcal, C., Maurer, G., 1994. Solubility of carbon dioxide in aqueous solutions of sodium chloride: Experimental results and correlation. Journal of Solution Chemistry 23, 431–448. doi:10.1007/BF00973113.

Saldana, A.G., Kaya, E., Zarrouk, S.J., Callos, V., Mountain, B.W., 2016. Numerical Simulation of Mixed Brine-CO_2/H_2S-Rock Interaction During the Reinjection of Non Condensable Gases, in: Stanford Earth (Ed.), Workshop on Geothermal Reservoir Engineering, pp. 1–12.

Sandrock, M., Maaß, C., Weisleder, S., Westholm, H., Schulz, W., Löschan, G., Baisch, C., Kreuter, H., Reyer, D., Mangold, D., Riegger, M., Köhler, C., 2020. Kommunaler Klimaschutz durch Verbesserung der Effizienz in der Fernwärmeversorgung mittels Nutzung von Niedertemperaturwärmequellen am Beispiel tiefengeothermischer Ressourcen: Abschlussbericht.

Sanjuan, B., Gourcerol, B., Millot, R., Rettenmaier, D., Jeandel, E., Rombaut, A., 2022. Lithium-rich geothermal brines in Europe: An up-date about geochemical characteristics and implications for potential Li resources. Geothermics 101, 102385. URL: https://www.sciencedirect.com/science/article/pii/S0375650522000372, doi:https://doi.org/10.1016/j.geothermics.2022.102385.

Sanjuan, B., Millot, R., Innocent, C., Dezayes, C., Scheiber, J., Brach, M., 2016. Major geochemical characteristics of geothermal brines from the Upper Rhine Graben granitic basement with constraints on temperature and circulation. Chemical Geology 428, 27–47. doi:10.1016/j.chemgeo.2016.02.021.

Satır, M., Friedrichsen, H., 1986. The origin and evolution of the Menderes Massif, W-Turkey: A rubidium/strontium and oxygen isotope study. Geologische Rundschau 75/3, 703–714.

Savary, V., Berger, G., Dubois, M., Lacharpagne, J.C., Pages, A., Thibeau, S., Lescanne, M., 2012. The solubility of CO_2 + H_2S mixtures in water and 2 M NaCl at 120 °C and pressures up to 35 MPa. International Journal of Greenhouse Gas Control 10, 123–133. doi:10.1016/j.ijggc.2012.05.021.

Schlagermann, P., Mergner, H., Kölbel, T., Fuchs, S., Kather, A., Möllmann, G.U., Birner, J., Bartels, J., Wolfgramm, M., Mertens, S., Bücherl, M., Schaber, K.H., 2014. OSGa: Optimierte Stromerzeugung aus hoch salinaren Thermalwässern mit hohen Gasgehalten: Erhöhung der Verfügbarkeit, Wirkungsgradsteigerung und Betriebsoptimierung für einen langfristig sicheren und wirtschaftlichen Betrieb von Geothermiekraftwerken im Oberrheingraben: Abschlussbericht.

Schmidt, M., 2017. Rohstoffrisikobewertung–Lithium (DERA Rohstoffinformationen 33). Berlin: Deutsche Rohstoffagentur (DERA) in der Bundesanstalt für Geowissenschaften und Rohstoffe .

Schmidt, M., 2022. Rohstoffrisikobewertung - Lithium 2030.

Schuiling, R.D., 1962. On petrology, age and structure of the Menderes migmatite complex (SW-Turkey). Bulletin of the Mineral Research and Exploration 58, 71 – 84.

Seibt, A., Naumann, D., Hoth, P., 1999. Lösung und Entlösung von Gasen in Thermalwässern - Konsequenzen für den Anlagenbetrieb. Geothermie Report, GFZ GeoForschungszentrum Potsdam .

Seibt, A., Thorwart, K., 2011. Untersuchungen zur Gasphase geothermisch genutzter Tiefenwässer und deren Relevanz für den Anlagenbetrieb. Zeitschrift für Geologische Wissenschaften 39 3/4, 261–274.

Seibt, A., Wolfgramm, M., 2012. Hochsaline Thermalwässer als Wärmeübertrager. VDI-Berichte Nr. 2167.

Şengör, A.M.C., Yilmaz, Y., 1981. Tethian Evolution of Turkey: A Plate Tectonic Approach. Tectonophysics 75, 181–241.

Şengün, F., Erlandsson, V.B., Hogmalm, J., Zack, T., 2019. In situ Rb-Sr dating of K-bearing minerals from the orogenic Akçaabat gold deposit in the Menderes Massif, Western Anatolia, Turkey. Journal of Asian Earth Sciences 185, 104048.

Serpen, U., Aksoy, N., 2005. Reinjection problems in overpressured geothermal reservoirs, in: Stanford Earth (Ed.), Workshop on Geothermal Reservoir Engineering, pp. 1–8.

Serpen, U., Aksoy, N., 2010. Reassessment of Reinjection in Salavatli-Sultanhisar Geothermal Field, Turkey, in: International Geothermal Association (Ed.), World Geothermal Congress, pp. 1–9.

Serpen, U., Aksoy, N., Öngür, T., 2015. Reinjection Update of Salavatli Geothermal Field in Turkey, in: International Geothermal Association (Ed.), World Geothermal Congress, pp. 1–15.

SET Plan Secretariat, 2016. SET Plan - Declaration of intent on Strategic Targets in the context of an Intitiative for Global Leadership in Deep Geothermal Energy.

Setschenow, J., 1889. Über die konstitution der salzlösungen auf grund ihres verhaltens zu kohlensäure. Zeitschrift für Physikalische Chemie 4U. doi:10.1515/zpch-1889-0409.

Shi, C., Jing, Y., Xiao, J., Wang, X., Yao, Y., Jia, Y., 2017. Solvent extraction of lithium from aqueous solution using non-fluorinated functionalized ionic liquids as extraction agents. Separation and Purification Technology 172, 473–479. doi:10.1016/j.seppur.2016.08.034.

Shi, X., Zhou, D., Zhang, Z., Yu, L., Xu, H., Chen, B., Yang, X., 2011. Synthesis and properties of $Li_{1.6}Mn_{1.6}O_4$ and its adsorption application. Hydrometallurgy 110, 99–106.

Siefert, D., Wolfgramm, M., Kölbel, T., Glodny, J., Kolb, J., Eiche, E., 2021. Geothermal reservoir rocks of the Büyük Menderes Graben (Turkey): stratigraphic correlation by a multiproxy approach. Turkish Journal of Earth Sciences 30, 1008–1031. doi:10.3906/yer-2104-11.

Sigloch, H., 2013. Strömungsmaschinen. Carl Hanser Verlag GmbH & Co. KG, München. doi:10.3139/9783446436589.

Şimşek, Ş., 1985. Geothermal model of Denizli, Sarayköy-Buldan area. Geothermics 14, 393–417. doi:10.1016/0375-6505(85)90078-1.

Slunitschek, K., Kolb, J., Eiche, E., 2021. Geothermische Solen als Lithiumressource. Wiley Analytical Science Magazine 1.

Spry, A., 1983. Metamorphic Textures. Pergamon international Library of science, technology, engineering and social studies. [reprint. with corr.] ed., Pergamon Pr, Oxford and Frankfurt.

Spycher, N., Pruess, K., 2010. A Phase-Partitioning Model for CO_2–Brine Mixtures at Elevated Temperatures and Pressures: Application to CO_2-Enhanced Geothermal Systems. Transport in Porous Media 82, 173–196.

Spycher, N., Pruess, K., 2011. A model for thermophysical properties of CO_2-brine mixtures at elevated temperatures and pressures, in: Stanford Earth (Ed.), Workshop on Geothermal Reservoir Engineering, pp. 1–6.

Stober, I., Bucher, K., 2020. Geothermie. Springer Berlin Heidelberg, Berlin, Heidelberg. doi:10.1007/978-3-662-60940-8.

Stober, I., Wolfgramm, M., Birner, J., 2014. Hydrochemie der Tiefenwässer in Deutschland—hydrochemistry of deep waters in Germany. Z Geol Wiss 41, 5–6.

Stringfellow, W.T., Dobson, P.F., 2021a. Technology for Lithium Extraction in the Context of Hybrid Geothermal Power, in: Stanford Earth (Ed.), Workshop on Gethermal Reservoir Engineering, pp. 1–20.

Stringfellow, W.T., Dobson, P.F., 2021b. Technology for the Recovery of Lithium from Geothermal Brines. Energies 14. URL: https://www.mdpi.com/1996-1073/14/20/6805, doi:10.3390/en14206805.

Sun, Y., Song, X., Wang, J., Yu, J., 2012. Preparation of Li_2CO_3 by gas-liquid reactive crystallization of LiOH and CO_2. Crystal Research and Technology 47, 437–442. doi:10.1002/crat.201100571.

Tödheide, K., Franck, E.U., 1963. Das Zweiphasengebiet und die kritische Kurve im System Kohlendioxid - Wasser bis zu Drucken von 3500 bar. Zeitschrift für Physikalische Chemie 37, 387–401.

Tostevin, R., Shields, G.A., Tarbuck, G.M., He, T., Clarkson, M.O., Wood, R.A., 2016. Effective use of cerium anomalies as a redox proxy in carbonate-dominated marine settings. Chemical Geology 438, 146–162. doi:10.1016/j.chemgeo.2016.06.027.

Trimeric Corporation, 2015. Early-Phase Evaluation of CO_2 Recovery at Geothermal Facilities, Energy Sector Management Assistance Program.

Upton, P.S., Santoyo, E., 2003. A comprehensive evaluation of empirical correlations for computing the solubility of CO_2 in water, in: Stanford Earth (Ed.), Workshop on Geothermal Reservoir Engineering, pp. 1–7.

U.S. Geological Survey, 2021. Mineral Commodity Summaries. doi:10.3133/mcs2021.

Vaccaro, M., Batini, F., Stolzuoli, M., Bianchi, S., Pizzoli, R., Lisi, S., 2016. Geothermal ORC plant case study in Italy: Castelnuovo Pilot Project - Design & technical features, in: European Geothermal Energy Council (Ed.), European Geothermal Congress, pp. 1–7.

Valley, J.W., O'Neil, J.R. (Eds.), 1986. Stable isotopes and high temperature geological processes. volume 16 of *Reviews in Mineralogy*.

van Hinsbergen, D.J.J., Kaymakci, N., Spakman, W., Torsvik, T.H., 2010c. Reconciling the geological history of western Turkey with plate circuits and mantle tomography. Earth and Planetary Science Letters , 674–686.

Vengosh, A., Helvacı, C., Karamanderesi, I.H., 2002. Geochemical constraints for the origin of thermal waters from western Turkey. Applied Geochemistry 17, 163–183. doi:10.1016/S0883-2927(01)00062-2.

Vetter, C., Wiemer, H.J., Kuhn, D., 2013. Comparison of sub- and supercritical Organic Rankine Cycles for power generation from low-temperature/low-enthalpy geothermal wells, considering specific net power output and efficiency. Applied Thermal Engineering 51, 871–879. doi:10.1016/j.applthermaleng.2012.10.042.

Vidal, J., Genter, A., 2018. Overview of naturally permeable fractured reservoirs in the central and southern Upper Rhine Graben: Insights from geothermal wells. Geothermics 74, 57–73. doi:10.1016/j.geothermics.2018.02.003.

Villa, I.M., De Bièvre, P., Holden, N., Renne, P., 2015. IUPAC-IUGS recommendation on the half life of ^{87}Rb. Geochimica et Cosmochimica Acta 164, 382–385.

Vivas, C., Salehi, S., Tuttle, J.D., Rickard, B., 2020. Challenges and opportunities of geothermal drilling for renewable energy generation. GRC Transactions 44, 904–918.

Vorum, M., Fritzler, E.A., 2000. Comparative Analysis of Alternative Means for Removing Noncondensable Gases from Flashed-Steam Geothermal Power Plants. National Renewable Energy Laboratory, 2000 .

Wanger, T.C., 2011. The Lithium future-resources, recycling, and the environment. Conservation Letters 4, 202–206. doi:10.1111/j.1755-263X.2011.00166.x.

Wärmewende durch Geothermie, 2022. Wärmewende durch Geothermie - Zahlen und Fakten. URL: https://waermewende-durch-geothermie.de/#03.

Warren, I., 2021. Techno-Economic Analysis of Lithium Extraction from Geothermal Brines. doi:10.2172/1782801.

Webb, G.E., Kamber, B.S., 2000. Rare earth elements in holocene reefal microbialites: a new shallow seawater proxy. Geochimica et Cosmochimica Acta 64, 1557–1565. doi:10.1016/S0016-7037(99)00400-7.

Wisotzky, F., 2011. Angewandte Grundwasserchemie, Hydrogeologie und hydrogeochemische Modellierung: Grundlagen, Anwendungen und Problemlösungen. Earth sciences, Springer, Berlin and Heidelberg.

Wittmann, J., 2017. Electrification and Digitalization as Disruptive Trends: New Perspectives for the Automotive Industry?, in: Khare, A., Stewart, B., Schatz, R. (Eds.), Phantom Ex Machina. Springer International Publishing, Cham, pp. 137–159. doi:10.1007/978-3-319-44468-0{\textunderscore}9.

Yawger, R., 2022. Accelerating the Transition to Vehicle Electrification [PSMA Corner]. IEEE Power Electronics Magazine 9, 12–14. doi:10.1109/MPEL.2022.3193861.

Yi, W.T., Yan, C.Y., Ma, P.H., Li, F.Q., Wen, X.M., 2007. Refining of crude Li_2CO_3 via slurry phase dissolution using CO_2. Separation and Purification Technology 56, 241–248. URL: https://www.sciencedirect.com/science/article/pii/S1383586607000640, doi:https://doi.org/10.1016/j.seppur.2007.01.015.

Yildirim Özcan, N., 2010. Modeling, simulation and optimization of flashed-steam geothermal power plants from the point of view of noncondensable gas removal systems: Dissertation. Izmir.

Yildirim (Özcan), N., Gokcen, G., 2015. Thermodynamic performance of single-flash geothermal power plants from the point of view of noncondensable gas removal systems, in: International Geothermal Association (Ed.), World Geothermal Congress, pp. 1–7.

Yücetaş, İ., Ergiçay, N., Akın, S., 2018. Carbon dioxide injection field pilot in Umurlu Geothermal Field, Turkey. GRC Transactions 42.

Zeebe, R., Wolf-Gladrow, D., 2001. CO_2 in Seawater: Equilibrium, Kinetics, Isotopes. Elsevier Oceanography Series, Elsevier Science. URL: https://books.google.de/books?id=g3j3Zn4kEscC.

Zhao, H., Fedkin, M.V., Dilmore, R.M., Lvov, S.N., 2015. Carbon dioxide solubility in aqueous solutions of sodium chloride at geological conditions: Experimental results at 323.15, 373.15, and 423.15 K and 150 bar and modeling up to 573.15 K and 2000 bar. Geochimica et Cosmochimica Acta 149, 165–189. doi:10.1016/j.gca.2014.11.004.

Zhou, F., 2013. Research on heat transfer in geothermal wellbore and surroundings: Ph.D. Thesis.

Zhou, Z., Liang, F., Qin, W., Fei, W., 2014. Coupled reaction and solvent extraction process to form Li_2CO_3 : Mechanism and product characterization. AIChE Journal 60, 282–288. doi:10.1002/aic.14243.

Personal Information and Publications

Personal Information

Name	Dorothee Sonja Fechner (geb. Siefert)
LinkedIn	Dorothee Fechner on LinkedIn

Publications, Posters and Presentations

2022	**CO_2 handling in binary geothermal systems - a modelling approach for different CO_2 contents, salinity, pressure and temperature conditions** Renewable Energy 201, 780-791 (2022) Part III of this thesis *Dorothee Fechner (Siefert), Milena Kondek, Thomas Kölbel, Jochen Kolb*
2022	**Radiochemical monitoring of geothermal systems: Case study Bruchsal (Upper Rhine Graben)** Applied Geochemistry 147 (2022): 105509 *Lena Kölbel, Thomas Kölbel, Dorothee Fechner*
2022	**CO_2 handling in binary geothermal systems – modelling CO_2 contents, salinity and p-T conditions** Poster and Short Presentation European Geothermal Congress, 8 October 2021 *Dorothee Fechner (Siefert), Milena Kondek, Thomas Kölbel, Jochen Kolb*
2021	**Geothermal reservoir rocks of the Büyük Menderes Graben (Turkey): Stratigraphic correlation by a multiproxy approach** Presentation International Workshop on Geothermal Energy for sustainable Development (TÜBITAK, online), 8 December 2021 *Dorothee Fechner (Siefert), Markus Wolfgramm, Thomas Kölbel, Elisabeth Eiche, Jochen Kolb*

2021 **CO_2 handling in binary geothermal systems – modelling CO_2 contents, salinity and p-T conditions**
Presentation
Focus on Geothermal - Energy for the Weekend (IGC online Webinar), 8 October 2021
Dorothee Fechner (Siefert), Milena Kondek, Thomas Kölbel, Jochen Kolb

2021 **Geothermal reservoir rocks of the Büyük Menderes Graben (Turkey): Stratigraphic correlation by a multiproxy approach**
Turkish Journal of Earth Sciences 30 (2021)
Part II of this thesis
Dorothee Fechner (Siefert), Markus Wolfgramm, Thomas Kölbel, Elisabeth Eiche, Jochen Kolb

2021 **CO_2 handling in binary geothermal systems – a modelling approach to the geothermal power plant in Bruchsal with different CO_2 contents, total dissolved solids (TDS) and p-T conditions**
Presentation
Workshop KIT Future Fields: Towards Net-Zero - CO_2 disposal in the Geosphere (online), 9 March 2021
Karlsruhe Institute of Technology
Dorothee Fechner (Siefert), Milena Kondek, Thomas Kölbel, Jochen Kolb

2021 **CO_2 handling in binary geothermal systems – a modelling approach for different CO_2 contents, TDS and p-T conditions with implications on the geothermal power plant in Bruchsal, Germany**
Poster and Presentation
European Geothermal PhD Day, France and Switzerland (online), 2021
Dorothee Fechner (Siefert), Milena Kondek, Thomas Kölbel, Jochen Kolb, Elif Kaymakci

2020 **CO_2 Handling in Binary Geothermal Systems – a Modelling Approach for Bruchsal, Germany**
Presentation and Conference Paper
1st Geoscience and Engineering in Energy Transition Conference (online), November 2020
European Association of Geoscientists and Engineers
Dorothee Fechner (Siefert), Milena Kondek, Thomas Kölbel, Jochen Kolb

2020 **Identification of fracture zones in geothermal reservoirs in sedimentary basins: A radionuclide-based approach**
Geothermics 85 (2020)
Lena Kölbel, Thomas Kölbel, Martin Sauter, Thorsten Schäfer, Dorothee Fechner (Siefert), Bettina Wiegand

2020 **Geothermal project Bruchsal - Overview and new developments**
Poster and Presentation
IGC online - Upper Rhine Graben, 17 June 2020
Dorothee Fechner (Siefert), Elif Kaymakci, Jochen Benz, Mehmet Demirkan, Clemens Patzschke, Thomas Kölbel

2020 **Handling of CO_2 in binary geothermal systems based on modelling calculations**
Poster and Presentation
European Geothermal PhD Day, Pamukkale, Turkey, 2020
Dorothee Fechner (Siefert), Milena Kondek, Thomas Kölbel, Elif Kaymakci, Jochen Kolb

2019 **Calculation of the CO_2-solubility in thermal waters in the context of geothermal utilization**
CO_2-bubble point analysis in thermal waters of the Büyük Menderes Graben
SPE Germany 29 (2019)
Valentin Goldberg, Sebastian Held, Dorothee Fechner (Siefert), Fabian Nitschke, Thomas Kölbel

2019 **Characterization and differentiation of two different marbles as possible reservoir rocks in geothermal systems by stable isotope investigation**
An example from Western Anatolia, Turkey
Presentation
GEOMÜNSTER, 22-25 September 2019
Dorothee Fechner (Siefert), Markus Wolfgramm, Thomas Kölbel, Elisabeth Eiche, Jochen Kolb

2018 **Anlagenmonitoring als Schlüsseltechnologie für den erfolgreichen Betrieb von Geothermiekraftwerken in Deutschland**
Schlussbericht zum Verbundprojekt ANEMONA (2014-2018)
Reservoircharakterisierung mittels Radionuklidanalytik (AP10)
Optimierung geothermischer Betriebsmonitoringsysteme am Beispiel von Bruchsal (AP11)
Lena Kölbel (Eggeling), Konstantin Herr, Valentin Goldberg, Dorothee Fechner (Siefert), Jan Köhler, Thomas Kölbel, Sören Welter (Reith)

2018 **Risk factors within techno-economic evaluation of soft-stimulation measures**
Presentation and Conference Paper
43rd Workshop on Geothermal Reservoir Engineering, Stanford University, Stanford, California
Sören Welter (Reith), Dorothee Fechner (Siefert), Hanna Mergner, Thomas Kölbel, Wolfram Münch

2018 **Optimized handling of non-condensable gases in binary geothermal systems with two phase flow**
bubble point estimation and economical calculations
Presentation and Conference Paper
6th International Ph.D. Day of the AAEE Student Chapter, Vienna University of technology, Austria
Friday, 7 September 2018
Dorothee Fechner (Siefert)

Eidesstattliche Versicherung

Eidesstattliche Versicherung gemäß § 13 Absatz 2 Satz 1 Ziffer 4 der Promotionsordnung des Karlsruher Instituts für Technologie (KIT) für die KIT-Fakultät für Bauingenieur-, Geo- und Umweltwissenschaften

1. Bei der eingereichten Dissertation zu dem Thema *Carbon dioxide in binary geothermal systems - Origin, handling and utilisation possibilities* handelt es sich um meine eigenständig erbrachte Leistung.

2. Ich habe nur die angegebenen Quellen und Hilfsmittel benutzt und mich keiner unzulässigen Hilfe Dritter bedient. Insbesondere habe ich wörtlich oder sinngemäß aus anderen Werken übernommene Inhalte als solche kenntlich gemacht.

3. Die Arbeit oder Teile davon habe ich bislang nicht an einer Hochschule des In- oder Auslands als Bestandteil einer Prüfungs- oder Qualifikationsleistung vorgelegt.

   Titel der Arbeit: *Carbon dioxide in binary geothermal systems - Origin, handling and utilisation possibilities*

   Hochschule und Jahr: *Karlsruher Institut für Technologie, 2023*

   Art der Prüfungs- oder Qualifikationsleistung: *Dissertation*

4. Die Richtigkeit der vorstehenden Erklärungen bestätige ich.

5. Die Bedeutung der eidesstattlichen Versicherung und die strafrechtlichen Folgen einer unrichtigen oder unvollständigen eidesstattlichen Versicherung sind mir bekannt.

Ich versichere an Eides statt, dass ich nach bestem Wissen die reine Wahrheit erklärt und nichts verschwiegen habe.

Emmendingen, 8. Mai 2023 _____

(Dorothee Fechner)